



**HAL**  
open science

# Cathodic Protection of carbon steel in the tidal zone : involved mechanisms

Clément Genin

► **To cite this version:**

Clément Genin. Cathodic Protection of carbon steel in the tidal zone : involved mechanisms. Materials. Université de La Rochelle, 2023. English. NNT : 2023LAROS028 . tel-04544505

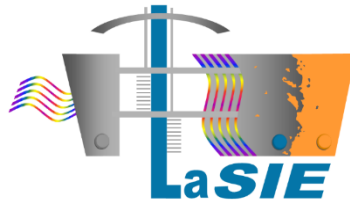
**HAL Id: tel-04544505**

**<https://theses.hal.science/tel-04544505>**

Submitted on 12 Apr 2024

**HAL** is a multi-disciplinary open access archive for the deposit and dissemination of scientific research documents, whether they are published or not. The documents may come from teaching and research institutions in France or abroad, or from public or private research centers.

L'archive ouverte pluridisciplinaire **HAL**, est destinée au dépôt et à la diffusion de documents scientifiques de niveau recherche, publiés ou non, émanant des établissements d'enseignement et de recherche français ou étrangers, des laboratoires publics ou privés.



La Rochelle Université

École Doctorale  
618 - EUCLIDE



Laboratoire des Sciences de l'Ingénieur pour l'Environnement (LaSIE)  
UMR-CNRS 7356

Thèse de Doctorat  
Présentée le 23/10/2023

par Clément GENIN

pour l'obtention du grade de Docteur de La Rochelle Université

Discipline : Génie Des Matériaux

## Cathodic Protection of Carbon Steel in Tidal Zone: Involved Mechanisms

*Protection Cathodique des aciers au carbone en Zone de Marnage :  
Mécanismes Impliqués*

---

**Pr. Bruno VUILLEMIN**  
**Pr. Virginie ROCHE**

Professeur, Université de Bourgogne, Rapporteur  
Professeure, Université Grenoble Alpes,  
Rapportrice

**Dr. Nadine PEBERE**  
**Pr. Philippe REFAIT**

Directrice de Recherche, CNRS  
Professeur, La Rochelle Université, Directeur de  
thèse

**Dr. Marc JEANNIN**

Maître de Conférence HDR, La Rochelle Université,  
Directeur de thèse

**Dr. Abdelkader MEROUFEL**  
**Anne-Marie GROLLEAU**

Senior Researcher, RISE, Invité  
Expert Senior, Naval Group Research, Expert  
Scientifique Industriel, Invitée

**Yves DENOS**

Ingénieur Chercheur EDF, Invité







## **Acknowledgments**

*First of all, I would like to express my gratitude to Naval Group and the Laboratoire des Sciences de l'Ingénieur pour l'Environnement (LaSIE) for allowing me to carry out my doctoral years among them, between La Rochelle and Cherbourg.*

*Entering the world of scientific research has not always been a smooth journey; there were projects that were too ambitious, experiments that did not succeed, and others that were carried out successfully but not without difficulties. However, there were also successes. All these opportunities to learn, move forward, and progress would have been real obstacles without Philippe and Marc. I have great thoughts and much gratitude for them, who supervised me together, complementing each other in the assistance they provided. Thank you.*

*I would also like to express my thanks to Anne-Marie, for the support and assistance she provided me, especially considering the context in which this project started (covid 19). Anne-Marie also enabled me to successfully conduct the most audacious experiment of my thesis project in the Naval Group corrosion laboratory.*

*In the corrosion laboratory of Naval Group, Alexia Bonnifet often accompanied me to help set up this simulation of the tidal zone experiment, find the right people, or prepare the coupons on time. I know she also spent a lot of time checking and performing control measurements and trying as much as possible to solve any problems that might arise in this experiment. A big thank you to Alexia, who supported me and greatly contributed to the success of this experimentation.*

*Regarding this project in the manipulation department at Naval Group, I owe a lot to Mathieu Lemaire and Bruno Peraudeau, the laboratory handymen who helped me a lot in the design and installation of the electrical system that connected all the samples to the cathodic protection system while allowing individual measurements on each of them. It was really no small feat, and without them, this experiment would have been significantly delayed. Many thanks for your help.*

*My thoughts then go to the entire team of the Naval Group corrosion laboratory who welcomed me during coffee breaks and with whom I could exchange technical or non-technical topics. Thanks to them for their hospitality.*

*Finally, I would like to have a thought for all the friends/colleagues, doctoral or post-doctoral, from the laboratory with whom I exchanged a lot over coffees or other beverages outside the laboratory. Without this team, this atmosphere, and this particularly fraternal and convivial working environment, this thesis would not have had the same flavor.*

*I would like to conclude by mentioning my two accomplices, Ismail and Caro(line), with whom I spent incredible moments. Our trio has always been united in trials as well as in successes, technical points at McEwan's, the doctoral conference, Slovenia, etc... What memories... Caro, always there to have a coffee, discuss, and laugh, you have been my alter ego throughout these years. When one of us is around, the other is never far away. We shared many moments both professionally and personally together... May it continue. Thank you for being there and supporting me as you did!*



# Contents

General Introduction (En) .....	1
References .....	7
Introduction Générale (Fr) .....	9
Références .....	16
Chapter I: Bibliography .....	19
I.1 Introduction .....	22
I.1.1 Marine medium .....	22
I.1.2 Carbon steel and marine medium .....	23
I.2 Marine corrosion mechanisms.....	24
I.2.1 The different local corrosion mechanisms occurring on carbon steel.....	25
I.2.2 Typical marine corrosion products .....	27
I.2.3 Corrosion under thin electrolyte layer .....	29
I.2.4 Corrosion in the tidal zone .....	33
I.3 Cathodic protection .....	39
I.3.1 Cathodic protection, the principle.....	39
I.3.2 Calcareous deposit: a consequence of cathodic protection.....	40
I.3.3 Cathodic protection in the tidal zone .....	45
Conclusion.....	47
References .....	49
Chapter II: Material and Methods .....	55
II.1 Electrochemical methods.....	59
II.1.1 Three-electrode set-up.....	59
II.1.2 Open circuit potential monitoring .....	60
II.1.3 Voltammetry.....	60
II.1.4 Potentiostatic method (or chronoamperometry) .....	63
II.1.5 Electrochemical Impedance Spectroscopy (EIS) [6].....	63
II.2 Characterization techniques .....	68
II.2.1 X-Ray Diffraction.....	68
II.2.2 Micro Raman spectrometry.....	69
II.2.3 Optical microscopy .....	70
References .....	72
Chapter III: Mineral Layer Evolution, from Immersion to Splash Zone .....	75

III.1 Introduction .....	78
III.2 Experimental features.....	79
III.2.1 Structure design [3] .....	79
III.2.2 Mineral layer analysis – methodology.....	81
III.3 Results .....	83
III.3.1 XRD analysis.....	84
III.3.2 Raman analysis .....	87
III.3.3 Corrosion rate estimation.....	90
III.4 Discussion.....	93
III.5 Conclusion .....	99
References .....	100
<b>Chapter IV: Cathodic Protection of Carbon Steel in Thin Layers of Seawater .....</b>	<b>105</b>
Introduction: .....	107
References .....	110
Cathodic protection of carbon steel in thin layers of seawater .....	111
<b>Chapter V: Cathodic Protection of Carbon Steel in Simulated Tidal Zone – Laboratory Scale Experiment.....</b>	<b>129</b>
V.1 Introduction .....	132
V.2 Materials and methods.....	132
V.2.1 Tide simulation .....	132
V.2.2 Samples design .....	134
V.2.3 Cathodic protection design .....	136
V.2.4 Measurement principle.....	138
V.3 Results and Discussions .....	143
V.3.1 Monitoring of CP parameters (I&E) over time .....	143
V.3.2 Mineral layer characterization .....	156
Conclusions: .....	167
References .....	170
<b>General Conclusion and Prospects .....</b>	<b>174</b>
References: .....	182



## General Introduction



*“Human activities, principally through emissions of greenhouse gases, have unequivocally caused global warming, with global surface temperature reaching 1.1°C above 1850-1900 in 2011-2020. Global greenhouse gas emissions have continued to increase over 2010-2019, with unequal historical and ongoing contributions arising from unsustainable energy use, land use and land-use change, lifestyles and patterns of consumption and production across regions, between and within countries, and between individuals (high confidence).”*

**Climate Change 2022: Adaptation and Vulnerability** [1].

A central milestone in the fight against climate change is the Paris Agreement, which aims to limit the global temperature increase to well below 2°C. Negotiated during the United Nations Framework Convention on Climate Change (COP21) in Paris 2015, this ambitious goal requires substantial reductions in global greenhouse gas emissions over the coming decades [2]. The global effort to combat climate change is being propelled by a combination of *international* climate agreements, growing *national* commitments to climate action, and an increasing awareness among the public. These collective efforts are driving initiatives to address climate change across various levels of governance. Mitigation policies have played a key role in reducing global energy and carbon intensity, leading to significant reductions in greenhouse gas emissions in several countries over the past decade. The emergence of affordable low-emission technologies has presented numerous options for sustainable energy use in sectors such as energy, buildings, transportation, and industry. In addition, the implementation of adaptation strategies not only helps mitigate climate risks but also contributes to sustainable development [1]. A key strategy in achieving this objective is the widespread adoption of renewable energy sources to displace carbon-intensive energy production. The European Union has set renewable energy targets, aiming for a contribution of at least 20% to total energy consumption by 2020 and 27% by 2030 [2]. Achieving this transition hinges on increasing renewable energy production, enhancing energy efficiency, and restraining overall energy consumption [2].

Offshore wind energy is a main actor in the renewable energy landscape. The growth of offshore wind projects in Europe and worldwide highlights the escalating interest in this renewable source [2]. Research anticipates a significant expansion of renewable wind energy use, with projections indicating that approximately half of the world's energy supply could be of renewable origin by 2040 [3]. This transition is expected to substantially reduce carbon dioxide emissions [3]. Wind energy, due to its mature status and rapid expansion has emerged as a preferred choice for governments [3].

Upscaling onshore wind farm is increasingly difficult, because of societal objections and the rarefaction of locations with sufficient exposure and size. Thus, the benefits of locating wind farms offshore become more apparent, particularly as technological and economic barriers are overcome. [4]

In this context, Naval Energy (a Naval Group Subsidiary from 2017 to 2021) aimed to develop an offshore wind farm. They imagined floating offshore wind turbines (OWT) entirely made out of steel as presented in figure 1 [5]. Steel plays a crucial role in the modern world as it serves not only as a fundamental material for construction and infrastructure but also enables a diverse range of manufacturing processes. Moreover, it holds an indispensable position in global research and development initiatives [6].

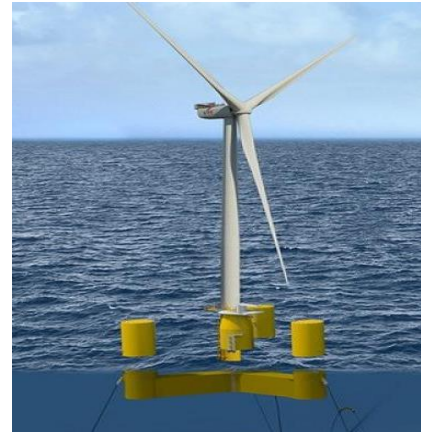


Figure 1: Steel floating wind turbine designed by Naval Energy [5]

The longevity and durability of offshore structures, basically constructed from carbon steel, are challenged by their constant exposure to the harsh marine environment. Platforms like OWT, converter platforms or even harbor wharfs and / or sheet piles are designed with a minimum intended lifetime of 25 years [2]. Seawater's corrosive nature, influenced by salinity, oxygen concentration, pH levels (typically 7.8–8.3), and temperature, influence the steel corrosion mechanisms. Various forms of corrosion, (uniform corrosion, pitting, crevice, galvanic corrosion, and erosion corrosion etc.) can be initiated by factors like waves, winds, and microorganisms. Stress corrosion cracking and corrosion fatigue can also be enhanced by these environmental elements [2].

To prevent corrosion, different strategies are employed for the various components of an OWT for instance, often using a combination of techniques. The OWT's turbine, tower, transition piece, and foundation experience atmospheric corrosion unless they are submerged. The foundation and transition piece are subdivided in different zones: at the bottom, the submerged underwater zone (below the low tide level), above, the tidal water zone affected by tides and external factors, and in the upper part, the splash water zone susceptible to waves and salt deposition because of droplets projection and ocean spray [2]. Corrosion is notably pronounced in these zones due to factors like high chloride concentrations, moisture, and pH fluctuations during wet and dry cycles [2].

Monopiles, integral to OWTs, incorporate the transition piece within this zone, connecting the monopile to the wind turbine tower [2]. Protecting these structures involves a range of measures such as (organic) coatings, corrosion allowances to counter corrosion-induced loss, and cathodic protection systems like galvanic anode cathodic protection (GACP) or impressed current cathodic protection (ICCP). Considering the substantial steel quantities in use (current monopiles weigh up to 805 tons), safeguarding against corrosion is of capital importance [2].

The concept of "corrosion allowance" involves consider larger steel thicknesses during the design as a form of corrosion protection. This serves as a backup strategy in case conventional protection systems fail. Additionally, corrosion allowance could be necessary to overcome the time gap until the complete polarization of the structure. According to Bandara et al. [7], fatigue corrosion arises due to synergetic interactions among the environment, material microstructure, and cyclic loads. The mechanisms underlying the process of aqueous fatigue corrosion can be described as follows: cracking occurs at corrosion pits due to high stress concentrations, reduced crack closure, and electrochemical attack. Combined corrosion and fatigue damage have been observed to exceed the sum of their individual effects. The thickness is determined based on the anticipated fatigue corrosion rate of the steel alloy in its environment. The recommended range for total corrosion allowance (i.e. the total thickness loss estimated in case of malfunction of the corrosion protection systems) between 0.2 and 1.2 cm according to DIN 50929-3 (2018), as reported in [7].

Cathodic protection systems are widely employed for various steel structures such as ships and marine infrastructures, including harbor wharfs and sheet piles. These systems work by decreasing the electrical potential of immersed structures, thereby slowing down corrosion (oxidation) processes. This can be achieved through either galvanic "sacrificial" anodes (GACP method) or inert anodes (ICCP method) [2], [8]. Impressed current cathodic protection (ICCP) represents an emerging technique in offshore wind farm construction. This method, already used for ships and waterway infrastructure, supplies direct current (DC) to the steel surface with a current generator through inert anodes [9]. Galvanic anodes facilitate polarization through the galvanic reaction of a less noble material compared to the steel structure. In the context of offshore structures, aluminum-based galvanic anodes are primarily preferred in seawater due to their high electrochemical efficiency and lightweight nature. Whilst GACP offers advantages such as its application to intricate foundations like jackets and minimal maintenance, it requires a significant volume of anode material and can be challenging to replace. For the protection of steel structures in offshore wind turbines or harbor structures for instance, substantial amounts of anode material are often necessary.

The issue of documenting corrosion protection in the tidal zone is intrinsically tied to structural design considerations and the potential necessity for future repairs. Within the tidal zone, the challenge of coating repair is most pronounced, and often, areas up to at least mean sea level (MSL) are deemed impractical to repair without resorting to high-cost cofferdam installations. Moreover, any repair work carried out in a humid environment tends to suffer from limited durability [10]. Ørsted, an experimented Danish company in the OWT field use electrical resistance corrosion sensors for OWT corrosion monitoring applications. These sensors have been tested and proofed in many conditions. They present rather good reliability except in the tidal zone because of the cyclic immersion character of the zone. Buhr et al., in their last publication, concluded that the reliability of current methods for verifying the performance of cathodic protection in the tidal zone remains a subject of uncertainty [10]. Techniques such as drop cell measurements, stabbing electrodes, and gravimetric coupons are called into question in this context [10].

On the other hand, various different studies observed a possible galvanic coupling between the tidal zone and the low water zone (below the low tide level). In 2012, Melchers et al. highlighted a minimum in corrosion rate in the tidal zone for continuous vertical structures exposed to both low water zone and tidal zone [11]. This low corrosion rate is due to the effect of differential aeration (a free corrosion phenomenon) between the tidal zone and the low water zone [11]. More recently, Ph. Refait et al. in 2015 concluded about CP persistence in the tidal zone due to a continuous residual seawater film on the steel after ebb tide [12]. In 2019, Law et al. noticed the same phenomenon on wharf structures exposed to cyclic immersion. And even more recently Erdogan et al. highlighted the existence of macro galvanic cells in the tidal zone due to this residual seawater persistence [13]. However, none of the cited studies is able to determine on the temporal efficiency of the CP persistence nor the protection level achieved in the tidal zone.

In addition, the exploitation of iron can lead to various ecological impacts across different stages of the process, such as deforestation on a large scale, soil erosion and disruption of local ecosystems, substantial water usage etc. contributing to significant greenhouse gas emissions. Moreover, the intensive extraction of metals over recent centuries raises concerns about their long-term availability for future generations. The tension between the finite geological availability of metals and their growing demand is a crucial issue to consider in the context of future requirements [14]. Despite their geological availability being constrained by their formation through geological events spanning millions of years, metals can be regenerated through recycling processes. The circular economy further

emphasizes the significance of efficient resource utilization, ensuring that resources are allocated optimally to products and services, thereby contributing to a sustainable future for all. Consequently, all steel products necessitate meticulous design for efficiency, durability, ease of reusability, remanufacturing, and eventual recycling [15].

In this regard, a study about cathodic protection of carbon steel in the tidal zone makes perfect sense. Indeed, better understanding the spatiotemporal parameters of CP in tidal zone could help:

- decrease installation costs and maintenance of organic coatings,
- decrease the sacrificial thickness of corrosion allowances and consequently save iron resources
- decrease the greenhouse gases emission per OWT, and / or sheet piles, and / or wharfs etc.

To answer this problematic, the presented PhD works have been divided in 3 main research sections. The first research section (*Chapter III: Mineral Layer Evolution, from Immersion Zone to Splash Zone*) deals with an a posteriori study of in situ CP in the commercial seaport of La Rochelle. Interconnected carbon steel coupons were exposed in La Rochelle natural tidal zone (during the J. Duboscq PhD works, 2016-2019[16]). The whole mineral layers covering the samples after 33 and 52 months of CP have been analyzed and the residual corrosion rate of the metal have been estimated to determine the CP efficiency transition zone.

In a second step, investigations were led on sufficiently protected and insufficiently protected steel behavior under thin electrolyte layer. The aim here was to investigate the steel behavior during the emerged phase at a laboratory scale (*Chapter IV: Cathodic Protection of Carbon Steel in Thin Layers of Seawater*).

Finally, the last axis is about the creation of a laboratory scale tidal zone to perform CP in the tidal zone with a direct monitoring of the CP parameters. CP current and potential evolution as a function of time in a simulated tidal zone (with natural seawater) are discussed in chapter V (*Chapter V: Cathodic Protection of Carbon Steel in Simulated Tidal Zone: Laboratory Scale Experiment*).

The project was initiated by Naval Group Marine Corrosion Department as part of their R&D program to sustain the development of OWT performed by Naval Energy. This research program is also of prime interest for other Naval Group infrastructures impacted by tides or naval platforms impacted by corrosion phenomena whether at the floating line or at larger zones submitted to immersed/emerged situations.

## References

- [1] H.-O. Pörtner *et al.*, « Climate Change 2022: Impacts, Adaptation and Vulnerability. Working Group II to the Sixth Assessment Report of the Intergovernmental Panel on Climate Change », *Cambridge University Press*, p. 3-33, 2022, doi: doi:10.1017/9781009325844.001.
- [2] T. Kirchgeorg, I. Weinberg, M. Hörnig, R. Baier, M. J. Schmid, and B. Brockmeyer, « Emissions from corrosion protection systems of offshore wind farms: Evaluation of the potential impact on the marine environment », *Marine Pollution Bulletin*, vol. 136, p. 257-268, nov. 2018, doi: 10.1016/j.marpolbul.2018.08.058.
- [3] K. Dai, A. Bergot, C. Liang, W.-N. Xiang, and Z. Huang, « Environmental issues associated with wind energy – A review », *Renewable Energy*, vol. 75, p. 911-921, mars 2015, doi: 10.1016/j.renene.2014.10.074.
- [4] E. A. Willsteed, S. Jude, A. B. Gill, and S. N. R. Birchenough, « Obligations and aspirations: A critical evaluation of offshore wind farm cumulative impact assessments », *Renewable and Sustainable Energy Reviews*, vol. 82, p. 2332-2345, févr. 2018, doi: 10.1016/j.rser.2017.08.079.
- [5] « Saipem and Naval Energies sign an agreement for the acquisition of Naval Energies' floating wind business », *Naval Group*. <https://www.naval-group.com/en/saipem-and-naval-energies-sign-agreement-acquisition-naval-energies-floating-wind-business> (consulté le 29 août 2023).
- [6] « Steel industry economic impact », *worldsteel.org*. <https://worldsteel.org/steel-topics/statistics/steel-industry-economic-impact/> (consulté le 29 août 2023).
- [7] C. S. Bandara, U. I. Dissanayake, and P. B. R. Dissanayake, « Novel Method for Developing S-N Curves for Corrosion Fatigue Damage Assessment of Steel Structures », presented at 6<sup>th</sup> International conference on Structural Engineering and construction Management, Kandy, Sri Lanka: CSECM, 2015, p. 100-104.
- [8] J. Creus, R. Sabot, and P. Refait, « Corrosion et protection des métaux en milieu marin », *Matériaux | Corrosion vieillissement*, vol 2, p. 14, 2013.
- [9] M. Roche, « L'ESSENTIEL SUR LA PROTECTION CATHODIQUE », *Cefracor*, p. 14, 2015.
- [10] B. Buhr, S. Ruth. E., A. M. Diederichs, L. P. Løvendahl Raun, and Y. Rezanja, « Benefits of corrosion monitoring for offshore wind structures », presented at Association for Materials Protection and Performance, Denver, Colorado, 2023, p. 11.
- [11] R. E. Melchers and R. Jeffrey, « Corrosion of long vertical steel strips in the marine tidal zone and implications for ALWC », *Corrosion Science*, vol. 65, p. 26-36, déc. 2012, doi: 10.1016/j.corsci.2012.07.025.
- [12] Ph. Refait, M. Jeannin, R. Sabot, H. Antony, and S. Pineau, « Corrosion and cathodic protection of carbon steel in the tidal zone: Products, mechanisms and kinetics », *Corrosion Science*, vol. 90, p. 375-382, janv. 2015, doi: 10.1016/j.corsci.2014.10.035.
- [13] C. Erdogan and G. Swain, « The effect of macro galvanic cells on corrosion impressed current cathodic protection for offshore monopile steel structures », *Ocean engineering*, vol. 265, n° 112575, p. 7, 2022.
- [14] K. Habib, L. Hamelin, and H. Wenzel, « A dynamic perspective of the geopolitical supply risk of metals », *Journal of Cleaner Production*, vol. 133, p. 850-858, oct. 2016, doi: 10.1016/j.jclepro.2016.05.118.
- [15] « Circular Economy », *worldsteel.org*. <https://worldsteel.org/circular-economy/> (consulté le 29 août 2023).
- [16] J. Duboscq, « Corrosion des aciers en milieu marin: processus se déroulant dans les zones cathodiques », Thèse de Doctorat, La Rochelle Université, 2019.



## *Introduction Générale*



*« Les activités humaines, principalement à travers l'émission de gaz à effet de serre, ont indiscutablement provoqué le réchauffement climatique, avec une augmentation de la température mondiale, en surface, atteignant, en 2011-2020, 1,1 °C de plus qu'entre 1850 et 1900. Les émissions mondiales de gaz à effet de serre ont continué d'augmenter entre 2010 et 2019, avec des contributions historiques et actuelles inédites découlant de l'utilisation de l'énergie fossile, de l'utilisation et du changement d'utilisation des terres, des modes de vie et des habitudes de consommation et de production à travers les régions, entre et au sein des pays, et entre les individus (confiance élevée). »*

**Climate Change 2022: Adaptation and Vulnerability [1].**

L'accord de Paris, visant à limiter l'augmentation de la température mondiale en dessous de 2°C est un événement majeur dans la lutte contre le réchauffement climatique. Négocié lors de la Convention-cadre des Nations unies sur les changements climatiques (COP21) à Paris en 2015, cet objectif ambitieux nécessite de diminuer considérablement les émissions mondiales de gaz à effet de serre au cours des prochaines décennies [2]. L'effort mondial pour lutter contre le changement climatique est soutenu par de nombreux accords *internationaux* sur le climat, d'engagements *nationaux* de plus en plus exigeants, et d'une sensibilisation croissante du public. Ces efforts collectifs stimulent les initiatives visant à lutter contre le changement climatique à différentes échelles. Les politiques d'atténuation ont joué un rôle clé dans la réduction de la consommation énergétique et de l'empreinte carbone mondiale, conduisant à des réductions significatives des émissions de gaz à effet de serre dans plusieurs pays au cours de la dernière décennie. L'émergence de technologies à faibles émissions carbone, de moins en moins coûteuses, a présenté de nombreux avantages pour une utilisation durable de l'énergie dans des secteurs tels que le bâtiment, les transports et l'industrie par exemple. De plus, la mise en œuvre de stratégies d'adaptation permet non seulement de réduire les risques climatiques, mais contribue également au développement durable [1]. Un point clé pour atteindre cet objectif est l'adoption généralisée de sources d'énergies renouvelables pour remplacer la production d'énergie intensive.

L'Union Européenne a défini que les énergies renouvelables devaient permettre de produire au moins 20 % de la consommation totale d'énergie en 2020 et 27 % d'ici 2030 [2]. De fait, cette transition repose sur l'augmentation de la production d'énergie renouvelable, l'amélioration de l'efficacité énergétique de ces technologies, et la maîtrise de la consommation d'énergie globale [2].

L'énergie éolienne offshore est l'un des acteurs principaux dans le paysage des énergies renouvelables. L'augmentation du nombre de projets éoliens offshore en Europe et dans le monde souligne l'intérêt croissant qui est porté à cette source d'énergie [2]. Des recherches prévoient une expansion significative de l'utilisation de l'énergie éolienne, allant jusqu'à envisager qu'environ la moitié de l'approvisionnement mondial en énergie pourrait être d'origine renouvelable d'ici 2040 [3]. Cette transition devrait réduire considérablement les émissions de dioxyde de carbone [3]. L'énergie éolienne, en raison de sa maturité et de son expansion rapide, est devenue un choix privilégié des différents gouvernements [3].

L'agrandissement des parcs éoliens onshore devient de plus en plus difficile en raison contestations sociétales et de la rareté des emplacements présentant une exposition (au vent) et une taille suffisante. De plus, les barrières techniques et économiques tendent à être surmontées, de fait l'implantation de parcs éoliens en mer devient plus intéressante. [4]

Dans ce contexte, Naval Energy (une filiale du groupe Naval de 2017 à 2021) avait pour projet de développer un parc éolien offshore. Ils ont imaginé des éoliennes flottantes entièrement en acier, comme présenté dans la figure 1 [5]. Cet alliage joue un rôle crucial dans le monde moderne. Il sert non seulement de matériau fondamental pour la construction et les infrastructures, mais permet également une la réalisation de nombreux processus de fabrication. De plus, il occupe une position centrale dans les initiatives mondiales de recherche et développement [6]. La longévité et la durabilité des structures offshore, essentiellement construites en acier au carbone, sont mises au défi par leur exposition constante au milieu marin. Les plates-formes telles que les éoliennes flottantes, les plates-formes de conversion ou même les quais de port et/ou palplanches sont conçues avec une durée de vie minimale de 25 ans [2].



Figure 2: Éolienne flottante en acier, conçue par Naval Energy [5]

La nature corrosive de l'eau de mer, influencée par la salinité, la concentration en oxygène, le pH (généralement de 7,8 à 8,3) et la température, influence les mécanismes de corrosion de l'acier. Diverses formes de corrosion (corrosion uniforme, piqûres, corrosion cavernueuse, corrosion galvanique et corrosion par érosion, etc.) peuvent être déclenchées par des facteurs tels que les vagues, les vents et les micro-organismes. La corrosion sous contrainte et corrosion par fatigue peuvent également être exacerbées par ces éléments environnementaux [2].

Pour lutter contre la corrosion, différentes stratégies (souvent combinées par deux ou trois) sont employées en fonction des parties de l'éolienne concernées. La turbine, la tour et la pièce de transition sont exposées à la corrosion atmosphérique sauf si elles sont immergées. La fondation et la pièce de transition sont subdivisées en différentes zones : au fond, la zone immergée (sous le niveau de la marée basse) ; au-dessus, la zone de marnage (ZdM) affectée par les marées et des facteurs externes ; la partie supérieure, la zone des éclaboussures susceptible d'être affectée par les vagues et le dépôt de sel suite à la projection de gouttelettes et d'embruns marins [2]. La corrosion est particulièrement prononcée dans ces zones à cause de la forte concentration de chlorure, l'humidité et les fluctuations du pH pendant les cycles de marées [2].

La protection de ces structures implique diverses mesures telles que les revêtements organiques, les épaisseurs d'acier sacrificielles pour compenser la perte de masse due à la corrosion, et les systèmes de protection cathodique tels que la protection cathodique par anode galvanique (PCAG) ou la protection cathodique par courant imposé (PCCI). Étant donné les quantités considérables d'acier utilisées (les monopieux actuels pèsent jusqu'à 805 tonnes), la protection contre la corrosion revêt une importance capitale [2].

Le concept de "épaisseur sacrificielle" implique, au moment de la conception, de prendre en compte des épaisseurs d'acier plus importantes comme mécanisme de protection contre la corrosion, en cas de défaillance des systèmes de protection classiques. De plus, cette tolérance à la corrosion (par surdimensionnements des épaisseurs) pourrait être nécessaire pour combler le temps de polarisation complète de la structure. Par ailleurs, selon Bandara et al. [7], la corrosion par fatigue se produit à cause d'une synergie de l'environnement, de la microstructure du matériau et des charges mécaniques cycliques. Les mécanismes sous-jacents au processus de corrosion aqueuse par fatigue peuvent être décrits comme suit : des fissures se forment au niveau des piqûres de corrosion à la suite de fortes concentrations de contraintes mécaniques, d'une réduction de la fermeture de fissure (stagnation locale de l'électrolyte) et d'une attaque électrochimique. Il a été observé que les dommages dus à la corrosion et à la fatigue combinées sont plus délétères que la somme de leurs effets individuels. L'épaisseur sacrificielle est déterminée en fonction de la vitesse de corrosion par fatigue estimée de l'acier dans son environnement. La plage recommandée pour la perte totale d'épaisseur estimée en cas de dysfonctionnement des systèmes de protection contre la corrosion se situe entre 0,2 et 1,2 cm selon la norme DIN 50929-3 (2018), comme indiqué dans [7].

Les systèmes de protection cathodique sont largement utilisés en milieu marin pour protéger les structures en acier telles que les navires, les quais de port et les palplanches par exemple. Ces systèmes fonctionnent en abaissant le potentiel électrique des structures immergées, ralentissant ainsi les processus de corrosion (oxydation). Cela peut être réalisé soit par des anodes galvaniques ou "sacrificielles" (méthode CPAG) soit par des anodes inertes (méthode PCCI) [2], [8]. La protection cathodique par courant imposé (PCCI) représente une technique émergente dans la construction de parcs éoliens en mer. Cette méthode, utilisée pour les navires et les infrastructures hydrauliques, fournit un courant continu à la surface de l'acier grâce à un générateur de courant à travers des anodes inertes. [9] Les anodes galvaniques permettent la polarisation de la structure grâce à la réaction galvanique d'un matériau moins noble (celui de l'anode) avec l'acier. En milieu marin, les anodes à base d'aluminium sont préférées grâce à leur haute efficacité électrochimique et de leur légèreté. Bien que la PCAG offre des avantages tels que son application à des structures complexes et un entretien minimal, elle nécessite une quantité significative de matériau anodique et peut s'avérer difficile à remplacer. Pour la protection des éoliennes offshore ou des structures portuaires par exemple, des quantités considérables de matériau anodique sont souvent nécessaires.

La problématique du suivi de la protection contre la corrosion en ZdM est intrinsèquement liée aux spécifications et à la nécessité potentielle d'opérer de futures réparations. Dans la ZdM, le défi de la réparation des revêtements est le plus compliqué. Dans les zones sous niveau de la marée moyenne, les réparations sont impraticables sans recourir à des installations de caisson batardeau (ou cofferdam) à coût élevé. De plus, tout travail de réparation de revêtement effectué dans un environnement humide a tendance à souffrir d'une durabilité limitée [10].

Ørsted, une entreprise danoise expérimentée dans le domaine des éoliennes en mer, utilise des capteurs de corrosion par résistance électrique pour des applications de suivi et prévention de la corrosion. Ces capteurs ont été testés et éprouvés dans de nombreuses conditions. Ils présentent une assez bonne fiabilité, dans toutes leurs applications sauf en ZdM en raison du caractère cyclique de l'immersion de cette zone. Buhr et al., dans leur dernière publication, ont conclu que la fiabilité des méthodes actuelles de vérification de la performance de la protection cathodique en ZdM reste un sujet d'incertitude [10]. Les techniques habituelles telles que les mesures par drop cell, et mesures gravimétriques sont remises en question dans ce contexte [10].

D'autre part, différentes études ont observé qu'un couplage galvanique est possible entre la ZdM et la zone des basses eaux (sous le niveau de la marée basse). En 2012, Melchers et al. ont mis en évidence un minimum de vitesse de corrosion dans la ZdM pour des structures verticales continues exposées à la fois à la zone des basses eaux et à la ZdM [11]. Cette faible vitesse de corrosion est due à l'aération différentielle (un phénomène de corrosion) entre la zone de marée et la zone de basse mer [11]. Plus récemment, Ph. Refait et al., en 2015 ont conclu sur la persistance de la protection cathodique en zone de marée grâce à un film résiduel continu d'eau de mer sur l'acier après la marée descendante [12]. En 2019, Law et al. ont observé le même phénomène sur des quais en conditions d'immersion cyclique. Plus récemment encore, Erdogan et al. ont mis en évidence l'existence de macro-cellules galvaniques dans cette zone à cause de cette persistance d'eau de mer résiduelle [13]. Cependant, aucune des études citées ci-dessus n'est en mesure de déterminer ni l'efficacité temporelle de la persistance de la PC ni le niveau de protection atteint en ZdM.

De plus, l'exploitation du fer peut avoir des impacts écologiques tels que la déforestation à grande échelle, l'érosion des sols et la perturbation des écosystèmes locaux, une utilisation importante de l'eau, etc., contribuant ainsi à de fortes émissions de gaz à effet de serre. En outre, l'extraction intensive des métaux au cours des derniers siècles soulève des inquiétudes quant à leur disponibilité à long terme. L'ambivalence entre la disponibilité géologique finie des métaux et leur demande croissante est un problème crucial à prendre en compte dans le contexte des besoins futurs [14]. Malgré leur disponibilité géologique limitée, les métaux peuvent être régénérés grâce à des processus de recyclage. L'économie circulaire souligne davantage l'importance de l'utilisation efficace des ressources, en veillant à ce que les ressources soient allouées de manière optimale aux produits et services, contribuant ainsi à un avenir durable pour tous. En conséquence, tous les produits en acier nécessitent une conception méticuleuse pour l'efficacité, la durabilité, la facilité de réutilisation, et le recyclage ultérieur [15].

Dans ce contexte, une étude sur la protection cathodique de l'acier au carbone en ZdM est tout à fait pertinente. En effet, une meilleure compréhension des paramètres spatiotemporels de la PC en ZdM pourrait contribuer à :

- Réduire les coûts d'installation et de maintenance des revêtements organiques,
- Diminuer l'épaisseur sacrifiée des marges de corrosion et, par conséquent, économiser les ressources en fer
- Réduire les émissions de gaz à effet de serre par éolienne offshore, et/ou parois de palplanches, et/ou quais, etc.

Pour répondre à cette problématique, les travaux de thèse présentés ici ont été divisés en trois principales sections de recherche. La première (*Chapitre III : Évolution de la couche minérale, de la zone d'immersion à la zone des éclaboussures*) traite d'une étude a posteriori de la PC in situ dans le port commercial de La Rochelle. Des coupons en acier au carbone interconnectés ont été exposés dans la ZdM naturelle de La Rochelle (pendant la thèse de J. Duboscq, 2016-2019 [16]). L'ensemble des couches minérales recouvrant les échantillons après 33 et 52 mois de protection cathodique a été analysé, et le taux résiduel de corrosion du métal a été estimé pour déterminer la zone de transition de l'efficacité de la protection cathodique.

Dans un deuxième temps, des recherches ont été menées sur le comportement de l'acier suffisamment et insuffisamment protégé sous une fine couche d'électrolyte. L'objectif ici était d'étudier le comportement de l'acier pendant sa phase émergée à l'échelle du laboratoire (*Chapitre IV : Protection Cathodique de l'Acier au Carbone sous de Fines Couches d'Eau de Mer*).

Enfin, le dernier axe porte sur la création d'une ZdM en laboratoire pour réaliser une PC en ZdM avec un suivi en direct des paramètres de la protection. L'évolution du courant et du potentiel de la PC en fonction du temps est discutée dans le chapitre V (*Chapitre V : Protection Cathodique de l'Acier au Carbone en zone de marnage Simulée : Expérience à Échelle de Laboratoire*).

Le projet a été initié par le Département de Corrosion Marine de Naval Group dans le cadre de leur programme de R&D pour soutenir le développement des éoliennes offshore réalisées par Naval Energy. Ce programme de recherche revêt également un intérêt primordial pour d'autres infrastructures de Naval Group impactées par les marées ou les plateformes navales soumises à des phénomènes de corrosion, que ce soit à la ligne de flottaison ou dans des zones plus étendues soumises à des situations immergées/émergées.

## Références

- [1] H.-O. Pörtner *et al.*, « Climate Change 2022: Impacts, Adaptation and Vulnerability. Working Group II to the Sixth Assessment Report of the Intergovernmental Panel on Climate Change », *Cambridge University Press*, p. 3-33, 2022, doi: doi:10.1017/9781009325844.001.
- [2] T. Kirchgeorg, I. Weinberg, M. Hörnig, R. Baier, M. J. Schmid, and B. Brockmeyer, « Emissions from corrosion protection systems of offshore wind farms: Evaluation of the potential impact on the marine environment », *Marine Pollution Bulletin*, vol. 136, p. 257-268, nov. 2018, doi: 10.1016/j.marpolbul.2018.08.058.
- [3] K. Dai, A. Bergot, C. Liang, W.-N. Xiang, and Z. Huang, « Environmental issues associated with wind energy – A review », *Renewable Energy*, vol. 75, p. 911-921, mars 2015, doi: 10.1016/j.renene.2014.10.074.
- [4] E. A. Willsteed, S. Jude, A. B. Gill, and S. N. R. Birchenough, « Obligations and aspirations: A critical evaluation of offshore wind farm cumulative impact assessments », *Renewable and Sustainable Energy Reviews*, vol. 82, p. 2332-2345, févr. 2018, doi: 10.1016/j.rser.2017.08.079.
- [5] « Saipem and Naval Energies sign an agreement for the acquisition of Naval Energies' floating wind business », *Naval Group*. <https://www.naval-group.com/en/saipem-and-naval-energies-sign-agreement-acquisition-naval-energies-floating-wind-business> (consulté le 29 août 2023).
- [6] « Steel industry economic impact », *worldsteel.org*. <https://worldsteel.org/steel-topics/statistics/steel-industry-economic-impact/> (consulté le 29 août 2023).
- [7] C. S. Bandara, U. I. Dissanayake, and P. B. R. Dissanayake, « Novel Method for Developing S-N Curves for Corrosion Fatigue Damage Assessment of Steel Structures », presented at 6<sup>th</sup> International conference on Structural Engineering and construction Management, Kandy, Sri Lanka: CSECM, 2015, p. 100-104.
- [8] J. Creus, R. Sabot, and P. Refait, « Corrosion et protection des métaux en milieu marin », *Matériaux | Corrosion vieillissement*, vol 2, p. 14, 2013.
- [9] M. Roche, « L'ESSENTIEL SUR LA PROTECTION CATHODIQUE », *Cefracor*, p. 14, 2015.
- [10] B. Buhr, S. Ruth. E., A. M. Diederichs, L. P. Løvendahl Raun, and Y. Rezanja, « Benefits of corrosion monitoring for offshore wind structures », presented at Association for Materials Protection and Performance, Denver, Colorado, 2023, p. 11.
- [11] R. E. Melchers and R. Jeffrey, « Corrosion of long vertical steel strips in the marine tidal zone and implications for ALWC », *Corrosion Science*, vol. 65, p. 26-36, déc. 2012, doi: 10.1016/j.corsci.2012.07.025.
- [12] Ph. Refait, M. Jeannin, R. Sabot, H. Antony, and S. Pineau, « Corrosion and cathodic protection of carbon steel in the tidal zone: Products, mechanisms and kinetics », *Corrosion Science*, vol. 90, p. 375-382, janv. 2015, doi: 10.1016/j.corsci.2014.10.035.
- [13] C. Erdogan and G. Swain, « The effect of macro galvanic cells on corrosion impressed current cathodic protection for offshore monopile steel structures », *Ocean engineering*, vol. 265, n° 112575, p. 7, 2022.
- [14] K. Habib, L. Hamelin, and H. Wenzel, « A dynamic perspective of the geopolitical supply risk of metals », *Journal of Cleaner Production*, vol. 133, p. 850-858, oct. 2016, doi: 10.1016/j.jclepro.2016.05.118.
- [15] « Circular Economy », *worldsteel.org*. <https://worldsteel.org/circular-economy/> (consulté le 29 août 2023).
- [16] J. Duboscq, « Corrosion des aciers en milieu marin: processus se déroulant dans les zones cathodiques », Thèse de Doctorat, La Rochelle Université, 2019.





## Chapter I: Bibliography



## Chapter I: Bibliography

I.1 Introduction .....	22
I.1.1 Marine medium .....	22
I.1.2 Carbon steel and marine medium .....	23
I.2 Marine corrosion mechanisms.....	24
I.2.1 The different local corrosion mechanisms occurring on carbon steel.....	25
<i>I.2.1.1 Differential aeration [9].....</i>	<i>25</i>
<i>I.2.1.2 Crevice corrosion.....</i>	<i>26</i>
<i>I.2.1.3 Corrosion in the marine mud.....</i>	<i>26</i>
I.2.2 Typical marine corrosion products .....	27
I.2.3 Corrosion under thin electrolyte layer .....	29
I.2.4 Corrosion in the tidal zone .....	33
<i>I.2.4.1 Special cases of the splash zone and the low water zone.....</i>	<i>34</i>
<i>I.2.4.2 Corrosion mechanisms in the tidal zone.....</i>	<i>34</i>
I.3 Cathodic protection .....	39
I.3.1 Cathodic protection, the principle.....	39
I.3.2 Calcareous deposit: a consequence of cathodic protection.....	40
<i>I.3.2.1 Precipitation mechanism of the calcareous deposit.....</i>	<i>40</i>
<i>I.3.2.2 Parameters influencing the deposit growth and composition.....</i>	<i>41</i>
I.3.2.2.1 Electrochemical parameters .....	41
I.3.2.2.2 Impact of the surrounding environment .....	43
I.3.3 Cathodic protection in the tidal zone .....	45
Conclusion.....	47
References .....	49

## I.1 Introduction

The aim of this chapter is to open the reflection and have an overview about research about cathodic protection of carbon steel in the tidal zone. Prior to developing cyclic corrosion mechanisms in marine environment, it is necessary to define the environment and the corrosion mechanism in permanent immersion.

### I.1.1 Marine medium

The chemical composition of seawater is rather complex as it contains many dissolved salts. The average marine salinity is about 35 g/kg<sub>seawater</sub>. Table I.1 sums up the 10 most concentrated chemical species (5 anions and 5 cations). These concentrations are almost the same whatever the origin of seawater [1]. The seawater global salinity combined with an important bio-activity induces a high corrosivity of the medium.

Table I.1 : Seawater chemical composition [1]

Anions	g/kg <sub>seawater</sub>	Cations	g/kg <sub>seawater</sub>
Cl <sup>-</sup>	19.354	Na <sup>+</sup>	10.77
SO <sub>4</sub> <sup>2-</sup>	2.712	Mg <sup>2+</sup>	1.290
HCO <sub>3</sub> <sup>-</sup> + CO <sub>3</sub> <sup>2-</sup>	0.118 to 0.146	Ca <sup>2+</sup>	0.412
Br <sup>-</sup>	0.0673	K <sup>+</sup>	0.399
F <sup>-</sup>	0.0013	Sr <sup>2+</sup>	0.0079

Except seawater composition, pH and dissolved dioxygen concentration are 2 parameters playing a crucial role in the corrosion mechanisms. The pH, ruled by the chemical equilibrium H<sub>2</sub>CO<sub>3</sub> / HCO<sub>3</sub><sup>-</sup> / CO<sub>3</sub><sup>2-</sup>, varies between 7.5 and 8.5 [2]. However, it can be strongly modified by electrochemical reactions on the surface of a metal (steel in this case). During free corrosion process, for a cathodic zone, pH value will tend to increase while for an anodic zone, it will tend to decrease. The precipitation of compounds linked to these variations influences the electrochemical processes involved (topic detailed further).

On the other hand, the concentration of dissolved dioxygen impacts the electrochemical nature and kinetic of the involved reactions. The concentration decreases with the increasing depth; indeed, this concentration is directly linked to the exchanges with the atmosphere. For instance, a continuous structure exposed to the tidal zone (or to different zones with a varying dioxygen concentration such as presented in figure I.1) can be subjected to differential aeration caused by an O<sub>2</sub> concentration gradient (this mechanism is detailed in the “2.1.1 Differential aeration” subsection) [3]. From the top to the bottom, a continuous vertical structure in contact with:

- Atmospheric zone: aerial area exposed to marine particles
- Splash zone: aerial area exposed to seawater droplets
- Tidal zone: area alternately immersed and emerged according to the tides
- Immersed area: permanently immersed zone (beneath the low tides)
- Sediment area: area embedded in the marine mud and sediment

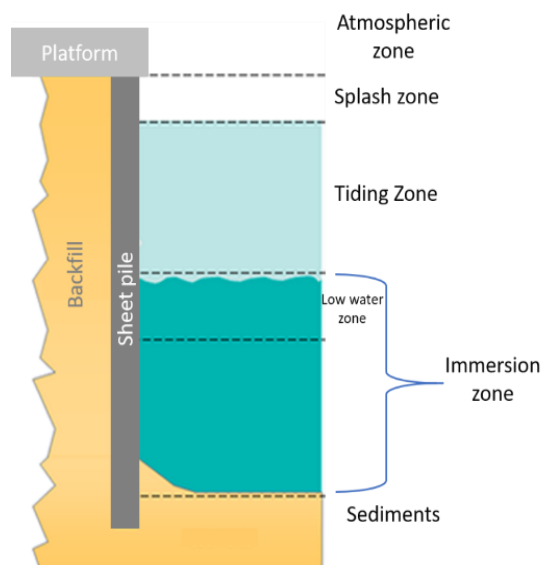


Figure I. 1: Schematic representation of the different zones crossed by a continuous vertical harbor structure

### I.1.2 Carbon steel and marine medium

This PhD is in the continuity of the work initiated by Julien Duboscq (and A. Bonnifet) in his own PhD. In this context, samples of carbon steel (EN10248-1) provided by Arcelor Mittal and used for the manufacture of sheet piles [3], were exposed in the tidal zone in the commercial seaport of La Rochelle. However, for the laboratory study carried out at Naval group Lab, samples of S355 NL steel were used. Such carbon steels are commonly used in port infrastructures and are not necessarily protected against corrosion (neither by cathodic protection nor organic coating). It is therefore essential to understand the basis of steel corrosion mechanisms in tidal zone in seawater. Carbon steel is widely used in the construction domain as it provides a good ratio mechanical resistance vs. cost [4].

The ISO 8044 standard defines corrosion as “an electrochemical interaction between a metal and his surrounding leading to modifications of the metal properties and often a functional degradation of the metal itself, of its environment or of the technical system composed by these two parameters” [5]. In other words, corrosion involves unavoidably 3 factors: the metal, its environment and the technical system in which it is involved. For this PhD the considered system is composed of:

- Metal: mild steel (carbon steel)
- Environment: marine medium
- Technical system: Harbor structure such as sheet piles, offshore structure...

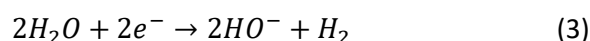
Aqueous corrosion is an electrochemical phenomenon involving an electrical current both electronic (through the metal) and ionic (through the electrolyte). At the metal/electrolyte interface, a charge transfer leads to a cation release in the electrolyte while the corresponding negative charges (electrons) are formed in the metal [6]: this is an oxidation reaction. Considering only the oxidation reaction, the metal is not neutral anymore so as the electrolyte. Then, to balance this destabilization, a counter reaction captures these electrons producing anions: this is a reduction reaction.

For carbon steel immersed in seawater, the corrosion is linked to the iron dissolution (electrochemical reactions presented below) and the dissolved dioxygen reduction in aerobic area or water reduction in anaerobic area. Carbon steel corrosion is usually considered as uniform. In other words, oxidation and reduction reactions take place at every point of the surface and with the same intensity:

- The main anodic reaction: iron oxidation

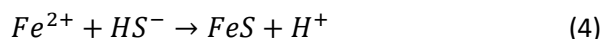


- The main cathodic reactions: dissolved dioxygen and water reduction



In this particular case, the anodic current and the cathodic current have the same absolute value (but opposite signs so as the global current equals 0): this is the corrosion current. The metal potential is called Open Circuit Potential (OCP) or corrosion potential [6]. The cathodic reactions (described above; reactions 2&3) lead to a local pH increase (with the HO<sup>-</sup> production).

Besides, as mentioned previously, (natural) seawater is a living environment with macro and micro-organisms which could influence the redox reactions. For example, in deaerated conditions, Sulphate Reducing Bacteria (SRB) could develop at the metal surface. As a consequence of the SRB metabolism, sulphates are reduced to sulfides, which induces the formation of iron sulfides FeS according to the reaction, where HS<sup>-</sup> is the main sulfide species in the pH range of seawater:



Consequently, these bacteria participate to the corrosion process [6], [7].

Moreover, in seawater (natural or synthetic) local corrosion areas can be observed. This critical degradation mode is triggered by the surface heterogeneities such as inclusions, grain boundaries, or the biofilm inherent heterogeneity.

## 1.2 Marine corrosion mechanisms

Basic (electro)chemical reactions describing the steel corrosion in seawater have been detailed in part « 1.2 Carbon steel and marine medium ». As a reminder, for the corrosion process, the oxidation and reduction reactions have the same intensity compensating each other (in other words  $j_a = -j_c$ ). It is then possible to assume in the case of a uniform corrosion process that local corrosion depth over the considered surface can be neglected as oxidation and reduction occur at the same intensity in every point of the surface. Thus, Melchers and Wells discussed a model predicting the average loss of steel with the exposure time due to uniform corrosion [8]. In this phenomenological model, different phases describing an evolution in the corrosion mechanisms have been identified (as presented in figure I.2):

- **The aerobic mode** (dioxygen still accesses to the steel surface):
  - Phase 0 is describing the earliest stages of the corrosion mechanisms governed by the kinetics of the anodic reaction (quite short-term phase)
  - During Phase 1, all the dioxygen has been consumed at the steel surface and the kinetic of the corrosion process is now limited by the dioxygen diffusion through the electrolyte.
  - Then, with the thickening of the corrosion products layer during Phase 2, this is the diffusion of the dioxygen through the corrosion products layer which limits the kinetics, i.e., the corrosion rate.
- **The anaerobic mode** occurs when the corrosion products layer is so thick that dioxygen does not reach the steel surface anymore. The consumption of the dioxygen is mainly due to aerobic bacteria located in the outer part of the corrosion product layer. Henceforth, the steel loss is limited by the income of the necessary nutrient for SRB activity.
  - At the beginning of the anaerobic mode, Phase 3 describes a high corrosion rate because of the initial abundance of organic nutrient for SRB.
  - Then, after the consumption of the initial amount of organic matter, the corrosion rate reaches a steady state (constant slope in figure 1.2) during Phase 4 because of the limitation due to the organic matter transport through the thickening corrosion products layer.

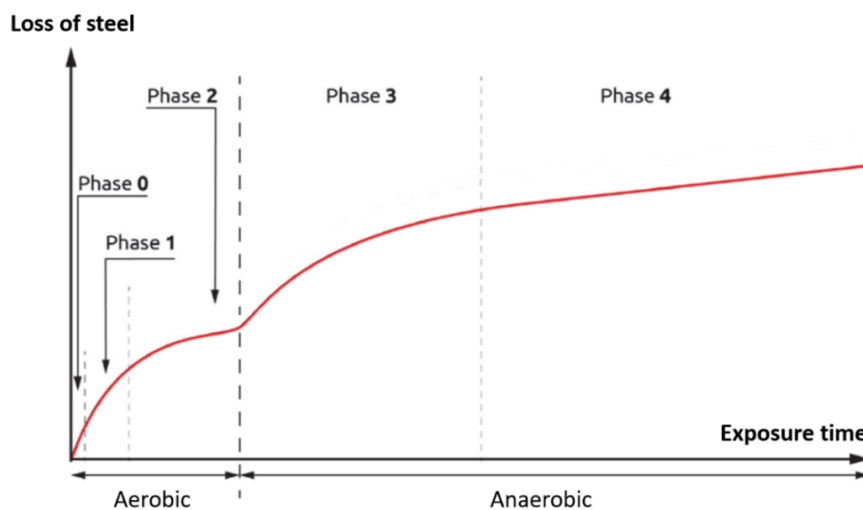


Figure 1.2: Phenomenological model for the uniform marine corrosion of steel [8]

The uniform corrosion processes are considered as well known and manageable. However, the localized corrosion processes are more damaging [9]. Indeed, in these particular cases the current can lead to a quick perforation of the metal. The common point between all severe localized corrosion processes is the formation of a local and rather small anodic zone close to a much larger cathodic zone. By definition, this is the opposite of the uniform corrosion process [3].

## 1.2.1 The different local corrosion mechanisms occurring on carbon steel

### 1.2.1.1 Differential aeration [9]

Differential aeration is a matter of galvanic coupling between two zones of the same immersed structure in a medium with a concentration gradient of dissolved  $O_2$ . Indeed, the areas close to the air/electrolyte interface are very aerated (high dissolved  $O_2$  concentration) while those deeper are

exposed to more deaerated conditions (figure I.3). The area exposed to the highest dissolved dioxygen concentration is in the cathode position (from the potential point of view) while the part of the structure seeing less oxygen behaves as an anode [3]. This phenomenon occurs at different scales. For instance, a sheet pile is strongly subjected to differential aeration because of its length and the different zones it passes through. Indeed, the highest part, exposed alternatively to air and to seawater is strongly aerated. On the other hand, the section just below the low tides and above the sediment is comparatively poorly aerated. Thus, this part of the sheet pile corrodes more rapidly.

Furthermore, the Evans drop experiment has shown that this is also the corrosion mode involved when a drop of water is present on the surface of a metal (a typical situation in the splash zone). Figure I.3 displays the mechanism of such a corrosion mode. In this case, a concentration gradient of dissolved  $O_2$  is created from the edges of the drop, tracing an annular cathodic zone, towards the center of the drop, the anodic zone.

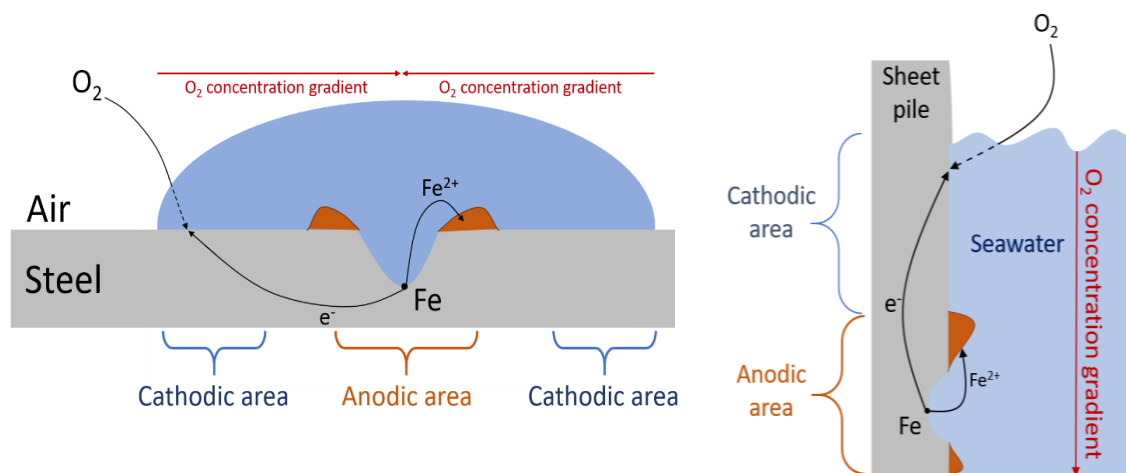


Figure I. 3: Schematic representation of the differential aeration mechanism under a droplet of seawater and applied at the sheet piles harbor structure

#### 1.2.1.2 Crevice corrosion

In this case, there is a geometrical heterogeneity initiating the corrosion. Geometrical defects such as scratches, perforations, presence of deposits and the initial surface condition of the substrate can lead to a local confinement of the electrolyte. Thus, the ionic exchanges with the bulk of the electrolyte are limited.

Corrosion or dissolution of the metal leads to a local accumulation of cations (i.e. positive charges). In fact, this electrical disequilibrium spontaneously leads to the migration of anions (mainly  $Cl^-$  in marine environment [9]) restoring then the electrical balance. Moreover, the hydrolysis of cations leads to an acidification of the electrolyte. The synergy of the chlorides accumulation and the acidification of the environment makes it much more corrosive than the external environment [9].

#### 1.2.1.3 Corrosion in the marine mud

In this particular zone, accelerated corrosion is the result of the synergy of two main factors:  $O_2$  concentration gradient and anaerobic bacterial activity. There is indeed a strong difference in dissolved oxygen concentration between the zone just above the sediment and the bulk of the sediment.

Moreover, the quasi absence of dioxygen in the mud favors the development of bacteria such as SRB, which play an important role in the corrosion mechanisms [10].

Other factors can influence corrosion in port areas. Port waters are polluted by hydrocarbons released from ships passing through the harbors. In the form of a film, they could block or drastically reduce the speed of corrosion and create cathodic zones likely to be at the origin of galvanic couplings. The same phenomenon could occur at the surface of galvanic anodes and limit cathodic protection (CP) efficiency [3].

### 1.2.2 Typical marine corrosion products

The layer formed by the corrosion products is usually seen as an indicator of the steel corrosion. Its structure, organization and composition have been widely studied to better understand the formation and growth mechanisms of this “rust” layer. Necessarily the various corrosion products formed are rather different and have their own properties and characteristics [7]. Their different nature attests of slightly different exposure conditions. Some products are representative of anodic areas while other are favored in the cathodic zones. Moreover, their different nature helps maintaining a competition between the different zones.

Uniform corrosion rate is governed by the O<sub>2</sub> accessibility to the anodic and cathodic zones. The corrosion layer thickness has a non-neglectable impact on the corrosion mechanism kinetics; indeed, the thicker the corrosion product the more limited the access of dioxygen to the surface. The inherent conductivity of corrosion products has to be considered too. For example, magnetite (Fe<sub>3</sub>O<sub>4</sub>) and iron sulfides (FeS), favored in the cathodic zones, do not hinder oxygen reduction and thus do not limit the corrosion rate as they permit the electronic conduction [3], [7].

PhD works of Samuel Pineau in 2006 give a better understanding of these different corrosion products stratification [11]. Carbon steel coupons have been exposed to harbor seawater for 6 to 12 months. The characterization of the formed rust layer led to the observation of the following stratification:

- An outer brown-orange stratum (the farthest to the steel surface) mainly composed of Fe(III) oxyhydroxides such as goethite ( $\alpha$ -FeOOH) and lepidocrocite ( $\gamma$ -FeOOH). These compounds result from the oxidation of Fe(II) compounds. This is therefore absolutely consistent to find these compounds in the external part of the corrosion layer, where the dioxygen concentration is maximal.
- An inner dark stratum in contact with the steel surface mainly composed of sulphated green rust GR(SO<sub>4</sub>), a Fe(II,III) hydroxysulfate (which formula is Fe<sup>II</sup><sub>4</sub>Fe<sup>III</sup><sub>2</sub>(OH)<sub>12</sub>SO<sub>4</sub>·8H<sub>2</sub>O [12]), magnetite and iron sulfides. With the increasing exposure time, the combination of those three compounds in the inner stratum is characteristic of deaerated conditions [13].

Complementary experimentations in artificial seawater have highlighted the first stages of this stratification mechanism. After two weeks of immersion, the metal is rapidly covered with two simple strata: an internal stratum of GR(SO<sub>4</sub>) and an external stratum of lepidocrocite  $\gamma$ -FeOOH [14]. During these first stages, the oxygenation of the corrosion products layer prevails on the metabolic activity of the SRB, which is perfectly coherent with the phenomenological model determined by R.E. Melchers [8]. GR(SO<sub>4</sub>) is then the result of the purely electrochemical oxidation of the steel while  $\gamma$ -FeOOH results from the GR(SO<sub>4</sub>) oxidation [15].

After 1 to 2 months, however, the stratification is more complex. Indeed, dissolved  $O_2$  gets less and less concentrated within the mineral layer. Thus, the oxygen has to diffuse through the pores of this layer towards the metallic surface. On the one hand, different oxidation products of  $GR(SO_4)$  can be obtained according to the perceived oxygenation rate: (i) in the most aerated zones, lepidocrocite is preferentially formed; (ii) in the fairly aerated zones goethite is favored while (iii) in the least oxygenated zones  $GR(SO_4)$  oxidize to magnetite  $Fe_3O_4$  [15]. On the other hand, the absence of  $O_2$  in the vicinity of the metal allows the SRB development and traces of  $FeS$  can be found in the inner layer. Indeed, dissolved dioxygen is consumed (i) by the aerobic micro-organisms activity and (ii) by the  $GR(SO_4)$  oxidation into  $Fe(III)$  oxyhydroxides [16]. It is then consistent to assume that  $FeS$  and magnetite form in the same areas as these two compounds both require deaerated conditions. In anoxic conditions, the reduction of 1 ion  $SO_4^{2-}$  from  $GR(SO_4)$  leads to the release (after the precipitation of 1  $FeS$ ) of a surplus of  $Fe^{2+}$  and  $Fe^{3+}$  from which magnetite (a mixed iron valence compound) could form [13].

Considering these observations summed up in figure I.4, it seems obvious that  $FeS$  plays a key role in the oxidation mechanisms of steel in seawater. Researches have been conducted to better understand how to characterize and observe it [17]. Indeed, in most cases, in marine corrosion, iron sulfides are not detected by X-ray diffraction (XRD). It appears then that micro-Raman spectroscopy is the most suitable method to identify  $FeS$ . This technique allows, indeed, to differentiate the crystallized mackinawite from the nanocrystalline  $FeS$ . Within the corrosion products layers, the most frequent form of iron sulfides is the nanocrystalline one. Indeed, the crystallization of  $FeS$  is governed by the ratio  $\frac{[Fe(II)]}{[S(-II)]}$  representing the abundance of divalent iron regarding the quantity of  $S^{II}$ . For a ratio of  $\frac{1}{2}$ , nanocrystalline mackinawite tends to be rather stable according to [17]. In this case, the crystallization is probably limited by  $S^{II}$  (or  $OH^-$ ) species adsorbed on the surface of the initial mackinawite nanocrystals. Nevertheless, the alkaline pH of seawater seems to favor the nanocrystalline form in the marine environment, regardless of the  $Fe/S$  concentration ratio [17].

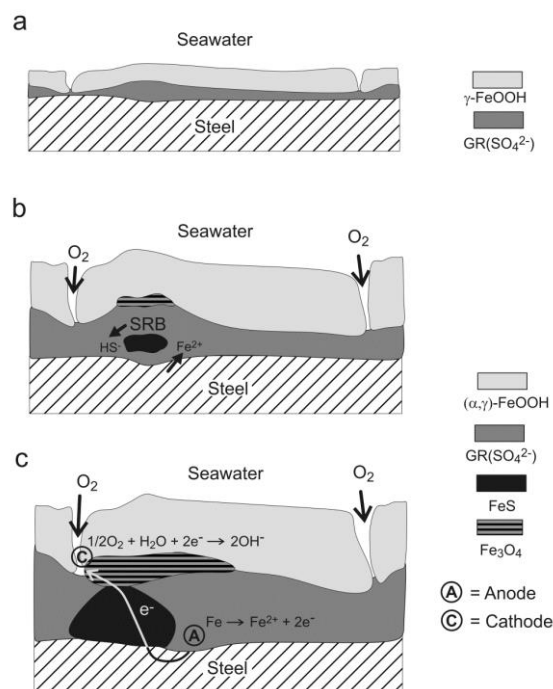


Figure I. 4 : Stratification process of the corrosion products layer representing the early stages leading to a localized degradation and presence of SRB. [15]

Let us consider now the case of a galvanic coupling spontaneously happening on an immersed steel structure. Some works have studied the role of the SRB in this case [3,18]. Distinction between anodic and cathodic zone is inherent to the galvanic coupling. This study has been able to visually discriminate both areas and then perform studies and characterization on those zones. The main corrosion products detected in the cathodic area were FeS and magnetite. Carbonated corrosion products have been detected too. This rather complex layer was totally covered with aragonite (an allotropic form of  $\text{CaCO}_3$  [19], [20]), consequence of the interfacial pH increase. The combination of  $\text{Fe}_3\text{O}_4$  and FeS, both conductors, allow the oxygen reduction. In the anodic zones, 2 strata have been observed, the inner stratum mainly composed of  $\text{GR}(\text{SO}_4)$  and the outer stratum mainly made of insulating Fe oxyhydroxides ( $\gamma\text{-FeOOH}$ ,  $\alpha\text{-FeOOH}$  ...). This is a self-sustaining phenomenon. Indeed, a galvanic coupling leads to different electrochemical behaviors between anodic and cathodic zones. In the anodic zones, the compounds formed are insulating, whereas the formation of magnetite, and maybe FeS [3], which are conductive, is favored in the cathodic zone. The reduction of oxygen is then facilitated, reinforcing the cathodic character of the zone [18].

On the other hand, marine corrosion is not limited to the study of corrosion mechanisms of permanently immersed structures. Indeed, in the tidal zone, the metal is alternately immersed and emerged. In the latter case, its surface remains wet due to the persistence of a residual water film on its surface [21]. It has been shown by Yadav et al. [22] that corrosion under a thin water film differs from the corrosion in the bulk electrolyte. The thickness of this film can vary from nanometer to millimeter. A thickness comparable to the oxygen diffusion layer thickness is however often studied [22], [23].

### 1.2.3 Corrosion under thin electrolyte layer

This is a complex experimental field to investigate. On the one hand, it is necessary to be able to create a water film on the surface of the steel with about a precision of ten microns; and on the other hand, it is necessary to be able to perform electrochemical measurements within this water film. First of all, it is important to define which thickness of film defines it as a “thin” one from the corrosion point of view.

In the mathematical study of R. Morris and W. Smyrl, a first approach of the definition of a finite vs infinite water film is given. It says: “the electrolyte layer could be considered to be infinitely deep if it is equal in depth to the sum of the anode and cathode dimensions” [24]. In other words, in the hypothetical case where the sample is so small that its dimensions are smaller or equal to the film thickness then the film could be considered as infinite. To better understand it, it is necessary to imagine the current lines reaching the anode through the electrolyte (as represented figure I.5). For an infinite electrolyte layer (figure I.5 -a) the current lines could reach any point of the surface without difficulties. Nonetheless, considering a finite electrolyte film, the paths of the current lines could be limited by the space under the electrolyte layer (represented by the dashed lines figure I.5-b). In figure I.5, the dashed blue lines cannot reach the anode because of the insufficient thickness of the electrolyte; in figure I.5 – b, the red lines represent a possible new path for those lines to reach the anode. It is clear here that the current lines interfere with each other. The electrochemical behavior of the sample would therefore differ from the behavior under an infinite film. Indeed, with the decreased thickness of the film the galvanic current becomes more concentrated close to the cathode/anode junction (“easier” for the current lines). This effect limits the total corrosion current in the system [24].

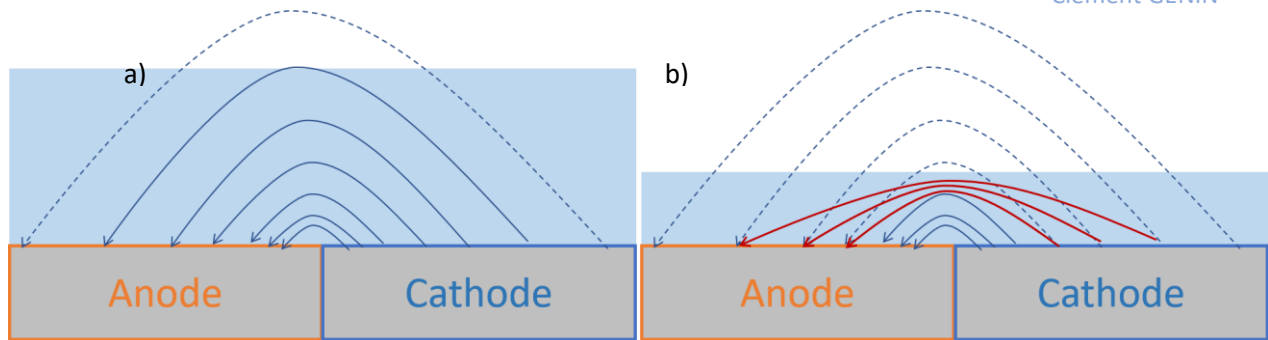


Figure I. 5: Two-dimension schematic representation of the galvanic current lines reaching the anode through – a) an infinite electrolyte layer – b) a finite electrolyte layer

Obviously, the infinite electrolyte layer is a hypothetical case as in practice the samples are always much larger than the electrolyte film covering it. Furthermore, this is not the only parameter to consider.

Indeed, in 1966, Thomashov (as quoted in [25]) presented a model describing the variation of corrosion rate with the thickness of the electrolyte layer. In this model, water films thinner than the oxygen diffusion layer were considered. Finally, with the decreasing thickness of this diffusion layer (i.e. the electrolyte thickness) the corrosion rate reaches a maximum for the thickness equivalent to the transition from cathodic control to anodic control (which mechanism is discussed further). Various studies, based on the Tomashov's model, have shown that the corrosion rate increases when the water film thickness is comparable to the oxygen diffusion layer ([25]–[27]). Although these works do not all lead to the exact same values, they all conclude that beyond 1 mm thickness there is little difference between the corrosion rates (or currents) for higher thickness (or immersion depth) of water. Figure I.6 displays the evolution of the 3 main electrochemical parameters as a function of the film thickness:

- 5 a) The current
- 5 b) The corrosion rate
- 5 c) The potential

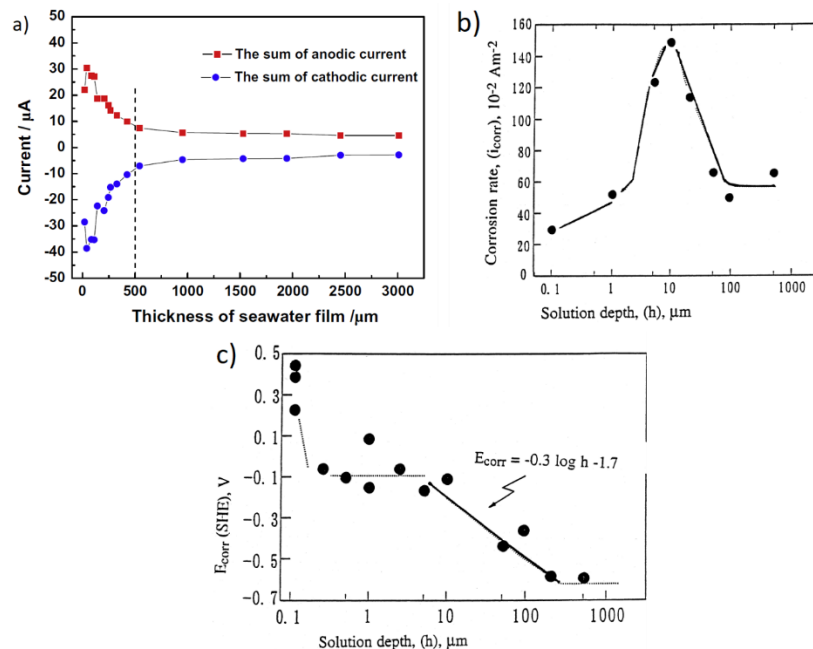


Figure I. 6: a) Corrosion current as a function of the electrolyte thickness [25] - b) Corrosion rate evolution as a function of the immersion depth [27] - c) OCP variation with the depth [27]

In their study, Liu et al. used a "wire beam electrode" (made of 121 different micro electrodes) with known and controlled level differences [25]. The wire beam electrode was immersed in such a way that each of its wires was at a different immersion depth (i.e. each electrode sees a different water film thickness). As soon as the value of the water thickness was known (with a precision of 10  $\mu\text{m}$ ) for each microelectrode, the wire of microelectrode number 1 was disconnected and the galvanic current between n°1 and the 120 others was measured. The same protocol was then performed with microelectrode n°2 and so on for each of the WBE electrodes. Based on Tomashov's theory, they have then demonstrated that the diffusion layer of dissolved oxygen is about 500  $\mu\text{m}$  and that the reaction switches from cathodic to anodic control at around 40  $\mu\text{m}$  [25]. In other words, over 500  $\mu\text{m}$  the oxygen transport mechanisms are essentially convective. Beyond this threshold value, the control is purely diffusional, and as the thickness decreases, the oxygen has less and less distance to cross to reach the steel surface. Thus, the corrosion rate is increased [26]. A maximum representative of the transition from cathodic to anodic control, according to Tomashov, is observed in this study around 40  $\mu\text{m}$  of film thickness. This means that for a thickness larger than 40  $\mu\text{m}$ , the oxygen diffusion kinetic limits the reaction, while for a smaller thickness (< 40  $\mu\text{m}$ ), the dissolution of the steel becomes slower than the reduction of  $\text{O}_2$  (i.e. iron oxidation is henceforth the limiting reaction) [27]. Indeed, the electrolyte resistance increases as its thickness decreases. When the water thickness decreases, the section through which the current must pass also decreases. In fact, the current lines are more and more "close to each other" ([24], [28]).

In the case of galvanic corrosion, the anodic attack intensifies in the vicinity of the cathode, but the phenomenon described above limits the galvanic current. There is then direct competition with the local increase in corrosion intensity. The thinner the water film, the closer the current lines are, implying an increase in electrolyte resistance. Consequently, as the thickness decreases, the current and potential gradient become steeper and steeper.

By cross-referencing these different studies, it appears that as long as the critical thickness of 40  $\mu\text{m}$  is not reached, the electrolyte resistance does not increase enough to limit the coupling and decrease the corrosion rate. On the other hand, below 40  $\mu\text{m}$ , the current lines are "too close to each other" and the galvanic current is innately limited. In addition, the solubility of the salts and corrosion products decreases and the medium in which the electrochemical reactions take place is then modified [26].

Yet, in 2007 Yadav et al. studied the potential distribution of a galvanic coupling under thin electrolyte layer [22]. A zinc / steel coupling was studied; half part of the sample was coated with zinc while the second half was made of bare steel. This study ended to the observation that even under a 10  $\mu\text{m}$  thick film the protection provided by the zinc could operate over relatively long distances. They observed the first traces of corrosion signs 9 mm far from the coupling point, which is a considerable distance regarding the film thickness and the size of the scratch. However, this distance remains really short if we consider the size of a CP installation.

Tsuru et al. in 1995 have schematically represented the evolution of the corrosion rate with the decrease of the oxygen diffusion layer thickness [26]. Figure I.7 shows the different phases determined in this study; the values presented here are nonetheless really different from [25]:

- **Phase IV** (above 1 mm and more) represents the mainly convective control of the corrosion reaction.
- **Phase III** (between 1 mm and 1  $\mu\text{m}$  in this study – or equivalent to 500  $\mu\text{m}$  and 40  $\mu\text{m}$  for [25]) shows the increase in corrosion rate according to the mechanism involved during the decrease of the oxygen diffusion layer thickness, described above.
- **Phase II** (between 1  $\mu\text{m}$  and 100  $\text{\AA}$  – or equivalent to 40  $\mu\text{m}$  to 10  $\mu\text{m}$  for Liu et al. [25]) graphically represents the anodic reaction drop linked to the increase in electrolyte and surface resistance due to the rapid precipitation of corrosion products. Indeed, in very small water quantities, the slightest corrosion product can significantly modify the composition of the solution and the limit of the corrosion products solubility is reached very quickly. Thus, the corrosion products rapidly cover the metal [27]. This results in a corrosion rate decrease.

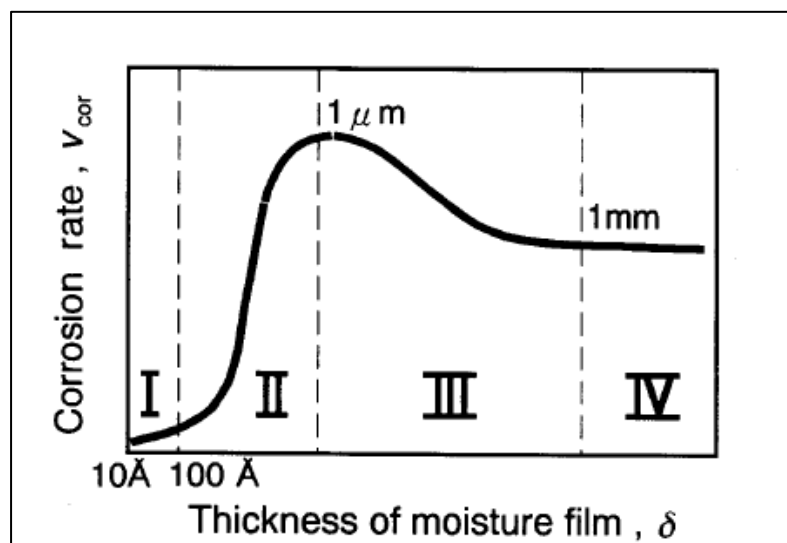


Figure 1. 7: Schematic representation of the different phases of the variation of the corrosion rate as a function of the electrolyte film thickness [26]

After defining these phases, they investigated the diffusion limiting current using a non-contact reference electrode (Kelvin probe) and electrochemical impedance spectroscopy to control the corrosion rate within the thin film. They observed that the diffusion limiting current first increases with decreasing film thickness before decreasing for very small thickness values. By following these variations and relying on the fact that the value of the limiting current depends directly on the diffusion layer thickness, they determined the following law:

$$i_{lim} = nFD_{ox} \frac{C_{ox}^b}{\delta} \quad (5)$$

With  $D_{ox}$  the oxidant diffusion coefficient and  $C_{ox}^b$  the oxidant concentration in the bulk electrolyte.

The studies cited above were all interested in the corrosion mechanism under a thin film proposed by Tomashov and were able to investigate and quantify, by local analysis techniques, with some precision, the critical values of this theory.

The study of the corrosion mechanisms under thin water film is very interesting in this context. Let us recall that the aim of this report is to open the reflection on the mechanisms involved in the cathodic protection in tidal zone. In this tidal zone, the water is at its highest and when it withdraws, a residual water film persists on the surface of the steel and may ensure a continuity with the seawater. However, all the studies presented here dealt with coplanar electrodes whereas for a CP device in the tidal zone, the anode is located in the low water zone (rather far from the structure to be protected).

### 1.2.4 Corrosion in the tidal zone

Corrosion in the tidal zone represents a special case of marine corrosion. Indeed, for a port infrastructure for example, the steel surface must be considered in its entire verticality, from the splash zone to the low water zone [29], [30]. Each of these zones involves different corrosion mechanisms depending on the exposure height (i.e. its immersion rate). In addition, differential aeration phenomena are to be expected for a continuous structure. As seen in part 2, corrosion is always triggered by surface heterogeneity. Actually, areas most likely to reach high corrosion rates are found in transition zones (i.e. equivalent to a transition in the exposure conditions). For example, the transition zones from the splash zone to the tidal zone or from the tidal zone to the low water zone are really sensitive to corrosion [3]. An electrically continuous structure exposed to the entire tidal zone as defined in introduction will have a very specific corrosion rate profile, such as the one presented Figure I.8. The most severe corrosion in this case occurs in the splash zone. A second very aggressive zone is located just below the mean low tide level. On the other hand, in this case, the lowest mass losses have been observed in the tidal zone [4]. For isolated coupons exposed similarly, no galvanic coupling can occur, and the corrosion rate is maximal in the tidal zone, a consequence of the corrosion mechanism involved by cyclic immersion (green curve in figure I.8), which is explained in section 1.2.4.2.

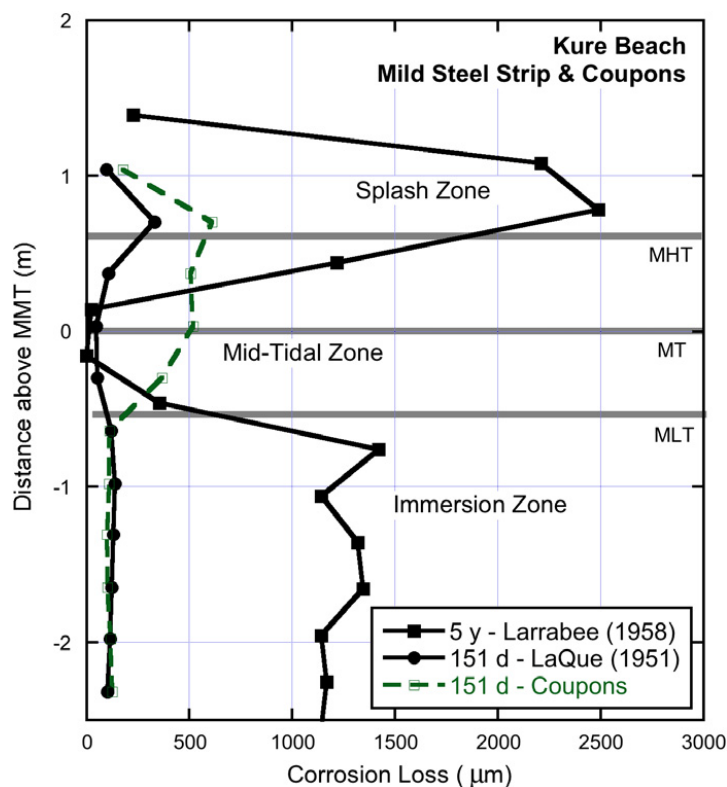


Figure I. 8: Typical corrosion rate profile of a continuous structure exposed in the tidal zone (MMT = Marine Mid Tide) [4]

#### 1.2.4.1 Special cases of the splash zone and the low water zone

Some studies observed that in the case of samples where only the lower part was immersed (the upper part being exposed to the air) the most critical corrosion rate is found in the splash zone [29], [30]. In this zone, corrosion is governed by a very particular mechanism. The exposed steel surfaces are perpetually covered with a continuously drying electrolyte film. This residual film, resulting from water movements, caused by port activities or weather conditions for instance, covers an emerged area. The metal is therefore wet in some zones and relatively dry in others. Numerous galvanic couplings are then created between the aerated and the wet areas for each droplet on the steel surface, as in the Evans drop experiment [3]. Furthermore, the continuous drying process leads to an increase in the salt concentration of the electrolyte, making it more aggressive. Despite the high salinity, the corrosion profile observed in this area is quite close to that of generalized corrosion, very little pitting has been observed by Melchers et al. in 2009 [29]. They have been able to determine the characteristic corrosion profile of a vertical steel section where one part is in permanent immersion while the other is in permanent emersion (floating samples were used in order to follow the tides). Two zones of huge corrosion rate have been observed, just above the wetting line (splash zone) and just below the water level line [29].

The second notable phenomenon is the accelerated corrosion in the low water zone, a clear example of a large-scale differential aeration stack. The part of the steel immersed in the tidal zone (and thus highly exposed to dissolved  $O_2$ ) behaves as a cathode when the part of the steel just below the lowest tide level (a more deaerated environment than the previous one) behaves as an anode.

Localized corrosion phenomena in the low water zone have been observed first in 1910. Abnormally deep pitting has been found on steel piers. Later, severe low water corrosion phenomena were observed in different British seaports, and then these observations were made all around the world [4]. The term dedicated to this mechanism is "Accelerated Low Water Corrosion, ALWC". Following these discoveries, the phenomenon has been extensively studied leading to the conclusion that it is a synergy between differential aeration and the presence of bacteria on the steel surface. In 2012 Melchers et al. re-exploited existing data to show on the one hand that ALWC is observable for relatively short immersion periods (about 1 year) and on the other hand that the amount of nutrients present in marine waters is a factor influencing this mechanism [4]. Laboratory experiments have been led in parallel with experiment carried out in natural environments. This showed that in artificial seawater (i.e. without nutrient for microorganism) ALWC is not detected. Moreover, the data collected for this work suggest that the increase in temperature would tend to slow down the phenomenon of biocorrosion, which is consistent with the first modern observations in cold British and French waters [4].

#### 1.2.4.2 Corrosion mechanisms in the tidal zone

Unlike sheet piles, isolated coupons exposed to the tidal zone have a different corrosion behavior [31]–[33]. They present a maximum corrosion rate (less pronounced than the previous ones) in the tidal zone whereas in continuous immersion the roles are reversed, partly due to differential aeration [4] [31].

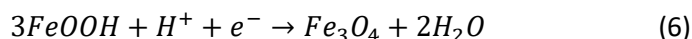
In their 2014 study, Mu et al. developed an experiment allowing them to have an in-situ monitoring of the corrosion in the tidal zone [31]. They exposed in a large tank 9 carbon steel coupons (40 mm x 25 mm x 3 mm), isolated from each other, to an artificial seawater simulated tidal zone of 40 cm amplitude and a half period of 6 h between each tide. A control coupon was placed in a permanent immersion

zone. They then estimated and ranked, in ascending order, the corrosion rates of each coupon and determined an order of aggressiveness of the encountered zones in the tidal zone, from the most corrosive to the least aggressive:

1. Middle tidal zone (in the exact middle, between the average high tide line and the average low tide line)
2. The central zone between the mid tide zone and the average low tidal zone
3. High tidal zone
4. Low tidal zone.

This corrosion rate ranking evolves in the same direction as the time the samples are exposed to a seawater film (depending on their height in the tidal zone). This concomitance of results led them to assume that the period during which the samples are emerged but covered with residual humidity is the most important (compared to the immersed period) in the tidal zone corrosion mechanisms [31].

This maximum corrosion rate in the tidal zone is often associated with the effect of alternating wet/dry cycles for isolated samples (whose behavior is different from continuous structures). In fact, the layer of corrosion products necessarily undergoes alternating drying and immersion cycles. Fe(II)-based corrosion products, such as GR(SO<sub>4</sub>) are oxidized in contact with oxygen which, according to the rate of oxygenation, give Fe(III)-based compounds (like lepidocrocite  $\gamma$ -FeOOH, cf. paragraph “2.2 Typical marine corrosion products”). These compounds enhance the cathodic reaction playing the role of oxidizing agent by reducing to magnetite Fe<sub>3</sub>O<sub>4</sub> at the beginning of each immersion period [21], [32], according to the following global reaction that does not take into account possible Fe(II)-based intermediate compounds:



The wet/dry cycles result then in a corrosion product layer rich in magnetite and ferric oxyhydroxides. The work of Refait et al. (2015) partially confirmed this mechanism [21], [32]. It is indeed necessary to consider that this alternation of dry and wet periods only takes place if drying is possible. However, depending on the exposure conditions, the emerging metal may be perpetually wet [3], [21].

In the study published in 2015 on corrosion and cathodic protection of carbon steels, P. Refait et al. exposed carbon steel coupons isolated from each other in the mid tide zone of the seaport of Le Havre [32]. These samples were facing south and were not sheltered from sunlight (or at least daylight). The complete drying of the residual water film during the emersion periods was thus possible. After 6 to 12 months of exposure, the analysis of the corrosion products layer revealed a 3 strata layer made of a really thin inner stratum of GR(SO<sub>4</sub>) covered with a thicker magnetite stratum topped by a really thin layer of oxyhydroxides ( $\gamma$  &  $\alpha$  -FeOOH). The corrosion product layer was similar after 7 years, mainly made of magnetite with an inner stratum of GR(SO<sub>4</sub>) and an outer layer of Fe(III) oxyhydroxides. In addition, because of the aerated conditions, iron sulfide was never identified. This confirms that effective wet/dry cycles lead to corrosion mechanism comparable to the atmospheric corrosion process [32].

A parallel study has been led simultaneously in the harbors of Nantes Saint Nazaire (estuary harbor) and Le Havre (seaport) in 2013 by P. Refait et al. [21]. The samples exposed in the seaport of Le Havre were in the same conditions as the ones previously described. The samples placed in Nantes-Saint Nazaire harbor were exposed to very different conditions, under a quay, between support piles, constantly in the shade. The corrosion products were therefore totally different from those collected at the Le Havre site:  $\text{GR}(\text{SO}_4)$  and  $\text{FeS}$  were formed in large quantities. These corrosion products, similar to those obtained in permanent immersion ([3], [21], [32]) reflect the absence of full drying of the emerged steel. Two phenomena can be distinguished. One, comparable to atmospheric corrosion, and the other one to marine corrosion. Considering that the steel surfaces can remain wet during the emerged periods, the notion of wet/dry cycle is not the most appropriate. It is then more relevant to reason in terms of cyclic immersion or immersion/emersion cycles [21]. Yet, this differentiation in the tidal corrosion process happens for relatively long exposure time. This study did not notice a difference between the two sites for the first year. During the first year, the composition of the corrosion products layer did not evolve, only its thickness increased. No  $\text{FeS}$  were detected. On the other hand, the analysis of corrosion products after 7 years of exposure discriminated 2 clear corrosion mechanisms (both detailed above).

During the first year, however, the corrosion patterns appear to have been relatively similar in all cases. The corrosion of the steel mainly takes place during the immersed periods. With tides and sea spray, the steel surface goes through an alternation of several states, immersion, emersion (or wet state covered by seawater residual film) and drying (depending on the conditions) [31]. As the emerged time increases, the thickness of the water film decreases because of its evaporation and the salt concentration increases while the corrosion layer forms (or grows) on the steel surface. The electrical resistance of the water film covering a coupon exposed to air is influenced by:

- On the one hand, the gradual increase in ionic concentration of the residual seawater,
- On the other hand, the continuous decrease of the film thickness, which thus decreases the section the current can/has to go through [31].

There is, therefore, competition between the first phenomenon which will tend to increase the conductivity of the solution facilitating the current flow and the second, increasing the electrolyte resistance at the structure surface.

The corrosion products obtained at the end of these exposure times to seawater are essentially composed of  $\text{GR}(\text{SO}_4)$ . Drying or exposure to oxygen leads to the oxidation of these mixed valence  $\text{Fe}(\text{II},\text{III})$ -compounds. The oxygen flow perceived by the green rust is determining on the product obtained, a weak flux favors magnetite while a stronger flow favors the formation of lepidocrocite. It is then possible to propose a scenario summarizing the free corrosion mechanism of steel in the tidal zone and the corrosion products associated to each step (schematized figure I.9).

During emersion,  $\text{GR}(\text{SO}_4)$  is oxidized to  $\text{Fe}_3\text{O}_4$  in the weakly aerated zones and to  $\gamma\text{-FeOOH}$  where air easily accesses to the surface [32]. Moreover, as explained above, during the first moments of the immersion period, lepidocrocite is reduced to magnetite ( $\text{Fe}_3\text{O}_4$ ). This reduction is added to that of the oxygen accelerating the corrosion. Thus, the wet/dry cycles result in the formation of a steel corrosion products layer rich in magnetite and poor in lepidocrocite [21], [32]. In this case, the corrosion of the steel is very aggressive, the oxygen supply is important and the ionic concentration of the electrolyte is higher than in continuous immersion because of the evaporation of the residual film [31].

However, if the alternation of these cycles continues, the corrosion products layer continues to grow and its electrical resistance increases. Thicknesses no longer allowing complete drying are reached [21] and the ionic conductivity is increased [31]. Consequently, the internal layers remain saturated with seawater and the corrosion mechanism is similar to that of continuous immersion. The  $O_2$  diffusion into the corrosion products layers is limited.  $GR(SO_4)$  accumulates and SRB can develop, forming FeS [21].

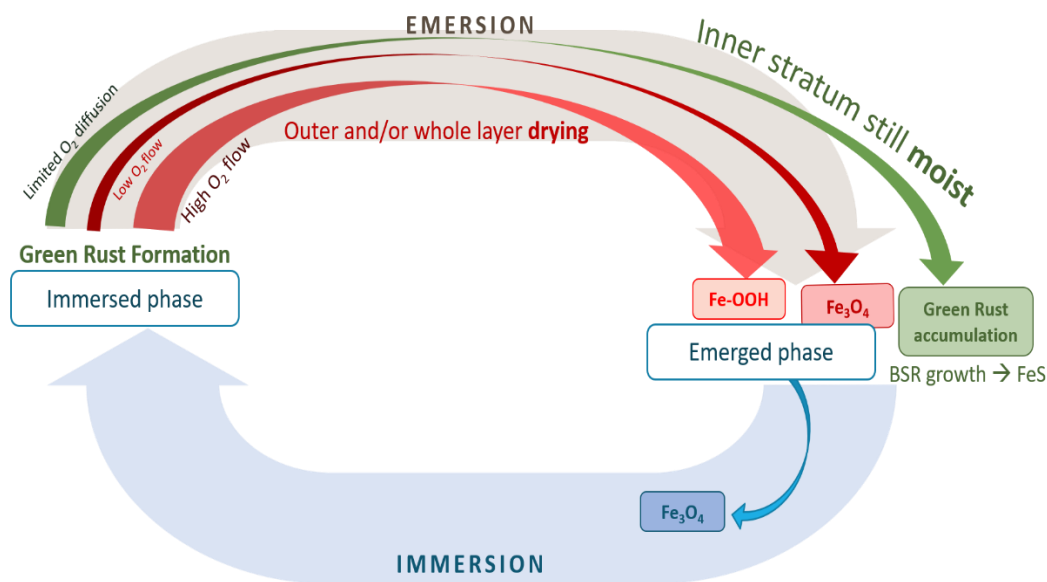


Figure I. 9: Schematization of the corrosion phenomenon in the tidal zone

Julien Duboscq has, for his PhD work, set carbon steel samples in free corrosion at different heights of the tidal zone in the commercial seaport of La Rochelle [3]. Coupons exposed to the low tidal zone (immersion rate > 90%) have been taken off for analysis. He was then able to highlight and determine the role of sulphate-reducing bacteria in the mechanism involved during the emersion phases of coupons covered with a thick porous layer (see Figure I.10) [3].

First of all, it must be considered that some SRB are able to survive in the presence of oxygen, and may not die even during emersion phases [3]. Moreover, given the very high immersion rate of these coupons, associated with the important thickness of the external layer covering them, it is quite plausible that these samples would never completely dry even out of the water. Therefore, an SRB development in this zone is quite conceivable. During submerged periods, these bacteria lead to the formation of FeS. However, during the emerged period, the SOB (sulfo-oxidizing bacteria) are active, they oxidize the sulfides into sulphate thus regenerating the environment close to the steel surface. This mechanism actively participates in the development of the SRB.

As mentioned above, this mechanism assumes the existence of a thick porous layer covering the metal, easily conceivable in anodic zones. In cathodic zones, the corrosion product layer is a priori less thick. Intuitively, it is possible to think that the persistence of deaerated zones is, in fact, less probable than in anodic zones. However, if a zone remains cathodic, even covered by a layer of corrosion products, it is because this layer is rich in conductive compounds ( $Fe_3O_4$  and FeS) allowing the reduction of oxygen at their surface. Therefore, the  $O_2$  flow does not reach the internal parts of the corrosion product layer. The internal layers are more deaerated. The green rusts are then the main compounds

of the inner layer as the oxygen (consumed on the surface) does not react with them [3]. As proposed previously [18], there is a self-sustaining mechanism involved in the persistence of cathodic zones (where oxygen is easily reduced) coupled with anodic zones covered with insulating FeOOH drastically limiting  $O_2$  diffusion. The refined mechanism proposed by Julien Duboscq [3], illustrated in figure I.10, includes the possible influence of microorganisms.

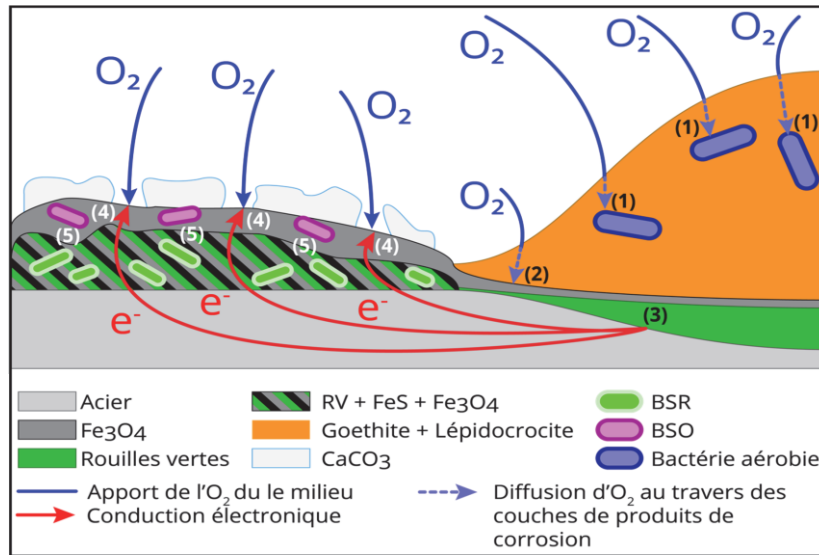


Figure I. 10: Self-sustaining corrosion mechanisms associated with the heterogeneity of the corrosion product layer: possible influence of micro-organisms [3]

Each number (from 1 to 5) reported on the figure above corresponds to a phenomenon of the global self-sustaining corrosion mechanism:

1. Oxygen consumption by aerobic bacteria. The fraction of residual  $O_2$  reaching the GRs can lead to the formation of magnetite [21]. For advanced corrosion stages, the inner layer composed of GR(SO<sub>4</sub>), FeS and Fe<sub>3</sub>O<sub>4</sub> thickens. The outer layer composed of Fe(III) oxyhydroxides remains relatively thin [34].
2.  $O_2$  reduction where the FeOOH outer stratum is thin enough to allow oxygen diffusion toward the metal.
3. Steel dissolution, mainly in the anodic zone, to counteract the oxygen reduction reaction.
4. Cathodic zone: oxygen reduction. The dissolved  $O_2$  must diffuse through a thin layer of CaCO<sub>3</sub> formed as a result of the local pH increase [35]. The presence of SRB leads to the formation of FeS at the detriment of GRs. The increase in interfacial pH favors for formation of magnetite at the detriment of GR(SO<sub>4</sub>) [18]. The conductive compounds enrichment of this layer is the key factor in this process. It allows the persistence of the cathodic zone [18].
5. Synergy of SOB and SRB favoring SRB and more generally, association of SRB with aerobic species consuming part of the  $O_2$  during periods of emersion. This association is often favored in low water zones (in other words, in tidal zones with a high immersion rate) [4].

## 1.3 Cathodic protection

### 1.3.1 Cathodic protection, the principle

In order to solve the corrosion problems of these structures many techniques are possible. The passive ones such as coatings application (organic or metallic) or the active ones such as Cathodic Protection (CP). The sine qua non condition of this technique is the exposition of the metal to protect to a conductive milieu (water, ground, or concrete [6]). The CP principle consists in placing the steel (or the structure to be protected) in its cathodic domain making the current run from the anode toward the metal. The potential of the metal is thus lowered to its so-called immunity area [3], [6]. In other word, the CP installation is designed to lower enough the potential of the structure in order to significantly decrease its corrosion rate, i.e. the corrosion current density (lower than  $j_{cor}/10$ ).

There are 2 types of CP methods. The first method is based on the use of a galvanic (or sacrificial) anode, which is coupled with the structure to be protected. This anode must then be made of a metal or alloy less noble than the metal of the protected structure. The second method makes use of a power supply to impress the CP current and is then called Impressed Current Cathodic Protection (ICCP). In this case, the anode, called energized anode, is more generally composed of an inert material and its role is only to complete the electrochemical cell. The potential value to achieve is also called protection threshold, or protection criterion. This value is defined, according to the electrolyte considered, by standards such as the NF EN 12463. Figure I.11 sums up the principle of this technique.

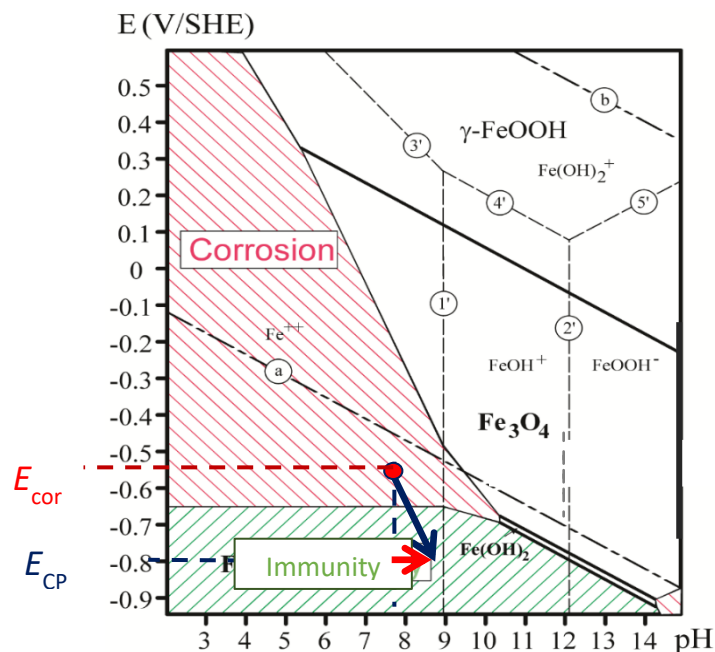


Figure I. 11: CP principle: Pourbaix diagram of iron in  $H_2O$  at 25°C

Iron immunity area starts (by convention, i.e., for equilibrium conditions between  $Fe^0$  (iron at oxidation state 0) and a solution with an activity of  $10^{-6}$  for dissolved species, in our case  $Fe_{aq}^{2+}$ ) for potential value around -0.65 V/SHE ( $\approx -0.9$  V/Ag/AgCl<sub>sw</sub>). Most standards define that the steel is protected below -0.8 V/Ag/AgCl<sub>sw</sub>, or below -0.9 V/Ag/AgCl<sub>sw</sub> in deaerated environments.

### I.3.2 Calcareous deposit: a consequence of cathodic protection

#### I.3.2.1 Precipitation mechanism of the calcareous deposit

The interfacial pH increases at the cathode surface because of the reduction of  $O_2$  and  $H_2O$ , reactions that both produce  $HO^-$  ions. As a consequence, a deposit of magnesium hydroxide and calcium carbonate, called a calcareous deposit, precipitates on the surface of the metal (figure I.12). The calcareous deposit precipitation constitutes a secondary protection against corrosion (as a physical barrier to oxygen diffusion) [36].

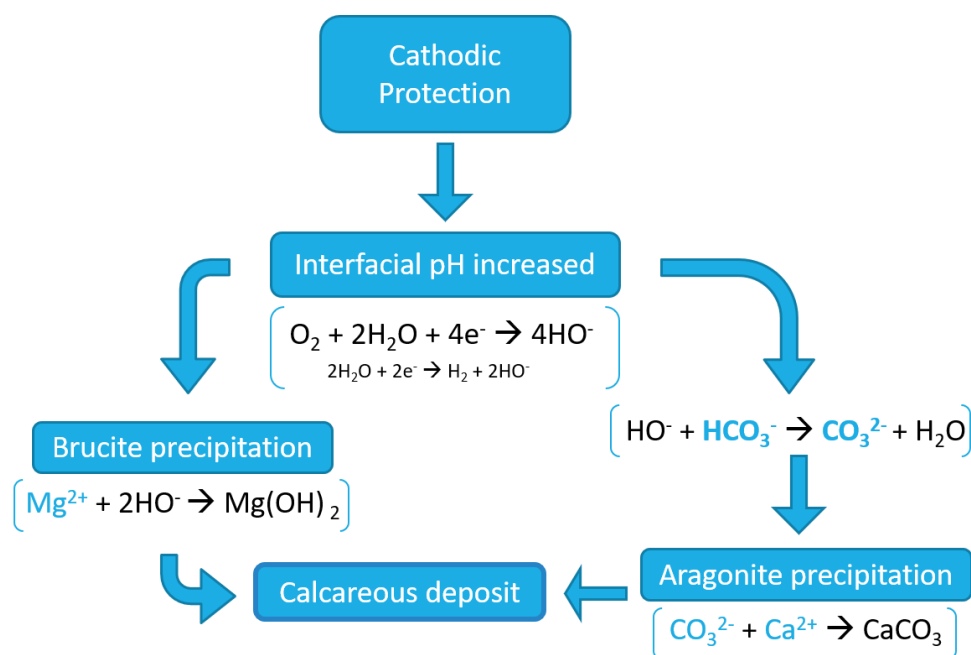


Figure I. 12: Chemical formation of the calcareous deposit [37]

From a macroscopic point of view, the polarization of a metallic surface in an electrolyte influences the transport of dissolved ionic species. The motion of ionic species involves three transportation modes: migration, diffusion and convection. This defines therefore three juxtaposed regions [38]:

- The migration layer in which ions highly undergo the electric field influence,
- The diffusion layer in which the motion is governed by the concentration gradient linked to the chemical reactions,
- The bulk electrolyte in which the ions movement is only affected by the convection forces due to temperature variations or mechanical stirring (ship movement or swell for instance).

Under the action of the electric field, the cations, e.g.,  $Ca^{2+}$  and  $Mg^{2+}$ , are attracted toward the cathode while anions migrate toward the anode, i.e., away from the cathode. The transport of carbonate species, which are consumed by the precipitation of  $CaCO_3$ , toward the cathode is then only ensured by diffusion and convection. The calcareous deposit precipitation mechanism could then be summarized in three steps: (i) the active species transfer toward the cathode, (ii) the mineral species colloidal nucleation (germination) [39] (iii) the mineral growth [40]. Step (ii) depends on both medium and process parameters. Step (iii) is conditioned by thermodynamics and kinetics conditions. For instance, brucite precipitation is governed by a minimum pH varying between 9.3 and 10 [41], [42]. Depending on the interfacial pH, the precipitate may then be mainly composed of calcium carbonate

$\text{CaCO}_3$  or magnesium hydroxide  $\text{Mg}(\text{OH})_2$ . The precipitation of magnesium hydroxide has much faster kinetics than calcium carbonate, which requires a shift in  $\text{HCO}_3^-/\text{CO}_3^{2-}$  carbonate equilibrium [43]. There are three different allotropic forms of calcium carbonate (calcite, vaterite and aragonite) but previous studies on the calcareous deposit formed under cathodic protection in seawater ([32], [36], [43]) showed that the carbonate polymorph formed is mostly aragonite. The study led by Barchiche et al. in 2003 showed that in presence of  $\text{Mg}^{\text{II}}$  species, calcium carbonate precipitates exclusively under the form of aragonite [20]. Actually, aragonite is less thermodynamically stable than calcite but the nucleation of calcite is inhibited by the presence of magnesium dissolved species [40], [44]. Magnesium hydroxide exists in a single form, named brucite ( $\text{Mg}(\text{OH})_2$ ), which precipitates initially in the form of a gel-like structure. This results in a crystal growth depending on the thermodynamic conditions of the medium (pH, ionic activity product, etc.) [44]. Consequently, the physical and mechanical characteristics of the material change over time.

As the average pH of the oceans is about 8.2, the formation of the deposit will depend on the pH evolution kinetics of the medium. This kinetic being a function of the charge flow through the surface of the electrode, the potential or the current imposed through the system will have an influence on the composition and the growth of the deposit.

### 1.3.2.2 Parameters influencing the deposit growth and composition

Various parameters can influence the composition and the growth kinetics of the calcareous deposit, such as the current flow, the electrochemical potential, the nature of the environment etc... In the following paragraphs, the most important parameters and their influences will be discussed.

#### 1.3.2.2.1 Electrochemical parameters

The main electrochemical parameters are the cathodic current density and the potential. Concerning the cathodic current density, it could be intuitive to think that its increase would lead to a bigger volume growth of the deposit by intensifying the  $\text{HO}^-$  ions production. Yet, to improve the knowledge about volumetric growth of the calcareous deposit under CP, Akamine et al. in 2003 have determined the optimal current conditions for its formation on a steel substrate [40]. They finally demonstrated that volumetric growth of both brucite and aragonite increases with the current density up to a maximum ( $0.05 \text{ mA/cm}^2$  for aragonite and  $7 \text{ mA/cm}^2$  for brucite) before slowing down as shown in figure I.13.

These results seem directly linked to the pH gradient and its influence on the electric surface charges of the mineral particles. An increase in the cathodic current density implies a faster cathodic reaction, thus a more important  $\text{HO}^-$  production, i.e., a more important increase in the interfacial pH. Aragonite particles have a positive surface charge for  $\text{pH} < 9$ . Then for a higher pH, the particles could not deposit onto the steel surface. For brucite, this transition occurs for  $\text{pH} = 11$  [40].

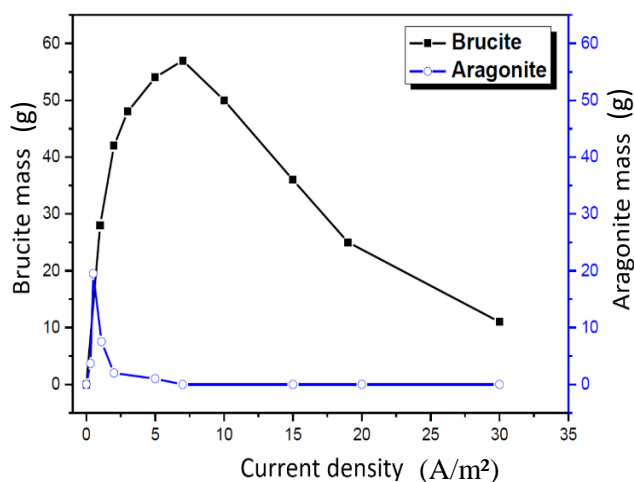


Figure I. 13: Variation of the precipitated quantity of deposit on the electrode surface as a function of the current density [40]

When CP is applied using a galvanic anode, or with a constant applied potential, the cathodic current density tends to decrease as a function of time due to the formation of the deposit, which reduces the active surface of the cathode and provides additional resistance to the mobility of charges in the media (carried by the ions) [38]. The residual cathodic current density, i.e., the current density necessary to maintain a given potential after formation of the calcareous deposit, is then very low (for applied potentials between  $-0.9$  V and  $-1.1$  V/SCE). The value of the residual cathodic current density is directly related to the covering rate of the surface by the calcareous deposit and its density. The denser the deposit, the slower the diffusion of oxygen through the deposit and the lower the residual current density. Moreover, brucite, when in contact with seawater at pH 8.2, could dissolve, releasing  $\text{HO}^-$  ions and then favoring the precipitation of aragonite as demonstrated by D.D. Nguyen et al. [45]. Therefore, for long enough observation times, the composition could be modified, in particular the Mg/Ca ratio should decrease. Similarly, for very short observation times, the applied potential value governs the current density value and thus the composition of the deposit formed in the early moments of the polarization.

In addition, the applied potential is responsible for the electrochemical reactions occurring at the metal/solution interface. Indeed, the potential value will influence the cathodic reaction taking place on the substrate. If this potential is weakly cathodic, only oxygen reduction will take place at the metal surface, and this reaction is controlled by the transport of matter. There is then preferential formation of aragonite. If the potential is sufficiently cathodic, the reduction of water (reaction 3) leads to a release of dihydrogen and a strong increase in  $\text{HO}^-$  ions production. There is then a preferential formation of brucite because of the high concentration of  $\text{HO}^-$  ions. Brucite starts to precipitate, in competition with aragonite from  $-1,1$  V/SCE and no more aragonite is found for potentials below  $-1,3$  V/SCE. The threshold value of potential between these two processes is then between  $-1.1$  V/SCE and  $-1.3$  V/SCE [41], [46].

These values are symbolized figure I.14. This figure has been extracted from the Barchiche et al. (2003) study and then the precipitation domains of the different calcareous compounds have been reported on the graph. On the one hand, in these conditions (steel rotating electrode, 600 rpm) there is a long oxygen diffusion plateau, limiting the cathodic current. This limiting current is directly linked to oxygen supply. Then for fixed oxygen diffusion conditions (defined by the 600 rpm here) the current will remain stable as long as the oxygen reduction governs the kinetics. For potentials lower than

-1 V/SCE, the kinetic is governed by water reduction leading to a harsh increase in absolute current density. In these conditions brucite starts to precipitate for potential lower than -1.1 V/SCE. On the other hand, if the oxygenation gets more and more intense because of an increase in oxygen supply (comparable to the first stage of emersion in the tidal zone for instance) then this limiting current would be much higher. The red curve figure I. 14 suggests what could happen for high  $O_2$  flow conditions. The limiting oxygen diffusion plateau is much higher and water reduction becomes significant (comparatively to  $O_2$  reduction) for a lower potential than previously. Consequently, the limiting cathodic current plateau crosses the precipitation domain of aragonite and brucite, and lead to brucite formation. According to this reasoning, the higher the dioxygen flow, the easier it is to precipitate brucite for relatively low potentials.

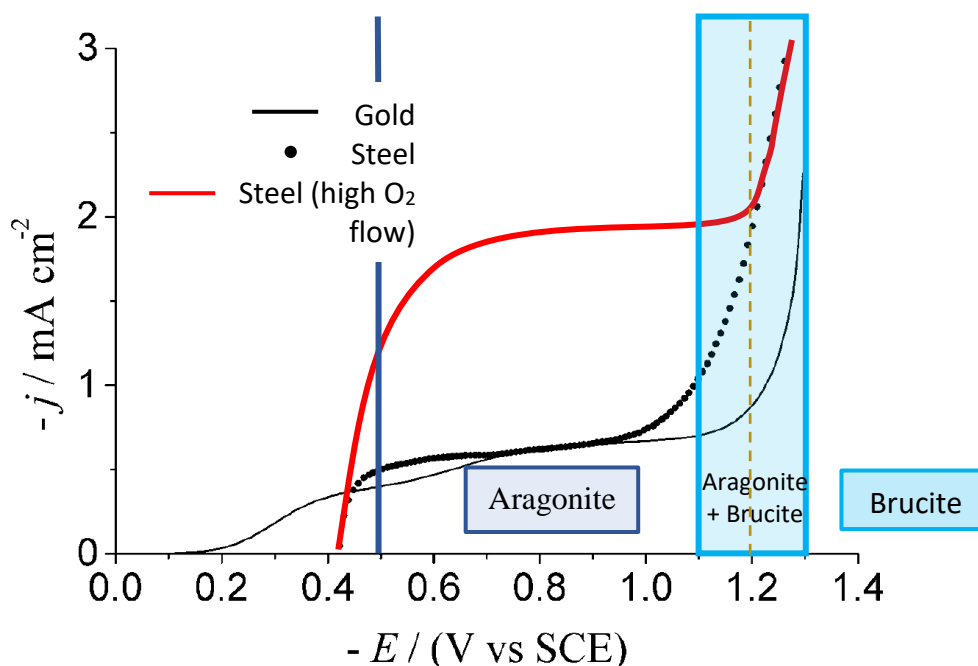


Figure I. 14 : Schematic representation of aragonite and brucite precipitation domain regarding  $O_2$  diffusion limiting current. [20]

#### 1.3.2.2.2 Impact of the surrounding environment

##### ➤ Chemical composition of the solution

It has been shown that the cathodic reactions are conditioned by the concentrations of calcium, magnesium and dissolved oxygen [47], [48]. A low concentration of dissolved oxygen is indeed a limiting factor for the oxygen reduction reaction and would lead the system towards the hydrogen evolution for very low cathodic potential values (lower than -1.2 V/SCE). Under these conditions, the deposit formed is mostly composed of brucite.

The concentration of the main species constituting the deposit can also influence its composition and structure. Several authors have for example highlighted the inhibiting effect of magnesium on the formation of carbonate minerals. For instance, Barchiche et al. (2003) studied calcareous deposit formation on a rotating carbon steel electrode (600 rpm) in artificial seawater at -1.0 V/SCE. Their study demonstrated that an increase in  $Mg^{2+}$  concentration in artificial seawater (from  $1,3 \times 10^{-2}$  to  $2,73 \times 10^{-2}$  mol/L) inhibited progressively calcite formation onto the substrate surface [20]. In addition, aragonite started to precipitate for a magnesium concentration of  $25\% [Mg^{2+}]_{ref, Art. SW}$  (considering

$[Mg^{2+}]_{ref,Art.SW} = 5.46 \times 10^{-2}$  mol/L as defined in the ASTM standard). Aragonite totally covered the considered surface for  $50\%[Mg^{2+}]_{ref,Art.SW}$  while calcite (the second allotropic form of  $CaCO_3$ ) did not precipitate. Those results clearly show that  $Mg^{2+}$  impacts negatively calcite nucleation. Conversely, from the aragonite point of view, magnesium seems to favor its precipitation. The study led by Deslouis et al. (1998) reinforce these observations since in aqueous solution without magnesium only calcite precipitated [49]. Moreover, another study reported the formation of an aragonite based calcareous deposit in artificial seawater containing  $Mg^{2+}$  while the deposit was made of calcite in the same conditions without  $Mg^{2+}$  [50]. This observation is also supported by the recent study of D. D. Nguyen (2017) [45]. Comparing  $Mg(OH)_2$  and NaOH medium for  $CaCO_3$  polymorphs, they observed that a higher  $Mg^{2+}$  concentration favored aragonite growth while calcite (and vaterite) were favored in strongly basic medium without magnesium [45]. Thus, in the absence of magnesium in solution, the deposit is formed of calcite, the most stable crystalline phase in the ambient conditions.

#### ➤ Bacteria and organic matter influence

The presence of bacteria and more particularly sulfidogenic bacteria can influence the characteristics of the deposit. Some authors have shown for example that in seawater with low bacterial concentration, brucite appears at lesser cathodic potential (-0.8 V/SCE) [51]. The comparison with a deposit formed in natural seawater with high bacterial concentration (thiosulfate-reducing bacteria) shows no difference from a composition point of view. However, the presence of bacteria could improve the resulting physical properties, such as compactness and density. Indeed, recent work carried out by Vincent et al. on 14 strains of bacteria has shown that the presence of these organisms allows the formation of calcium carbonates (calcite), in the absence of polarization [52], [53]. The work of Colin et al. (2022) also emphasizes that the biofilm formed in the presence of bacteria has no impact on the variation of the cathodic current [50]. A notable influence is however noticed in artificial medium in the presence of a bacterial culture of "*Pseudoalteromonas*" and "*Virgibacillus halodenitrificans*". Thus, the coupling of cathodic polarization and bacterial presence in a marine environment is almost unavoidable, especially since polarization does not seem to influence the development of bacteria on the metal surface [53], [54].

Concerning the impact of organic matter, according to Godart and Dagbert (2004), the precipitation of carbonate and magnesium minerals is inhibited by a high concentration of organic matter [55]. This seems to be confirmed by the study of B. Colin (2022) where the formation of calcareous deposits was studied in the case of a synergy between cathodic protection and biocalcifying bacteria influence [50]. The results showed that the nature of the deposit is deeply changed in the presence of the above-mentioned strains, the aragonite (carbonate compound) and the brucite (magnesian compound) were totally inhibited. The calcareous deposit obtained was actually formed of Mg-containing calcite.

#### ➤ Composition and surface state of the cathode

The influence of the composition of the cathode has also been evaluated. In their study, Sarlak et al (2009) showed for example that according to the composition of the cathodic material (mild steel, 316L stainless steel, copper), a threshold value of potential could or could not exist, thus separating the precipitation domains of brucite and aragonite [56]. According to this study, the modification of the steel composition modifies the obtained deposit composition for a given potential. As presented in figure I. 15, a threshold potential value of -1200 mV/SCE constitutes a clear separation between the aragonite and brucite precipitation domains, the latter precipitating for lower potentials for mild steel while the value is -1100 mV/SCE for the 316L stainless steel.

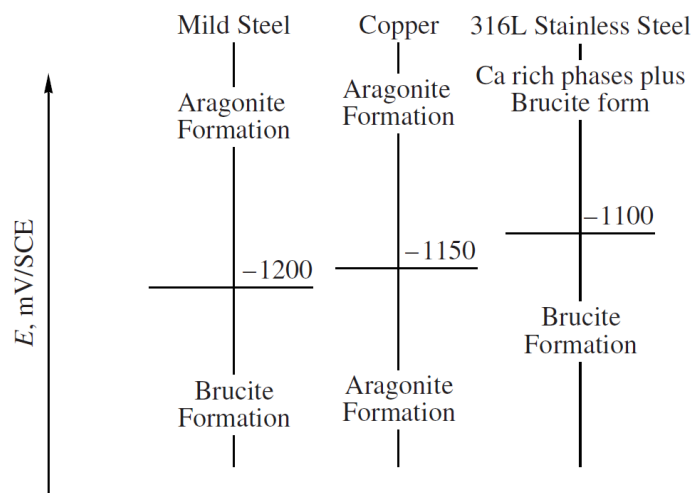


Figure I. 15 Schematic diagram of calcareous deposits formation on mild steel, copper and 316L stainless steel [56]

The phenomena involved in the formation of the calcareous deposit are essentially surface phenomena. It could be intuitive to assume that surface roughness may have a non-negligible impact on the calcareous deposit. Yet, it has been proved that it has an effect on the calcareous deposit nature for surfaces rough enough to induce a significantly irregular potential distribution (i.e., changing then the local electrochemical behavior of the surface). Most authors have shown from experimental studies that the surface state has no influence on the formation of the deposit [41], [57], [58]. However, it should be noted that these authors highlighted the influence of the surface state on the formation of the deposit and not on its protective ability.

### 1.3.3 Cathodic protection in the tidal zone

Considering the corrosion mechanism highlighted in the “2.4 Corrosion in the tidal zone” section, the cathodic protection functioning mechanism in the tidal zone, even during the emerged periods, appears much clearer. This phenomenon was indeed observed by Refait and al. for steel samples placed under CP in the site of Le Havre in spite of the alternation of actual wet/dry cycles [32].

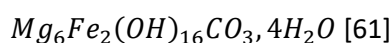
The retained hypothesis to explain the CP persistence out of water is based on the presence of a thick porous layer on the steel surface capable of retaining a film of water allowing the cathodic current to pass. The hypothesis of the persistence of a residual film of moisture has already been demonstrated in studies on galvanic couplings between different parts of the tidal zone [29], [33].

In 2015, P. Refait et al. analysed coupons that were exposed to the tidal zone under cathodic protection (permanent or delayed) for 7 years [32]. At the end of these 7 years, the metal was covered with a thick white mineral layer (seeming to incorporate parts of macro-organism shells [34]) that overlaid a thinner, black internal stratum [32]. This white layer contained an important proportion of brucite.

The applied potential resulting from the galvanic anode CP device varied from -0.75 to -0.95 V/SCE with the tide. In this range of potential, oxygen from seawater is reduced onto the metallic surface (according to the oxygen reduction reaction described in the part “1.2 Carbon steel and marine medium”) releasing  $\text{HO}^-$  ions which locally increase the pH. This shifts the  $\text{HCO}_3^-/\text{CO}_3^{2-}$  equilibrium favoring the  $\text{CaCO}_3$  precipitation [6], [32], [59]. For pH value above 9.3, in natural seawater, brucite  $\text{Mg}(\text{OH})_2$  could precipitate too [60]. On the other hand, the 2003 study of Barchiche et al.

demonstrated that brucite starts to precipitate for potential more negative than -1.1 V/SCE in competition with aragonite down to -1.3 V/SCE where brucite is the only compound formed [20]. Brucite detection in the tidal zone could then be linked mainly to the succession of immersion cycles. Indeed, this may be an evidence of unusual high currents running through the steel surface during the early stages of the emerged phase (just after emersion, because of the extremely high dioxygen flow as explained previously). As mentioned above, during this phase the O<sub>2</sub> diffusion is favored by the thinness of the film covering the steel surface, the reduction kinetics is therefore enhanced, releasing a large quantity of HO<sup>-</sup> ions without electrolyte renewal. As a result, the interfacial pH strongly increases locally [21], [32].

Underneath this calcareous deposit, magnetite was the main corrosion product observed. In addition, micro Raman-spectroscopy of this black layer revealed GR(SO<sub>4</sub>) and GR(CO<sub>3</sub>) as well as FeS. Similarly, lepidocrocite was found as a minor compound [34]. The analysis of the corrosion products under the calcareous deposit also detected pyroaurite. This is a compound similar to GR(CO<sub>3</sub>) where Fe<sup>2+</sup> ions have been replaced by Mg<sup>2+</sup> ions:



This corrosion product is characteristic of the residual corrosion mechanism of carbon steel under CP in the presence of Mg. The increase in pH caused by CP provides the necessary conditions for its formation [32].

Finally, in the study conducted by Ph. Refait et al. in 2015 [32], the effect of CP on pre-corroded surfaces were studied. Samples left for 6 years in a free corrosion state were polarized for one year. The result is that the application of CP on an existing corrosion products layer does not imply any drastic modification of its composition. Only a small portion of ferric oxyhydroxides would probably be reduced to magnetite under the effect of CP, which is even more likely for actual wet/dry cycles [19]. A similar experiment, which confirms these results, was carried out in 2013 by P. Refait et al, for 5 years of exposure to free corrosion followed by one year of polarisation [34]. The same corrosion products were observed: nanocrystalline FeS, green rust, lepidocrocite and magnetite. The main difference was the detection of GR(CO<sub>3</sub>). The GR(SO<sub>4</sub>) formed at OCP was transformed into carbonated green rust by CP [19], [34]. As with the formation of calcareous deposit, this transformation takes place due to the increase in pH which shifts the HCO<sub>3</sub><sup>3-</sup>/CO<sub>3</sub><sup>2-</sup> carbonate equilibrium in favor of CO<sub>3</sub><sup>2-</sup>. Usually this leads to the formation of CaCO<sub>3</sub> but in this case, the increase in carbonate concentration also induced the transformation of GR(SO<sub>4</sub>) to GR(CO<sub>3</sub>). This transformation only involves an anion exchange, preserving the main frame of the crystal structure, i.e., the stacking of the hydroxide layers, and only changing the distance between them [34].

In any case, the efficiency of CP was demonstrated and sometimes quantified. The corrosion with CP was estimated to be 1/10th of the corrosion rate without CP using residual thickness measurements on coupons left 6-7 years in natural seawater whether in the tidal zone (mid-tide) [19] [32] or in the immersion zone [34], i.e., about 4-10 μm yr<sup>-1</sup>. Laboratory experiments showed that depending on applied potential and protectiveness of calcareous deposit, the corrosion rate can be divided by 100 with CP, i.e., as low as about 0.4 μm yr<sup>-1</sup> [36].

## Conclusion

Carbon steels exposed to marine environments have different corrosion behaviors depending on the exposure zone. The corrosion products obtained in each case are characteristic of the zone where they were formed.

- In the (permanent) immersion zone, the corrosion product layer is mainly made of two strata:
  - An inner one in contact with the steel: the main compounds present in this stratum are  $\text{GR}(\text{SO}_4)$ ,  $\text{Fe}_3\text{O}_4$  and  $\text{FeS}$ , which are characteristic of anoxic conditions.
  - An outer one, in contact with seawater. In contact with oxygen,  $\text{Fe}(\text{II})$ -based phases, and in particular  $\text{GR}(\text{SO}_4)$ , are oxidized by dissolved  $\text{O}_2$  to  $\text{Fe}(\text{III})$  oxyhydroxides ( $\gamma\text{-FeOOH}$  and  $\alpha\text{-FeOOH}$ ) and magnetite, depending on the  $\text{O}_2$  flow. The formation of magnetite from  $\text{GR}(\text{SO}_4)$  requires a very low oxygen flow so that the outer stratum is mainly made of  $\text{FeOOH}$  phases.

The presence of iron sulfides reflects the growth and activity of SRB, which are anaerobic bacteria that may survive with difficulty in the presence of oxygen.

The corrosion process of carbon steel permanently immersed in seawater is commonly considered as uniform, but localized corrosion processes may take place. Whatever the heterogeneity that initiated this process, it seems that it can persist because it induces a heterogeneity of the corrosion product layer because different compounds formed on cathodic and anodic zones. On the one hand, magnetite and carbonate products (such as chukanovite or  $\text{GR}(\text{CO}_3)$ ) are favored in the cathodic zone. On the other hand,  $\text{GR}(\text{SO}_4)$  and ferric oxyhydroxides are characteristic of anodic zones. A self-sustaining phenomenon allowing the persistence of anodic and cathodic zones is then established: oxygen is reduced in contact with conductive corrosion products such as magnetite and  $\text{FeS}$  (more likely favored initially in the cathodic zones [3]) while it is consumed by the oxidation of  $\text{GR}(\text{SO}_4)$  and by aerobic bacteria in the corrosion product layer covering the surface of the anodic zones. Green rust therefore continues to form in the anodic zone to counterbalance the reduction of oxygen in the cathodic zone.

- In the tidal zone, steel undergoes immersion/emersion cycles with a possible drying period depending on atmospheric conditions. During the emersion phase a residual water film remains on the surface, the corrosion mechanisms directly depend on the film thickness and its "lifetime". Several studies have shown that the free corrosion rate increases as soon as the film thickness reaches the same value as the oxygen diffusion layer (between 1 mm and 500  $\mu\text{m}$ ). This corrosion rate then reaches a maximum at 40  $\mu\text{m}$ , a critical point at which  $\text{Fe}^{2+}$  production is slower than oxygen reduction. Below this threshold value, the electrolyte resistance increases sharply due to the reduction in the cross-section through which the corrosion current flows. Corrosion in the tidal zone is therefore governed by these laws.

A continuous structure exposed to the tides will reach a maximum of corrosion in the splash zone and in the low water zone (according to the ALWC phenomenon). For isolated samples, however, the maximum is reached in the tidal zone. Two cases can be distinguished when it comes to corrosion in the tidal zone: wet/dry cycles and immersed/emerged cycles. In both cases, the first stages are similar,  $\text{GR}(\text{SO}_4)$  is produced during the immersion phase and then oxidized to  $\text{Fe}_3\text{O}_4$  and  $\gamma\text{-FeOOH}$  during drying periods. This oxyhydroxide acts as an oxidant in the early stages of immersion and is reduced to  $\text{Fe}_3\text{O}_4$ . These wet/dry cycles therefore result in a magnetite rich corrosion product layer. For longer exposure times, the drying may become incomplete when the layer becomes too thick to allow water

evaporation. In this case, the outer stratum will follow the same mechanism while the inner stratum will follow a mechanism closer to the permanent immersion corrosion mechanism:  $\text{GR}(\text{SO}_4)$  will continue to form and the SRB metabolic activity will be unaffected or almost unaffected.

- The persistence of a water film on the surface of the steel is also responsible for the persistence of CP in the tidal zone. This CP results in the precipitation of a calcareous layer caused by the local increase in pH. Indeed, as the seawater pH is around 8.2, this local pH increase usually leads to aragonite  $\text{CaCO}_3$  formation in seawater as aragonite is the main compound to precipitate between 8 and 9 pH. On the other hand, some studies pointed out the precipitation of brucite, particularly in the tidal zone. Cross-referencing the articles, this brucite eruptions could be linked to the important pH increase taking place during the early stage of emersion. Precisely, in these conditions, electrolyte pH could easily reach 11, the transition value for which the aragonite is inhibited and the brucite formation is enhanced.

Under this deposit, residual corrosion products are formed (the corrosion rate is divided by at least 10) such as pyroaurite, magnetite or FeS. In addition, the application of CP on corroded steel leads to a slight modification of the products already present. Pre-existing  $\text{GR}(\text{SO}_4)$  is transformed to  $\text{GR}(\text{CO}_3)$  by the increase in interfacial pH.

The following thesis work was then designed to understand the phenomena occurring on steel under CP in the tidal zone:

- Following the thesis work of J. Duboscq, carbon steel coupons set all along the tidal zone (5.1 m height) of the commercial seaport of La Rochelle, protected by CP using an Al-Zn-In anode, were thoroughly analyzed after 33 and 52 months of exposure to the marine environment. The mineral layer covering each of them was characterized by XRD and  $\mu$ -Raman spectroscopy and its composition linked to both corrosion mechanisms and CP efficiency (chapter 3).

- Laboratory experiments were conducted with coupons set under thin films of water (1 mm and 5 mm thickness) and cathodically polarized at -750 mV/Ag-AgCl-3M (insufficient CP) and -950 mV/Ag-AgCl-3M (correct CP). The electrochemical behavior of the coupons and the protective ability of the obtained calcareous deposits were studied by voltammetry, LPR and EIS measurements coupled with XRD analysis (chapter 4).

- Finally, coupons subjected to CP in simulated tidal conditions were studied in the lab (Naval Group research, Cherbourg) so that the potential, corrected from ohmic drop, and the protection current, could be recorded for each coupon over 6 months (chapter 5). The mineral layers were analyzed by XRD and  $\mu$ -Raman spectroscopy.

Next chapter 2 presents the materials and methods used to achieve this work.

## References

- [1] G. Copin-Montégut, « Propriétés physiques de l'eau de mer », *Caractérisation et propriétés de la matière*, nov. 2002, doi: 10.51257/a-v1-k170.
- [2] G. Copin-Montégut, *Chimie de l'eau de mer*. Institut océanographique, 1996.
- [3] J. Duboscq, « Corrosion des aciers en milieu marin: processus se déroulant dans les zones cathodiques », Thèse de doctorat, La Rochelle Université, 2019.
- [4] R. E. Melchers et R. Jeffrey, « Corrosion of long vertical steel strips in the marine tidal zone and implications for ALWC », *Corrosion Science*, vol. 65, p. 26-36, déc. 2012, doi: 10.1016/j.corsci.2012.07.025.
- [5] « ISO 8044:2020(fr), Corrosion des métaux et alliages — Vocabulaire ». <https://www.iso.org/obp/ui/#iso:std:iso:8044:ed-5:v1:fr> (consulté le 12 décembre 2020).
- [6] M. Roche, « L'ESSENTIEL SUR LA PROTECTION CATHODIQUE », *Cefracor*, p. 14, 2015.
- [7] J. Duboscq, R. Sabot, M. Jeannin, et P. Refait, « Localized corrosion of carbon steel in seawater: Processes occurring in cathodic zones », *Materials and Corrosion*, vol. 70, n° 6, p. 973-984, juin 2019, doi: 10.1002/maco.201810675.
- [8] R. E. Melchers et T. Wells, « Models for the anaerobic phases of marine immersion corrosion », *Corrosion Science*, vol. 48, p. 1791-1811, juill. 2006, doi: 10.1016/j.corsci.2005.05.039.
- [9] J. Creus, R. Sabot, et P. Refait, « Corrosion et protection des métaux en milieu marin », *Techniques de l'ingénieur, Matériaux | Corrosion vieillissement*, 2013.
- [10] K.-M. Moon, H.-R. Cho, M.-H. Lee, S.-K. Shin, et S.-C. Koh, « Electrochemical analysis of the microbiologically influenced corrosion of steels by sulfate-reducing bacteria », *Metals and Materials International*, vol. 13, n° 3, p. 211-216, juin 2007, doi: 10.1007/BF03027807.
- [11] S. Pineau, « Interactions entre les communautés bactériennes et les processus de corrosion accélérée des structures métalliques en environnement marin », Thèse de doctorat, La Rochelle Université, 2006.
- [12] L. Simon, M. François, P. Refait, G. Renaudin, M. Lelaurain, et J.-M. R. Génin, « Structure of the Fe(II-III) layered double hydroxysulphate green rust two from Rietveld analysis », *Solid State Sciences*, vol. 5, n° 2, p. 327-334, févr. 2003, doi: 10.1016/S1293-2558(02)00019-5.
- [13] Ph. Refait, D. D. Nguyen, M. Jeannin, S. Sable, M. Langumier, et R. Sabot, « Electrochemical formation of green rusts in deaerated seawater-like solutions », *Electrochimica Acta*, vol. 56, n° 18, p. 6481-6488, juill. 2011, doi: 10.1016/j.electacta.2011.04.123.
- [14] I. Lanneluc, M. Langumier, R. Sabot, M. Jeannin, P. Refait, et S. Sablé, « On the bacterial communities associated with the corrosion product layer during the early stages of marine corrosion of carbon steel », *International Biodeterioration & Biodegradation*, vol. 99, p. 55-65, avr. 2015, doi: 10.1016/j.ibiod.2015.01.003.
- [15] Ph. Refait, M. Jeannin, R. Sabot, S. Sablé, I. Lanneluc, A. Romaine, S. Necib, S. Pineau, « On the iron-sulphur interactions involved in biocorrosion », *Interactions Materials-Microorganisms*, p. 221-237, 2018.
- [16] R. E. Melchers, « Mathematical modelling of the diffusion controlled phase in marine immersion corrosion of mild steel », *Corrosion Science*, vol. 45, n° 5, p. 923-940, mai 2003, doi: 10.1016/S0010-938X(02)00208-1.
- [17] J.-A. Bourdoiseau, M. Jeannin, R. Sabot, C. Rémazeilles, et Ph. Refait, « Characterisation of mackinawite by Raman spectroscopy: Effects of crystallisation, drying and oxidation », *Corrosion Science*, vol. 50, n° 11, p. 3247-3255, nov. 2008, doi: 10.1016/j.corsci.2008.08.041.
- [18] P. Refait, A.-M. Grolleau, et M. Jeannin, « Localized corrosion of carbon steel in marine media : galvanic coupling and heterogeneity of the corrosion product layer », *Corrosion Science*, vol. 111, p. 583-595, 2016.

- [19] M. Jeannin, R. Sabot, H. Antony, S. Pineau, et P. Refait, « Effets des ruptures et reprises de protection cathodique sur la couche de produits de corrosion des aciers en zone de marnage », *Matériaux & Techniques*, vol. 101, n° 5-6, p. 503, 2013, doi: 10.1051/mattech/2013086.
- [20] Ch. Barchiche, C. Deslouis, D. Festy, O. Gil, Ph. Refait, S. Touzain, B. Tribollet, « Characterization of calcareous deposits in artificial seawater by impedance techniques 3 - Deposit of CaCO<sub>3</sub> in presence of Mg(II) », *Electrochimica Acta*, vol. 48, n° 12, p. 1645-1654, mai 2003, doi: 10.1016/S0013-4686(03)00075-6.
- [21] P. Refait, S. Pineau, R. Sabot, H. Antony, et M. Jeannin, « Mécanismes de la corrosion des aciers au carbone en zone de marnage », *Matériaux & Techniques*, vol. 101, n° 5-6, p. 501, 2013, doi: 10.1051/mattech/2013084.
- [22] A. P. Yadav, H. Katayama, K. Noda, H. Masuda, A. Nishikata, et T. Tsuru, « Surface potential distribution over a zinc/steel galvanic couple corroding under thin layer of electrolyte », *Electrochimica Acta*, vol. 52, n° 9, p. 3121-3129, févr. 2007, doi: 10.1016/j.electacta.2006.09.061.
- [23] S. Palani, T. Hack, J. Deconinck, et H. Lohner, « Validation of predictive model for galvanic corrosion under thin electrolyte layers: An application to aluminium 2024-CFRP material combination », *Corrosion Science*, vol. 78, p. 89-100, janv. 2014, doi: 10.1016/j.corsci.2013.09.003.
- [24] R. Morris et W. Smyrl, « Current and Potential Distribution in Thin Electrolyte Layer Galvanic Cells », *J. Electrochem. Soc.*, vol. 136, n° 11, p. 3229-3236, nov. 1989, doi: 10.1149/1.2096430.
- [25] Z. Liu, W. Wang, J. Wang, X. Peng, Y. Wang, P. Zhang, H. Wang, C. Gao, « Study of corrosion behavior of carbon steel under seawater film using the wire beam electrode method », *Corrosion Science*, vol. 80, p. 523-527, mars 2014, doi: 10.1016/j.corsci.2013.11.012.
- [26] T. Tsuru, A. Nishikata, et J. Wang, « Electrochemical studies on corrosion under a water film », *Materials Science and Engineering: A*, vol. 198, n° 1-2, p. 161-168, juill. 1995, doi: 10.1016/0921-5093(95)80071-2.
- [27] M. Yamashita, H. Nagano, et R. A. Oriani, « Dependence of corrosion potential and corrosion rate of a low-alloy steel upon depth of aqueous solution », *Corrosion Science*, vol. 40, n° 9, p. 1447-1453, sept. 1998, doi: 10.1016/S0010-938X(98)00041-9.
- [28] J. T. Waber and Bertha Fagan, « Mathematical Studies on Galvanic Corrosion », *J. Electrochem. Soc.*, vol. 103, p. 64, 1956.
- [29] R. Jeffrey and R. E. Melchers, « Corrosion of vertical mild steel strips in seawater », *Corrosion Science*, vol. 51, n° 10, p. 2291-2297, oct. 2009, doi: 10.1016/j.corsci.2009.06.020.
- [30] D. Zhang, X. Gao, G. Su, L. Du, Z. Liu, et J. Hu, « Corrosion Behavior of Low-C Medium-Mn Steel in Simulated Marine Immersion and Splash Zone Environment », *Journal of Material Engineering and Performance*, vol. 26, n° 6, p. 2599-2607, juin 2017, doi: 10.1007/s11665-017-2723-6.
- [31] X. Mu, J. Wei, J. Dong, et W. Ke, « In Situ Corrosion Monitoring of Mild Steel in a Simulated Tidal Zone without Marine Fouling Attachment by Electrochemical Impedance Spectroscopy », *Journal of Materials Science & Technology*, vol. 30, n° 10, p. 1043-1050, oct. 2014, doi: 10.1016/j.jmst.2014.03.013.
- [32] Ph. Refait, M. Jeannin, R. Sabot, H. Antony, et S. Pineau, « Corrosion and cathodic protection of carbon steel in the tidal zone: Products, mechanisms and kinetics », *Corrosion Science*, vol. 90, p. 375-382, janv. 2015, doi: 10.1016/j.corsci.2014.10.035.
- [33] C. Erdogan and G. Swain, « The effect of macro galvanic cells on corrosion impressed current cathodic protection for offshore monopile steel structures », *Ocean engineering*, vol. 265, n° 112575, p. 7, 2022.
- [34] Ph. Refait, M. Jeannin, R. Sabot, H. Antony, et S. Pineau, « Electrochemical formation and transformation of corrosion products on carbon steel under cathodic protection in seawater », *Corrosion Science*, vol. 71, p. 32-36, juin 2013, doi: 10.1016/j.corsci.2013.01.042.
- [35] S. Elbeik, A. C. C. Tseung, et A. L. Mackay, « The formation of calcareous deposits during the corrosion of mild steel in sea water », *Corrosion Science*, vol. 26, n° 9, p. 669-680, janv. 1986, doi: 10.1016/0010-938X(86)90032-6.

- [36] P. Refait, A.-M. Grolleau, M. Jeannin, et R. Sabot, « Cathodic Protection of Complex Carbon Steel Structures in Seawater », *Corrosion and Materials Degradation*, vol. 3, n° 3, p. 439-453, août 2022, doi: 10.3390/cmd3030026.
- [37] A. Zanibellato, « Synthèse et études physico-chimiques d'un agglomérat calco-magnésien formé sur un acier en milieu marin : un éco-matériau pour la protection du littoral », Thèse de doctorat, Université de La Rochelle, La Rochelle, 2016.
- [38] D. L. Zadi, « Mécanismes physico-chimiques impliqués dans la formation et l'évolution à l'abandon d'un matériau sédimentaire innovant généré en milieu marin par polarisation cathodique », Thèse de doctorat, La Rochelle Université, 2022.
- [39] K. Akamine and Isamu Kashiki, « Corrosion protection of steel by calcareous electrodeposition in seawater (Part 1) », *Zairyo-to-Kankyo*, vol. 51, p. 496-501, 2002.
- [40] K. Akamine and I. Kashiki, « Corrosion protection of steel by calcareous electrodeposition in seawater (Part 2) », *Zairyo-to-Kankyo*, vol. 52, p. 401-407, 2003.
- [41] C. Barchiche, C. Deslouis, O. Gil, P. Refait, et B. Tribollet, « Characterisation of calcareous deposits by electrochemical methods: role of sulphates, calcium concentration and temperature », *Electrochimica Acta*, vol. 49, n° 17-18, p. 2833-2839, juill. 2004, doi: 10.1016/j.electacta.2004.01.067.
- [42] M. Zamanzade, T. Shahrabi, et A. Yazdian, « Improvement of corrosion protection properties of calcareous deposits on carbon steel by pulse cathodic protection in artificial sea water », *Anti-Corrosion Methods and Materials*, vol. 54, n° 2, p. 74-81, mars 2007, doi: 10.1108/00035590710733566.
- [43] W. Stumm and J. J. Morgan, « Chemical equilibria and rates in natural waters », in *Aquatic Chemistry*, 3<sup>rd</sup> edition, Wiley, 1995.
- [44] Y. Yang, J. Scantlebury, and E. Koroleva, « A Study of Calcareous Deposits on Cathodically Protected Mild Steel in Artificial Seawater », *Metals*, vol. 5, n° 1, p. 439-456, march 2015, doi: 10.3390/met5010439.
- [45] D. D. Nguyen, S. Gascoin, A. Zanibellato, C. G. Da Silva, M. Lemoine, B. Riffault, R. Sabot, M. Jeannin, D. Chateigner, O. Gil, « Role of brucite dissolution in calcium carbonate precipitation from artificial and natural seawaters », *Crystal Growth and Design*, vol. 17, n° 4, p. 1502-1513, april 2017, doi: 10.1021/acs.cgd.6b01305.
- [46] H. Karoui, B. Riffault, M. Jeannin, A. Khaoul, O. Gil, M. Ben Amor, M; M. Tlili, « Electrochemical scaling of stainless steel in artificial seawater: Role of experimental conditions on CaCO<sub>3</sub> and Mg(OH)<sub>2</sub> formation », *Desalination*, vol. 311, p. 234-240, févr. 2013, doi: 10.1016/j.desal.2012.07.011.
- [47] L. Beaunier, C. Gabrielli, G. Poindessous, G. Maurin, et R. Rosset, « Investigation of electrochemical calcareous scaling Nuclei counting and morphology », *Journal of Electroanalytical Chemistry*, vol. 501, n° 1-2, p. 41-53, 2001.
- [48] C. Gabrielli, G. Maurin, H. Perrot, G. Poindessous, et R. Rosset, « Investigation of electrochemical calcareous scaling: Potentiostatic current- and mass-time transients », *Journal of Electroanalytical Chemistry*, vol. 538-539, p. 133-143, 2002.
- [49] C. Deslouis, D. Festy, O. Gil, G. Rius, S. Touzain, et B. Tribollet, « Characterization of calcareous deposits in artificial sea water by impedance techniques I - Deposit of CaCO<sub>3</sub> without Mg(OH)<sub>2</sub> », *Electrochimica Acta*, vol. 43, n° 12-13, p. 1891-1901, 1998.
- [50] H. Möller, « The influence of Mg<sup>2+</sup> on the formation of calcareous deposits on a freely corroding low carbon steel in seawater », *Corrosion Science*, vol. 49, n° 4, p. 1992-2001, 2007, doi: <https://doi.org/10.1016/j.corsci.2006.10.011>.
- [51] C. Godart, C. Dagbert, et J. Galland, « Formation du dépôt calco-magnésien sous protection cathodique, action des bactéries sulfurogènes naturelles », *Matériaux et Techniques*, p. 11-18, 2002.
- [51] J. Vincent, B. Colin, I. Lanneluc, R. Sabot, V. Sopéna, Ph. Turcry, P.Y. Mahieux, Ph. Refait, M. Jeannin, S. Sablé, « New Biocalcifying Marine Bacterial Strains Isolated from Calcareous Deposits and Immediate Surroundings », *Microorganisms*, vol. 10, n° 1, p. 76, déc. 2021, doi: 10.3390/microorganisms10010076.

- [52] B. Colin, J. Vincent, L. Kozirowski, A. Frein, I. Lanneluc, R. Sabot, Ph. Refait, S. Sablé, M. Jeannin, « Calcareous deposit formation under cathodic polarization and marine biocalcifying bacterial activity », *Bioelectrochemistry*, vol. 148, p. 108271, déc. 2022, doi: 10.1016/j.bioelechem.2022.108271.
- [54] J. Guezennec, E. Antoine, and M. Conte, « Intéraction protection cathodique et biofilm en milieu marin », *Matériaux et Techniques*, p. 11-14, 1992.
- [55] C. Godart and C. Dagbert, « Impact de l'environnement marin sur la formation du dépôt calco-magnésien: rôle de la matière organique », *Matériaux et Techniques*, p. 27-32, 2004.
- [56] M. Sarlak, T. Shahrabi, et M. Zamanzade, « Investigation of calcareous deposits formation on copper and 316L stainless steel under cathodic polarization in artificial seawater », *Protection of Metals and Physical Chemistry of Surfaces*, vol. 45, n° 2, p. 216-222, mars 2009, doi: 10.1134/S2070205109020166.
- [57] K. Mantel, W. H. Hartt, et T. Chen, « Substrate , Surface Finish , and Flow Rate Influences on Calcareous Deposit Structure », p. 489-500, 1992, doi: doi: 10.5006/1.3315965.
- [57] S. Touzain, « Etude de la structure des dépôts calco-magnésien formés en présence d'écoulement: application à la protection cathodique en milieu marin », Thèse de doctorat, La Rochelle Université, 1996.
- [59] J. Genesca, « 09520 - Effect of calcareous deposit formation on galvanic anode cathodic protection of steel in seawater », presented at NACE international corrosion conference & expo, 2009, p. 11.
- [60] C. Deslouis, D. Festy, O. Gil, V. Maillot, S. Touzain, et B. Tribollet, « Characterization of calcareous deposits in artificial sea water by impedances techniques: 2-deposit of  $Mg(OH)_2$  without  $CaCO_3$  », *Electrochimica Acta*, vol. 45, n° 11, p. 1837-1845, févr. 2000, doi: 10.1016/S0013-4686(99)00403-X.
- [61] R. Allmann, « The crystal structure of Pyroaurite », *Acta Crystallographica Section B: Structural Crystallography and Crystal Chemistry*, vol. 4, n° 7, p. 972-977, 1968.





## *Chapter II: Material and Methods*



## Chapter II: Material and Methods

2.1 Electrochemical methods.....	59
2.1.1 Three-electrode set-up.....	59
2.1.2 Open circuit potential monitoring.....	60
2.1.3 Voltammetry.....	60
2.1.5 Potentiostatic method (or chronoamperometry).....	63
2.1.6 Electrochemical Impedance Spectroscopy (EIS) [6].....	63
2.1.6.1 Mathematical principle.....	64
2.1.6.2 Measurement principle.....	65
2.1.6.3 Data analysis.....	65
2.2 Characterization techniques.....	68
2.2.1 X-Ray Diffraction.....	68
2.2.1.1 Principle.....	68
2.2.2 Micro Raman spectrometry.....	69
2.2.3 Optical microscopy.....	70
References.....	72

The aim of this section is to present the various techniques and physico-chemical principles on which the experiments carried out in the course of this thesis are based. The protocols used will be detailed and explained in the relevant chapters.

The physico-chemical characterization of the samples was carried out at the LaSIE laboratory (Laboratoire des Sciences de l'Ingénieur pour l'Environnement). However, the experiments were carried out at 3 different sites:

- The LaSIE at La Rochelle
- The commercial Seaport of La Rochelle
- The corrosion laboratory of Naval Group Cherbourg

## II.1 Electrochemical methods

### II.1.1 Three-electrode set-up

Every electrochemical characterizations carried out for this PhD were performed using a three-electrode set-up (as shown in Figure II.1). The principle of the set-up used with such a device is the same whether the measurements are carried out in the laboratory or in situ. Each element (electrolyte, reference electrode, working electrode and counter electrode) plays the same role, although its nature may be slightly modified:

- The electrolyte: Ensures the ionic current conduction. For the topic treated here, natural seawater plays this role (which average composition is detailed table II.1).
- Counter electrode (dashed blue line figure II. 1): allows the electronic current connection with the working electrode. Here a titanium platinum plated grid has been used in each case.
- The working electrode (dashed red line figure II. 1): Is the site of the electrochemical reactions to be studied. Here carbon steel was studied, the steel grade is mentioned in the introduction of each chapter.

The reference electrode (dashed gray line Figure II.1): Used to measure the electrochemical potential of the working electrode from its relative value compared to the standard hydrogen electrode. The nature of the reference electrode will be specified at the outset of each chapter. The Ag/AgCl<sub>3M</sub> was usually used for short or punctual measurements ( $E_{ref} = +0,208$  V/SHE at 25°C) and the Ag/AgCl<sub>seawater</sub> electrode for long term experiment ( $E_{ref} = +0,25$  V/SHE at 25°C).

Table II. 1 Seawater chemical composition [1]

Anions	g/kg	Cations	g/kg
Cl <sup>-</sup>	19.352	Na <sup>+</sup>	10.784
SO <sub>4</sub> <sup>2-</sup>	2.712	Mg <sup>2+</sup>	1.284
HCO <sub>3</sub> <sup>-</sup>	0.108	Ca <sup>2+</sup>	0.412
Br <sup>-</sup>	0.067	K <sup>+</sup>	0.399
CO <sub>3</sub> <sup>2-</sup>	0.015	Sr <sup>2+</sup>	0.008

The chemical composition of seawater is intricate, it contains around 35 g of salts per kg of seawater. Table II.1 summarizes the 10 most concentrated chemical species (5 anions and 5 cations). These values display minimal variation across different marine environments [2]. The overall salinity and high chloride content make seawater highly conductive and corrosive. Beyond the water composition, pH is a key parameter in the development of corrosion phenomena. The pH of seawater, governed by the chemical equilibrium H<sub>2</sub>CO<sub>3</sub> / HCO<sub>3</sub><sup>-</sup> / CO<sub>3</sub><sup>2-</sup>, varies between 7,5 et 8,5 [1].

To be able to control and apply different potentials (or currents) in electrochemical techniques, to the working electrode, the use of a potentiostat (computer-controlled) is required. For the work presented below, a Biologic VSP potentiostat controlled by the EC-Lab<sup>®</sup> software was employed for the experiments carried out at LaSIE (results presented in chapter 4).

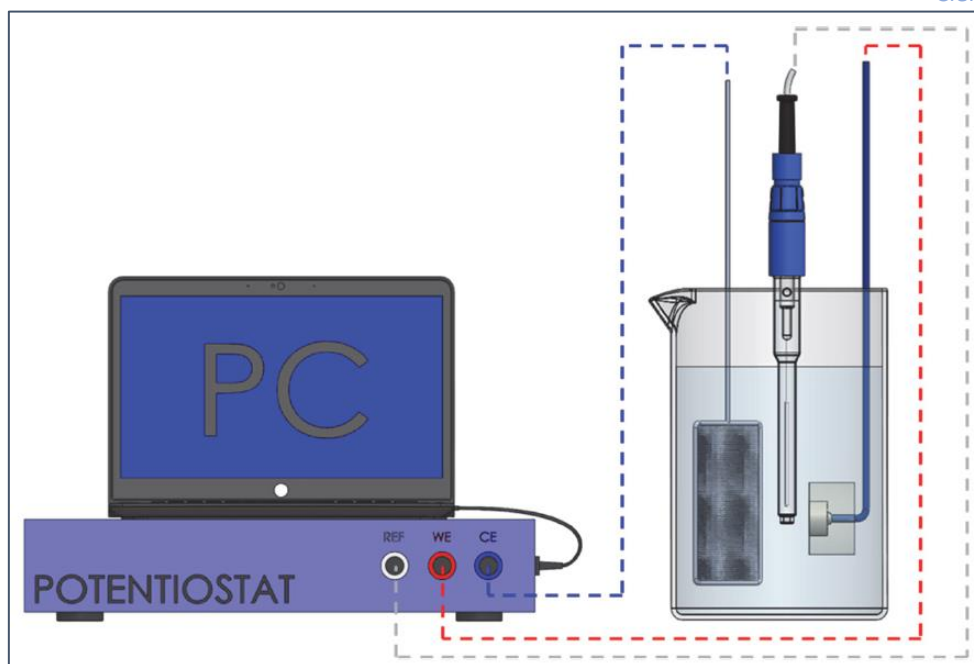


Figure II. 1: Schematic representation of the 3-electrode set-up [3]

### II.1.2 Open circuit potential monitoring

Open Circuit Potential (OCP) is the natural potential of an immersed electrode at  $I = 0$ . Monitoring this potential as a function of time gives (passively and non-destructively) information about surface changes of the sample and its immediate environment (e.g. changes in pH, changes in  $O_{2(aq)}$  concentration, changes in the mineral layer and biofilm covering the metal, etc.).

### II.1.3 Voltammetry

Voltammetry is a method that involves applying a potential scan to the working electrode to measure the current resulting from polarization. In our work, the voltammetry experiment typically starts from OCP, and involves a variation in the potential:

- Towards a cathodic potential previously defined,
- Then towards an anodic potential,
- Prior to go back to OCP to get information about the device electrochemical behavior in each potential domain.

From this information it is also possible to determine the reactions occurring at the working electrode surface and their intensity. Shifting the electrode potential towards a more negative potential favors cathodic reactions. The anodic component of the current becomes negligible compared with the cathodic component. The total current (or current density  $J$ ) is therefore:  $I \sim I_c$  (or  $J \approx J_c$ ). Similarly, when the electrode potential is shifted towards less negative potentials (anodic potentials), anodic reactions are favored so that  $I \sim I_a$  (or  $J \approx J_a$ ). Figure II.2 illustrates that, for an impressed polarization, the difference between the dashed curve (red and/or blue) and the solid curve decreases as the potential shift increases.

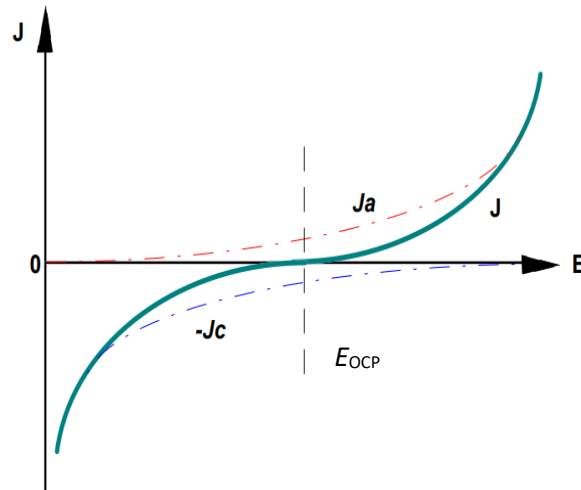


Figure II. 2: Schematic representation (linear scale) of the current evolution as a function of the electrode potential

If anodic reactions are governed by pure charge transfer, the current density can be written as follows [4]:

$$J = \underbrace{J_{cor} e^{\frac{\Delta E}{\beta_a}}}_{J_a} - \underbrace{J_{cor} e^{-\frac{\Delta E}{\beta_c}}}_{J_c}$$

With

$$\Delta E = E - E_{OCP}$$

This explains that when  $E \gg E_{OCP}$  (or  $E \ll E_{OCP}$ )  $J_c$  becomes negligible compared to  $J_a$  (or  $J_a$  compared to  $J_c$ ). On the other hand,  $\beta_a$  et  $\beta_c$  are the Tafel coefficients defined by the following relations [4]:

$$\beta_a = \frac{RT}{\alpha_a zF} \quad \text{et} \quad \beta_c = \frac{RT}{(1 - \alpha_c)zF}$$

With  $\alpha_a$  and  $\alpha_c$  the anodic and cathodic charge transfer coefficients representative of the involved semi reactions (oxidation and reduction).

Consequently, when the electrode potential is shifted in a clearly cathodic or clearly anodic domain, it is possible to write:

$$\ln|J| = \ln|J_{cor}| \pm \frac{\Delta E}{\beta_i}$$

With  $i = a$  or  $c$  depending on the domain in which the electrode is polarized. It then appears that this current equation in a logarithmic representation is actually a straight-line equation with slope  $\frac{-1}{\beta_c}$  in the cathodic domain and  $\frac{1}{\beta_a}$  in the anodic domain. It is possible to plot these lines only if the studied reaction is a pure charge transfer reaction. As shown schematically in Figure II.3, these lines intersect at the corrosion current  $J_{cor}$  and corrosion potential  $E_{cor}$ , which in principle equals the OCP:  $E_{OCP} = E_{cor}$ .

Actually, the various effects induced by high amplitude polarization most often lead to a discrepancy between  $E_{OCP}$  and  $E_{cor}$ . These may be due to capacitive effects or alterations of the surface condition and/or the metal/medium interface caused by polarization.

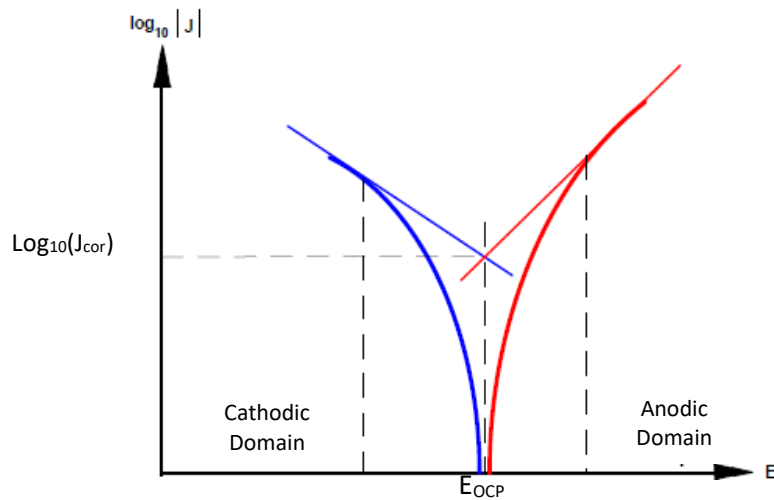


Figure II. 3: Schematic polarization curve and tafel straight-lines

Figure II.4 displays an example of cyclic polarization in Tafel representation on a steel sample covered with aragonite. This curve exhibits 2 distinct current minima which are indicative of polarization-induced effects. If these effects are limited, then the two peaks are very close, i.e.,  $E_{cor}(1) \approx E_{cor}(2) \approx E_{OCP}$ . On the other hand, if the experiment results in significant surface modification (or in other words has been destructive), or is accompanied by a strong capacitive effect, then these current minima occur at potentials different from  $E_{OCP}$ . In the case of a surface condition change, this shift can illustrate the OCP variation due to surface modifications. For example, in Figure II. 4, the cathodic potential scan modified the surface and shifted the corrosion potential to more negative values ( $\approx -0.77$  mV/Ag/AgCl<sub>3M</sub> vs  $E_{OCP} = -0.72$  mV/Ag/AgCl<sub>3M</sub>). The anodic scan of the potential also modified the surface and shifted the corrosion potential towards more anodic values than the starting point of the cycle (equivalent to the sample OCP). In case of a capacitive effect, it is possible to correct the data by averaging the polarization curve obtained during the forward scan ( $dE/dt > 0$ ) with the curve obtained during the return sweep ( $dE/dt < 0$ ) [5].

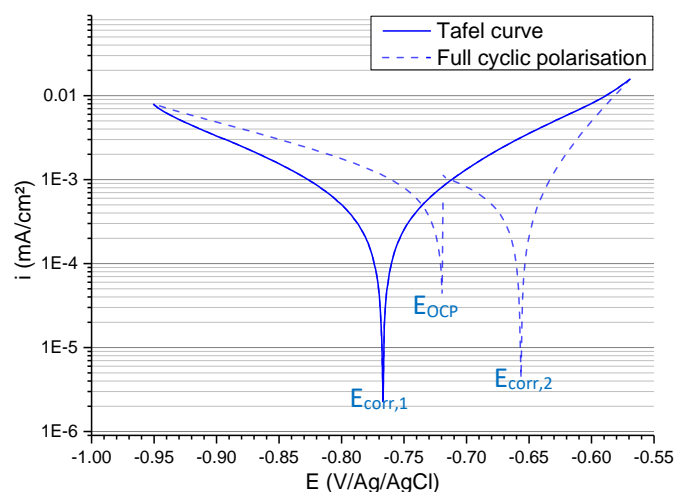


Figure II. 4: Experimental voltammetry curve of carbon steel covered by calcareous deposit

### II.1.4 Potentiostatic method (or chronoamperometry)

It consists in monitoring the current response of a sample subjected to a constant imposed potential over time. This method (illustrated here in figure II.5) is used in chapter 4 for assessing the cathodic protection of samples under a thin layer of water.

The curve shown figure II.5 was obtained using an Ag/AgCl<sub>3M</sub> reference electrode. In this example, the current of a steel sample polarized at -950 mV/Ag/AgCl<sub>3M</sub> for 4 days was followed over time. This method provides information about the surface state and conductivity of the layer that forms on the surface of the sample. At this applied potential, the main reaction occurring at the electrode surface is oxygen reduction. As detailed in the previous chapter, this reaction involves a strong local increase in pH resulting in the precipitation of CaCO<sub>3</sub> (and Mg(OH)<sub>2</sub> in some cases). These insulating compounds gradually cover the steel surface, acting as a physical barrier that limits the diffusion of oxygen to the active surface where it can be reduced. This explains the rapid decrease in current measured in Figure II.5.

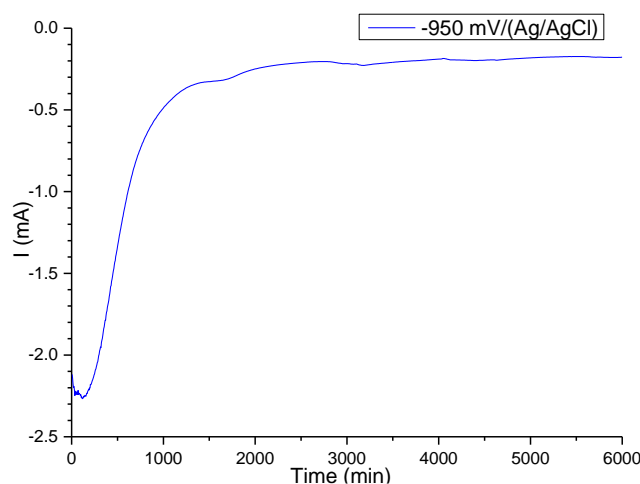


Figure II. 5: Sample current response  $I(t)$  of a potentiostatic monitoring Polarization at -950 mV/(Ag/AgCl<sub>3M</sub>)

### II.1.5 Electrochemical Impedance Spectroscopy (EIS) [6]

EIS consists in applying a low-amplitude sinusoidal signal (usually  $\pm 10\text{mV}$  to  $\pm 30\text{mV}$ ) at different frequencies around a potential value to an electrochemical system in its stationary state. The frequency range can vary from 1 mHz to 1 MHz allowing discrimination between different surface phenomena according to their response kinetics or relaxation time.

A low-frequency signal (i.e. a slow potential sweep signal) stimulates all the phenomena occurring on the sample. Conversely, as the frequency increases, reactions with longer relaxation times (such as matter transport) have less influence on the surface reactions. Instead, faster phenomena (such as the charge transfer reaction) become more significant contributors to the electrical response of the impedance.

## II.1.5.1 Mathematical principle

The potential perturbation can be written as follows:

$$E(t) = E_0 + \Delta E(t)$$

And

$$\Delta E(t) = \Delta E \cdot \sin(\omega t)$$

With:  $E_0$  = Studied potential;  $\Delta E$  = the potential variation amplitude;  $\omega$  the pulsation =  $2\pi f$

The sinusoidal current response can be out of phase of angle  $\phi$  so that:

$$\Delta I(t) = I_0 + \Delta I \cdot \sin(\omega t + \phi)$$

With:  $I_0$  the stationary current value at the studied potential,  $\Delta I$  the maximum signal amplitude.

The system impedance can be written as a function of the modulus  $|Z(\omega)|$  and the phase difference  $\phi$ , as a law comparable to the Ohm law:

$$|Z(\omega)| = \frac{TF(\Delta E(t))}{TF(\Delta I(t))}$$

And

$$\arg(Z) = \phi$$

With: TF represents the Fourier transformation.

The response signal can be represented as a sum of a real and an imaginary component according to:

$$e^{j\phi} = \cos(\phi) + j \cdot \sin(\phi)$$

with  $j^2 = -1$

The impedance becomes:

$$Z(\omega) = |Z(\omega)|e^{j\phi} = |Z(\omega)| \cdot (\cos(\phi) + j \cdot \sin(\phi))$$

Yet in a complex plan, impedance  $Z(\omega)$  can be represented by a vector:

$$Z(\omega) = Z_{Re} + j \cdot Z_{Im}$$

With

$$Z_{Re} = |Z(\omega)| \cos(\phi)$$

And

$$Z_{Im} = |Z(\omega)| \sin(\phi) \quad |Z(\omega)| = \sqrt{(Z_{Re}^2 + Z_{Im}^2)} \quad \phi = \tan^{-1} \left( \frac{Z_{Im}}{Z_{Re}} \right)$$

## II.1.5.2 Measurement principle

Measurements are done using the 3-electrode set-up described above. The precise protocol for impedance measurements will be detailed in the relevant chapter. However, they were carried out between 100 kHz and 10 mHz with a signal amplitude of 10 mV.

## II.1.5.3 Data analysis

Obtained data can be plotted:

- Either as a Nyquist diagram (orthonormal diagrams) with  $-Z_{\text{Im}}$  on the y axis and  $Z_{\text{Re}}$  on the x axis. Each point represents a  $Z$  value for a precise frequency (as shown figure II. 6a).
- Either as a Bode diagram with  $\log|Z(\omega)|$  and  $\phi(\omega)$  plotted as functions of the frequency on a logarithmic scale (shown figure II. 6b)

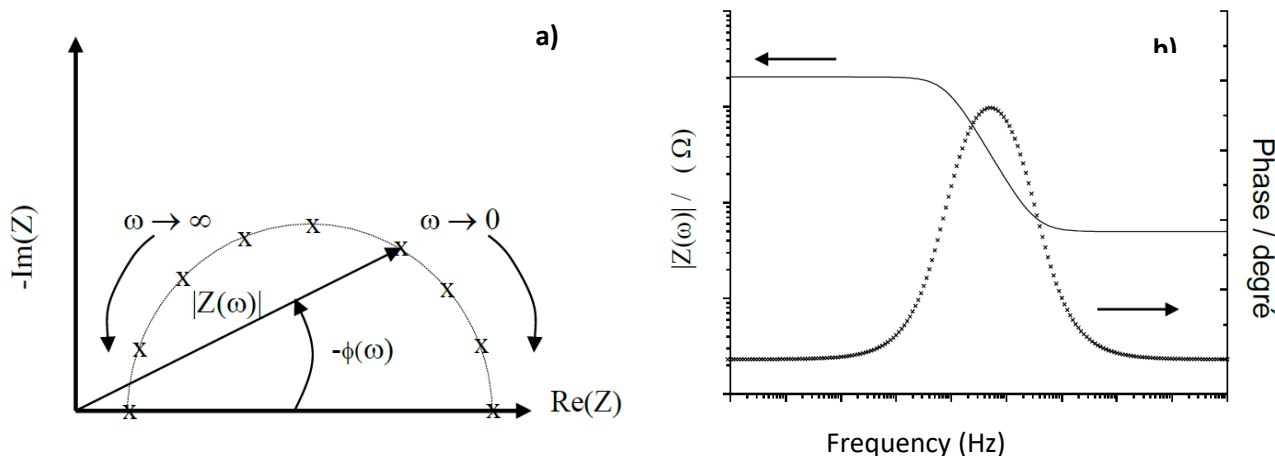


Figure II. 6: a) – Representation in the Nyquist complex plan; b) – Bode Diagram [6]

Modelling the studied electrochemical system using equivalent electrical circuits (EECs) allows to establish the link between experimentally obtained results and their physico-chemical interpretation. In other words, the electrochemical reactions taking place at the electrolyte/electrode interface are represented as an electrical circuit, typically consisting of resistors and capacitors (or even inductive elements in some cases).

Immersion of a metal electrode results in the separation of charge at the electrolyte/electrode interface (Figure II.7). This forms a layer behaves like an electrical capacitor, charging and discharging according to the shifts in the applied potential [7]. Indeed, the EIS study of the reactions occurring at the metal/electrolyte interface leads to a distinction between the faradaic component (related to electronic current from electrochemical reactions) and the double layer charge component (associated with ionic process). The total current is thus the sum of the faradic and capacitive currents, each having a corresponding impedance:

- Double layer impedance:  $Z_{dl} = -\frac{j}{C_{dl}\omega}$  with  $C_{dl} = \frac{\epsilon\epsilon_0 A}{e}$
- Faradic impedance:  $Z_f$

with:  $C_{dl}$  (or  $C_d$ ) the double layer capacity,  $\epsilon$  the medium relative permittivity,  $\epsilon_0$  the vacuum dielectrical permittivity,  $A$  the reaction area and  $e$  the double layer thickness

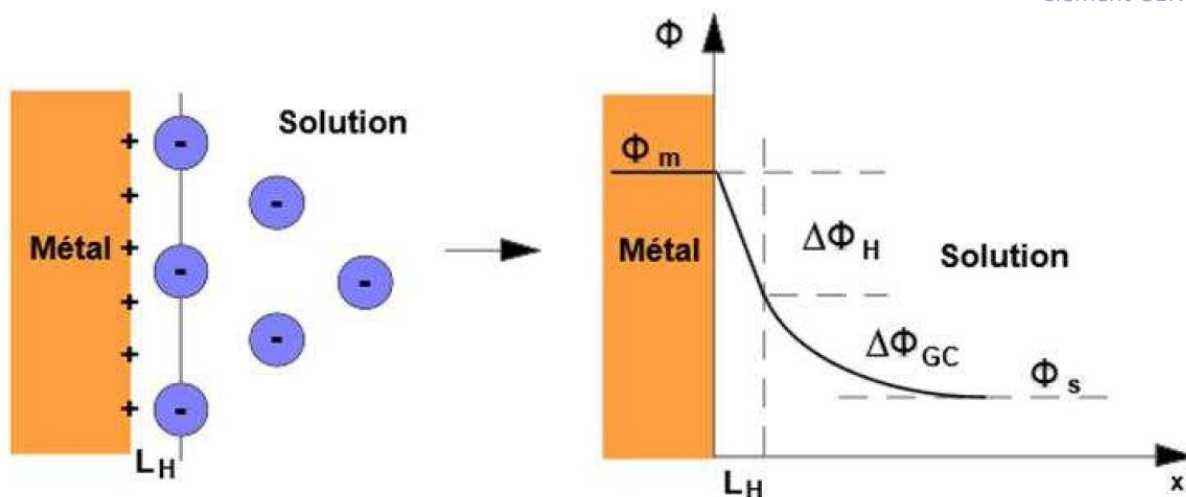


Figure II. 7: Schematic representation of the double layer according to Stern model

Electronic currents can be limited either by charge transfer reactions or diffusion of the species in the surrounding medium. In case where the limits arise because of pure charge transfer, the electrochemical behavior of the electrode interface is modeled using an RC circuit. On the other hand, when a combination of activation and diffusion kinetics is responsible for the limitation, a diffusion impedance is added in series with the charge transfer resistance ( $R_{ct}$  or  $R_t$ ). The thickness of the diffusion layer can be either infinite (represented Warburg impedance, usually noted as  $W$ ) or finite. As shown in Figure 8, the control of reaction kinetics by diffusion is associated with phenomena visible at low frequencies on the Nyquist complex plane, resulting in a fairly long relaxation time. The natural resistance of the electrolyte must then be considered, it can be read directly from the Nyquist diagram (by assessing offset from 0 of the initial point on the diagram, e.g. in figure II.8-a)).

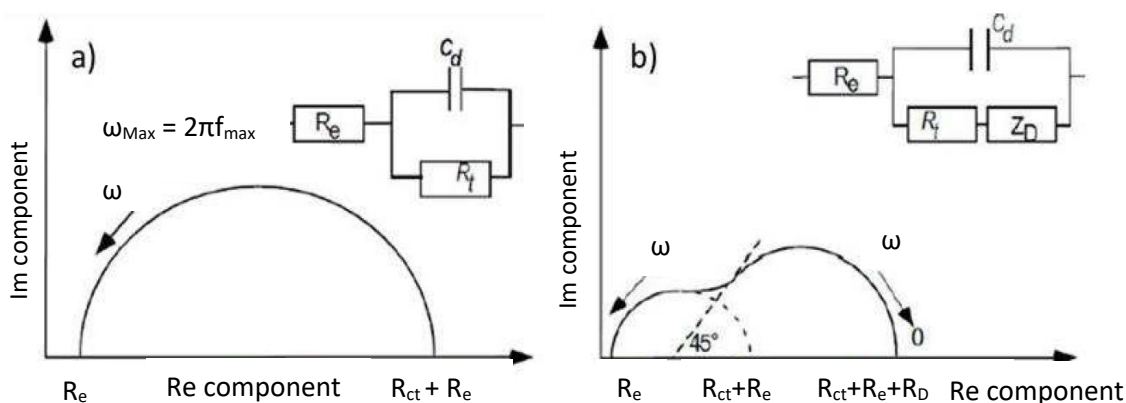


Figure II. 8: Schematic data representation in the Nyquist complex plan - a) of a pure charge transfer kinetic governed system - b) of a diffusion mixed kinetic governed system [8]

Figure II.8-a) illustrates the graphical representation of electrolyte resistance ( $R_e$ ) and charge transfer resistance ( $R_{ct}$  or  $R_t$ ).  $R_e$  is read at the first intersection point between experimental curve intersects the abscissa axis, while  $R_{ct}$  corresponds to the value obtained at the second intersection point between the abscissa axis and the end of the first capacitive loop after subtracting  $R_e$ . If several loops are convoluted, the first loop must be extrapolated to a perfect semicircle to extract the above-mentioned information (e.g. figure 8-b)).

In the specific case of cathodic protection of carbon steels in seawater, a calcareous deposit forms on the steel surface. In other words, the active surface is gradually covered by a porous, non-conductive layer which can be compared to a film capable of accumulating charges. Consequently, the total capacitive current is then composed of the capacitive current arising from the double-layer phenomenon  $I_{dl}$  and the capacitive current attributed to the film of calcareous deposit,  $I_f$ .

Furthermore, at the potentials of cathodic protection (located at the  $O_2$  diffusion plateau), reduction reactions at the cathode surface involve:

- $O_2$  reduction limited by matter transportation:
  - $R_{tc,H_2O}$  (water charge transfer) is really low
  - $R_{tc,O_2}$  (dissolved  $O_2$  charge transfer) is low
  - $Z_{D,O_2}$  (dissolved  $O_2$  diffusion impedance) is relatively high, depending on the hydrodynamic conditions
- $R_{tc,O_2}$  and  $R_{tc,H_2O}$  increase with the progressive decrease of the active surface because of the calcareous deposit precipitation.

Several studies have focused on this specific case to propose equivalent electrical circuits that model reactions on the surface of the steel electrode as closely as possible. For instance, Tu et al. in 2010 [9] (figure II. 9-a)) and Yang et al. in 2012 [10] (figure II. 9-b)) worked on mild steel in complete artificial seawater. It is important to note that the second model considers an outer layer rich in Ca and an inner layer richer in Mg, thereby introducing the parameters  $C_{inner}$ ;  $C_{outer}$ ;  $R_{inner}$ ;  $R_{outer}$  for internal and external resistances and capacitances. The interface is characterized by a  $C_{dl}$  (double layer capacitance), an anodic charge transfer resistance  $R_a$  and a diffusion impedance  $W_c$  associated with a diffusion layer of finite thickness.

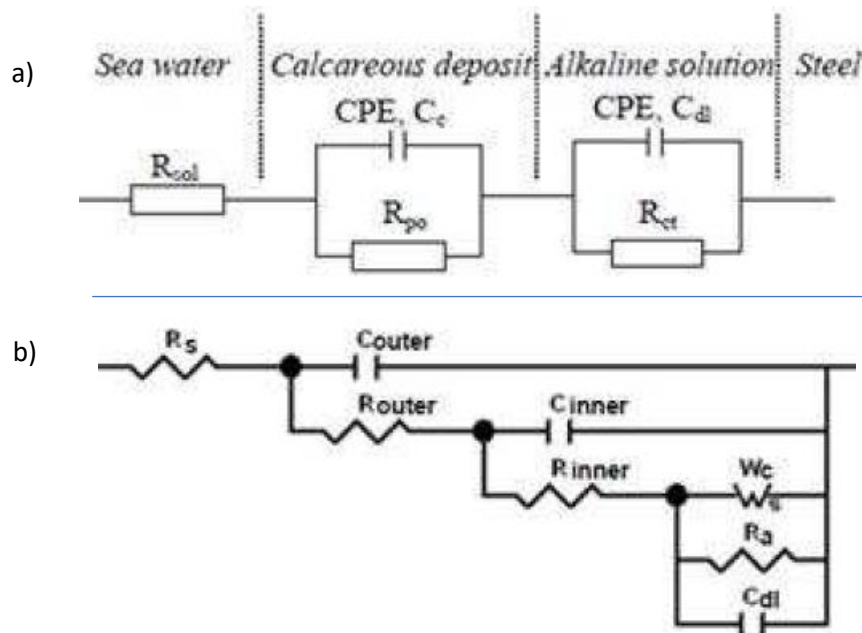


Figure II. 9: Equivalent electrical circuit to calcareous deposit precipitation on mild steel electrode in artificial seawater: a) Tu et al. 2010 [9]; b) Yang et al. 2012 [10]

## II.2 Characterization techniques

### II.2.1 X-Ray Diffraction

#### II.2.1.1 Principle

X-ray Diffraction (XRD) (schematic diagram of a diffractometer explained Figure II.10-a) is based on the interactions of X-rays with the ordered atoms of a crystallized solid phase. These X-rays are generated by applying a very high electrical voltage (40 kV in our case) between a cathode (W filament) and an anode, often called an anticathode or target, made of a specific metal (e.g. copper or cobalt). This choice of metal determines the wavelength of the X-rays used for the diffraction analysis. This voltage generates a flow of electrons from the cathode to the anode, exciting the atoms of the target metal.

When the X-ray beam penetrates the analyzed solid sample, coherent wave interferences are resulting from diffraction of the radiation by the crystals (geometric arrangement of the atoms). The direction of the diffracted rays, governed by Bragg's law (written below and illustrated in figure II.10-b), directly depends on the parameters of the diffracted mesh (e.g. inter-reticular distance, geometric structure, etc.).

$$n\lambda = 2d_{hkl} \sin(\theta)$$

with:

$\theta$  the diffraction angle;  $d_{hkl}$  the inter-reticular distance (distance between plans h,k,l);  $\lambda$  incident X-ray wavelength (directly depending on the target used);  $n$  diffraction order, usually equal to 1.

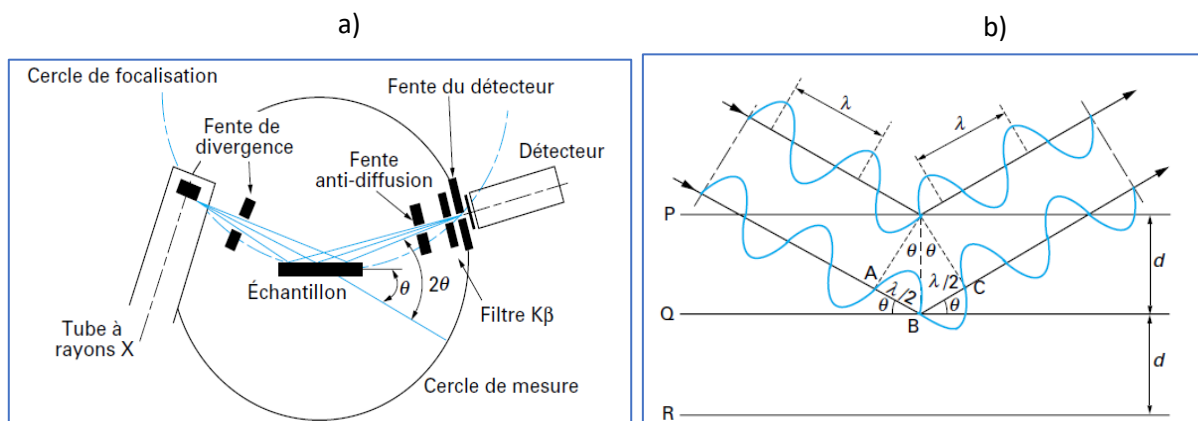


Figure II. 10: a) Diffractometer Schema – b) Bragg law Illustration [11]

For these works, both diffractometers described below have been used at the LaSIE:

- INEL EQUINOX 6000: equipped with a cobalt target ( $\lambda_{Co,K\alpha} = 1,7903 \text{ \AA}$ ), a parabolic mirror permitting to get rid of the  $K\beta$  ray and a curved detector allowing the instantaneous detection of every diffracted X-ray on an angular range of  $90^\circ$ .
- Bruker-AXS D8-Advance diffractometer Theta-Theta, equipped a linear SDD (Standard Drift Detector) LynxEye XE-T detector (192 channels). The anode is a line focus made of Cu (40 mA – 40 kV) of  $K\alpha$  radiation  $\lambda = 0.15406 \text{ nm}$ . Primary slits of  $0.3^\circ$  are installed. A spinner (60 rpm) and a motorized anti-air scatter screen were used for Chapter V analyses.

For both corrosion product and calcareous deposit analyses, samples were stored at  $-18^{\circ}\text{C}$  to stop ionic transport and limit access to atmospheric oxygen, thus avoiding any change in the oxidation state of the products analyzed. Phase identification was carried out using the ICDD (International Center for Diffraction Data) PDF-4 database.

### II.2.2 Micro Raman spectrometry

$\mu$ -Raman spectrometry is a method for characterizing the molecular composition of non-metallic materials [12]. This characterization technique offers various advantages:

- It is a non-destructive method: The analyzed sample can be kept for further analysis.
- It is a relatively fast method. This is a significant advantage for corrosion products that may be reactive towards oxygen. Fe(II) compounds, for example, can be analyzed.
- This is a local technique. It can be used to pinpoint a zone in the  $\mu\text{m}^3$  range. This permits to characterize zones with a priori different electrochemical behaviors. On the other hand, this precision of characterization means that a sufficient number of characterizations must be carried out to obtain an overview of the sample composition. In the specific case of corrosion product layers, the chemical composition of these layers can be very heterogeneous, which means that a large number of measurements are required to characterize the sample in its entirety.

The technique is based on the principle of photon-matter interaction. A monochromatic laser source of frequency  $\nu_0$  is focused on the sample. The photons absorbed by the material are scattered either elastically (Rayleigh scattering at frequency  $\nu_0$ ), or inelastically (Raman scattering at frequency  $\nu_d$ ). Inelastic scattering is characteristic of an energy exchange between the incident photons and the molecule analyzed. This results in a transition between vibrational levels (as shown in Figure II. 11), known as Raman scattering. Two cases are then likely to occur [12]:

- Diffusion Raman Stokes:  $\nu_d < \nu_0 \rightarrow \nu_d = \nu_0 - \nu_v$
- Diffusion Raman anti-Stokes:  $\nu_d > \nu_0 \rightarrow \nu_d = \nu_0 + \nu_v$

In each of the above cases, the frequency differences are equal to the vibrational frequencies of the analyzed molecule. By convention, the Raman spectra obtained are represented in wavenumbers ( $\text{cm}^{-1}$ ) and not in frequency.

In this study, the samples were analyzed using a LABRAM HR Evo Raman spectrometer from Horiba Jobin Yvon, calibrated on the  $520.5 \text{ cm}^{-1}$  silicon line and equipped with:

- an Olympus microscope with x10, x50 long focal length and x100 objectives
- two exciter laser sources with wavelengths of 785 nm and 532 nm
- a CCD sensor cooled by the Peltier effect

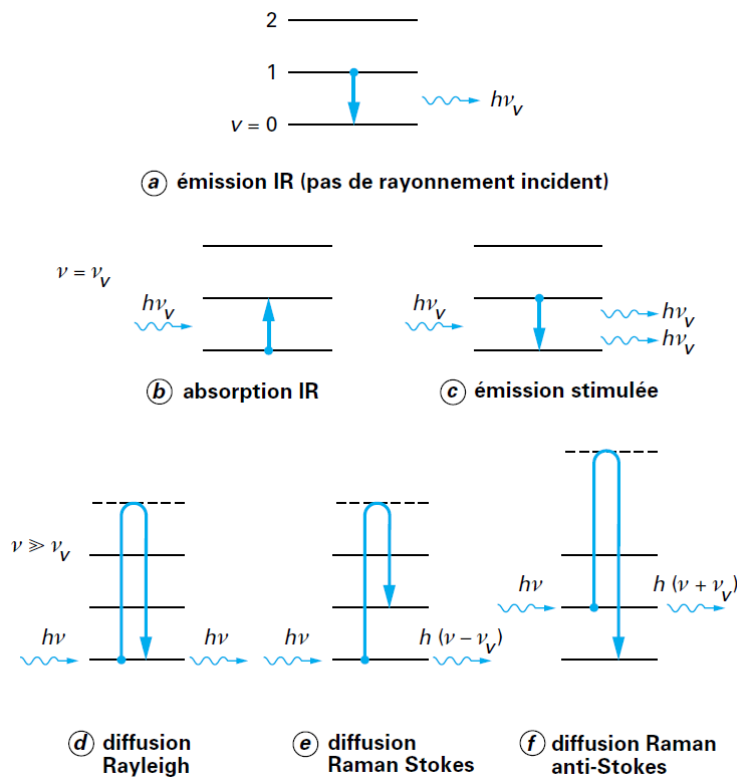


Figure II. 11: Schematic representation of the photon-matter interaction energy levels [12]

### II.2.3 Optical microscopy

As part of this study, optical microscopy was used for surface observations. After the various characterizations of the corrosion products, these surface observations provide quantitative and qualitative information on the corrosion damages resulting from the exposition to the tidal zone. After characterizing the corrosion products layer, the samples were chemically stripped and stabilized (as shown in figure II.12) using a hydrochloric acid and hexamethylene tetraamine solution, which composition is defined in standard ASTM G1.

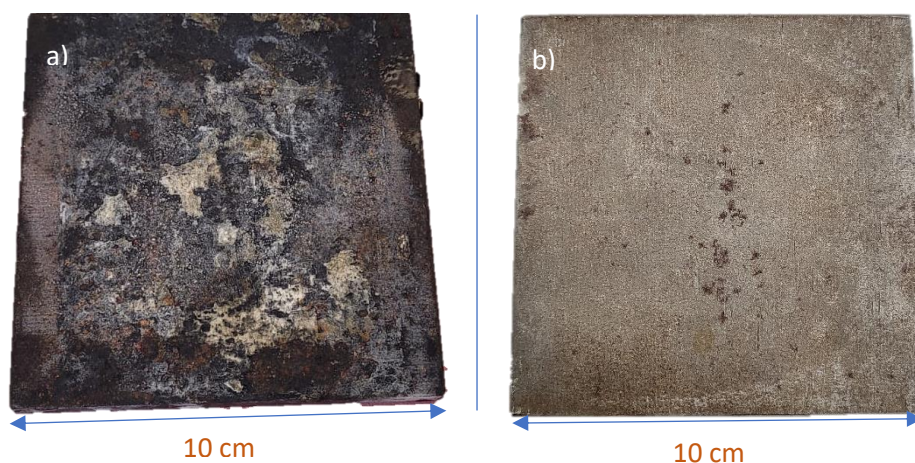


Figure II. 12 : Comparison of the surface state of a corroded steel coupon before and after desquamation

Estimating thickness loss by difference with a reference surface (surface not exposed to corrosion) was actually impossible either because the studied surface was polished before the experiment to remove the excess of protective resin or because the metal was corroded even under the resin supposed to protect it. Thus, it was no longer possible to consider the embedded and unexposed surface as a reference (as it is shown Figure II.13).



Figure II. 13: Surface state of some corroded steel coupons after resin removal

Consequently, the interest here is to characterize the depth of the craters caused by residual corrosion to estimate its intensity. A representative area of 3 cm x 3 cm was considered in the center of the sample to avoid any former edge effects. A range of motion in the z-direction was subsequently established by selecting boundaries that ensured full coverage of this area, i.e. the complete image is blurred for  $z_{\min}$  and for  $z_{\max}$ . Finally, a 3D reconstruction of the area was made using VHX advance<sup>®</sup> software by compiling photos taken at regular intervals (determined automatically by the software) as shown in figure II.14.

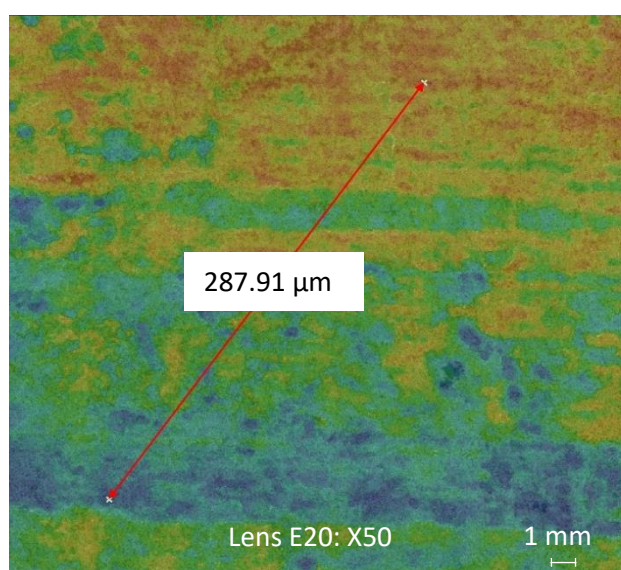


Figure II. 14: Representation of the estimation of the corrosion intensity by 3D imaging

## References

- [1] G. Copin-Montégut, *Chimie de l'eau de mer*. Institut océanographique, 1996.
- [2] « Le milieu marin », *Encyclopédie de l'environnement*, 14 mars 2016. <https://www.encyclopedie-environnement.org/eau/le-milieu-marin/> (consulté le 12 décembre 2020).
- [3] J. Duboscq, « Corrosion des aciers en milieu marin: processus se déroulant dans les zones cathodiques », Thèse de doctorat, La Rochelle Université, La Rochelle, 2019.
- [4] C. Gabrielli and H. Takenouti, « Méthodes électrochimiques appliquées à la corrosion - Techniques stationnaires », *Techniques de l'ingénieur*, vol. COR810v1, 2010.
- [5] X. L. Zhang, Zh. H. Jiang, Zh. P. Yao, Y. Song, and Zh. D. Wu, « Effects of scan rate on the potentiodynamic polarization curve obtained to determine the Tafel slopes and corrosion current density », *Corrosion Science*, vol. 51, n° 3, p. 581-587, mars 2009, doi: 10.1016/j.corsci.2008.12.005.
- [6] C. Gabrielli, « Méthodes électrochimiques - Mesures d'impédance », *Techniques de l'ingénieur*, vol. P2210v1, 1994.
- [7] A. Allagui, H. Benaoum and O. Olendski « On the Gouy-Chapman-Stern model of the electrical double-layer structure with a generalized Boltzmann factor », *Physica A*, vol. 582, n° 126252, p. 9, 2021.
- [8] H. Teghidet, « Etude de la cristallisation contrôlée de la calcite par voie électrochimique : Effet des ions étrangers au système calcocarbonique sur la nucléation-croissance de la calcite », Thèse de Doctorat, Paris 6 - Bézaiia, Paris, 2012.
- [9] K. Tu, « Enhancing the performance of current applied coatings for corrosion protection », PhD Thesis, Manchester university, Manchester, 2010.
- [10] Y. Yang, J. D. Scantlebury, and E. Koroleva, « Underprotection of mild steel in seawater and the role of calcareous film », presented at *NACE International*, vol. 68, n° 5, p. 8, 2012.
- [11] N. Broll, « Caractérisation de solides cristallisés par diffraction X », *Techniques de l'ingénieur*, vol. P1080 V2, 1996
- [12] J. Barbillat, D. Bougeard, G. Buntix, M. Delhayé, P. Dhamelincourt, and F. Fillaux, « Spéctrométrie Raman », in *Mesures - Analyses / Contrôle non destructif*, Techniques de l'Ingénieur, vol P2865 V2, 1999, p. 33.





*Chapter III: Mineral Layer Evolution, from  
Immersion to Splash Zone*



## Chapter III: Mineral Layer Evolution, from Immersion to Splash Zone

III.1 Introduction .....	78
III.2 Experimental features.....	79
III.2.1 Structure design [3] .....	79
III.2.2 Mineral layer analysis – methodology.....	81
III.3 Results .....	83
III.3.1 XRD analysis.....	84
III.3.2 Raman analysis .....	87
III.3.3 Corrosion rate estimation.....	90
<i>III.3.3.1 Definition of the mass/surface ratio .....</i>	<i>90</i>
<i>III.3.3.2 Optical microscope observation – estimation of the degradation due to corrosion .....</i>	<i>91</i>
III.4 Discussion.....	93
III.5 Conclusion .....	99
References .....	100

### III.1 Introduction

Harbours sheet piles are precisely meant to be installed in the tidal zone. Sheet piles are then subjected to cyclic immersion with specific corrosion profiles [1]. Because the top of the sheet piles is rarely immersed, cathodic protection (CP) does not work up to the top of the structure. Furthermore, as the area is constantly moist, organic coating application requires complicated and really expensive industrial techniques. The study of the CP of carbon steel in the tidal zone is therefore a point of major interest from the industrial point of view. For now, the common practice is to consider that CP is efficient approximately up to the mid tide zone and that organic coating has to be used above this level. In addition, experiments led in natural exposure conditions always represent a considerable asset in the study of physicochemical phenomena. In the context of carbon steel corrosion and CP studies, having the opportunity to set samples under quasi-real aging conditions is extremely interesting. However, although laboratory studies allow a complete control of the external parameters of the experiments, this control can be very limited in natural environment studies. It is therefore necessary to make concessions on the parameters to be considered in this type of type of scientific approach. The aim of this chapter is to understand *a posteriori* the corrosion and anti-corrosion involved mechanisms in the tidal zone and to try to evaluate the maximum height of efficiency of CP.

A previous study led by P. Refait *et al* in 2015 showed that CP could work in the tidal zone (during emerged phases) in specific conditions [2]. Indeed, the study has been performed on carbon steel coupons (AISI 1010) free of any rust layer. The samples have been exposed for 7 years at mid height (between the average low water zone and average high-water zone) in the tidal zone of Le Havre seaport. They were facing south and were not sheltered from daylight. The experimental structure is presented figure III.1 below. CP was achieved using galvanic Zn-based anodes. After 7 years, CP induced an important corrosion rate decrease compare to unprotected coupons set in the same conditions (1 order of magnitude). This confirms the hypothesis of an efficient protection around the mid tide zone. Then a “spread-out” CP could be defined.

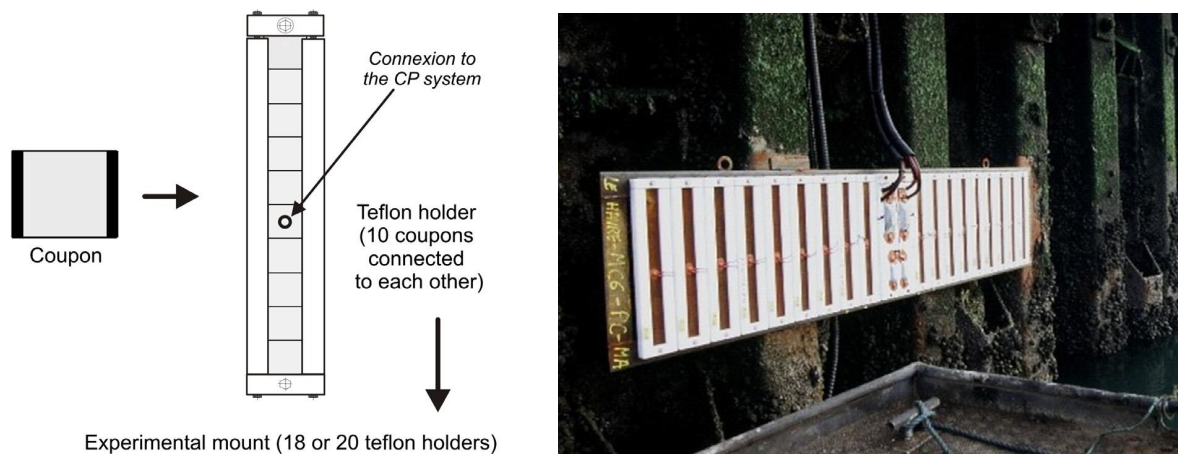


Figure III.1: Experimental set up used to study steel coupons subjected to CP in the tidal zone of le Havre [2]

The study presented in this chapter deals with really similar issues as the general idea here was to expose samples in conditions close to those of real harbour infrastructures.

The considerable advantage of a natural exposure in La Rochelle lies in the tidal conditions. The French west coast **tidal range** (difference in water height between high and low tide) reaches **6 m** for high coefficients. An experimental platform has been designed to capture the full impact of the tides by

positioning samples from the constant immersion zone to the splash zone. This finally resulted in the installation of a 6 m high structure (described below).

## III.2 Experimental features

### III.2.1 Structure design [3]

The present study has been designed and initiated by Julien Duboscq for his PhD work published in 2020. A high-density polyethylene structure, made by the LECAMUS company has been used as frame for the exposed samples. Those coupons are made of EN 10248-1 carbon steel provided by Arcelor Mittal which nominal composition is given in table III.1 (steel usually used for sheet piles). The coupons were exposed in La Rochelle commercial seaport. As they were facing north, they were not facing the sun, and drying conditions were then disfavoured. The sample disposition has been designed by J. Duboscq as presented in figure III.2 [3]. Though the whole assemblage is composed of four columns, the study here focuses on the two columns dedicated to the CP study in the tidal zone. The aim was to simulate as close as possible the behaviour of a continuous structure (such as sheet pile, offshore piles etc...). In order to limit the number of samples, 2 sizes of coupons have been used: squares of 10 cm side (the classical coupons) and long plate of 10 cm x 50 cm, not treated here (represented in the “3D view of one column” of the figure III.2). Each column is composed of 3 sections with 7 samples for the two first sections and 6 samples for the last part. A 3-number code was initially used to name the coupons. For instance, the coupon **125** was the **fifth sample** of the **second plank** in the **first column**.

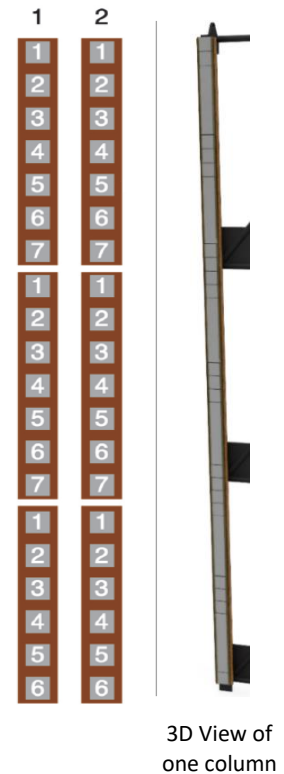


Figure III.2: Schematic representation of the sample disposition; from J. Duboscq PhD [2].

Both columns were studied and gave similar results and so data coming from only one of the two columns are displayed. Consequently, to simplify the discussion, the samples have been re-numbered from 1 to 20 from the top of the structure to the bottom. So, the first plank samples are numbered from 1 to 7; the second plank samples from 8 to 14 and the third plank samples from 15 to 20.

Conversely to the study led in Le Havre seaport [2], the structure designed here stretches from the constant immersion zone to the splash zone to cover the whole tidal zone. The geometrical continuity (each coupon is carefully juxtaposed to the previous one and the following one without apparent discontinuity) is ensured all along the structure to allow the residual seawater film formation and flow. The CP is ensured by an Al based galvanic anode whose chemical composition is presented in table III.2.

Then, such as it was explained in the study led by P. Refait (2015) [2], considering the total height of the exposed structure and its geometrical continuity, various situations must be considered (schematically represented in figure III.3):

- The structure is fully immersed so the CP works as usual (case - a)
- The structure is totally emerged and all the samples are dried so there is no CP but no corrosion either (case – b)
- The structure is fully or partially emerged and is covered by a **discontinuous** seawater film or **discontinuous** residual humidity (case – c); there is no CP but the corrosion process is active.

- The structure is fully or partially emerged and is covered by a **continuous** seawater film or **continuous** residual humidity film allowing current flow and thus CP efficiency even if the steel surface is not immersed (case – d).

This latter case is the “spread-out” CP as it has been defined in [2]. The aim of this chapter is then to determine which part of the tidal zone is exposed to situation a, b, c or d, in order to specify the maximum height of CP efficiency.

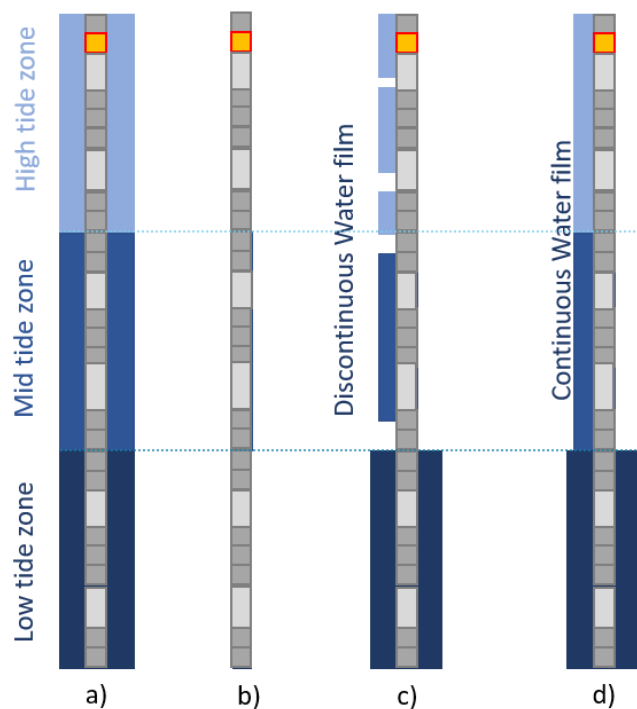


Figure III. 3: Different situations encountered in the tidal zone – a) coupons totally immersed – b) coupons totally dried – c) coupons covered in thin discontinuous seawater film – d) coupons covered in thin seawater film

Table III. 1: Composition of the Carbon steel EN 10248-1

Element	C	Mn	Si	S	P	Al	Fe
%Weight	≤ 0.27	≤ 1.7	≤ 0.6	≤ 0.055	≤ 0.055	0.02	Remainder

Table III. 2: Chemical composition of the Al based galvanic anode

Element	Zn	In	Mn	Fe	Si	Cu	Al
%Weight	3.5 – 6.5	0.01 – 0.03	≤ 0.01	≤ 0.13	≤ 0.10	≤ 0.006	Remainder

### III.2.2 Mineral layer analysis – methodology

The results have been collected in two campaigns. The first one consisted only in removing the mineral layer from the samples of the column 1 (cf. figure III.2) to analyse it after 33 months of exposure (i.e., 2 years and 9 months). The second one was to totally dismount the column 2 to analyse the whole coupons (mineral layer and steel sample) after 52 months of exposure (i.e. 4 years and 4 months).

For the first results collection, the mineral layer has been removed from the samples scrubbing off the surface. For each coupon, the obtained products were stored in a freezer (-24°C) to prevent any further oxidation. The samples of mineral layers were mixed one by one in a mortar and crushed until a homogenous paste was obtained. For technical reasons (tide amplitude) the lowest sample analysed was coupon 17. X-ray diffraction (XRD) was used to identify the solid phases constituting the mineral layers.

The XRD analysis was carried out using an Inel EQUINOX 6000 diffractometer equipped with a curved detector (CPS-590). The curved detector is designed for the simultaneous detection of the diffracted photons on a  $2\theta$  range of  $90^\circ$ . Acquisition was made with a constant angle of incidence ( $7^\circ$ ) during 45 minutes). The Co-K $\alpha$  radiation ( $\lambda = 0.17903$  nm) was used.

For the second campaign, after the disassembly of the column, the whole samples were stored frozen at -18°C to prevent any further corrosion or corrosion product evolution. The outer layer was analysed by  $\mu$ -Raman spectroscopy to discriminate the different solid phases and establish their spatial organisation. Then, the mineral layer was collected, crushed and homogenised to be analysed (following the exact same protocol as the first campaign) by XRD with a Bruker-AXS D8-Advance diffractometer equipped the LynxEye XE-T detector. The Cu-K $\alpha$  radiation ( $\lambda = 0.15406$  nm) was used, and the acquisition was made with a constant angle of incidence ( $7^\circ$ ) during 30 minutes. However, to compare the XRD patterns with those obtained previously, the data were converted to be given in a  $2\theta$  scale corresponding to the Co-K $\alpha$  radiation.

Finally, the last traces of mineral layers remaining on the steel samples were removed by dissolution in a mixture of HCl and ethylenediaminetetraacetic acid (EDTA). The surface of the steel coupons was then characterized by optical microscopy, in particular to analyse the differences between the well protected samples and the more corroded samples.

To describe accurately the effects of tide on the steel coupons, an average immersion rate has been calculated over a complete year by J. Duboscq in his PhD work [3]. As the altitude of each sample is precisely known, if we compare these altitudes with the tide levels, the immersed and emerged time can be determined in every moment for all the samples. Then, the accumulated immersed time has been calculated for 365 days and then the percentage of immersion time has been extracted. In other words, this immersion rate is, for a sample at a given altitude, the ratio of the accumulated immersed time over 365 days.

Atlantic tide levels data are coming from the SHOM (Service Hydrographique et Océanographique de la Marine) and are consistent with the tide gauge installed in the La Rochelle commercial seaport. Figure III.4 shows an extract of the data used by J. Duboscq and provided by the SHOM on the exposure period (here from the 01/10/2018 to the 01/02/2019). The grey curve represents the tide alternation. Indeed, regarding the tide coefficient, the tide range varies over time. Yet, a pattern that repeats itself every month can be defined as a “short range” cycle followed by a “wide range” cycle, materialized by

the orange squares. During the wide range cycles, the maximum high tide can be high up to 6.77 m while the minimal low tide could go down to 0.5 m, both materialised by the high and low green lines. The red line indicates the mid tide level. This is the height for which the steel is immersed 50% of the time over a year. The calculation is based on the whole exposure time data. Yet, the light blue line indicates the mid height (considering the widest tide range) of the tidal zone (i.e., the exact area swept by the wide range tide, from 0.5 m to 6.77 m). So, the 50% immersion rate altitude is equivalent to about 60% of the maximum high tide level and about 67% of mean high tide level. For the following results discussion, only the immersion rate will be used as the parameter for comparison between each sample.

Now, if the SHOM data are compared to the sample position in the tidal zone, the immersion rate notion is clarified (Figure III.5). The blue lines in figure III.5 show the samples positions (the first sample of each plank is indicated in the graph). For instance, sample 15 has an altitude of 4.96 m (compared to 0 equivalent to a low tide with a coefficient of 120) and has an immersion rate of 25.5%. This sample has been immersed for 93.1 days in a year. All the samples positions and their immersion rates are listed in table III.3.

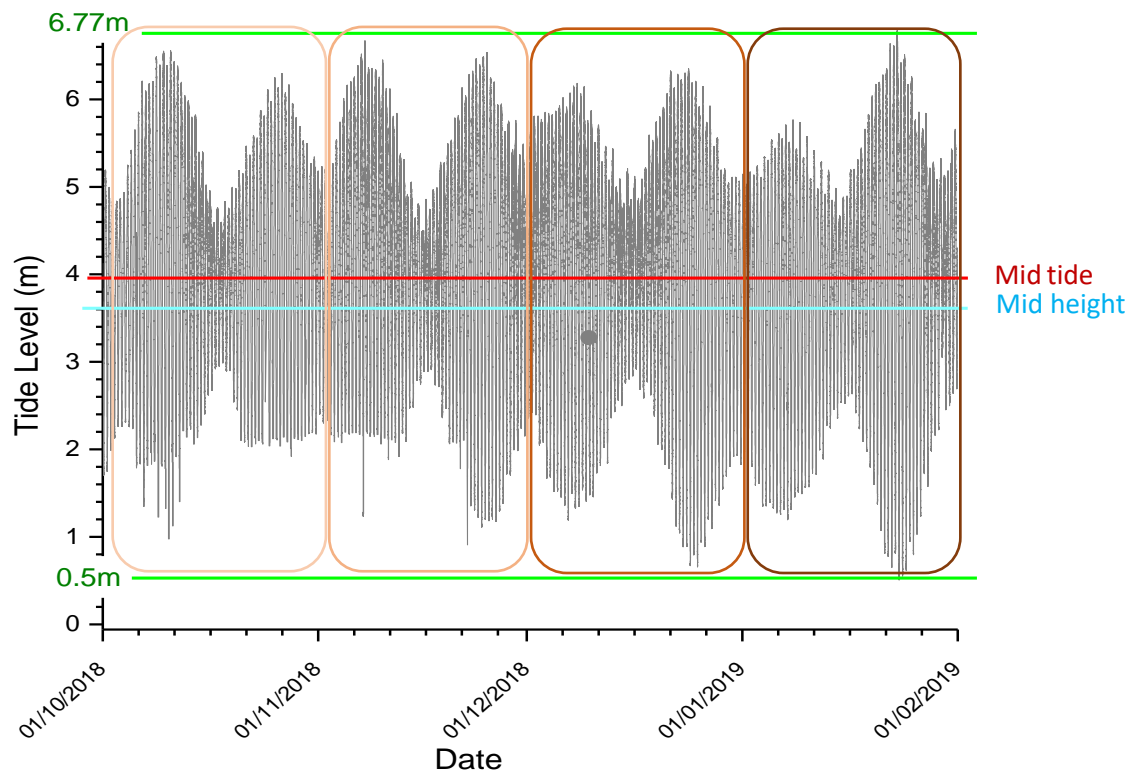


Figure III.4: Graphic representation of the tide levels from the SHOM data from the 10/01/2018 to 02/01/2019

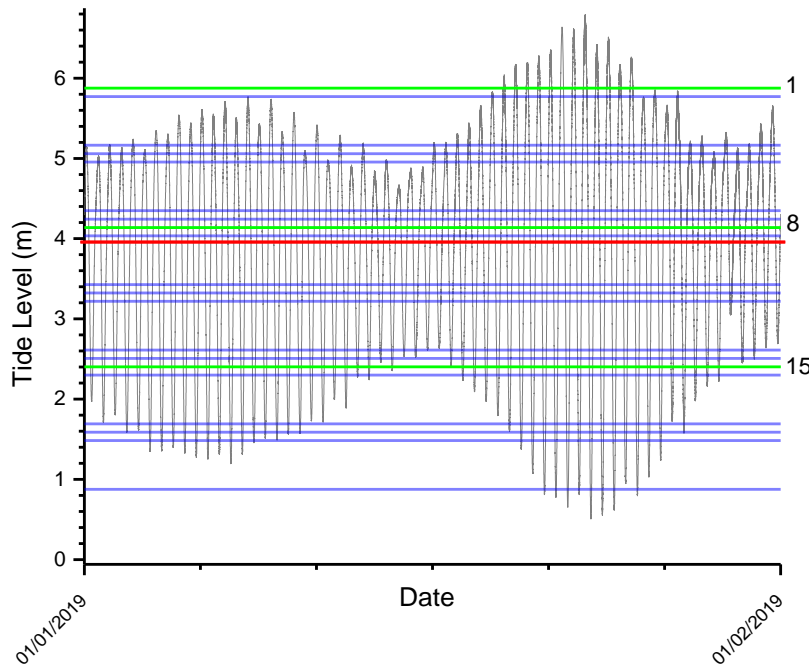


Figure III.5: Graphic representation of the sample position in the tidal zone regarding the tide levels

Table III 3: Marine altitude and immersion rate of each sample

	Marine altitude (m)	Immersion rate (%)
1	5.88	4.2
2	5.77	5.8
3	5.16	19.3
4	5.06	22.3
5	4.96	25.5
6	4.35	44.8
7	4.24	47.4
8	4.14	49.9
9	4.04	52.3
10	3.43	66.1
11	3.32	68.5
12	3.22	70.9
13	2.61	84.3
14	2.51	86.4
15	2.4	88.2
16	2.3	89.9
17	1.69	96.7
18	1.59	97.4
19	1.48	98
20	0.88	99.5

### III.3 Results

The analysed features of these samples will be presented here from the bottom to the top of the tidal zone. In other words, results are described here from the best protected zone to the least protected area. This should help to make the further discussions clearer and to better identify the transition zone between protected coupons and corroding coupons. In addition, representative photographs of the concerned zone will be presented in the discussion as they will provide a good parallel with the mineral layer stratification schemas.

Four representative zones have been chosen to illustrate the evolution of the composition of the mineral layer covering the coupons (presented in figure III.6):

- The low tide zone with an immersion rate of **90 % to 84 %** of the time; corresponding to coupons 16 to 13 (*focus on coupon 15*)
- The mid tide zone with an immersion rate of **52 % to 45 %** of the time; corresponding to coupons 9 to 6 (*focus on coupon 7*)
- The high tide zone with an immersion rate of **26 % to 19 %** of the time, corresponding to coupons 5 to 3 (*focus on coupon 4*)
- The extreme high tide zone with an immersion rate of **5.8 % to 4.2 %** of the time, corresponding to coupons 1 & 2 (*focus on coupon 2*)

As mentioned above, the low tide zone is treated separately from the other zones because it can be considered as the reference, i.e., the zone where coupons are necessarily protected by CP because they are (almost) always immersed.

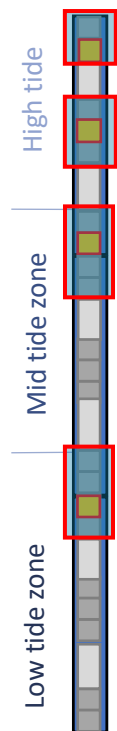


Figure III. 6: Schematic representation of the treated zones

### III.3.1 XRD analysis

The XRD patterns presented here are dealing with the characterisation of column 2 as they confirm the observations made with the XRD analysis of the mineral layers covering the coupons of the first column.

The first XRD pattern presented in this study is representative of the **low tide zone** (coupons 16-13), and is actually that of the mineral layer covering coupon 15. This zone is highlighted by a red rectangle in figure III.7. The immersion rate of the coupons in this zone goes from 90% to 84% (cf. table III.3). The most intense peak of this pattern is the main diffraction peak of calcite ( $\text{CaCO}_3$ ), a compound mainly coming from the shells that have been crushed with the mineral layer prior the XRD analysis. Numerous diffraction peaks are also associated with minerals coming from the marine environment. This the case of quartz ( $\text{SiO}_2$ ), i.e., sand and halite ( $\text{NaCl}$ ), salt. This is also the case of kaolinite and illite, clay minerals present in marine sediments [3].

Another important compound, as revealed by the strong intensity of its diffraction peaks, is aragonite, another  $\text{CaCO}_3$  polymorph. The presence of aragonite is directly linked to CP and results from the increase of the interfacial pH induced by the cathodic polarization, which leads to the formation on the steel surface of the so-called calcareous deposit [1], [4]–[6]. At the CP potential considered here, i.e., the potential of the coupons due to the coupling with the Al-Zn-In galvanic anode (around -1.0 V vs Ag-AgCl-seawater), aragonite is known to be the main component of the calcareous deposit [4], [5], [7], [8]. Another common phase present in such deposit is brucite ( $\text{Mg}(\text{OH})_2$ ) [9]–[12] which is also identified here.

Finally, magnetite ( $\text{Fe}_3\text{O}_4$ ) is also identified as a very minor phase, via only its main diffraction peak (M311). It results from the residual corrosion process that occurs, at very low rate, even when CP is efficient [13], [14]. The characteristics of this mineral layer are then consistent with an effective CP.

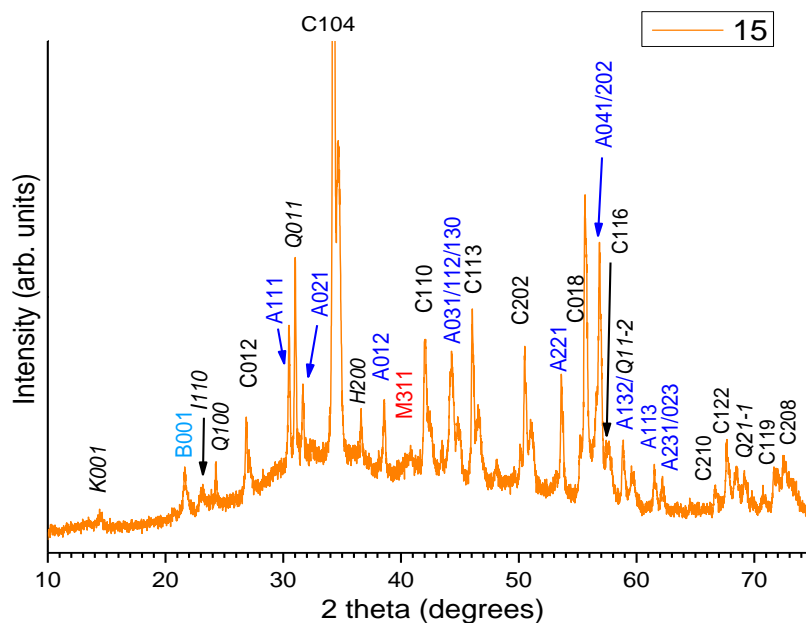


Figure III.7: X-ray diffraction pattern representative of the **low tide zone** (sample 15) -  $\text{Co-K}\alpha$  radiation. A = aragonite, B = Brucite, C = calcite, H = halite, I = illite, K = kaolinite, M = magnetite, Q = quartz, with corresponding Miller index.

Figure III.8 shows typical XRD patterns obtained in the other zones, and more precisely those corresponding to coupons 7, 4 and 2. The **mid tide zone**, where coupons 9 to 6 were located, is characterized by immersion rates from 52% to 45%. Coupon 7 has been chosen as a representative sample of this zone. The coupons in this zone were covered with shellfish and, as a result, the most intense peak detected on the diffractogram showed figure III.8-a) is the main peak of calcite. Aragonite is the other important compound identified, which indicates that CP was active most of the time. In agreement, brucite is also clearly identified here. Pyroaurite ( $\text{Mg}^{\text{II}}_6\text{Fe}^{\text{III}}_2(\text{OH})_{16}\text{CO}_3, 4\text{H}_2\text{O}$ ) [15] is also observed. This compound has already been reported on coupons subjected to CP in seawater and its formation was attributed, as that of aragonite and brucite, to the increase in interfacial pH [2]. As it contains Fe atoms, it may be considered as a corrosion product, but it does not form at OCP and is characteristic of the “residual” corrosion process of the metal subjected to CP. It must also be noted that pyroaurite and carbonate green rust,  $\text{GR}(\text{CO}_3^{2-})$  are structurally identical.  $\text{GR}(\text{CO}_3^{2-})$  only contains Fe(II) cations, and its chemical formula is  $\text{Fe}^{\text{II}}_4\text{Fe}^{\text{III}}_2(\text{OH})_{12}\text{CO}_3, 2\text{H}_2\text{O}$  [16], while pyroaurite contains only Mg(II) ions. However, intermediate compounds, containing both Fe(II) and Mg(II) cations, may form [17]. Therefore it is impossible, with XRD analysis only, to state whether the compound detected here is pyroaurite *sensu stricto*, or a Mg(II)-Fe(II)-Fe(III) hydroxycarbonate. This compound is then denoted as “pyroaurite” in the following.

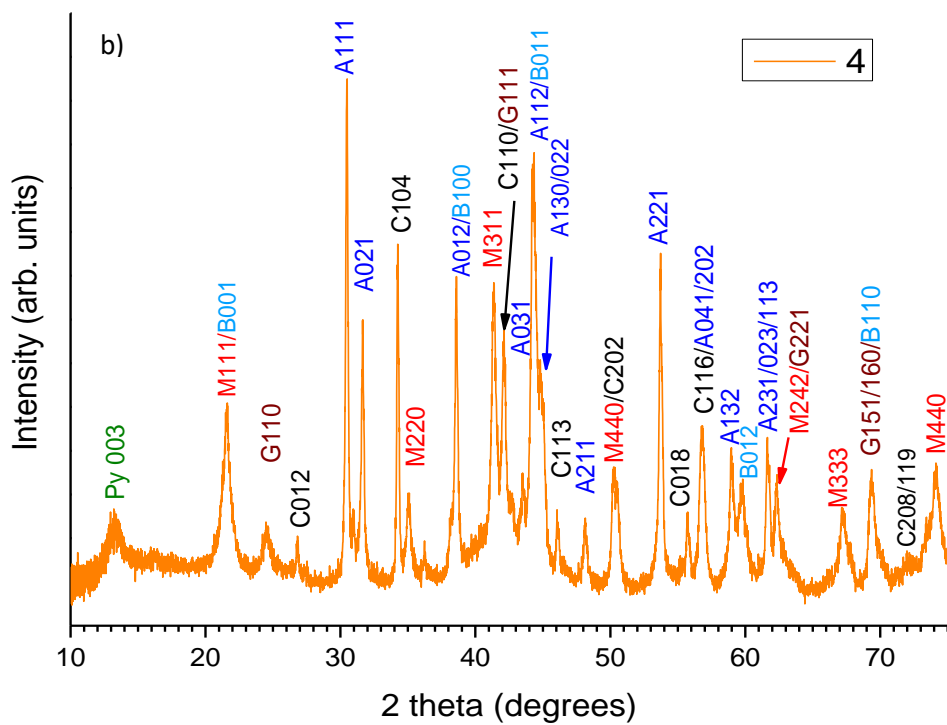
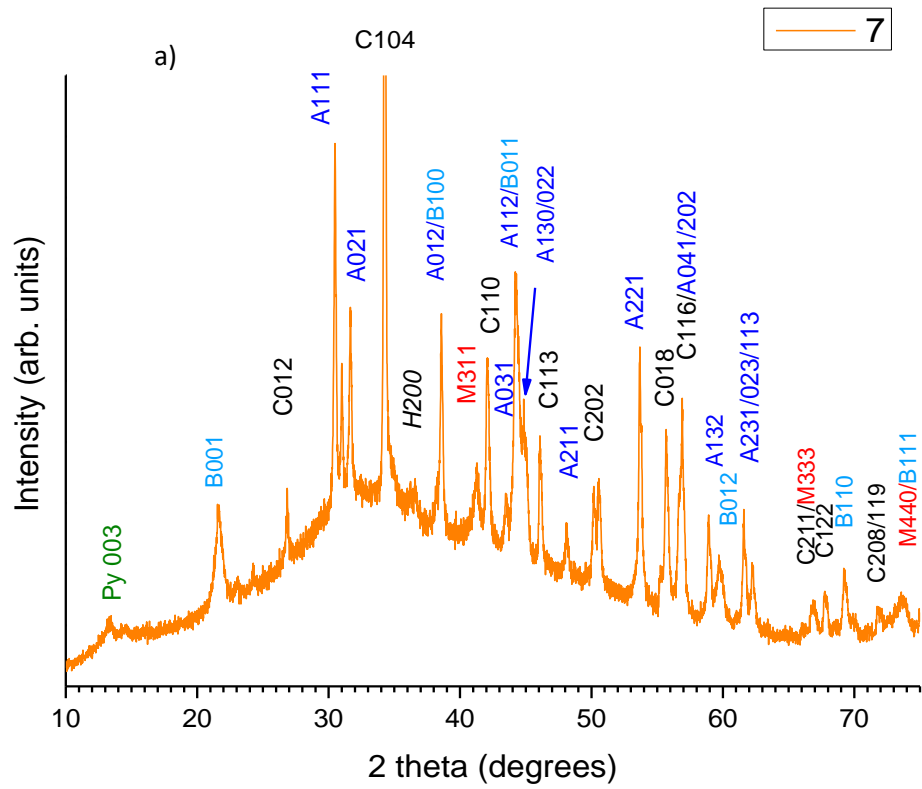
Finally, magnetite is detected as a minor component. It is noticeable that the formation of magnetite is favoured by an increase in pH [18,19] which may explain why it is the main compound resulting from the “residual” corrosion process occurring when CP is applied.

The **high tide zone**, corresponds to coupons 3, 4 and 5. The XRD pattern of Figure III.8-b is that of coupon 4, chosen as a representative example of this area. The immersion rate of the zone starts at 19% for coupon 3 and ends at 26% for coupon 5. The most intense peak is no more the main diffraction peak of calcite, but that of aragonite. This is simply due to the fact that shellfishes were less present on the surface of the coupons, more likely because of the smaller immersion rate. Brucite and “pyroaurite” are once again identified.

The most significant difference with the previous coupons is the strong intensity of the diffraction peaks of magnetite, which demonstrates that the corrosion process was more active in the case of coupon 4 if compared with coupons 7 and 14. Consistently, another corrosion product, goethite ( $\alpha\text{-FeOOH}$ ), is also clearly identified.

The **extreme high tide** zone corresponds to coupons 1 and 2 and figure III.8-c presents the XRD pattern of coupon 2 as an example. In this area, the immersion rate of coupon 1 was 4.2% and that of coupon 2 was 5.8%. In this case, various corrosion products are detected, still coexisting with aragonite, the main compound resulting from CP. The most intense peak is the main peak of aragonite (A111) but the main peaks of magnetite (M311) and goethite (G111) are very intense too. Akaganeite ( $\beta\text{-FeOOH}$ ) and lepidocrocite ( $\gamma\text{-FeOOH}$ ) are clearly detected too. Brucite is no more detected and “pyroaurite” is hardly seen.

Although XRD analysis give really important information about the composition of the mineral layer, it does not give any information about the spatial organisation of the identified compounds. Moreover, this method does not give any clue about the presence of amorphous or nanocrystalline compounds. Raman analysis is then a good complement to X-ray diffraction. The  $\mu\text{-Raman}$  spectroscopy results are presented in the following using the same structure as for the XRD analysis section.



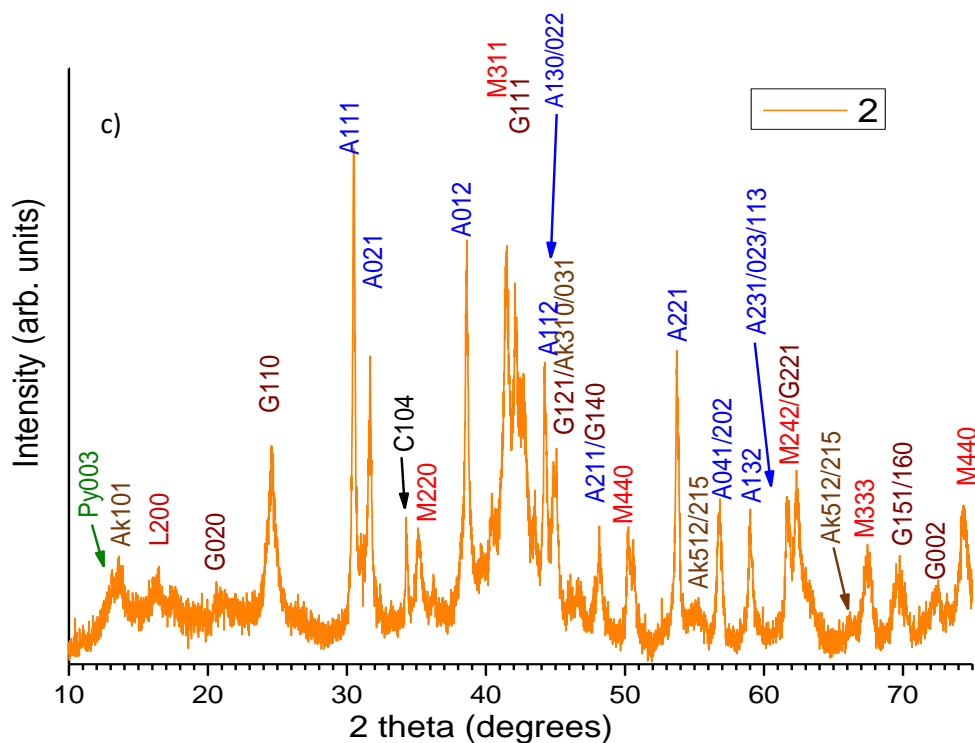


Figure III.8: X-ray diffraction pattern representative of the – a) mid tide zone (sample 7) – b) high tide zone (sample 4) – c) extreme high tide zone (sample 2) - Co-K $\alpha$  radiation.  
 A = aragonite, Ak = Akaganeite, B = Brucite, C = calcite, H = halite, I = illite, K = kaolinite, M = magnetite, Py = Pyroaurite, Q = quartz, with corresponding Miller index.

### III.3.2 Raman analysis

The results obtained with coupon 15, typical of the low tide zone, are displayed in figure III.9. Figures III.9-a) and -b) show respectively a characteristic Raman spectrum of nano-crystalline mackinawite (FeS) [20] and magnetite (Fe<sub>3</sub>O<sub>4</sub>) [21]. Both of them have been collected at the interface between the metal surface and the mineral layer, in a black inner stratum directly in contact with the steel substrate.

Figure III.9-c) shows various compounds. Two ellipses were drawn to highlight the difference between the previous spectra and the new compound identified here. The peaks inside the green ellipse are representative of a green rust compound [22-25]. The yellow ellipse encircles various unidentified peaks representative of organic matter. The three other peaks are those detected in a) and b), corresponding to nanocrystalline mackinawite (205 and 280 cm<sup>-1</sup>) and magnetite (675 cm<sup>-1</sup>).

Finally, the last Raman spectrum (figure III.9 – d), collected on the outer part of the mineral layer (under the fouling) is characteristic of aragonite (CaCO<sub>3</sub>) [26], i.e., the main solid phase constituting the calcareous deposit associated with the cathodic polarization.

Figure III.10 displays spectra obtained with coupons typical of the mid tide and high tide zones. Let us first focus on sample 7, located in the mid tide zone. The first collected spectrum (a – 7.1) is attributed to a mixture of nanocrystalline FeS and magnetite, “residual corrosion” products also identified on coupon 15. Aragonite is detected too (a - 7.2) [26]. In the O-H stretching region, a sharp peak located at 3650 cm<sup>-1</sup> have been detected a few times (a – 7.3). It can be attributed to brucite Mg(OH)<sub>2</sub> [27], also identified via XRD (Fig. III.8-a).

It is important to note that FeS could only be detected via Raman spectroscopy. More precisely, Raman analysis revealed that FeS was only present as nanocrystalline mackinawite. This finding is consistent with previous works [13,18,19], and it was proposed that mackinawite remained nanocrystalline because of the alkalinity of seawater [20].

In the high tide zone, FeS is not detected any more. Aragonite and magnetite are still identified (spectra not presented), as well as brucite (spectrum b-4.1), in agreement with XRD analysis (Fig. III.8-b). Various corrosion products were identified: The spectra gathered in Figure b – 4.3 correspond to goethite [21], a compound that was often detected at the surface of coupon 4. Akaganeite was also identified (spectrum b – 4.4) [28]. The last two spectra (Figure b – 4.5) correspond to lepidocrocite  $\gamma$ -FeOOH [21], which was not detected by X-ray diffraction more likely because it is a very minor component of the rust layer.

Finally, goethite, lepidocrocite, akaganeite, aragonite and brucite were also detected in different proportions in the extreme high tide zone (spectra not shown). The stratification proved similar too.

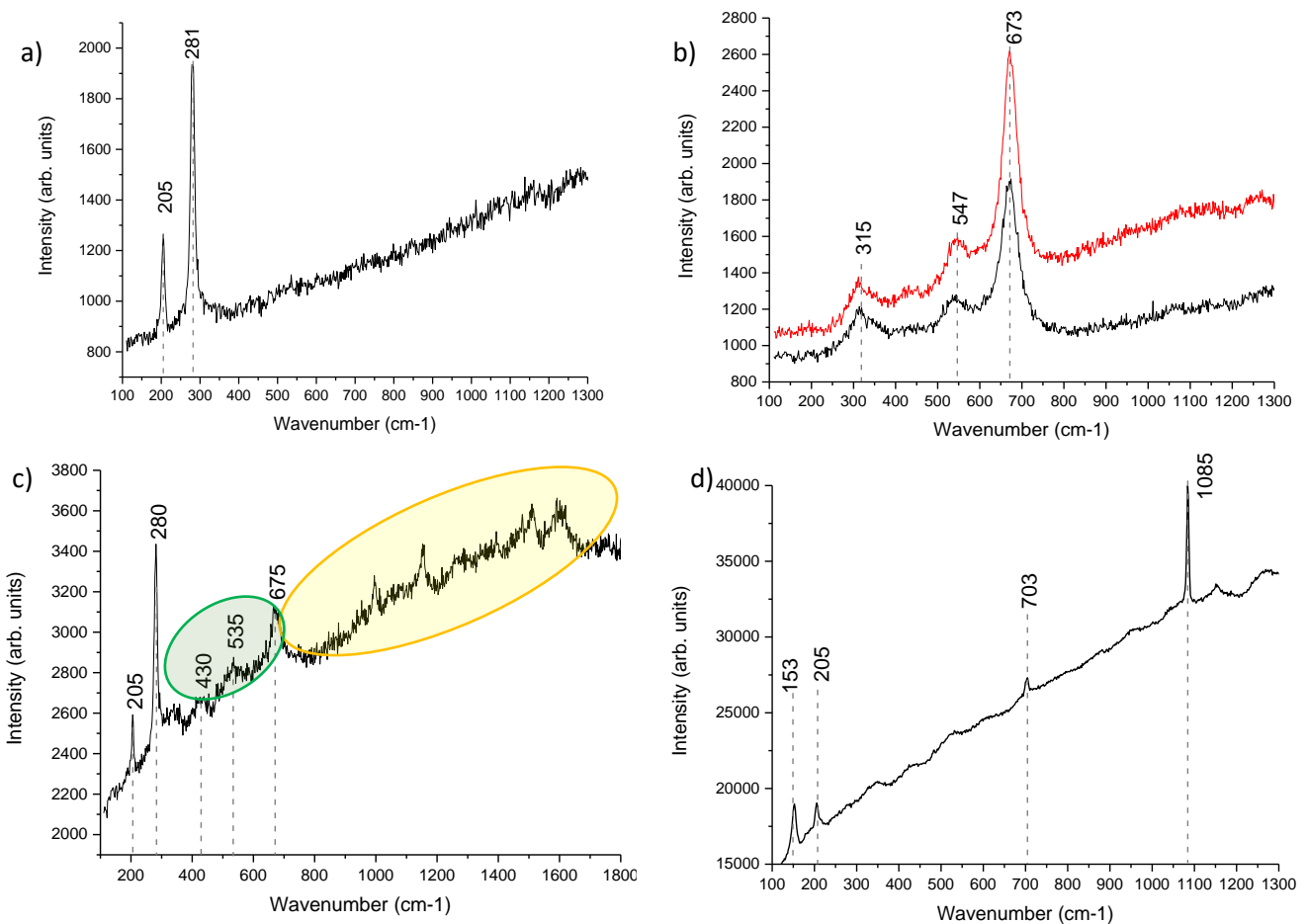


Figure III.9:  $\mu$ -Raman spectroscopy results for the **coupon 15** – a) characteristic spectrum of FeS – b) Characteristic spectrum of magnetite ( $\text{Fe}_3\text{O}_4$ ) – c) mixed compound spectrum of FeS; green rust and magnetite – d) characteristic spectrum of aragonite ( $\text{CaCO}_3$ )

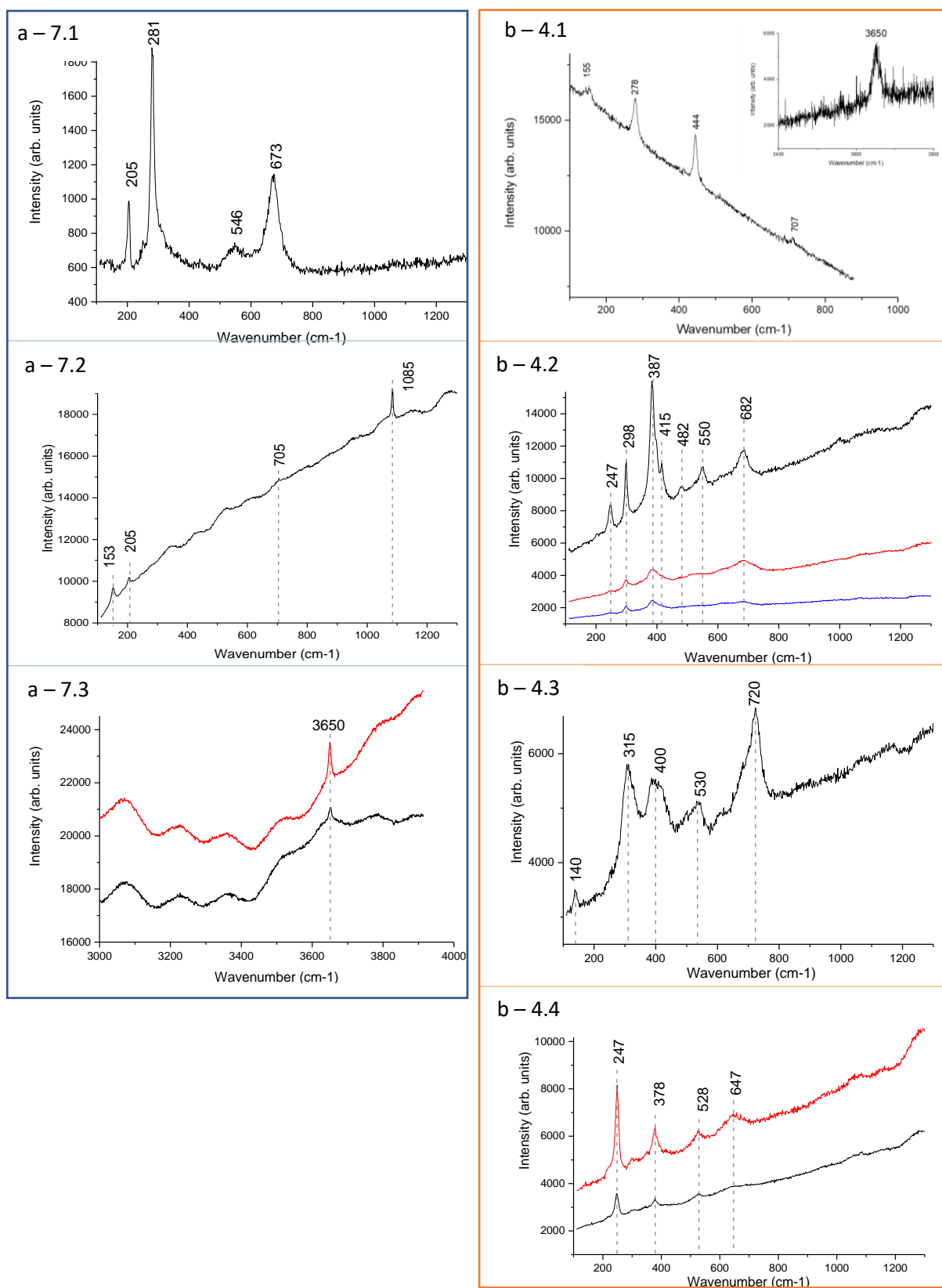


Figure III.10:  $\mu$ -Raman spectroscopy results for – a) **Coupon 7**: 7.1 FeS and  $Fe_3O_4$  spectrum; 7.2 Aragonite ( $CaCO_3$ ) spectrum; 7.3 OH band spectrum = Brucite – b) **Coupon 4**: 4.1 Brucite spectrum; 4.2 Goethite ( $\alpha$ -FeOOH); 4.3 Akaganeite spectrum; 4.4 Lepidocrocite ( $\gamma$ -FeOOH) spectrum

### III.3.3 Corrosion rate estimation

The previous analysis method could give a qualitative point of view about the CP efficiency based on the composition of the outer layer and the combination of the compounds to understand the mechanisms that occurred during the exposure. Yet, it could not quantify the effect of CP. Two strategies were exploited to try to quantify the residual corrosion rate, i.e., the efficiency of CP:

- An estimation of the residual corrosion rate by comparison between coupons
- An estimation of the surface roughness to determine the more aggressive condition

#### III.3.3.1 Definition of the mass/surface ratio

Many obstacles have been encountered to estimate the residual corrosion rate. As the initial mass of the samples was unknown, a classical mass loss measurement could not be performed. Then, the idea was to determine which sample got the most corroded during the exposure time by quantifying its final mass regarding the exposed surface via the mass to surface (m/S) ratio. This analysis has been performed on the samples exposed for 52 months as they were the ones that have been totally dismantled. Figure III.11 displays the obtained results. The black crosses represent the m/S value of each sample analysed. The position number of the previously studied samples is reported on the graph. The red points are the average value of this ratio as a function of the average immersion rate for the samples located in the same zone. The standard deviation of this value is represented by the solid red lines. Finally, the dash red rectangles make visible the range of m/S values for each zone of the column. The blue line shows the obtained m/S value for a non-exposed coupon of the same steel with the same dimensions prepared in the same conditions.

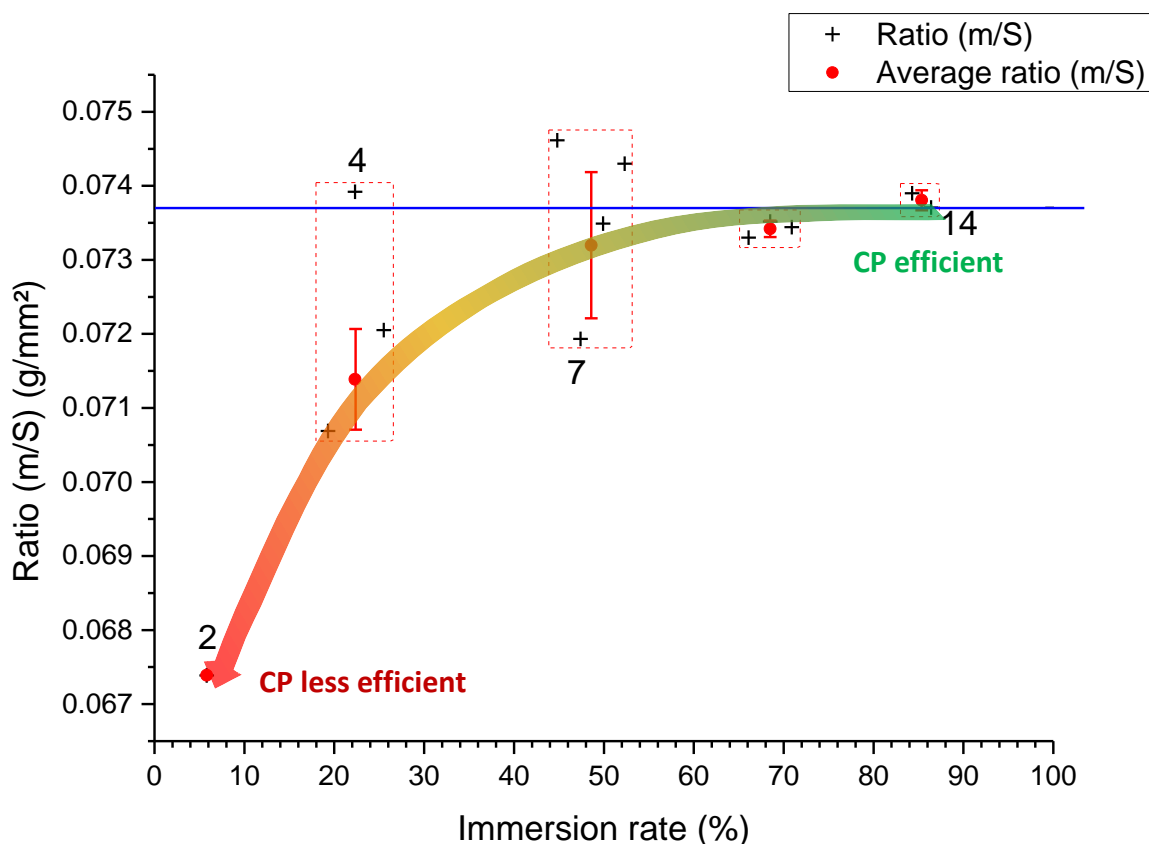


Figure III.11: Ratio  $\frac{\text{mass (g)}}{\text{Surface (mm}^2\text{)}}$  estimation regarding the immersion rate of the samples i.e., their height in the tidal zone

As the mass is divided by the exposed surface, the smaller the mass the smaller the ratio and subsequently the higher the residual corrosion rate. As expected, the extreme high tide zone (coupon 2) presents the lowest m/S ratio thus the higher residual corrosion rate. In the high tide zone, around coupon 4, the results also indicate that corrosion took place. In contrast, the average values obtained in mid tide zone, intermediate low tide zone, and low tide zone are similar to that corresponding to an uncorroded coupon. This shows that CP was efficient up to the mid-tide zone.

In addition, comparing the m/S ratio of the exposed coupon and the control coupon (0,0737 g/mm<sup>2</sup>) permit to evaluate a residual corrosion rate of the most corroded coupons, i.e. the rate of the corrosion phenomenon still occurring under cathodic protection. For instance, for the coupon 2 (the least protected one) the corrosion rate is estimated at **19 μm/year**. In their 2013 study about *Electrochemical formation and transformation of corrosion product of carbon steel under cathodic protection in seawater*, Ph Refait et al. found corrosion rates of **66±5 μm/year for unprotected coupons** and **6 or 8±2 μm/year for well protected coupons**. [13] This result tends to show that even for extreme high tide zone (≈ 5.8% immersion rate) CP may not be deactivated or inefficient.

It is however observed that the average m/S ratio tends to decrease slightly from a value really close to that of an uncorroded coupon (low tide zone) to slightly smaller values, indicating that CP may be slightly less efficient for coupons that are not continuously immersed. Moreover, the scattering of the m/S measured values increases when the immersion rate decreases, suggesting that CP may not be totally reliable in sort of a transition zone. According to our results, this transition zone should be located around coupons 7 and 6 in the mid tide zone, i.e., for immersion rates about 44-48%. However, as this analysis has been performed only on 1 column, a second estimation of this ratio is required to determine accurately where this transition occurs.

#### III.3.3.2 Optical microscope observation – estimation of the degradation due to corrosion

To confirm these results, the residual corrosion rate has been estimated through a second approach. The first idea was to estimate average thickness loss through a 3D imaging of the surface of a sample with an optical microscope. As a part of the exposed surface was embedded in the resin and should not have been corroded, it could then have been used as a “zero” for the thickness loss measurement. Unexpectedly, the samples were corroded even under the resin (as presented in figure III.12), preventing any thickness loss measurement.

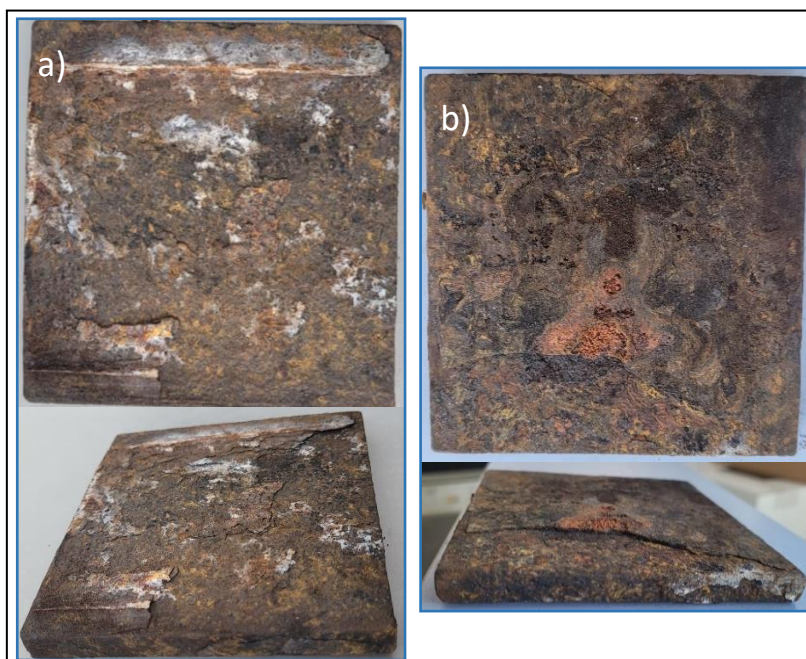


Figure III.12: photographs of the sample 2 - a) view of the exposed surface - b) view of the back of the sample (the embedded surface)

Finally, the chosen option was to analyse the surface state through the “surface roughness analysis” carried out by optical microscopy after removing the corrosion product layer from all sides of the coupon.

For each coupon, a representative 30 mm x 30 mm surface was considered. In general, it was located approximately at the centre of the coupon (see chapter II). An example is shown in figure III.13. The highest and lowest points have been highlighted and the maximum amplitude represents the altitude difference between them. This difference should be representative of the amplitude of the degradation in this zone of the coupon.

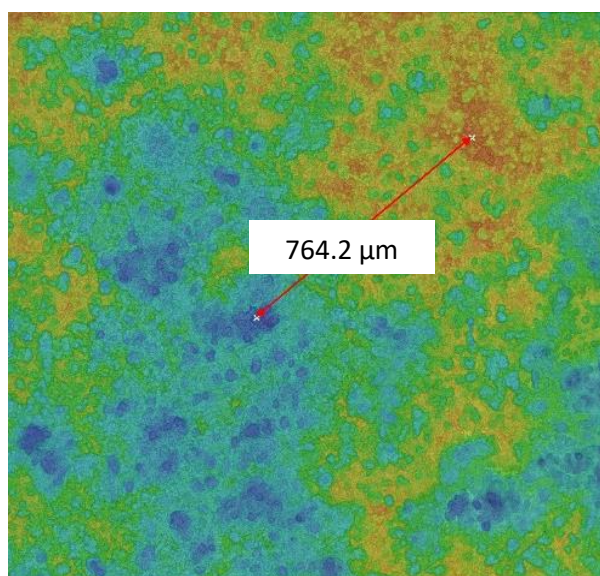


Figure III.13: Example: maximum amplitude estimation of coupon 2.

Based on the representation scheme already used in the previous section, the black crosses in figure III.14 indicate the maximum degradation difference determined for each coupon. The red points and lines represent the average value and the standard deviation in the considered immersion zone. The dashed red squares point out the various considered immersion zones. The assumption here is that the bigger the degradation difference, the higher the corrosion rate. The idea is to consider that, if the coupon is protected, the corrosion rate is low and then the difference between anodic and cathodic areas of the surface is small. Conversely, if the coupon is insufficiently protected, the anodic areas of the surface are expected to corrode much more rapidly than the cathodic zones. Therefore, the maximum degradation difference, which corresponds to the difference between the most corroded anodic areas and the less corroded cathodic areas, should increase with the corrosion rate reached in the anodic areas.

In agreement with this hypothesis, the coupons located in the extreme high tide zone (1 & 2) and in the high tide zone (3, 4 & 5) have a higher maximum degradation difference than the samples located in the lower zones. Considering the average values and their standard deviation, 2 values can be distinguished, about 800 – 850  $\mu\text{m}$  of maximum degradation difference for the extreme high tide zone and the high tide zone, and about 350  $\mu\text{m}$  for the mid tide zone, the intermediate low tide zone and the low tide zone.

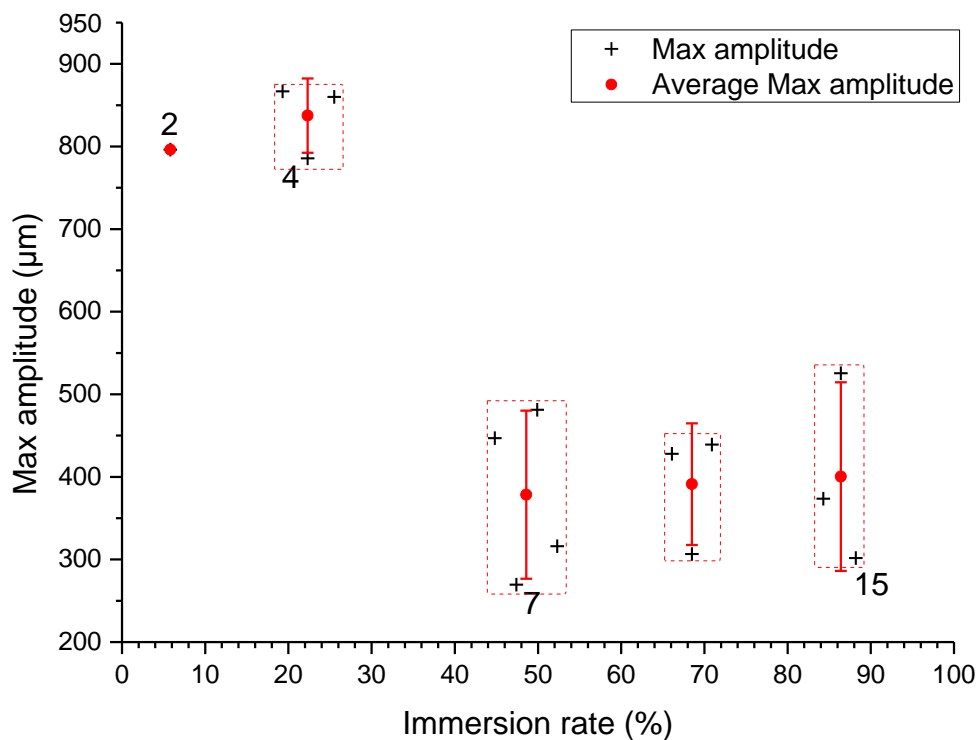


Figure III.14: Maximum degradation difference of the coupons sample with respect to their immersion rate

### III.4 Discussion

The XRD results demonstrate that in **the low tide zone** the coupons are mainly covered with aragonite, the main component of the calcareous deposit at the cathodic potential applied here via the Al-Zn-In galvanic anode [29]. Of course, minerals coming from seawater are also predominant, such as calcite coming from shells and clays coming from marine sediments. This result is typical of a coupon protected by CP and (almost) permanently immersed in seawater. Magnetite is detected as a minor

component, in agreement with previous works [2,13]. Its formation results from the “residual corrosion” process occurring even when CP is considered as efficient. It is also noticeable that the formation of magnetite is favoured, with respect to other corrosion products and in particular the sulphate green rust, by an increase in interfacial pH [18,19].

In addition, Raman analysis brings complementary information. It showed that magnetite was not the only corrosion product. First, a green rust (GR) compound could be identified. It was not detected via XRD probably because the residual corrosion process is really slow in this case (i.e., CP is efficient) leading to an extremely thin GR layer. Actually, GR compounds were already identified as products of the residual corrosion process of coupons permanently immersed in seawater [13,30]. Secondly, nanocrystalline mackinawite (FeS) was detected too. The formation of FeS is the consequence of sulphate reducing bacteria metabolic activity. Because SRB are anaerobe microorganisms, this implies that anoxic conditions are met close to the steel surface, at least locally. Note that actually, dissolved  $O_2$  is more likely consumed partially by the aerobic macro- and micro-organisms forming the biofouling outer layer covering the steel surface. Moreover,  $O_2$  molecules finally reaching the inner part of the outer layer may be reduced on magnetite particles connected to the steel surface so that a very small proportion of  $O_2$  molecules may reach the steel surface.

Moreover, the brucite main peak was detected too in the XRD pattern of the 15<sup>th</sup> sample. As mentioned in the section “3.2 CP in the tidal zone” of the first chapter, brucite detection here could be rather surprising as it requires specific conditions to precipitate ( $pH > 9.3$  and  $E_{\text{applied}} \leq -1.2 \text{ V/SCE}$ ) [7], [8], [31]. However, a thin brucite film may be detected, for instance using SEM, below the aragonite layer [32]. The formation of brucite could be linked to the initial high pH increase that takes place at the beginning of the cathodic polarization, as suggested by Yan et al. [33]. Precisely, in these initial conditions, electrolyte pH could easily reach 11, the transition value for which the formation of aragonite is inhibited and that of brucite is enhanced (cf. chapter 1). Only one peak was detected on the XRD pattern of coupon 15 of column 2 while no peaks were found on coupon 15 of the other analysed column. Moreover, regarding the immersion rate, coupons in the low tide zone are rarely emerged and seldom submitted to a high dioxygen flow. Though brucite precipitation is possible during the emerged phases because of the high pH and the huge dioxygen flow, it may only form locally in the most aerated parts of the surface and may dissolve subsequently during the longer immersion periods. Then, during the immersion and immersed period, brucite could dissolve and so on and so forth for every emersion / immersion cycle. This mechanism gives an explanation to the scarce detection of  $Mg(OH)_2$  in this case.

Subsequently to these analyses, it is possible to determine the stratification of the mineral layer (cf. Figure III.15). The steel surface is covered by a rather thin layer of corrosion products (magnetite, nanocrystalline mackinawite and green rust) which is overlaid by aragonite and fouling (mainly made of oysters encrusted in the mineral layer as displayed in the photograph enclosed in figure III.15). Some scattered zones of brucite are present under the thick fouling layer (and maybe also as a thin layer between aragonite and corrosion products).

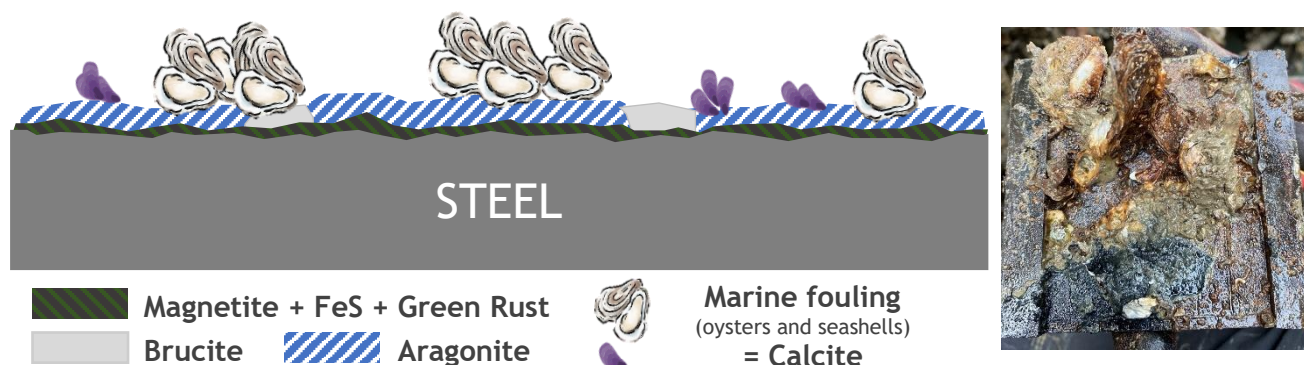


Figure III. 15: Schematic representation and photograph of the corrosion product stratification of the low tide zone

The composition diversity found in this area of the tidal zone is really similar to what was expected from carbon steel samples under CP in constant immersion. It is reasonable to assume that CP is as efficient in this zone as for coupons permanently immersed. This is actually confirmed by the mass/surface ratio measurements. Since the features of the coupons in the low tide zone are comparable to those of a protected sample in constant immersion, this case can indeed be used as the reference to make comparison with the upper zones.

For the **mid tide zone**, XRD results show some slight differences with the low tide zone in the detected compounds. About the similarities, calcite coming from the shells is still one of the main detected compounds as it is well crystallised and the coupons were totally covered with fouling. The other main compound is aragonite, the main component of the calcareous deposit resulting from CP. Magnetite is still the only corrosion product detected via XRD. However, Raman spectroscopy led, as for the coupons of the low tide zone, to the identification of nanocrystalline FeS.

The main difference with the low tide zone is the presence of a higher amount of brucite, clearly detected by XRD in this case and by Raman spectroscopy as well. This is really interesting because of the conditions required for brucite formation, i.e. high dioxygen flow and high pH value [8,9], which are not usually achieved in marine media by coupling carbon steel and Al based galvanic anodes. Yet, as mentioned above, during the emersion phase,  $\text{HO}^-$  production, due to the persistence of a residual protection current, could continuously increase the mineral layer internal pH without any seawater renewal. Then, the exposition to open air of this  $\text{HO}^-$  enriched layer creates favourable conditions for brucite precipitation during the emerged phase. This phenomenon has already been observed in the study about CP in the tidal zone in 2015 by P. Refait et al. [2]. The second difference of interest in these features is the detection of the main diffraction peak of “pyroaurite”.

In this area, Raman analysis confirms the features observed through the XRD pattern. Yet, it also gives additional information. Indeed, iron sulphides have been detected, which was rather unexpected regarding the immersion rate of the analysed coupon, i.e., 47.4%. Coupon 7 is the highest one where nano-crystallised mackinawite was detected. This clearly demonstrates that the dense the mineral layer remains wet in (at least) some areas of the coupon. This information leads to the stratification schema for the mid tide zone presented figure III.16. First, a thin corrosion product layer is in contact with the metal surface. In this case, only magnetite and FeS were identified, but the presence of a small amount of GR cannot be discarded. Actually “pyroaurite” would be really similar to  $\text{GR}(\text{CO}_3^{2-})$  if it contained an important proportion of Fe(II) cations. Secondly, a thick aragonite layer with large spots of brucite tops the corrosion product layer. It is itself covered with a dense fouling layer composed of

oysters, mussels and acorn barnacles as it is shown by the photographs enclosed in figure III.16. The picture on the left shows the “raw” mid tide zone with really few observations of the mineral layer because of the huge density of the fouling layer. The picture on the right displays the exact same zone after removing some oysters in the middle of the coupon (highlighted by the red line), a black layer with some spots of a white veil appears. This is the magnetite layer with traces of brucite as explained above.

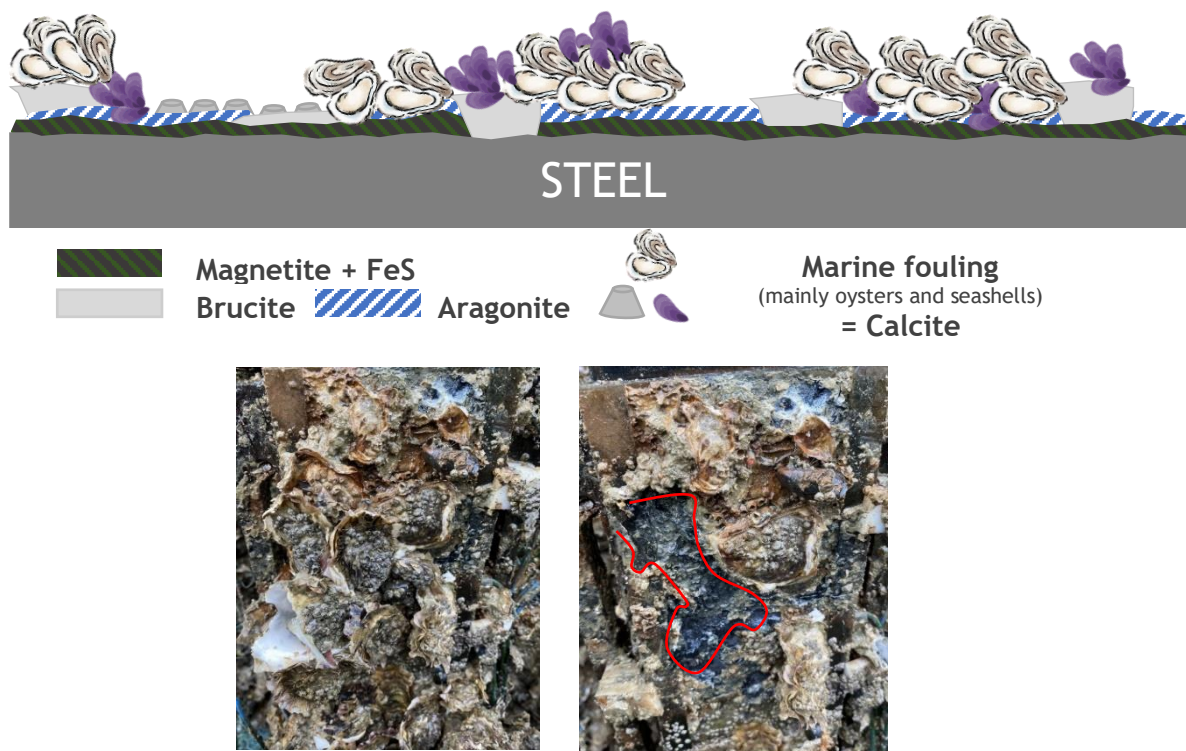


Figure III. 16 : Schematic stratification and representative photographs (before and after removing some oysters) of the mid tide zone

Moreover, the persistent humidity is consistent with the persistence of the CP efficiency up to the mid tide zone and strongly plausible according to the above pictures. Actually, all the observations made in this zone are consistent with a high CP efficiency, including the estimations of corrosion degradation (section III.3). Not only the evident presence of aragonite (and brucite) but also the kind of corrosion products detected testify for the efficiency of CP. As it has been already mentioned, magnetite formation is enhanced by the cyclic immersion and by the increase in interfacial pH. The formation of “pyroaurite”, that is of a hydroxycarbonate, is also due to the increase in interfacial pH. It has for instance been observed that the application of CP to a steel coupon previously covered with sulphate GR, i.e.,  $\text{GR}(\text{SO}_4^{2-})$ , could induce the transformation of  $\text{GR}(\text{SO}_4^{2-})$  to  $\text{GR}(\text{CO}_3^{2-})$  [13]. As for the formation of aragonite, that of a hydroxycarbonate is associated with the increase in interfacial pH via its influence on carbonic equilibrium. When CP is applied on an uncorroded coupon, the iron dissolution is slow and so the Fe(II) production rate is so low that the  $\text{GR}(\text{CO}_3^{2-})$ -like compound that forms also contains Mg(II) cations.

Figure III.11 relates to the ratio m/S (defined in the part III.3.3.1) and shows that this ratio is (on average) similar to that observed in the lower zones, where CP is efficient. Figure III.14 displaying the optical microscopy results about the maximum degradation difference leads to the same conclusion: The efficiency of CP is decreased only for zones located higher than the mid tide zone.

It is consequently reasonable to suppose, from the results and observations made here, that the corrosion protection efficiency seems to be still persistent in the mid tide zone ( $\approx 50\%$  of immersion rate). This is exactly the spread-out CP case presented in the background. The steel surface is emerged but wet, the residual seawater film (or humidity) allows the protection to be still active.

Finally, the **high tide zone** (samples 5 to 3) presents significant differences with the previous zones. The presence of aragonite and brucite indicates that CP is active, when the coupons are immersed and for some time after their emersion. Nevertheless, the presence of large proportions of magnetite and goethite, the last one a corrosion product not present in the lower zones, reveals that a rather active corrosion process took place. The predominance of magnetite is typical of cyclic immersion conditions [2]. Moreover, the combination of magnetite and goethite, without lepidocrocite, is also typical of the cyclic immersion corrosion [2,34] process which is comparable to that of atmospheric corrosion [35-37] as it involves wet/dry cycles. Indeed, during the emersion phases, there is a high  $O_2$  flow which leads to the formation of Fe(III)-oxyhydroxides as the main corrosion products, mainly lepidocrocite ( $\gamma\text{-FeOOH}$ ) and goethite ( $\alpha\text{-FeOOH}$ ). Both compounds can be reduced when the coupon is immersed, due to the cathodic polarization, but goethite is more stable and thus less prone to reduction [38]. Actually, as far as atmospheric corrosion is concerned, goethite is considered as an inactive phase that does not participate to the corrosion process of the metal because of its greater stability while lepidocrocite is active [39], i.e., indeed acts as an oxidant for the metal and is reduced during the wetting stage of the wet/dry cycle. This reduction process can lead to magnetite [35,39], maybe via interactions with  $Fe^{2+}$  ions [40].

Raman analysis confirmed these results but led to the identification of lepidocrocite and akaganeite (figure III.10- plots 4.3 & 4.4). Stratification determined owing to Raman analysis is schematised in figure III.17 with its representative picture of the real high tide zone. Akaganeite is a corrosion product forming only when very rich chloride concentrations, higher than that of seawater, are reached [28]. Here, its scarce detection means that seawater evaporated in some points of the coupon surface, concentrating the salts in the remaining residual humidity. Then, in this  $Cl^-$  enriched medium, akaganeite could form. On the other hand, the detection of lepidocrocite via Raman spectroscopy only suggests a really few amounts of it, which is consistent with the hypothesis of the cyclic immersion corrosion mechanism. Thus, even though CP is efficient part of the time, the main compounds covering the steel surface in this area are corrosion products typical of cyclic immersion. This shows that the protection has a limited efficiency here, letting corrosion mechanisms be active.

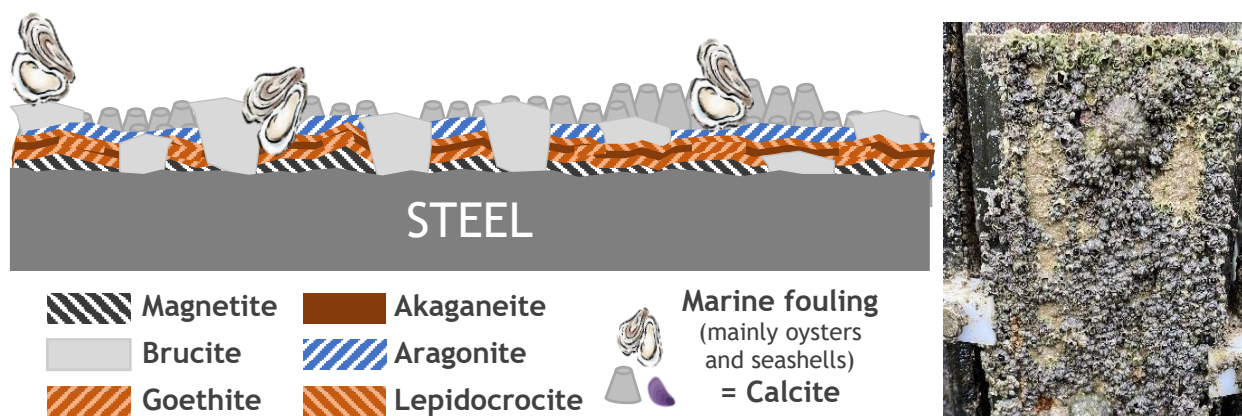


Figure III. 17: Stratification schema and representative photograph of the high tide zone

In the **extreme high tide zone**, magnetite, goethite, akaganeite and lepidocrocite were all detected by XRD. However, aragonite is still a major component of the mineral layer covering the steel surface. As demonstrated in the results (section III.3.3) CP is not totally deactivated in this area as corrosion rate for coupons exposed to free corrosion can reach about  $66 \pm 5 \mu\text{m}/\text{year}$  vs  $19 \mu\text{m}/\text{year}$  in this case. This obviously corroborate the large detection of aragonite.

On the other hand, its presence at this level of the tidal zone could not only come from CP, but might also come from the galvanic coupling occurring under seawater droplets during the corrosion periods. These samples might be exposed to short well protective periods with long-lasting effects and long corrosion periods (during the drying phases). Indeed, the outer annular surface of the droplet where  $\text{O}_2$  is reduced has a strong cathodic character compared to the droplet centre which plays the role of the anode. This local corrosion mechanisms, characteristic of the splash zone, may enhance the aragonite formation.

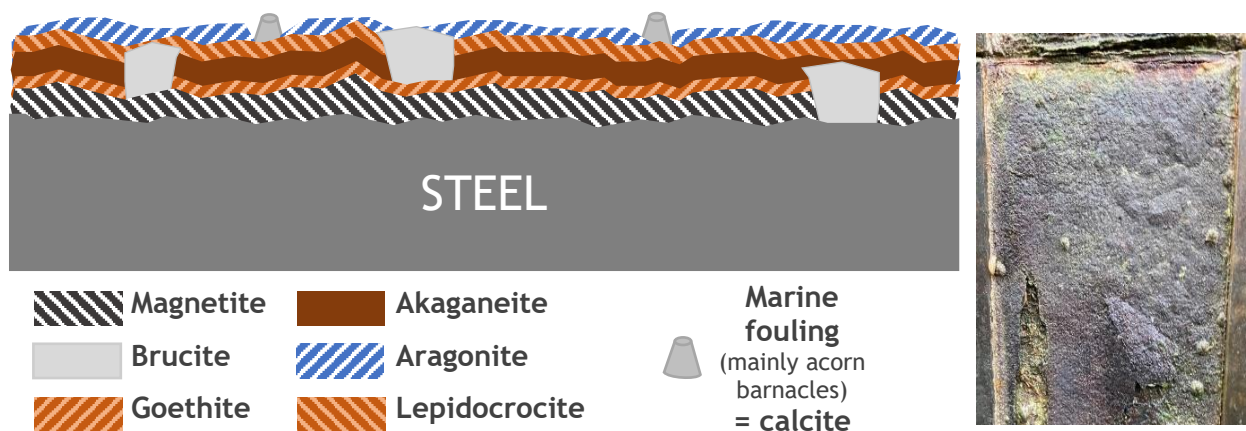


Figure III. 18: Stratification schema and representative photograph of the high tide zone

In this zone, conversely to the high tide zone, each corrosion product is detected on the XRD pattern, and then its presence is confirmed by Raman analysis (stratification schema and picture of the real extreme high tide zone are presented in figure III.18). This means that the amount of corrosion products was even higher. Yet, there is once again the magnetite-goethite combination. As mentioned above akaganeite (widely detected here) is a corrosion product requiring a high chloride concentration to precipitate. This is highly consistent with the droplet corrosion phenomenon reminded in the previous paragraph. As this zone is seldom immersed, it could be considered similar to the splash zone (just above the water level). Droplets are projected onto the surface leading to the formation of akaganeite [41,42]. In addition, the picture displayed above testifies for the low immersion rate with extremely low amount of fouling. This is also consistent with a low capacity to trap residual humidity compared to the mid tide zone or even the high tide zone.

### III.5 Conclusion

The mineral layer composition is varying all along the tidal zone depending on the immersion rate of the considered area. However, corrosion products and components of the calcareous deposit have been detected in any case. In the lower part of the tidal zone (from sample 13 to the bottom) the coupons show features alike carbon steel under CP in constant immersion. In the extreme high tide zone (samples 1 and 2), the situation is comparable to carbon steel exposed in the splash zone. An important and uncommon amount of brucite has been found on the coupons 9 to 4. According to the hypothesis of the CP persistence and the mechanism detailed above and in the chapter 1, brucite could be used as a marker of the spread-out CP mechanism. Yet it could not be used as the only evidence of the CP efficiency. The results obtained in the high tide zone show the presence of both aragonite and brucite even though the protection is not efficient enough to prevent corrosion phenomenon. Another study is necessary to estimate the corrosion rate.

Cross sourcing the results from the nature of the detected compounds and the qualitatively estimated corrosion rate, it is possible to define the CP efficiency up to the mid tide zone. According to this hypothesis, CP could still be efficient up to 45-52% immersion rate, which corresponds to **69-74% of the total height**. The whole structure is 5.88 m long (the sample 1 altitude is 5.88 m) the altitude of the sample 9 is 4.05 m (68.7% of the maximum height) the 6<sup>th</sup> coupon altitude is 4.35 m (74% of the maximum height).

The study and the conclusion made in this chapter are relying on “small” coupons (10 cm x 10 cm) analyses. However, the column was composed of an alternance of 2 or 3 small coupons followed by a long plate of 50 cm x 10 cm. Those long plates have not been studied yet. Consequently, this study does not permit yet to precisely discriminate the transition zone between the protected steel and the unprotected steel since the high tide zone and the mid tide zone are separated by 50 cm (one long plate). The thorough analysis of this long sample should permit to determine the exact position of the transition zone.

Macro-galvanic cells can play an important role and change the structure behaviour, especially on a scale as large as 6 m [5]. The studied structure was made of coupons connected to each other via copper wires (linked to the galvanic anode) but separated from each other by a thin resin layer so that electrochemical measurements could be performed on each coupon separately [2]. This may have induced some bias difficult to evaluate.

Finally, the hypothesis made here was to consider a steel surface under CP covered by a thin seawater film. Even if the seawater film notion must be used here as a first approach to understand the phenomenon because the steel surface is actually covered by fouling and a more or less thick porous mineral layer trapping humidity. Then, it is more precise to talk about residual humidity than residual electrolyte film.

Another problematic arises: “Is the cathodically protected steel behaviour known under thin seawater film? How does the residual humidity and dioxygen flow impact the CP ?” This topic is addressed in the next chapter.

## References

- [1] R. E. Melchers and R. Jeffrey, « Corrosion of long vertical steel strips in the marine tidal zone and implications for ALWC », *Corrosion Science*, vol. 65, p. 26-36, déc. 2012, doi: 10.1016/j.corsci.2012.07.025.
- [2] Ph. Refait, M. Jeannin, R. Sabot, H. Antony, and S. Pineau, « Corrosion and cathodic protection of carbon steel in the tidal zone: Products, mechanisms and kinetics », *Corrosion Science*, vol. 90, p. 375-382, janv. 2015, doi: 10.1016/j.corsci.2014.10.035.
- [3] J. Duboscq, « Corrosion des aciers en milieu marin: processus se déroulant dans les zones cathodiques », Thèse de Doctorat, La Rochelle Université, 2019.
- [4] Y. Yang, J. Scantlebury, and E. Koroleva, « A Study of Calcareous Deposits on Cathodically Protected Mild Steel in Artificial Seawater », *Metals*, vol. 5, n° 1, p. 439-456, mars 2015, doi: 10.3390/met5010439.
- [5] C. Erdogan and G. Swain, « The effect of macro galvanic cells on corrosion impressed current cathodic protection for offshore monopile steel structures », *Ocean Engineering*, vol. 265, n° 112575, p. 7, 2022.
- [6] K. Akamine and I. Kashiki, « Corrosion protection of steel by calcareous electrodeposition in seawater (Part 1) », *Zairyo-to-Kankyo*, vol. 51, p. 496-501, 2002.
- [7] C. Deslouis, D. Festy, O. Gil, V. Maillot, S. Touzain, and B. Tribollet, « Characterization of calcareous deposits in artificial sea water by impedances techniques: 2-deposit of  $Mg(OH)_2$  without  $CaCO_3$  », *Electrochimica Acta*, vol. 45, n° 11, p. 1837-1845, févr. 2000, doi: 10.1016/S0013-4686(99)00403-X.
- [8] Ch. Barchiche, C. Deslouis, D. Festy, O. Gil, Ph. Refait, S. Touzain and B. Tribollet, « Characterization of calcareous deposits in artificial seawater by impedance techniques 3 - Deposit of  $CaCO_3$  in presence of  $Mg(II)$  », *Electrochimica Acta*, vol. 48, n° 12, p. 1645-1654, mai 2003, doi: 10.1016/S0013-4686(03)00075-6.
- [9] K. Akamine and Isamu Kashiki, « Corrosion protection of steel by calcareous electrodeposition in seawater (Part 1) », *Zairyo-to-Kankyo*, vol. 51, p. 496-501, 2002.
- [10] K. Akamine and I. Kashiki, « Corrosion protection of steel by calcareous electrodeposition in seawater (Part 2) », *Zairyo-to-Kankyo*, vol. 52, p. 401-407, 2003.
- [11] S. Touzain, « Etude de la structure des dépôts calco-magnésien formés en présence d'écoulement: application à la protection cathodique en milieu marin », Thèse de Doctorat, La Rochelle Université, 1996.
- [12] A. Zanibellato, « Synthèse et études physico-chimiques d'un agglomérat calcomagnésien formé sur acier en milieu marin : un éco-matériau pour la protection du littoral », Thèse de Doctorat, La Rochelle Université, 2016.
- [13] Ph. Refait, M. Jeannin, R. Sabot, H. Antony, et S. Pineau, « Electrochemical formation and transformation of corrosion products on carbon steel under cathodic protection in seawater », *Corrosion Science*, vol. 71, p. 32-36, juin 2013, doi: 10.1016/j.corsci.2013.01.042.
- [14] M. Jeannin, R. Sabot, H. Antony, S. Pineau, et P. Refait, « Effets des ruptures et reprises de protection cathodique sur la couche de produits de corrosion des aciers en zone de marnage », *Matériaux & Techniques*, vol. 101, n° 5-6, p. 503, 2013, doi: 10.1051/mattech/2013086.
- [15] R. Allmann, « The crystal structure of Pyroaurite », *Acta cryst*, vol. 4, n° 7, p. 972-977, 1968.
- [16] S. H. Drissi, Ph. Refait, M. Abdemoula, et J. M. Génin, « Preparation and thermodynamic properties of  $Fe(II)$ - $Fe(III)$  hydroxyde carbonate (green rust one), Pourbaix diagram of iron carbonate-containing aqueous media », *Corrosion Science*, vol. 37, p. 2025-2041.
- [17] Ph. Refait, M. Abdemoula, F. Trolard, J.M. Génin, J.J. Ehrhardt, et G. Bourrié, « Mössbauer and XAS study of a green rust mineral ; the partial substitution of  $Fe^{2+}$  by  $Mg^{2+}$  », *American Mineralogist*, Vol. 86, p. 731-739, 2001.
- [18] P. Refait, A.-M. Grolleau, et M. Jeannin, « Localized corrosion of carbon steel in marine media: galvanic coupling and heterogeneity of the corrosion product layer », *Corrosion Science*, vol. 111, p. 583-595, 2016.

- [19] Ph. Refait, M. Jeannin, E. François, R. Sabot, et A.-M. Grolleau, « Galvanic corrosion in marine environments: effects associated with the inversion of polarity of Zn / carbon steel couples », *Materials and Corrosion*, vol. 70, p. 950-961, 2019. doi: 10.1002/maco.201810568.
- [20] J.-A. Bourdoiseau, M. Jeannin, R. Sabot, C. Rémaizeilles, et Ph. Refait, « Characterisation of mackinawite by Raman spectroscopy: Effects of crystallisation, drying and oxidation », *Corrosion Science*, vol. 50, n° 11, p. 3247-3255, nov. 2008, doi: 10.1016/j.corsci.2008.08.041.
- [21] D.L.A. De Faria, S.V. Silva, et M.T.D. Oliveira, « Raman micro spectroscopy study of some iron oxides and oxyhydroxides », *Journal of Raman Spectroscopy*, vol. 28, p. 873-878, 1997.
- [22] N. Boucherit, A. Hugot-Le Goff, S. Joiret, « Raman studies of corrosion films grown on Fe and Fe-Mo in pitting conditions », *Corros. Sci.*, vol. 32, p. 497-507, 1991.
- [23] L. Legrand, G. Sagon, S. Lecomte, A. Chaussé, R. Messina, « A Raman and infrared study of a new carbonate green rust obtained by electrochemical way », *Corros. Sci.*, vol. 43, p. 1739-1749, 2001.
- [24] R. Sabot, M. Jeannin, M. Gadouleau, Q. Guo, E. Sicre, Ph. Refait, « Influence of lactate ions on the formation of rust, *Corros. Sci.*, vol. 49, p. 1610-1624 (2007).
- [25] M. Reffass, R. Sabot, C. Savall, M. Jeannin, J. Creus, Ph. Refait, « Localised corrosion of carbon steel in NaHCO<sub>3</sub>/NaCl electrolytes: role of Fe(II)-containing compounds », *Corros. Sci.*, Vol. 48, p. 709-726, 2006.
- [26] Z. Tomic, P. Makreski et Bosko Gajic, « Identification and spectra–structure determination of soil minerals: Raman study supported by IR spectroscopy and X-ray powder diffraction », *J. Raman Spectrosc.*, Vol. 10, p. 582-586, 2010.
- [27] B. Weckler, H.D. Lutz, « Near-infrared spectra of M(OH)Cl (M = Ca, Cd, Sr), Zn(OH)F,  $\gamma$ -Cd(OH)<sub>2</sub>, and brucite-type hydroxides M(OH)<sub>2</sub> (M = Mg, Ca, Mn, Fe, Co, Ni, Cd) », *Spectrochim. Acta Part A*, vol. 52, p. 1507-1513, 1996.
- [28] C. Rémaizeilles et Ph. Refait, « On the formation of  $\beta$ -FeOOH (akaganéite) in chloride-containing environments », *Corrosion Science*, vol. 49, n° 2, p. 844-857, févr. 2007, doi: 10.1016/j.corsci.2006.06.003.
- [29] K. Zakowski, J. Orlikowski, K. Darowicki, M. Czekajlo, P. Iglinski, et K. Domanska, « The Effect of Increasing the Amount of Indium Alloying Material on the Efficiency of Sacrificial Aluminium Anodes », *Materials*, vol. 14, n° 7, p. 1755, avr. 2021, doi: 10.3390/ma14071755.
- [30] Ch. Barchiche, C. Deslouis, O. Gil, S. Joiret, Ph. Refait, B. Tribollet, « Role of sulphate ions on the formation of calcareous deposits on steel in artificial seawater: the formation of Green Rust compounds during cathodic protection », *Electrochimica Acta*, vol. 54, p. 3580-3588, 2009.
- [31] D. D. Nguyen *et al.*, « Role of Brucite Dissolution in Calcium Carbonate Precipitation from Artificial and Natural Seawaters », *Crystal Growth & Design*, vol. 17, n° 4, p. 1502-1513, avr. 2017, doi: 10.1021/acs.cgd.6b01305.
- [32] R. Grinon-Echaniz, S. Paul, R. Thornton, Ph. Refait, M. Jeannin, R. Sabot, « Study of cathodic reaction in defects of thermal spray aluminium (TSA) coatings on steel in artificial seawater », *Corrosion Science*, Vol. 187, art. 109514, 2021, doi: 10.1016/j.corsci.2021.109514
- [33] J. -F. Yan, R. E. White, et R. B. Griffin, « Parametric Studies of the Formation of Calcareous Deposits on Cathodically Protected Steel in Seawater », *J. Electrochem. Soc.*, vol. 140, n° 5, p. 1275-1280, mai 1993, doi: 10.1149/1.2220970.
- [34] P. Refait, S. Pineau, R. Sabot, H. Antony, et M. Jeannin, « Mécanismes de la corrosion des aciers au carbone en zone de marnage », *Matériaux & Techniques*, vol. 101, n° 5-6, p. 501, 2013, doi: 10.1051/mattech/2013084.
- [35] R. Stratmann et K. Hoffmann, « In situ Mossbauer spectroscopic study of reaction within the rust layers », *Corrosion Science*, vol. 29, n° 11/12, p. 1329-1352, 1989.
- [36] A. Cox et S.B. Lyon, « An electrochemical study of the atmospheric corrosion of iron-II. Cathodic and anodic processes on uncorroded and pre-corroded iron », *Corrosion Science*, Vol. 36, p. 1177-1192, 1994.

- [37] J.A. Jaen, M. Sanchez de Villalaz, L. de Araque, et A. de Bosquez, « Kinetics and structural studies of the atmospheric corrosion of carbon steels in Panama, *Hyperfine Interactions* », Vol. 110, p. 93-99, 1997.
- [38] V. Lair, H. Antony, L. Legrand, et A. Chaussé, « Electrochemical reduction of ferric corrosion products and evaluation of galvanic coupling with iron », *Corrosion Science*, Vol. 48, p. 2050-2063, 2006.
- [39] M. Yamashita, M. Miyuki, Y. Matsuda, H. Nagano, et T. Misawa, « The long term growth of the protective rust layer formed on weathering steel by atmospheric corrosion during a quarter of century », *Corrosion Science*, Vol. 36, p. 283-299, 1994.
- [40] Wenjing Yan, Jinming Zhou, Hui Liu, Rufen Chen, Yanfeng Zhang, et Yu Wei, « Formation of Goethite and Magnetite Rust via Reaction with Fe(II), *Journal of The Electrochemical Society* », Vol. 163, p. C289-C295, 2016.
- [41] M. Morcillo, J. Alcántara, I. Díaz, B. Chico, J. Simancas, et D. De la Fuente, « Marine atmospheric corrosion of carbon steels », *REVMETAL*, vol. 51, n° 2, p. e045, juin 2015, doi: 10.3989/revmetalm.045.
- [42] M. Morcillo, B. Chico, J. Alcántara, I. Díaz, J. Simancas, et D. de la Fuente, « Atmospheric corrosion of mild steel in chloride-rich environments. Questions to be answered: Marine atmospheric corrosion of mild steel », *Materials and Corrosion*, vol. 66, n° 9, p. 882-892, sept. 2015, doi: 10.1002/maco.201407940.





*Chapter IV: Cathodic Protection of Carbon Steel  
in Thin Layers of Seawater*



## Introduction:

The study of cathodic protection beneath a thin layer of seawater presents a complex experimental challenge. To our knowledge, scarce experimental researches on corrosion under a thin electrolyte film were led due to the technical difficulties involved. Investigating CP under such conditions, where seawater thickness is minimal, is even rarer due to the increased complexity. Achieving this requires both creating a water film on the steel surface, and conducting electrochemical measurements within it.

To visualize the situation, it is necessary to imagine the current lines reaching the anode through the electrolyte (as shown in Figure I.5 of chapter I, reported below). In the case of a galvanic coupling under an infinitely thick electrolyte layer (Figure I.5-a), current lines can freely access any part of the surface. However, with a finite electrolyte film, the paths of current lines can be restricted by the space under the electrolyte layer (Figure I.5-b). This interference leads to current lines affecting each other's paths. As the film thickness decreases, the galvanic current lines become more concentrated close to the cathode/anode junction. Consequently, this phenomenon restricts the total current within the system. [1]

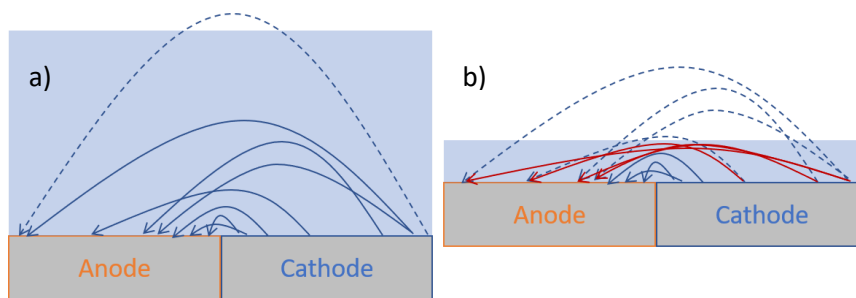


Figure I.5: Two-dimension schematic representation of the galvanic current lines reaching the anode through – a) an infinite electrolyte layer – b) a finite electrolyte layer

However, the consideration of parameters extends beyond this single factor. In 1966, Thomashov (cited in [2]) introduced a model describing the relationship between corrosion rate and electrolyte layer thickness. This model considered water films thinner than the oxygen diffusion layer. As the diffusion layer thickness (or electrolyte thickness) decreases, the corrosion rate peaks at the thickness where the shift from cathodic control to anodic control occurs. In their study based on Tomashov's theory, Liu et al. conducted a study in 2014, demonstrating that the diffusion layer of dissolved oxygen spans around 500  $\mu\text{m}$ , and the reaction transition happens at approximately 40  $\mu\text{m}$  [2]. This aligns with the predictive model proposed in [3], which defines a critical thickness range of 1 to 100  $\mu\text{m}$  based on factors like electrode size, electrolyte conductivity, and anodic kinetics (such as zinc oxidation in this case). When the water thickness decreases, the current lines are more and more "close to each other" ([1], [4]). There is then direct competition with the local increase in corrosion intensity and as the thickness decreases, the current and potential gradient become steeper and steeper. Yet, as long as the critical thickness is not reached, the electrolyte resistance does not increase enough to limit the coupling and decrease the corrosion rate. In 2007, Yadav et al. proved that even under a 10  $\mu\text{m}$  thick film the protection provided by the zinc could operate over 9 mm from the coupling point [5].

Within the tidal zone, where water recedes, a residual film remains on the steel surface, potentially maintaining continuity with seawater [6], [7]. However, all the studies reported here focused on coplanar electrodes. For a CP setup in the tidal zone, the anode resides in the low water zone, which is notably distant from the structure requiring protection. In addition, the studies quoted above were

all interested in the corrosion mechanism under a thin film proposed by Tomashov and have shown that the corrosion rate increases up to a maximum when the water film thickness is comparable or lower to the oxygen diffusion layer ([2], [3], [8], [9]). While discrepancies exist in the precise thickness values among these studies, they concur that beyond 1 mm thickness, marginal differences persist in the corrosion rates (or currents) for higher thicknesses (or immersion depths) of water.

Complementary works focused on the practical part of this problem: how to create a seawater film and control its thickness on a metal electrode?

In 2014 Palani et al. applied the pellicular condensation theory developed by Nusselt in 1916 to recreate a homogeneous film (as schematised Figure IV.1 – a) [10]. Basic principle of this theory consists in condensing a film, from a mist of the electrolyte on an isothermal and vertical surface. Droplets form on top of the plate and flow along it because of gravity. However, many conditions must be met before such a system can be implemented:

- Mist temperature must homogenous
- Only gravity must influence the droplets flow
- The electrolyte must be homogeneous (no property variations)
- There must be no disturbance or convective movements in the mist, so as not to exert any force on the film flow.

This method, valid for vertical samples, also works for inclined planes as long as the inclination angle allows permanent drainage of the electrolyte film (schematised figure IV.1 – b). Based on this theory, the film thickness can be calculated as follows according to Nusselt theory [10]:

$$\delta = \left\{ \frac{4\mu_L k_L z (T_{sat} - T_w)}{\rho_L (\rho_L - \rho_G) g \sin(\alpha) h_{LG}} \right\}^{1/4}$$

With:

- $\mu_L$ : liquid electrolyte viscosity ( $\text{kg m}^{-1} \text{s}^{-1}$ )
- $k_L$ : thermal conductivity of liquid electrolyte ( $\text{W m}^{-1}$ )
- $T_{sat}$ : saturated pressure temperature ( $^{\circ}\text{C}$ )
- $T_w$ : plate temperature ( $^{\circ}\text{C}$ )
- $\rho_L$ : liquid electrolyte density ( $\text{kg m}^{-3}$ )
- $\rho_G$ : gas density ( $\text{kg m}^{-3}$ )
- $h_{LG}$ : latent heat ( $\text{kJ kg}^{-1}$ )
- $z$ : z coordinate from the top of the plate (m)
- $g$ : gravity acceleration ( $\text{m}^2 \text{s}^{-1}$ )
- $\alpha$ : inclination angle

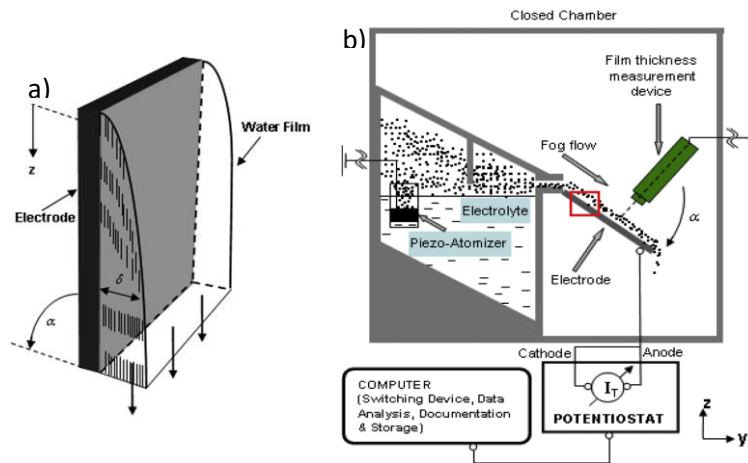


Figure V. 1 : Creation of a thin electrolyte film – a) Schematisation of the Nusselt's theory principle – b) Experimental set up for creating an electrolytic film on inclined surface

In [10], Palani *et al.* validated this experimental approach and obtained results consistent with the study of Liu *et al.* They observed a current peak for a 40  $\mu\text{m}$  thick film (NaCl 0.6 mol/L) [2]. However, in this paper no clue about the film thickness measurement was given. To our knowledge, really few studies display explanation on the method to create thin electrolytic film with a 10  $\mu\text{m}$  precision. The method to accurately measure such a film is even less often explained. In addition, the described method requires a lot of technical means and a whole study to find out and then validate a reliable method to measure film thickness. On the other hand, as seen in the previous chapter, the residual film concept used to qualify the phenomenon occurring on carbon steel under CP during ebb tide is skewed by the presence of a thick fouling layer on the metal surface. Subsequently, it has finally been chosen to study the protected steel behaviour under thin layers of electrolyte, i.e., with seawater thickness larger than 500  $\mu\text{m}$ .

Furthermore, Refait *et al.* in 2015 studied cathodic protection on carbon steel in le Havre seaport. They found that at low tide, the potential of the studied coupons reached -750 mV/Ag/AgCl<sub>3M</sub> while the potential of the same coupons reached -950 mV/Ag/AgCl<sub>3M</sub> during the immersed period (as shown in figure IV.3, an alternate version of the figure displayed in their publication) [6]. Not only this highlights the CP persistence but it also means that during ebb tide, the potential of coupons goes from -950 mV/Ag/AgCl<sub>3M</sub> to -750 mV/Ag/AgCl<sub>3M</sub> while they are only covered with the so-called residual humidity.

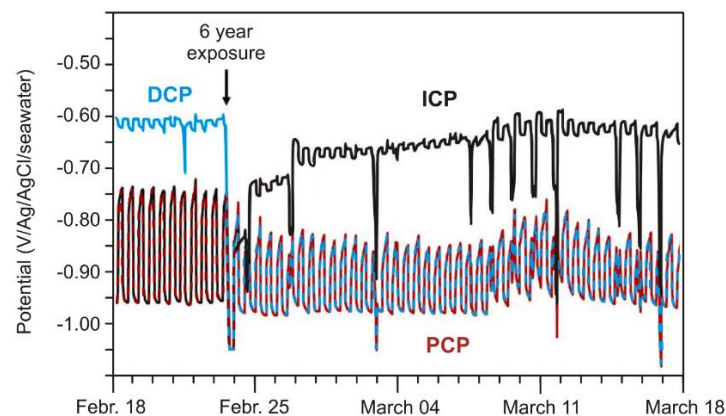


Figure IV. 1: "Potential vs. time curves of coupons under cathodic protection in the tidal zone. Evolution between 02/18/2010 and 03/18/2010" [6]

Consequently, this chapter is focusing on the comparison between the behaviour of well protected steel ( $E_{CP} = -950$  mV/Ag/AgCl<sub>3M</sub>) and the behaviour of insufficiently protected steel ( $E_{CP} = -750$  mV/Ag/AgCl<sub>3M</sub>) under 1 mm and 5 mm of seawater.

This study led to the article reported thereafter, published in *Anti-Corrosion Methods and Materials* (doi: [10.1108/ACMM-05-2023-2811](https://doi.org/10.1108/ACMM-05-2023-2811)).

The results obtained in this chapter are also further commented, together with those obtained in chapter 3, in the introduction to chapter 5.

## References

- [1] R. Morris et W. Smyrl, « Current and Potential Distribution in Thin Electrolyte Layer Galvanic Cells », *J. Electrochem. Soc.*, vol. 136, n° 11, p. 3229-3236, nov. 1989, doi: [10.1149/1.2096430](https://doi.org/10.1149/1.2096430).
- [2] Z. Liu *et al.*, « Study of corrosion behavior of carbon steel under seawater film using the wire beam electrode method », *Corrosion Science*, vol. 80, p. 523-527, mars 2014, doi: [10.1016/j.corsci.2013.11.012](https://doi.org/10.1016/j.corsci.2013.11.012).
- [3] F. Thébault, B. Vuillemin, R. Oltra, C. Allely, et K. Ogle, « Modeling bimetallic corrosion under thin electrolyte films », *Corrosion Science*, vol. 53, n° 1, p. 201-207, janv. 2011, doi: [10.1016/j.corsci.2010.09.010](https://doi.org/10.1016/j.corsci.2010.09.010).
- [4] J. T. Warer, « Mathematical Studies on Galvanic Corrosion », *J. Electrochem*, vol. 103, p. 64-72, 1956.
- [5] A. P. Yadav, H. Katayama, K. Noda, H. Masuda, A. Nishikata, et T. Tsuru, « Surface potential distribution over a zinc/steel galvanic couple corroding under thin layer of electrolyte », *Electrochimica Acta*, vol. 52, n° 9, p. 3121-3129, févr. 2007, doi: [10.1016/j.electacta.2006.09.061](https://doi.org/10.1016/j.electacta.2006.09.061).
- [6] Ph. Refait, M. Jeannin, R. Sabot, H. Antony, et S. Pineau, « Corrosion and cathodic protection of carbon steel in the tidal zone: Products, mechanisms and kinetics », *Corrosion Science*, vol. 90, p. 375-382, janv. 2015, doi: [10.1016/j.corsci.2014.10.035](https://doi.org/10.1016/j.corsci.2014.10.035).
- [7] D. W. Law, P. Nicholls, et C. Christodoulou, « Residual protection of steel following suspension of Impressed Current Cathodic Protection system on a wharf structure », *Construction and Building Materials*, vol. 210, p. 48-55, juin 2019, doi: [10.1016/j.conbuildmat.2019.03.135](https://doi.org/10.1016/j.conbuildmat.2019.03.135).
- [8] T. Tsuru, A. Nishikata, et J. Wang, « Electrochemical studies on corrosion under a water film », *Materials Science and Engineering: A*, vol. 198, n° 1-2, p. 161-168, juill. 1995, doi: [10.1016/0921-5093\(95\)80071-2](https://doi.org/10.1016/0921-5093(95)80071-2).
- [9] M. Yamashita, H. Nagano, et R. A. Oriani, « Dependence of corrosion potential and corrosion rate of a low-alloy steel upon depth of aqueous solution », *Corrosion Science*, vol. 40, n° 9, p. 1447-1453, sept. 1998, doi: [10.1016/S0010-938X\(98\)00041-9](https://doi.org/10.1016/S0010-938X(98)00041-9).
- [10] S. Palani, T. Hack, J. Deconinck, et H. Lohner, « Validation of predictive model for galvanic corrosion under thin electrolyte layers: An application to aluminium 2024-CFRP material combination », *Corrosion Science*, vol. 78, p. 89-100, janv. 2014, doi: [10.1016/j.corsci.2013.09.003](https://doi.org/10.1016/j.corsci.2013.09.003).

## Cathodic protection of carbon steel in thin layers of seawater

*Clément Genin<sup>1,2</sup>, Marc Jeannin<sup>1</sup>, Anne-Marie Grolleau<sup>2</sup> and Philippe Refait<sup>1</sup>*

(1) Laboratoire des Sciences de l'Ingénieur pour l'Environnement (LaSIE), UMR 7356 CNRS-La Rochelle Université, La Rochelle, France.

[clement.genin@univ-lr.fr](mailto:clement.genin@univ-lr.fr); [marc.jeannin@univ-lr.fr](mailto:marc.jeannin@univ-lr.fr); [philippe.refait@univ-lr.fr](mailto:philippe.refait@univ-lr.fr)

(2) Naval Group, CESMAN/CM(TTCM), Marine Corrosion & Cathodic Protection Department, Cherbourg-en-Cotentin, France.

[anne-marie.grolleau@naval-group.com](mailto:anne-marie.grolleau@naval-group.com)

### **Abstract**

**Purpose** – The purpose of this study was to investigate cathodic protection efficiency in the tidal zone and its associated processes.

**Design/methodology/approach** – Specific features of cathodic protection in the tidal zone, that is persistence of a thin seawater film and insufficient cathodic potential due to ohmic drop, were addressed. In this preliminary study, carbon steel electrodes were polarized at two cathodic potentials (correct or insufficient protection) while immersed in 1 mm or 5 mm thick natural seawater layers. After CP interruption, the protective ability of the layers covering the steel electrodes was studied using various electrochemical methods, including electrochemical impedance spectroscopy. The layers were characterized by XRD.

**Findings** – The protective ability of calcareous deposits was increased in thin seawater films. Insufficient cathodic protection could promote protective aragonite/corrosion products layer.

**Originality** – The combined effects of thin seawater film and applied potential was never addressed and the conclusions drawn from this preliminary study give new insight on the efficiency of cathodic protection in the tidal zone.

**Keywords** Cathodic protection, thin natural seawater films, calcareous deposit, tidal zone, EIS

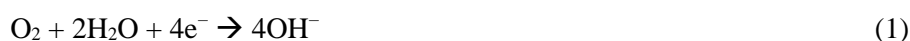
**Paper type** Research paper

## 1. Introduction

Carbon steel is commonly used for marine structures, e.g., sheet piling, pipelines, marine renewable energy (MRE) devices, ships, etc. In most cases, steel is protected against corrosion with various methods, e.g., cathodic protection, organic or galvanic metallic coatings. Cathodic protection (CP) is an efficient method as far as immersed structures are concerned because the CP current must flow through a continuous electrolyte between the protected steel and the anode of the CP system. In the tidal zone, CP can also be efficient because of the persistence of a thin seawater film on the steel surface at low tide (Refait *et al.*, 2015). However, the resistance  $R$  of a thin layer of seawater may be important, leading to significant ohmic drop ( $\Delta E = RI$ , with  $I$  the CP current) so that the actual potential  $E$  of the protected structure may be lower than required and the CP level insufficient for full protection. In the previous study (Refait *et al.*, 2015), the potential measured at low tide, when the protected steel surface was emerged, was 200 mV higher than the potential measured at high tide when steel was immersed.

Similarly, MRE devices such as ocean current turbines involve carbon steel structures with inner channels of small dimension where seawater flows. The efficiency of CP inside such channels is then questionable, but may be finally ensured owing to the formation of a calcareous deposit (Refait *et al.*, 2022). This deposit constitutes a physical barrier against  $O_2$  diffusion so that the current density required for CP decreases with time, which decreases the ohmic drop taking place in thin film (small section) of electrolyte.

The formation of the calcareous deposit results from the increase in interfacial pH due to the increase in cathodic reaction rate, a direct consequence of CP. The main reaction involved is the reduction of dissolved  $O_2$ , which produces  $OH^-$  ions:



The increase in pH modifies the inorganic carbonic equilibrium at the steel/seawater interface, leading to the precipitation of  $CaCO_3$  on the steel surface (Humble, 1948; Wolfson and Hartt, 1981, Mantel *et al.* 1990, Yan *et al.*, 1993; Barchiche *et al.*, 2003):



To our better knowledge, the topic of CP and calcareous deposition on steel surfaces covered with thin layers of seawater has rarely been addressed. However, information is needed, in particular with respect to CP of steel structures located in the tidal zone (seaport sheet piles, off-shore wind turbines, etc.). To address this problem, steel electrodes were set horizontally in 1 mm or 5 mm of seawater, and polarized cathodically for 6 to 28 days, depending on the applied potential. The growth of the calcareous deposit was monitored by chronoamperometry. The corrosion behaviour of the steel electrodes covered with

calcareous deposit was studied, after interruption of CP, by linear polarization resistance (LPR) measurements, electrochemical impedance spectroscopy (EIS) and voltammetry. The deposits were characterized by X-ray diffraction (XRD).

## 2. Materials and methods

### 2.1. Material, electrolyte and electrodes preparation

The material studied was carbon steel EN 10248-1 used for the manufacture of seaport sheet piles. The nominal composition is (in wt.%)  $C \leq 0.27$ ;  $Si \leq 0.6$ ;  $Mn \leq 1.7$ ;  $Al = 0.02$ ;  $S \leq 0.055$ ;  $P \leq 0.055$  and Fe (bal.). The electrodes were made from 5 cm long, 2 cm wide and 1 cm thick steel plates. A copper wire was welded to one side of the plate to ensure connection with the potentiostat. The plate was then embedded in epoxy resin so that the weld could not be in contact with seawater and only one face was exposed to seawater (active area =  $2 \text{ cm} \times 5 \text{ cm} = 10 \text{ cm}^2$ ). This face was finally abraded with SiC papers up to grade 320 to obtain a roughness typical of industrial structures.

The electrolyte used for all experiments was natural seawater, sampled from the Atlantic Ocean near La Rochelle (France). The average concentrations of the main ionic species were:  $[Cl^-] = 19 \text{ g kg}^{-1}$ ,  $[SO_4^{2-}] = 2.8 \text{ g kg}^{-1}$ ,  $[HCO_3^-] = 0.14 \text{ g kg}^{-1}$ ,  $[Na^+] = 10 \text{ g kg}^{-1}$ ,  $[Mg^{2+}] = 1.29 \text{ g kg}^{-1}$ ,  $[Ca^{2+}] = 0.4 \text{ g kg}^{-1}$  and  $[K^+] = 0.4 \text{ g kg}^{-1}$ . The pH was  $8.1 \pm 0.1$  at room temperature (RT), i.e.  $21 \pm 2^\circ\text{C}$ . All experiments were carried out at RT in triplicate. The presented experiments are representative of the average observed trends.

### 2.2. Electrochemical setup

The main concern was to maintain a constant thickness of water over the electrode surface and a specific experimental setup had to be designed (Figure 1).

For each experiment, 20 L of seawater were used, set in two 10 L glass tanks. The main tank was used to immerse the electrodes, the secondary tank (not represented in Figure 1) was used as a reservoir. The electrodes were placed on a 3D-printed sample holder equipped with 4 Teflon screws lying on the walls of the main tank so that the electrode surface could be set parallel to the seawater/air interface and the thickness of the seawater layer fixed at the desired value, i.e., 1 mm or 5 mm. To avoid changes of water film thickness because of water evaporation, the seawater level was kept constant by an overflow system, associated with an aquarium pump placed in the secondary tank to refill continuously the main tank. The seawater input was set at the bottom of the main tank so that water was not stirred and moved slowly and regularly above the electrodes.

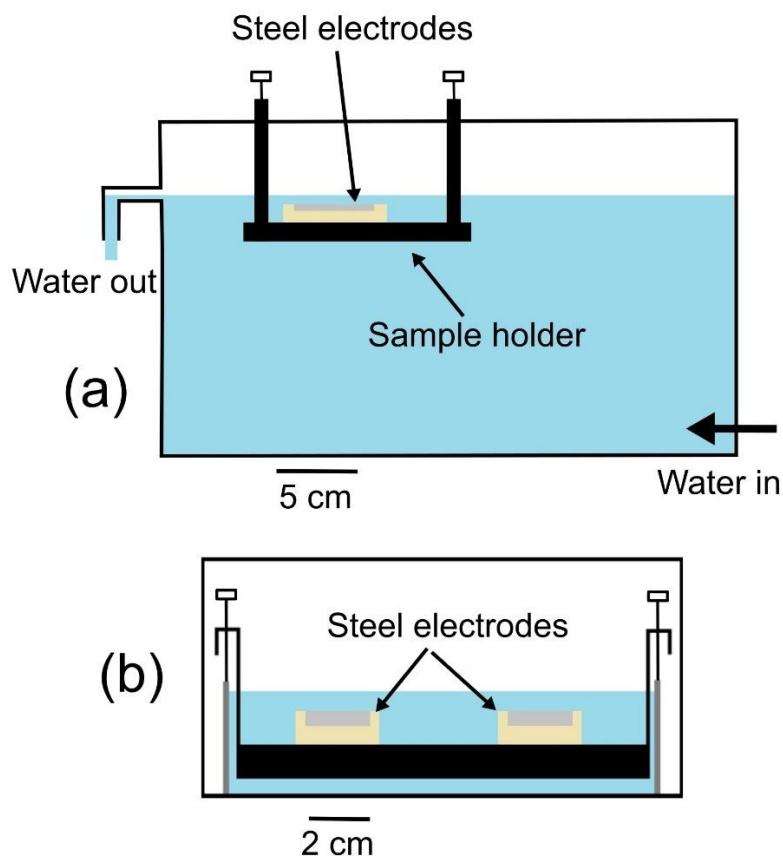


**Figure 1** Experimental setup

### 2.3. Electrochemical measurements

All electrochemical measurements were performed with a Bio-Logic VSP potentiostat using an Ag-AgCl-3M reference electrode ( $E = +0.210$  V vs SHE at  $25^{\circ}\text{C}$ ) and a titanium grid as counter electrode. CP was applied at a constant potential  $E_{\text{CP}}$  equal to  $-950$  mV/<sub>Ag-AgCl-3M</sub> (correct CP) or  $-750$  mV/<sub>Ag-AgCl-3M</sub> (insufficient CP). Note that the relevant standards consider that CP is correctly applied when  $E_{\text{CP}} \leq -800$  mV/<sub>Ag-AgCl-seawater</sub> (i.e.,  $-760$  mV/<sub>Ag-AgCl-3M</sub>) in aerobic conditions (BS EN 12473:2014). Once the cathodic protection current was stabilized, CP was interrupted and the open circuit potential (OCP) was monitored for 3 hours. The electrochemical behavior of the steel electrode was then studied using successively 3 methods: LPR measurements, EIS, and voltammetry. The electrodes were left at OCP for 15 minutes between each method.

For LPR measurements, the potential was swept from OCP to OCP+15 mV, then down to OCP-15 mV, with  $dE/dt = 0.1$  mV  $\text{s}^{-1}$ . The polarization resistance  $R_p$  was determined via a linear fitting of the obtained polarization curve  $E(j)$  around  $j = 0$ . The error was less than 5% of the computed  $R_p$  value. For EIS, the frequency was varied from 100 kHz to 10 mHz with ten points per decade and the AC voltage perturbation amplitude was  $\pm 10$  mV/OCP. The obtained data were modelled using

equivalent electrical circuits (EEC) with the EC-Lab software (Bio-Logic). For voltammetry, the potential was decreased from OCP down to the previously applied  $E_{CP}$  and increased up to OCP+150 mV, with  $dE/dt = 0.15 \text{ mV s}^{-1}$ .

For comparison, LPR measurements and voltammetry experiments were also carried out on unprotected steel electrodes left 3 hours at OCP.

## 2.4. XRD analysis

The phase composition of the layers covering each coupon after the experiment was determined by XRD using an Inel EQUINOX 6000 diffractometer equipped with a curved detector (CPS-590;  $2\theta$  range from  $0^\circ$  to  $90^\circ$ ), with Co-K $\alpha$  radiation ( $\lambda = 0.17903 \text{ nm}$ ). The acquisition was made with a constant angle of incidence ( $10^\circ$ ) during 45 minutes. Three areas ( $1 \text{ cm} \times 1 \text{ cm}$ ) of each electrode were analyzed to check the homogeneity of the mineral layer covering the surface ( $5 \text{ cm} \times 2 \text{ cm}$ ). The various phases were identified via the ICDD-JCPDS database using files 01-075-2230 (aragonite, i.e.,  $\text{CaCO}_3$ ), 03-065-4899 ( $\alpha$ -Fe) and 01-071-1663 (magnesian calcite with 10% Mg, i.e.,  $\text{Mg}_{0.1}\text{Ca}_{0.9}\text{CO}_3$ ).

## 3. Results

The various experiments were denoted with a letter and a number. The letter corresponds to CP conditions with “p” for  $E_{CP} = -950 \text{ mV}/_{\text{Ag-AgCl-3M}}$ , “i” for  $-750 \text{ mV}/_{\text{Ag-AgCl-3M}}$ , and “u” for the unprotected electrodes. The number corresponds to the water layer thickness. For instance, p1 corresponds to the experiment performed with 1 mm of seawater at  $E_{CP} = -950 \text{ mV}/_{\text{Ag-AgCl-3M}}$ .

### 3.1. Cathodic polarization and evolution of OCP during depolarization

Figure 2 displays the evolution of CP current over time (a) and that of OCP after the interruption of CP (b). The decrease in CP current (in absolute value) is displayed as the evolution of the ratio,  $I/I_0$ , of the current  $I$  at a given time  $t$  to the current  $I_0$  measured at the beginning of the polarization. In any case,  $I/I_0$  decreases with time, which is usually attributed to calcareous deposition (Humble, 1948; Wolfson and Hartt, 1981). For  $E_{CP} = -950 \text{ mV}/_{\text{Ag-AgCl-3M}}$ , the decrease is much faster, due to the stronger cathodic polarization (Yan *et al.*, 1993). The minimum ( $I/I_0 \sim 0.08$ ) is reached after 1-2 days and varies only slightly afterwards. For  $E_{CP} = -750 \text{ mV}/_{\text{Ag-AgCl-3M}}$ , the initial decrease in current is similar but the current stabilizes after 1 day, before decreasing again more slowly after 6 days (i5) or 4 days (i1).  $I/I_0$  actually reached a minimum after 12-15 days (not represented) that was slightly higher (average 0.15) than the minimum observed for  $E_{CP} = -950 \text{ mV}/_{\text{Ag-AgCl-3M}}$ . CP was then interrupted after 6 days for p1 and p5 experiments, after 28 days for i1 and i5.

At both applied potentials, the decrease in current is delayed for the experiments carried out in 1 mm of seawater (i1 and p1). However, the same  $I/I_0$  ratios were finally reached whatever the water thickness, after 2 days for p1 and p5 and after 9 days for i1 and i5.

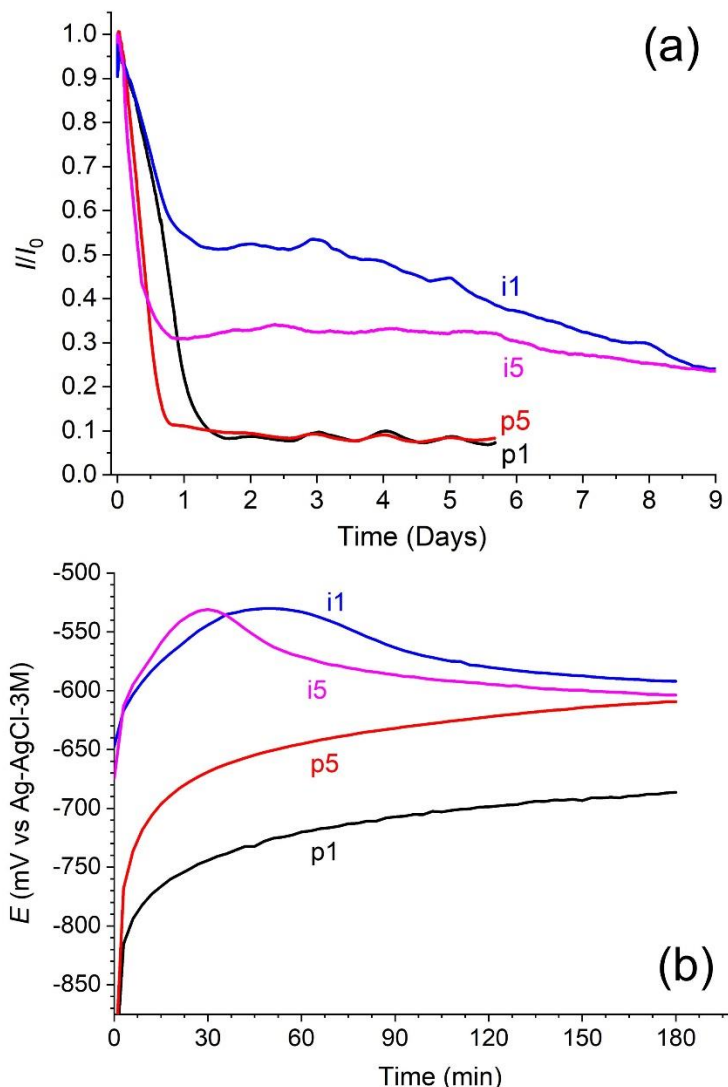


**Figure 2** Chronoamperometric curves during formation of deposits (a) and OCP vs time curves obtained after interruption of CP (b).

When CP is interrupted, the potential increases. The evolution over time of OCP (Figure 2b) shows that the changes are faster in 5 mm of water. For i1 and i5, OCP first increases up to  $-530 \text{ mV}/_{\text{Ag-AgCl-3M}}$ , before decreasing slightly down to  $-600 \text{ mV}/_{\text{Ag-AgCl-3M}}$ . Actually, various phenomena occur during depolarization. First, the charges accumulated at the steel/solution interface decrease, a process similar to the discharge of an electric capacitor. The migration of  $\text{OH}^-$  ions from the surface moreover induces a decrease in pH. The slower rate of cathodic reaction should also lead to an increase in  $\text{O}_2$  concentration at the vicinity of the electrode. Such “re-aeration” of the interface should be more rapid for i1 and i5, because the  $\text{O}_2$  consumption rate during previous CP was smaller, and could then

have led to the observed “pulse” of OCP. The following decrease and stabilization of OCP would correspond to the resumption of the corrosion reactions, leading to a decrease in  $O_2$  concentration.

### 3.2. Electrochemical measurements after depolarization

The polarization curves obtained at the end of each experiment are compared in Figure 3 with those obtained with bare steel electrodes (u1 and u5). In any case, the current density is lower (about 1 order of magnitude) in both anodic and cathodic regions for the electrodes previously polarized and thus covered with a calcareous deposit. This is a clear illustration of the beneficial effect of the deposit, which blocks most of the steel surface. It is also consistent with the final  $I/I_0$  values, that were around 0.1 in any case (0.08 and 0.15, section 3.1).

The polarization curves were acquired starting from OCP and going in the cathodic direction to the previously applied  $E_{CP}$ . This procedure revealed a hysteresis effect, as displayed for p1 and i1. After reversal of potential scanning, the cathodic current is decreased and the corrosion potential  $E_{cor}$  is then lower than the initial OCP. The effect is more important for p1, i.e., when the potential is decreased to -950 mV/Ag-AgCl-3M. It may be attributed to the decrease in dissolved  $O_2$  concentration close to the steel surface because of accelerated cathodic reaction rate. The important hysteresis effect indicates that the transport of  $O_2$  molecules from bulk electrolyte to steel surface is hindered by the layer covering the surface.

It can also be noted that the slope of the anodic branch of the curves is the smallest for p1 and p5 and the highest for i1 and i5.

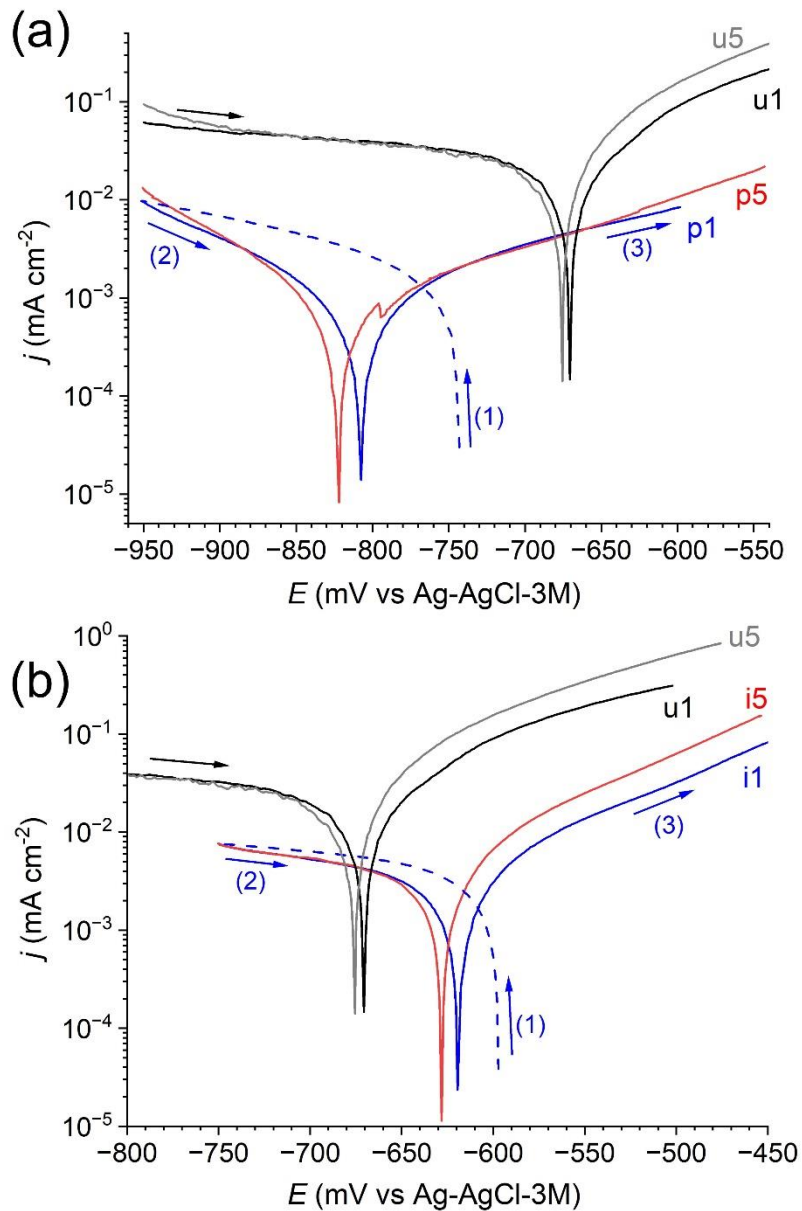


**Figure 3** Polarization curves obtained after CP and 3 hours at OCP for p1 and p5 (a) and i1 and i5 experiments (b). The curves are compared in each case to those obtained with bare steel electrodes left 3 hours at OCP (u1 and u5).

$R_p$  values were measured between 3700 and 15000  $\Omega$  cm<sup>2</sup> (Table 1). In similar conditions, after 1-4 weeks in seawater,  $R_p$  values were measured between 1500 and 2500  $\Omega$  cm<sup>2</sup> for unprotected carbon steel coupons (Refait *et al.*, 2019). LPR measurements thus confirm the protective ability of the calcareous deposit. The highest values are obtained for p1 and i1, showing a beneficial influence of the thinner seawater layer. The  $R_p$  values obtained for p5 and i5 are similar, i.e., the insufficient CP level promoted in this case the formation of a layer as protective as that obtained at a correct CP level. In contrast, the protective ability is significantly higher for p1 if compared to i1, which reveals a synergistic effect between CP level and seawater layer thickness.

**Table 1.** Electrochemical parameters after CP and 3 hours at OCP:  $R_p$  determined from LPR measurements and EIS parameters ( $R_e$ ,  $R_f$ ,  $R_{ct}$ ,  $Q_{dl}$ ,  $Q_f$ ,  $\sigma$ ,  $R_d$  and  $t_d$ ) obtained via modelling with EEC (see figure 4). See text for the description of the EIS parameters.

<b>Experimental conditions: <math>E_{CP}</math> (mV/Ag-AgCl-3M); layer thickness (mm)</b>				
<b>Electrochemical parameters</b>	<b>-950 mV; 5 mm (p5)</b>	<b>-950 mV; 1 mm (p1)</b>	<b>-750 mV; 5 mm (i5)</b>	<b>-750 mV; 1 mm (i1)</b>
$R_p$ ( $\Omega \text{ cm}^2$ )	3700	15000	3800	5100
$R_e$ ( $\Omega \text{ cm}^2$ )	107	346	77	223
$R_{ct}$ ( $\Omega \text{ cm}^2$ )	3310	14650	1120	1750
$Q_{dl}$ ( $10^{-3} \Omega^{-1} \text{ cm}^{-2} \text{ s}^{n1}$ )	0.17	0.17	0.19	0.20
$n_1$	0.78	0.78	0.82	0.71
$R_f$ ( $\Omega \text{ cm}^2$ )	61	224	372	344
$Q_f$ ( $10^{-6} \Omega^{-1} \text{ cm}^{-2} \text{ s}^{n2}$ )	4.3	1.8	1.1	1.8
$n_2$	0.79	0.79	0.68	0.65
$\sigma$ ( $\Omega \text{ cm}^2 \text{ s}^{-0.5}$ )	396	383	-	-
$R_d$ ( $\Omega \text{ cm}^2$ )	-	-	2980	3140
$t_d$ (s)	-	-	4.3	4.3
$R_{ct}+R_f$ or $R_{ct}+R_f+R_d$	3371	14996	4472	5234

EIS results are presented as Nyquist plots in Figure 4. In any case, two capacitive loops are seen, a small one at high frequency, and the main one at lower frequency. For p1 and p5, the high frequency loop is hardly visible at normal scale (Figure 4a) but can be seen in the detailed view displayed in Figure 4b. The influence of a diffusion process, i.e., dissolved  $O_2$  diffusion, is also noticeable, but it corresponds

to bounded diffusion (finite-length diffusion for a planar electrode) at  $-750 \text{ mV}/_{\text{Ag-AgCl-3M}}$  and to semi-infinite diffusion at  $-950 \text{ mV}/_{\text{Ag-AgCl-3M}}$ .

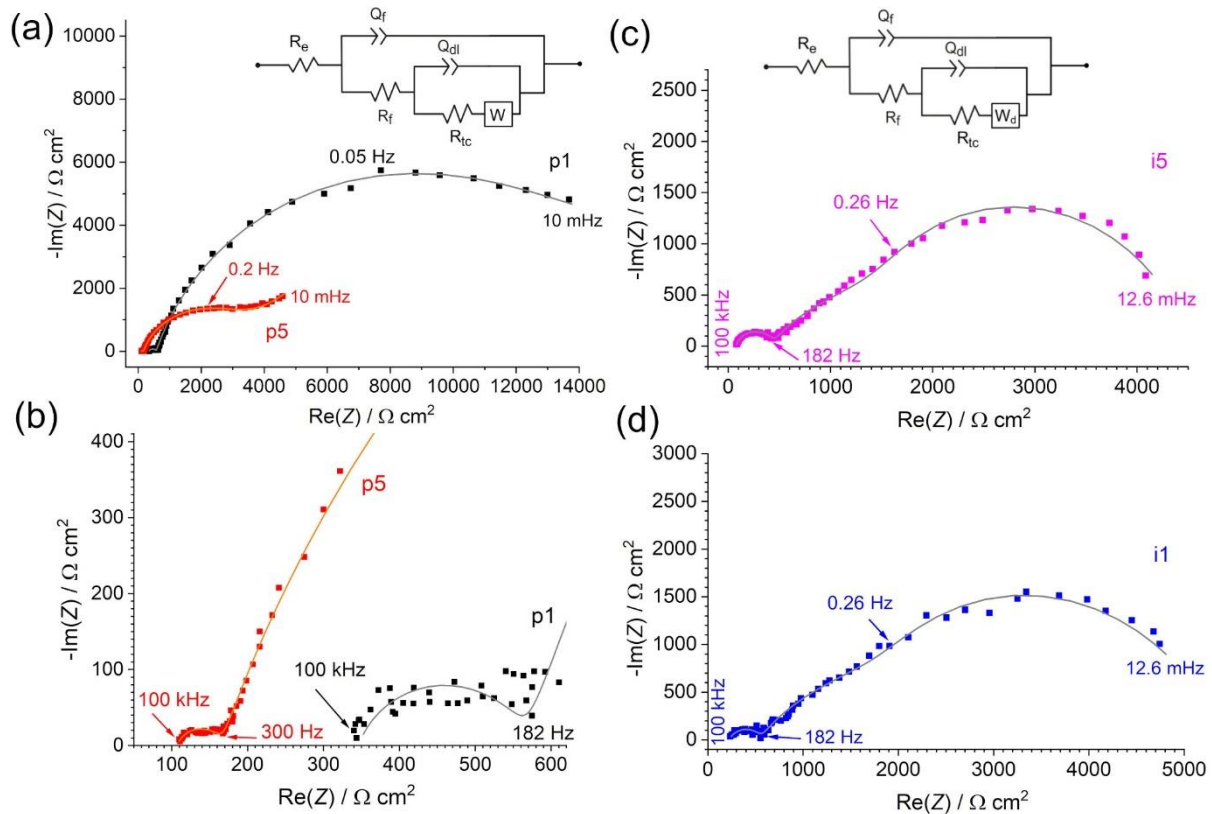


**Figure 4** Nyquist plots for p1 and p5 experiments with EEC used for modelling (a), detailed view at high frequency (b), Nyquist plot for i5 experiment and EEC (c), and Nyquist plot for i1 experiment (d).

In each case, the experimental curve is drawn with squares, the computed curve with a full line.

The EIS data were then modelled using similar EECs, with a Warburg impedance  $W$  for p1 and p5, and a bounded diffusion element  $W_d$  for i1 and i5 (Figures 4a and 4c).  $R_e$  is the electrolyte resistance while  $R_f$  is the resistance associated with a porous film covering the steel surface and  $R_{ct}$  is the charge transfer resistance. The double layer and the porous film capacitances could not be represented by true capacitances and constant phase elements (CPE)  $Q_{dl}$  and  $Q_f$  were used instead. CPE is commonly used in place of capacitance to compensate for deviations from ideal dielectric behavior, due to the heterogeneous nature of the electrode surface.

A good fitting, as shown in figure 4, could be obtained in each case (note that for i1 and i5, due to an important experimental error, the data at 10 mHz had to be discarded). The EIS parameters are listed in Table 1. Coefficients  $n_1$  and  $n_2$  measure the constant phases of CPE, i.e.,  $-(90 \times n_1)^\circ$  for  $Q_{dl}$  and  $-(90 \times n_2)^\circ$  for  $Q_f$  and  $\sigma$  is the Warburg coefficient. The bounded diffusion element  $W_d$  depends on resistance  $R_d$ , a scaling factor linked to kinetics of interfacial reaction and bulk concentration of electroactive species,

and on diffusion time constant  $t_d$  linked to the thickness of the diffusion layer (Orazem and Tribollet, 2008).

EIS results, discussed thoroughly in section 4, are consistent with LPR measurements. For p1 and p5,  $R_p$  should approximately correspond to the sum ( $R_f+R_{ct}$ ), for i1 and i5 to the sum ( $R_f+R_{ct}+R_d$ ), which is indeed the case.

### 3.3 XRD characterization of the calcareous deposits

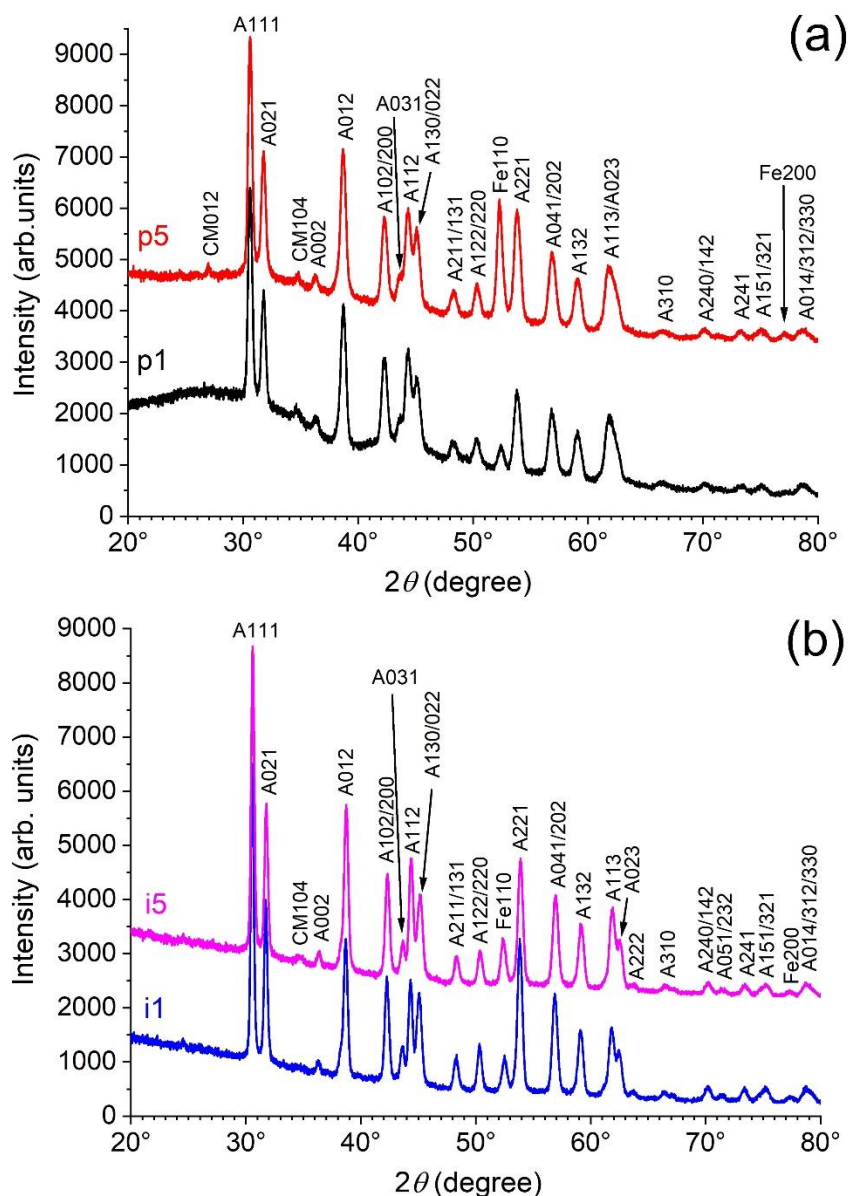


**Figure 5** XRD analysis (Co-K $\alpha$  radiation) of the mineral layer covering the steel electrodes after the experiments with  $E_{CP} = -950$  mV/Ag-AgCl-3M (a) and  $E_{CP} = -750$  mV/Ag-AgCl-3M (b).  $A_{hkl}$  are the diffraction lines of aragonite,  $CM_{hkl}$  those of magnesium calcite and  $Fe_{hkl}$  those of the steel substrate ( $\alpha$ -Fe) with corresponding Miller index.

The XRD patterns (Figure 5) show that all layers are mainly composed of aragonite  $\text{CaCO}_3$ , with traces of magnesian calcite. Other diffraction peaks are those of the steel substrate ( $\alpha\text{-Fe}$ ). Aragonite is the major component of the calcareous deposit forming on steel surfaces under CP (Mantel *et al.*, 1990; Barchiche *et al.*, 2003). It can even form on cathodic zones at OCP (Refait *et al.*, 2016; Duboscq *et al.*, 2019), which explains why the insufficient CP level also finally led to a homogenous aragonite layer.

The final  $I/I_0$  values were observed to be lower with  $E_{\text{CP}} = -950 \text{ mV}/_{\text{Ag-AgCl-3M}}$ , which indicates that the aragonite layer should be less porous. However, due to a longer polarization time (28 days vs 6 days), the calcareous deposits formed at  $E_{\text{CP}} = -750 \text{ mV}/_{\text{Ag-AgCl-3M}}$  may be thicker. Actually, the main influence of  $E_{\text{CP}}$  on the XRD patterns relates to the width of the diffraction lines of aragonite. Those lines are thinner for  $E_{\text{CP}} = -750 \text{ mV}/_{\text{Ag-AgCl-3M}}$ . This can be clearly seen looking at angular regions where aragonite diffraction lines overlap. For instance, around  $2\theta = 62^\circ$ , the A113 and A023 diffraction lines cannot be distinguished at  $-950 \text{ mV}/_{\text{Ag-AgCl-3M}}$ , while they are both visible at  $-750 \text{ mV}/_{\text{Ag-AgCl-3M}}$ . The same applies around  $2\theta = 44^\circ$  for the A031 line. This shows that aragonite particles are larger at  $-750 \text{ mV}/_{\text{Ag-AgCl-3M}}$ . The deposits obtained for i1 and i5 are then more likely thicker but more porous than those obtained for p1 and p5.

## 4. Discussion

CP decreases considerably the corrosion rate but a “residual” corrosion process remains, as reported in previous works: Green rust compounds have been observed to form during the first hours of CP, before aragonite precipitated on the surface (Barchiche *et al.*, 2009). In agreement, a thin layer of green rust and iron sulphide has been detected, lying under a thick calcareous deposit, after 6 years of CP in natural seawater (Refait *et al.*, 2013). Therefore, the film of “residual” corrosion products, though often too thin to be detected, must be taken into account. The differences in the slope of the anodic part of the polarisation curves (Fig. 3) could for instance be due to differences in the properties of the “residual” corrosion films obtained at  $-750 \text{ mV}/_{\text{Ag-AgCl-3M}}$  and  $-950 \text{ mV}/_{\text{Ag-AgCl-3M}}$ .

### 4.1. Influence of $E_{\text{CP}}$

The protective ability of the calcareous deposit is assessed by high  $R_p$  values, and associated whether with high  $R_{\text{ct}}$  values and/or with strong effects on  $\text{O}_2$  diffusion (with respect to bare steel). The increase in  $R_{\text{ct}}$  indicates that the active area is decreased and that  $\text{O}_2$  reduction can only take place on the uncovered part of the surface, i.e., in the pores of the calcareous deposit. This effect is the strongest for  $-950 \text{ mV}/_{\text{Ag-AgCl-3M}}$  showing that the deposit is more dense and less porous.

For the higher applied potential of  $-750 \text{ mV}/_{\text{Ag-AgCl-3M}}$ , CP is less efficient and the residual corrosion rate is higher. Moreover, the experiments were run for a longer period so that the underlying film of corrosion products was necessarily thicker and/or covered a more important part of the surface. The small capacitive loop observed at high frequency (Figure 4) can then be attributed, for  $i_1$  and  $i_5$ , to the corrosion product layer. Because the aragonite particles are larger (see section 3.3), and thus the pores inside the aragonite layer are wider, dissolved  $\text{O}_2$  may easily reached the outer surface of the thin corrosion product film. The finite-length diffusion process revealed by EIS then corresponds to  $\text{O}_2$  diffusion in the pores of the corrosion product film, the thickness of this film corresponding to the thickness of the diffusion layer. The semi-infinite diffusion process revealed by EIS for  $p_1$  and  $p_5$  conversely corresponds to  $\text{O}_2$  diffusion inside the much thicker and denser aragonite layer.

#### 4.2. Influence of seawater layer thickness

The electrolyte resistance  $R_e$  proved significantly higher for the smaller seawater layer thickness of 1 mm (Table 1). The average  $R_e$  is  $90 \Omega \text{ cm}^2$  for 5 mm thickness and  $280 \Omega \text{ cm}^2$  for 1 mm, i.e., three times higher. The increased electrical resistance of the 1 mm thick seawater layer is a direct consequence of the smaller section of electrolyte where the CP current has to flow. It has necessarily an effect on the migration of ionic species. When CP is applied,  $\text{Ca}^{2+}$  cations have to migrate towards the steel surface to form aragonite and when CP is stopped, the accumulated  $\text{OH}^-$  species migrate away from the steel surface so that the interfacial pH decreases. The increased resistance to migration would then explain the slower formation of the aragonite layer (Figure 2a) and the slower depolarization (Figure 2b).

The other observed effect of seawater layer thickness is the increased protective ability of the calcareous deposit. This effect is more pronounced at  $E_{\text{CP}} = -950 \text{ mV}/_{\text{Ag-AgCl-3M}}$ , with  $R_p$  and  $R_{\text{ct}}$  being increased up to  $15000 \Omega \text{ cm}^2$ . Looking closely at the XRD patterns (figure 5), it can be seen that the diffraction peaks of the substrate are much more intense for  $p_5$  than for  $p_1$ . Considering that both aragonite layers should have a similar thickness, this would indicate that the layer obtained for  $p_1$  was much less porous, i.e., that the active area was much smaller. This is consistent with the much higher  $R_{\text{ct}}$  measured value. On the other hand, the delayed formation of aragonite for  $p_1$  may be due to the growth of an underlying  $\text{Mg}(\text{OH})_2$  thin film. It has been observed that at the beginning of CP, when the concentration of dissolved  $\text{O}_2$  is the highest,  $\text{Mg}(\text{OH})_2$  formed preferentially to  $\text{CaCO}_3$  (Yan *et al.*, 1993a). For  $p_1$ , this initial stage may have been promoted by the greater accessibility of oxygen, due to the smaller distance between steel surface and atmosphere. This thin  $\text{Mg}(\text{OH})_2$  film is in most cases difficult to detect by XRD but can be evidenced by scanning electron microscopy analysis on cross sections (Griñon-Echaniz *et al.*, 2021). Besides, after 6 years of CP in the tidal zone, the deposit formed on the steel surface proved enriched in  $\text{Mg}(\text{OH})_2$  (Refait *et al.*, 2015).

A more dense and more protective underlying  $\text{Mg}(\text{OH})_2$  film would lead to the observed higher  $R_{ct}$  for p1. Moreover, the decrease of interfacial pH associated with the depolarization could have induced the dissolution of brucite particles, favouring the precipitation of aragonite in the pores of the deposit and thus increasing its protective ability (Nguyen Dang *et al.*, 2017).

## 5. Conclusions

Based on the obtained results, the following conclusions can be drawn:

- An insufficient CP can promote the formation of a bi-layer, i.e., an aragonite thick layer associated with an underlying thin residual corrosion product film, which has a protective ability similar to that of the calcareous deposit obtained after a correct CP.
- With correct CP and thin seawater film (1 mm thick) the protective ability of the calcareous deposit is increased, more likely because the formation of  $\text{Mg}(\text{OH})_2$  is favoured, which may induce, in particular, a reinforcement of the deposit during depolarization.

## References

- Barchiche C., Deslouis, C., Festy, D., Gil, O., Refait, Ph., Touzain, S. and Tribollet, B. (2003) “Characterization of calcareous deposits in artificial sea water by impedance techniques. 3- Deposit of  $\text{CaCO}_3$  in the presence of  $\text{Mg(II)}$ ”, *Electrochimica Acta*, Vol. 48(12), pp. 1645-1654. [https://doi.org/10.1016/S0013-4686\(03\)00075-6](https://doi.org/10.1016/S0013-4686(03)00075-6).
- Barchiche, Ch., Deslouis, C., Gil, O., Joiret, S., Refait, Ph., and Tribollet B. (2009) “Role of sulphate ions on the formation of calcareous deposits on steel in artificial seawater: the formation of Green Rust compounds during cathodic protection”, *Electrochimica Acta*, Vol. 54(13), pp. 3580-3588. <https://doi.org/10.1016/j.electacta.2009.01.023>.
- BS EN 12473:2014, “General Principles of Cathodic Protection in Sea Water”, The British Standards Institution, London, UK, 2016.
- Duboscq, J., Sabot, R., Jeannin, M. and Refait, Ph. (2019) “Localized corrosion of carbon steel in seawater: processes occurring in cathodic zones”, *Materials and Corrosion*, Vol. 70(6), pp. 973-984. <https://doi.org/10.1002/maco.201810675>.
- Grinon-Echaniz, R., Paul, S., Thornton, R., Refait, Ph., Jeannin, M. and Sabot R. (2021) “Study of cathodic reaction in defects of thermal spray aluminium (TSA) coatings on steel in artificial seawater”, *Corrosion Science*, Vol. 187, 109514. <https://doi.org/10.1016/j.corsci.2021.109514>.
- Humble, R.A. (1948) “Cathodic protection of steel in sea water with magnesium anodes”, *Corrosion*, Vol. 4(7), pp. 358–370. <https://doi.org/10.5006/0010-9312-4.7.358>.
- Mantel, K.E., Hartt, W.H. and Chen, T.-Y. (1990) “Substrate, surface finish and flow rate influence upon calcareous deposit structure and properties”, Paper No. 374 presented at “CORROSION/90”, NACE, Houston, USA.
- Nguyen Dang, D., Gascoin, S., Zanibellato, A., Da Silva, C.G., Lemoine, M., Riffault, B., Sabot, R., Jeannin, M., Chateignier, D. and Gil, O. (2017) “Role of brucite dissolution in carbonate precipitation from artificial and natural seawaters”, *Crystal Growth & Design*, Vol. 17(4), pp. 1502-1513. <https://doi.org/10.1021/acs.cgd.6b01305>.
- Orazem, M.E. and Tribollet, B. (2008), *Electrochemical Impedance Spectroscopy*, John Wiley & Sons, Hoboken, NJ.
- Refait, Ph., Jeannin, M., Sabot, R., Antony, H. and Pineau, S. (2013) “Electrochemical formation and transformation of corrosion products on carbon steel under cathodic protection in seawater”, *Corrosion Science*, Vol. 71, pp. 32-36. <https://doi.org/10.1016/j.corsci.2013.01.042>.

Refait, Ph., Jeannin, M., Sabot, R., Antony, H. and Pineau, S. (2015) “Corrosion and cathodic protection of carbon steel in the tidal zone: Products, mechanisms and kinetics”, *Corrosion Science*, Vol. 90, pp. 375-382. <https://doi.org/10.1016/j.corsci.2014.10.035>.

Refait, Ph., Grolleau, A.-M., Jeannin, M., François, E. and Sabot, R. (2016) “Localized corrosion of carbon steel in marine media: galvanic coupling and heterogeneity of the corrosion product layer”, *Corrosion Science*, Vol. 111, pp. 583-595.

<https://doi.org/10.1016/j.corsci.2016.05.043>.

Refait, Ph., Urios, T., Jeannin, M., Fagot, A. and Sabot, R. (2019) “Corrosion of low alloy steel in stagnant artificial or stirred natural seawater: role of Al and Cr”, *Materials and Corrosion*, Vol. 70(6), pp. 985-995. <https://doi.org/10.1002/maco.201810753>.

Refait, Ph., Grolleau, A.-M., Jeannin, M. and Sabot, R. (2022) “Cathodic protection of complex carbon steel structures in confined marine media”, *Corrosion and Materials Degradation*, Vol. 3(3), pp. 439-453. <https://doi.org/10.3390/cmd3010001>.

Wolfson, S.L. and Hartt, W.H. (1981) “An initial investigation of calcareous deposits upon cathodic steel surfaces in sea water”, *Corrosion*, Vol. 37(2), pp. 70-76.

<https://doi.org/10.5006/1.3593848>.

Yan, J.-F., Nguyen, T.V., White, R.E. and Griffin, R.B. (1993a) “Mathematical modelling of the formation of calcareous deposits on cathodically protected steel in seawater”, *Journal of the Electrochemical Society*, Vol. 140(3), pp. 733-742. <https://doi.org/10.1149/1.2056150>.

Yan, J.-F., White, R.E. and Griffin, R.B. (1993b) “Parametric studies of calcareous deposits on cathodically protected steel in seawater”, *Journal of the Electrochemical Society*, Vol. 140(5), pp. 1275-1280. <https://doi.org/10.1149/1.2220970>.





Chapter V: Cathodic Protection of Carbon Steel  
in Simulated Tidal Zone – Laboratory Scale  
Experiment



## Chapter V: Cathodic Protection of Carbon Steel in Simulated Tidal Zone – Laboratory Scale Experiment

V.1 Introduction .....	132
V.2 Materials and methods.....	132
V.2.1 Tide simulation .....	132
V.2.2 Samples design .....	134
V.2.3 Cathodic protection design .....	136
V.2.4 Measurement principle .....	138
V.2.4.1 <i>Current measurement accuracy estimation</i> .....	139
V.2.4.2 <i>Measurement principle: Electrical patterns</i> .....	140
V.2.4.3 <i>Impact of seawater evaporation on the potential measurement</i> .....	141
V.3 Results and Discussions .....	143
V.3.1 Monitoring of CP parameters (I&E) over time .....	143
V.3.1.1 <i>Overview of column B after 20 days tide exposure</i> .....	143
V.3.1.2 <i>Comparison of the CP features at longer time for B2; B3; B6 and B9</i> .....	146
V.3.2 Mineral layer characterization .....	156
V.3.2.1 <i>Visual observation of the coupons previously analyzed from columns A &amp; B after 9 and 16 months of exposure to tidal zone</i> .....	156
V.3.2.2 <i>Characterization of the mineral layer (XRD and Raman analysis)</i> .....	160
Conclusions: .....	167
References .....	170

## V.1 Introduction

Chapter 3 gave crucial information about the mineral layer composition of samples exposed to natural tidal zone for 50 months. Yet, no information could have been obtained about the precise electrochemical mechanisms occurring on the steel during the ebb tide (or during flood tide). On the other hand, chapter 4 tried to investigate the steel behavior under various seawater layers thicknesses considering two protection level:  $-750 \text{ mV/Ag/AgCl}_{3M}$  (insufficiently protected steel) and  $-950 \text{ mV/Ag/AgCl}_{3M}$  (correctly protected steel). Finally, it could be concluded that an insufficient CP led to an aragonite layer with an underlying residual corrosion product layer with no clear difference in the calcareous deposit protective capacity compared to a similar deposit obtained after a correct CP. In addition, CP under thin seawater film (or residual humidity) enhanced the protective feature of the deposit. However, these experimentations were led horizontally in permanent immersion (as the purpose was to investigate the steel behavior in these conditions).

Based on the observation of the previous chapters, the last part of this work is focusing on laboratory experiments designed to obtain global information about the phenomena resulting from CP in the tidal zone. Indeed, coupons exposed in natural environment are subjected to many uncontrolled parameters likely to influence CP. The aim here is to reproduce a downsized vertical structure comparable to sheet piles in natural environment with simplified conditions to focus only on the influence of cyclic immersion on the cathodic protection efficiency.

## V.2 Materials and methods

### V.2.1 Tide simulation

Since the objective is to reproduce as accurately as possible an industrial structure that could be exposed to 6 m height tidal zone (such as in chapter 3) it was imperative not to overly reduce the design to retain all pertinent information. Consequently, an experimental set up has been designed to a scale factor as close as possible to the real structure. This experiment has been carried out in the Naval group corrosion laboratory at Naval Group Cherbourg where a 2 m long and 1.3 m high tank could be used. These dimensions allowed us simulating a 1 m high tidal zone.

The tide simulation of this experiment was a challenging part as it required a permanent inlet of natural seawater (the Naval Group corrosion laboratory directly pumps seawater from the English Channel) and a pump set in the tank able to control the water level to reproduce the tide. For maximum accuracy and to observe the chemical kinetics of the corrosion (and corrosion protection) phenomena taking place in a natural tidal zone, a sinusoidal 12 hours period has been chosen i.e., 6 hours are separating high tide and low tide. Finally, to fulfil these requirements, the tide simulation was led by an Arduino controlled water pump constantly emptying the tank. Indeed, during flood tide the pump flow has to be slower than the seawater alimentation whereas during ebb tide the pump flow must be greater than the seawater inlet. Figure V.1 schematically represents the tide simulation system.

The monitoring system conceived by Thomas Quiniou, Arnaud Serres and Marc Jeannin is designed as follows (images showed in figure V.2):

- The water pump: the considered pump can bring water up to 2.5 m high and deliver 2000 L per hour.
- The water level sensor was an infrared laser sensor reflecting on a polystyrene floater (guided in a plastic pipe).
- The Arduino system regulates the water level, considering the laser sensor level, the minimum seawater level authorized, the maximum seawater level (equivalent to the upper evacuation system of the tank) and the signal period of 12 h as explained above.

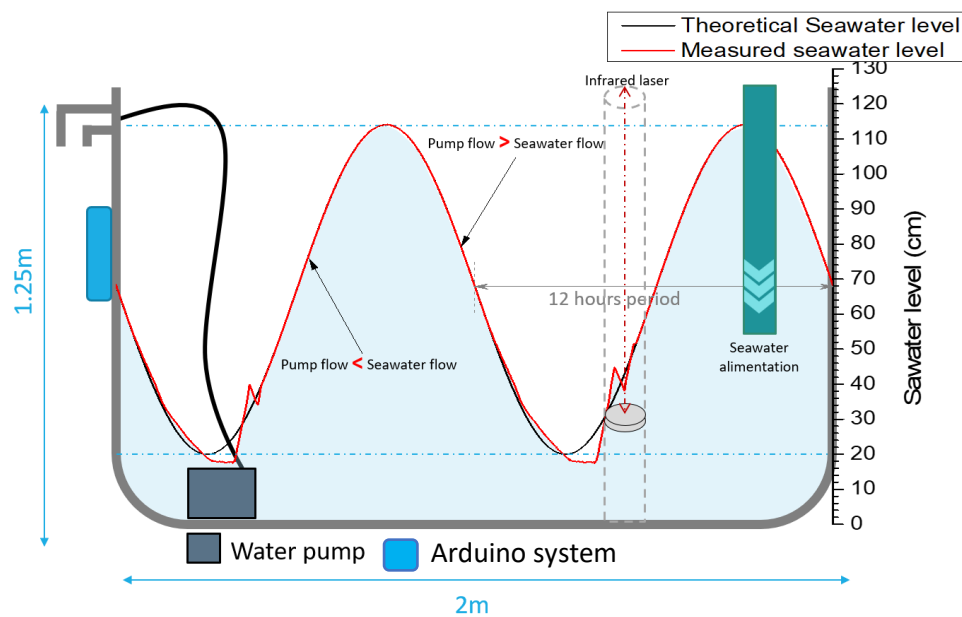


Figure V.2: Schematic representation of the tide simulation principle



Figure V.3: Photographs of the experimental set up

This tide simulation device had never been tested on a long-term experiment. So, the tide-simulating device did not work perfectly on the whole experiment duration. Indeed, sometimes the pump was struggling to maintain the seawater level. Many factors could be responsible for the dysfunction: the flow variation of the seawater alimentation played a key role but sometimes a siphon effect occurred emptying the pipe between the pump in the bottom and the overflow evacuation at the top of the tank or sometimes a simple informatic bug could throw the tide simulating device working balance off. Some examples are shown in figure V.3.

Each example presented here is considered as a malfunction of the device. Since these periods of dysfunction are not neglectable, the efficiency of the device has been estimated at **65.3 %**. Indeed, the tide simulating system was not checked every day but rather once a week. Consequently, from one time to other, problems could occur and on the 320 days period of monitoring, 24 malfunctions of the system have been reported for an average duration of 4 days 15 hours and 50 minutes and a total of 112 days out of correct working. This efficiency rate directly plays a role on the theoretical immersion rate calculated below (section V.1.3). Yet, correcting the theoretical immersion rate with the efficiency rate of the device would be wrong as the water level randomly stays at low water level, or could create a tide only in the upper part of the tank or even remain at the high-water level.

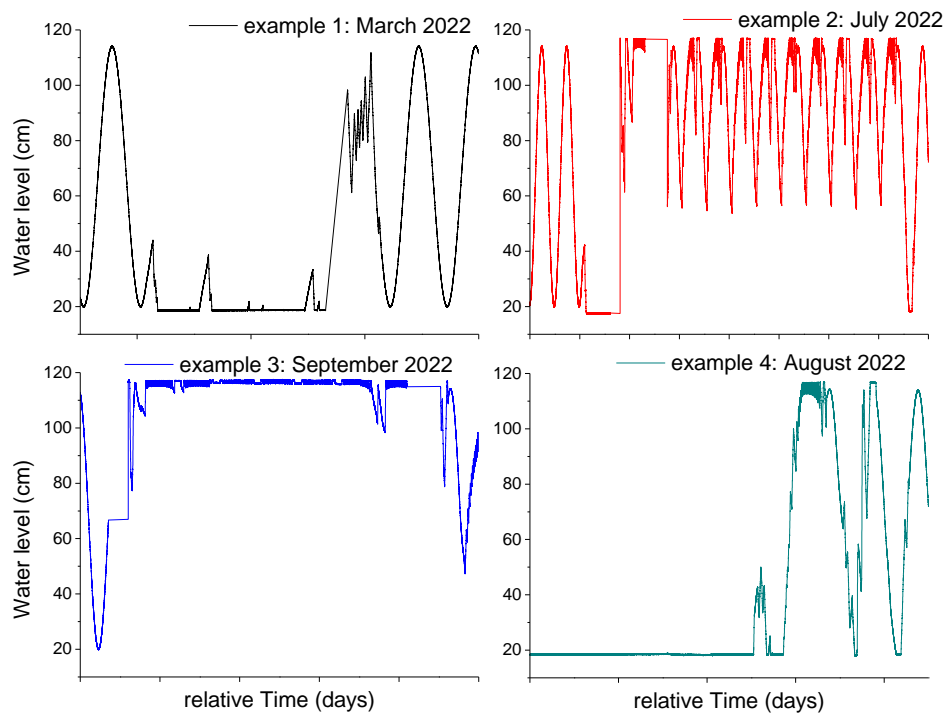


Figure V.4: Examples of tide simulation malfunction

### V.2.2 Samples design

Samples were designed according to several specifications too. It was important to be able to study the phenomena at different depths and to be able to perform electrochemical tests in specific areas of the tidal zone. The coupons assemblage had to be electrically and geometrically continuous to accurately simulate the electrochemical phenomena occurring in the tidal zone and allow the residual seawater flow along the structure. Hence, the chosen structure was made up with 10 square coupons of 10 x 10 cm. Each coupon was embedded in epoxy resin to control the exposed surface. They were then insulated from the others but each coupon connected to the Al-Zn-In anode used for CP.

Nevertheless, it was also important to confirm that the same phenomena occurred all along the tidal zone on a structure electrically and geometrically continuous. Then, long carbon steel plates (1.10 m) have been prepared to be exposed to the same cyclic immersion effects. A long plate and a column of coupons makes one unit. 3 conditions were studied, each one with a different unit:

- Permanent cathodic protection for 9 months to analyze the early steps of corrosion product and calcareous deposit formation under CP in tidal zone (**Denominated as column A**).
- Permanent CP, for the whole time of experimentation (16 months) (**Denominated as column B**)
- Tidal corrosion for 6 months and delayed CP till the end of the experiment (**results not presented here**).

The coupons were thoroughly assembled (figure V.4-c) to allow the formation of a seawater film during the emersion phase, but without direct electrical contact between two adjacent coupons. The schema presented figure V.4-a) shows how samples were designed. The steel coupon is embedded in epoxy resin with left and right edges also covered with resin to avoid edge effects. The top and bottom edges are not covered allowing water flowing from a sample to the lower one. A micro-reference Ag/AgCl electrode (presented in figure V.4-b) is inserted in the center of the coupon. The reference extremity was carefully set in a coplanar position to the surface to be analyzed. This electrode is preliminarily dipped in epoxy resin to create an insulating film all around and prevent any contact between the sample and its reference electrode. It was chosen to use a micro reference for each coupon because the phenomena of interest are located in the residual seawater film. This geometry has been designed to permit a local study of the steel behavior even during the emerged phase i.e., when the surface of the coupon is still wet but may not be connected to the bulk seawater where a reference electrode would have usually been set. It would permit potential measurements of the coupons without ohmic drop when the residual humidity is present.

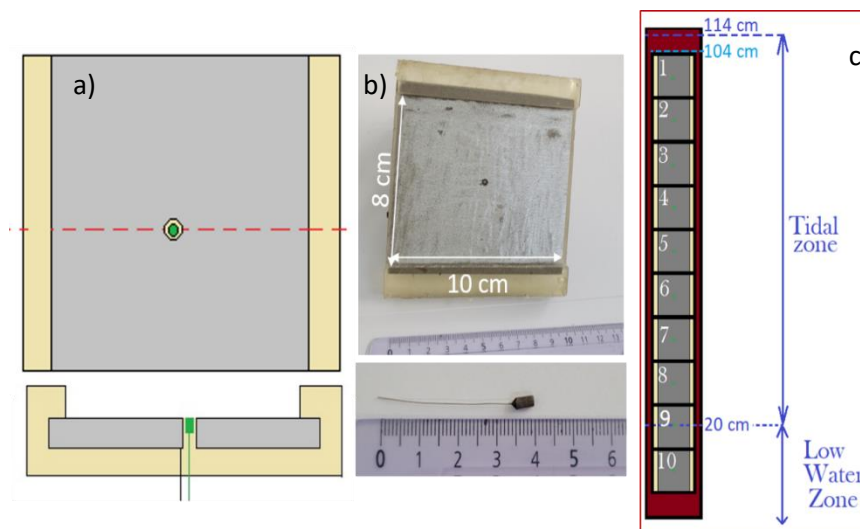


Figure V.5: Representation of the sample design – a) schematic representation of the sample conception – b) photographs of a real sample and a micro reference electrode – c) schematic representation of an assembled column with the water levels.

The samples are numerated from 1 to 10 starting at the top. The long plates are prepared in a similar manner. They were fully painted except for one surface. 3 micro-reference electrodes were inserted in the plate at 1/3; 1/2 and 2/3 of its height. As for the coupons, the plates were abraded before being

exposed to seawater. Finally, the whole experiment was designed with 3 units A, B and C composed of 1 column and 1 long plate. However, the results obtained with the long plates are not presented here.

### V.2.3 Cathodic protection design

The whole system was protected with a single Al-Zn-In anode. The design was calculated as follows to confirm the anode efficiency for the experiment lifespan, i.e., a year and a half:

- Standard current densities: The document used as reference is DNV RPB 401. Considering that English Channel is a temperate seawater (7°C – 11°C), the current densities given by the standard for uncoated steel are:
  - For the polarization:  $-0.200 \text{ A/m}^2$
  - For the polarization maintenance:  $-0.100 \text{ A/m}^2$
  - For the repolarization:  $-0.130 \text{ A/m}^2$
  - Anode utilization factor: 0.85 (this means that at the end of the considered lifespan, 85% of the mass of the anode should be consumed)
- Current demand estimation: the whole protected surface is obviously a key parameter to evaluate the required current demand of the structure. The determination of the whole surface to be protected is detailed in table V.1 below. The total current demand determination, based on DNV RPB 401, is obtained considering a whole year of polarization, a whole year (in cumulated time) of repolarization and the remaining time as the polarization maintenance. However, this standard is suitable for industrial structures with a designed lifespan of 20 years or more. In the present case, the repolarization time can be considered negligible compared to the polarization time. Then the total current demand was calculated as follows:
  - $I_{lifespan} = S_{steel} \times 0.2 \times 1_{year} + S_{steel} \times 0.1 \times 0.5_{year} = 0.15 \text{ A}$
  - With:  $I_{initial} = S_{steel} \times 0.2 \times 1_{year} = 0.12 \text{ A}$
  - And:  $I_{mean} = \frac{I_{lifespan}}{lifespan} = \frac{0.15}{1.5} = 0.1 \text{ A}$

Table V.1: Total steel surface calculation

	Coupons	Long plate
Width (cm)	8	10
Length (cm)	10	110
Surface (cm <sup>2</sup> )	80	1100
Surface of 1 column (cm <sup>2</sup> )	800	
Surface of 3 columns (cm <sup>2</sup> )	2400	3300
Total surface (cm <sup>2</sup> )	5700	
<b>Total surface (m<sup>2</sup>)</b>	<b>0.57</b>	<b>≈ 0.6</b>

- Anode characteristics: The anode chosen for the experiment was a 1.5 kg anode BERA 15 AL (BAC Corrosion Control) with geometrical characteristics and nominal composition detailed in the tables V.2 and V.3.

Table V.2: Properties of BERA 15 AL anode (from BAC Corrosion Control)

Anode characteristics		Anode material features	
Weight (kg)	1.5	Alloy density (kg/m <sup>3</sup> )	2180
Length (m)	0.25	Mass consumption in seawater (kg/A.year)	3.5
Short length (m)	0.15	Electrochemical capacity in seawater (A.h/kg)	2500
Height (m)	0.03	Electrochemical potential in seawater (V/Ag/AgCl <sub>sw</sub> )	-1.1
Large base (m)	0.095		
Short base (m)	0.065		
Insert width (m)	0.025		
Insert height (m)	0.006		

Table V.3 : Composition of the anode in wt% (from BAC Corrosion Control)

Zn	In	Fe	Si	Cu	Mn	Al
4 to 5	0.015 to 0.040	< 0.09	< 0.10	0.005	0.01	> 90

- **Anode maximal current determination:** The maximal current is used to evaluate the number of anodes necessary to protect the considered structure. It corresponds to the maximal current that can be released by an anode.  $I_{max}$  is determined using the Ohm's law:  $I_{max} = \frac{U}{R_a}$  (With U the considered potential difference and  $R_a$  the resistance of the anode). The resistance of the anode results from a calculation based on its geometrical characteristics, which is made using the Dwight mathematical relation:

$$R_a = \frac{\rho}{2\pi L} \left[ Ln \left\{ \frac{2L}{r} \left( 1 + \sqrt{\left( 1 + \frac{r}{2L} \right)^2} \right) \right\} + \frac{r}{2L} - \sqrt{1 + \left( \frac{r}{2L} \right)^2} \right] = 0.671 \Omega$$

- The considered potential difference is actually the difference between the protection potential threshold of -0.8 V/(Ag/AgCl<sub>sw</sub>) and the potential of the anode, i.e., -1.1 V/(Ag/AgCl<sub>sw</sub>). Therefore:
- $U = E_{anode} - E_{protection} = -0.3 \text{ V}/(\text{Ag}/\text{AgCl}_{sw})$   
 $\rightarrow I_{max} = 0.447 \text{ A} \approx 0.45 \text{ A}$
- **Estimation of the required number of anodes:** the required number of anodes is determined by figuring out **the maximum** between:
  - (i) the number of anodes ( $N_{anodes}$ ) suitable to provide enough current to polarize the whole surface. In this case, an initial current of 0.12 A is required to polarize the whole steel surface while the maximum current which could be delivered by 1 anode is 0.45 A. The question is then, how many anodes are required to reach the maximum current demand (i.e. the initial current) of the structure:  $N_{anodes} = \frac{I_{initial}}{I_{max}} = 0.27 < 1$ 
    - with this method the minimum anode required is 0.27 anode

- (ii) the required number of anodes to overcome the global anode material consumption.

$$\text{Anode consumption} = \frac{\text{Mass consumption in seawater} \times I_{\text{mean}} \times \text{lifespan}}{\text{Utilisation factor}} = 0.62 \text{ kg}$$

$$\text{Number of anodes} = \frac{\text{Anode consumption}}{\text{Anode mass}} = 0.41 < 1$$

➔ this method indicates that at least about half an anode is necessary to protect the structure

Both methods explained above led to the conclusion that 1 BERA 15 AL anode was enough to protect all the coupons and plates immersed in the tank for the whole lifespan experiment. The global experiment design is presented figure V.5 with the pump, the anode and the 3 units (coupons column + long plate) in the tank. The grey percentage written on the left of the tank recount the theoretical immersion rate of the coupons.

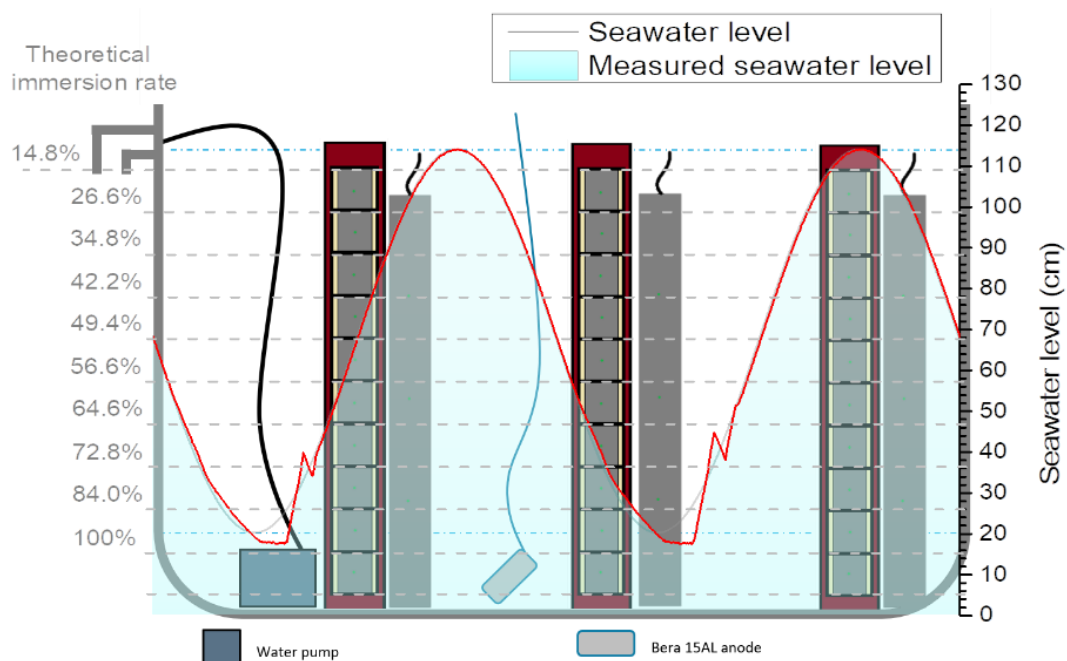


Figure V.6: Final experimental set up with the theoretical immersion rate indicated for each coupon

#### V.2.4 Measurement principle

As presented in section V.1.2, the coupons were designed so that the evolution of potential and current demand of each sample could be monitored as a function of tide. To achieve this monitoring, an Agilent data acquisition system (DAS), designed for voltage measurements, has been used. Since this DAS only permits voltage measurements, the current measurement had to be done through a voltage measurement, using a resistance set between each coupon and the anode. Then, using the Ohm's law, the current could be estimated.

## V.2.4.1 Current measurement accuracy estimation

This method requires to be careful, because setting a too high resistance between the coupon and the anode could slightly disrupt the studied electrochemical system. On the other hand, the stronger the resistance the greater the measured potential. The DAS accuracy is 50  $\mu\text{V}$  (or 0.05 mV). Table V.4 and figure V.6 display the theoretical error as a function of cathodic protection current and considered resistance with the values for a 5  $\Omega$  resistance in blue, the values for a 1  $\Omega$  resistance in orange and the values for a 0.1  $\Omega$  resistance in grey.

Table V.4 : Error values as a function of the inserted resistance

U (mV)	Error	R = 0.1 $\Omega$		R = 1 $\Omega$		R = 5 $\Omega$	
		I (mA)	j (mA/cm <sup>2</sup> )	I (mA)	j (mA/cm <sup>2</sup> )	I (mA)	j (mA/cm <sup>2</sup> )
0.1	50%	1	0.0125	0.1	0.00125	0.02	0.00025
0.5	10%	5	0.0625	0.5	0.00625	0.1	0.00125
1	5%	10	0,125	1	0.0125	0.2	0.0025
5	1%	50	0,625	5	0.0625	1	0.0125

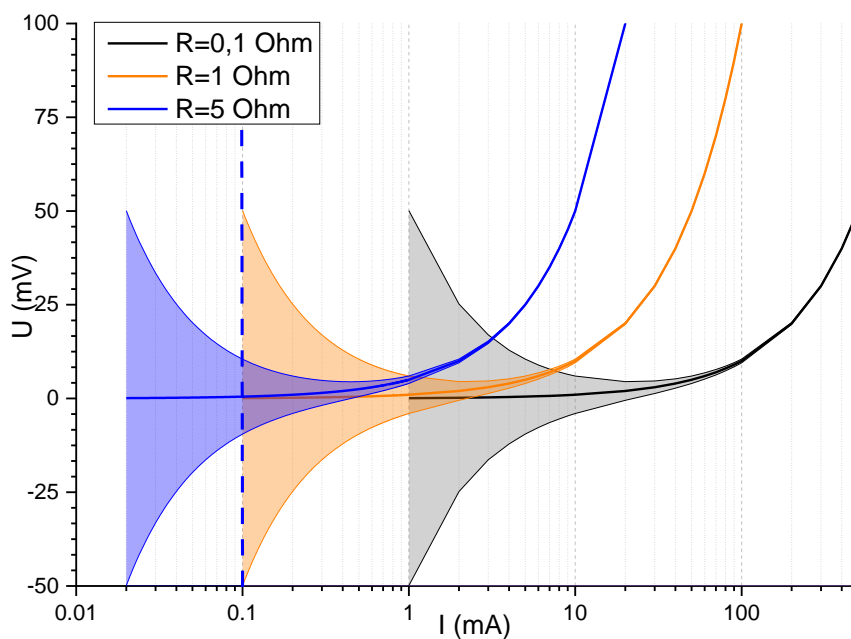


Figure V.7: Evolution of the error on the measured potential value as a function of the current flowing through the resistance

Considering a maximal error of 10%, the minimum measurable current is 0.1 mA, i.e., the minimum measurable current density is  $1.25 \times 10^{-3}$  mA/cm<sup>2</sup>, with the 5  $\Omega$  resistance. Not only this resistance allows the widest range of measurements but also provides the greatest accuracy on the measured potential.

## V.2.4.2 Electrical patterns

Finally, for each coupon, the potential is measured between the coupon surface and its own  $\mu$ -reference electrode. This measurement is very local and can give accurate information provided that the area around the reference electrode is still moist. It does not require a continuous electrolyte film from the coupon to the bulk seawater below. The current is calculated from the voltage measured at the terminals of the resistance set between the coupon and the anode. The sample must also be linked to a second circuit allowing the connection to a potentiostat for performing individual and punctual electrochemical tests. Electric patterns are presented in figure V.7-a) for one coupon and V.7-b) for the 10 coupons of one column.

The interesting point with this design is that all the samples are interconnected through the connection with the anode (green line in figure V.7-b) then the column is electrically and geometrically continuous but it is possible to switch a sample on the second circuit to study the steel coupon behavior at that precise height (and/or immersion rate) without disrupting the others coupons. In figure V.7-b), the blue lines are dedicated to micro-reference electrodes, the red ones to the coupons connections and the black ones to the counter electrode (either the Al-Zn-In anode or a titanium grid covered in platinum for electrochemical tests on a given coupon). The principle is exactly the same for the long plates except that there are 3 channels dedicated for the measurement of potential as there are 3 reference electrodes. Since the results obtained with these plates are not detailed here, the corresponding electric patterns are not presented.

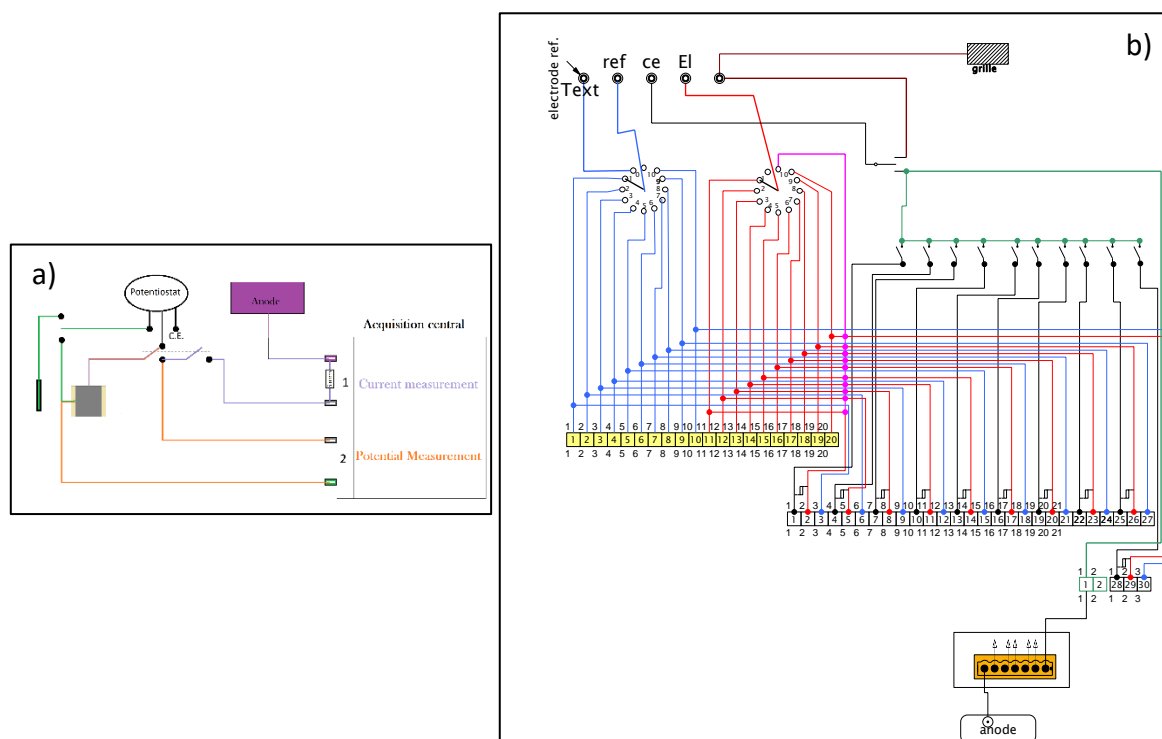


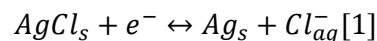
Figure V.8 : Electric patterns – a) Simplified schema for a single coupon – b) For a whole column

Unfortunately, a technical problem occurred and the computer used for monitoring broke down at 320 days of experiment and could not be replaced in time. Consequently, the monitoring of the CP parameters will be analyzed up to 320 days. Although there was no recording of the potential and current, the sample remained in the tank submitted to simulated tides for 16 months.

Whilst this measurement system is innovative and should permit to get really accurate and local information about the potential, it is important to keep in mind that the values measured with these  $\mu$ -reference electrodes are directly dependent on seawater composition.

#### V.2.4.3 Impact of seawater evaporation on the potential measurement

When a  $\mu$ -reference electrode is immersed in bulk seawater, its potential is the potential of an Ag-AgCl seawater electrode, i.e., +0.25 V/SHE at 25°C. When the coupon and its  $\mu$ -reference electrode are no more in the bulk seawater, they remain covered with a thin seawater film. When the water evaporates, the  $\text{Cl}^-$  concentration increases and the potential  $E$  of the  $\mu$ -reference electrode decreases according to Nernst's law, applied here for the equilibrium conditions of the  $\text{AgCl(s)}/\text{Ag(s)}$  redox couple:



$$E_{\mu\text{Ref}} = E_{\text{Ag}/\text{AgCl}}^0 - 0.059 \log([\text{Cl}^-])$$

Where  $[\text{Cl}^-]$  is, rigorously, the activity of  $\text{Cl}^-$  in the solution.

Consequently, the potential of the  $\mu$ -reference electrode could decrease, because of water evaporation, up to the potential corresponding to the saturation of seawater, i.e., about  $E = +0.20$  V/SHE at 25°C if we consider the potential of an Ag/AgCl/KCl saturated electrode. Figure 8 displays the evolution with  $[\text{Cl}^-]$  of the potential of an Ag/AgCl electrode, drawn with  $E^\circ = 0.2343$  V/SHE [1].

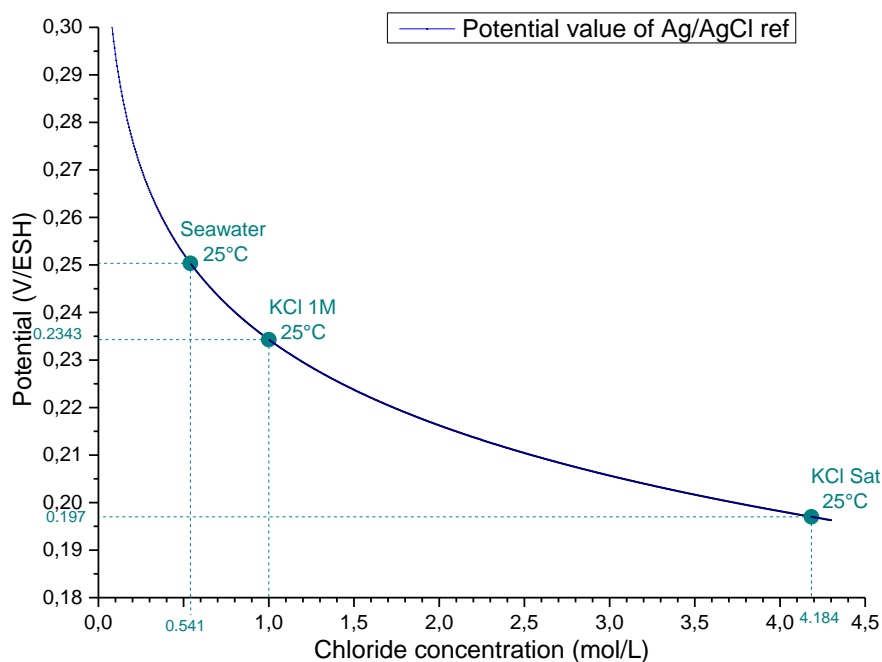


Figure V. 9: Theoretical evolution in potential of the Ag/AgCl reference as a function of the chloride concentration

Finally, the potential of the  $\mu$ -reference electrode could vary from 0.25 V/SHE to 0.20 V/SHE. The measured value could then be shifted at worst of  $\Delta E \approx -50$  mV. Potential values of the upper coupons (such as A1 or B1) will be the most impacted by seawater evaporation as they have the smallest theoretical immersion rate.

In addition, on many occasions and for various reasons, the  $\mu$ -reference electrode potential shifted with time, subsequently shifting the measured value of the corresponding coupon potential. To remedy this unwanted phenomenon all the presented data have been corrected to cancel this shift. As the potential of the coupons, when immersed, have been measured several times at  $E_{\text{prot}} = -1.075$  V/Ag/AgCl<sub>sw</sub>, this value was used as a reference to discriminate and compensate the shift in potential of the associated  $\mu$ -reference electrode. This value, which was expected, actually corresponds to the potential of the Al-Zn-In alloy in seawater [2]. This result shows that all coupons were correctly protected. The data correction principle is illustrated figure V.9. The data file is sequenced in cycles. Then, for each cycle the shift is calculated as follows by differencing the protection potential with the lowest potential measured during the cycle. Finally, the shift for each cycle is corrected and applied to all the data set.

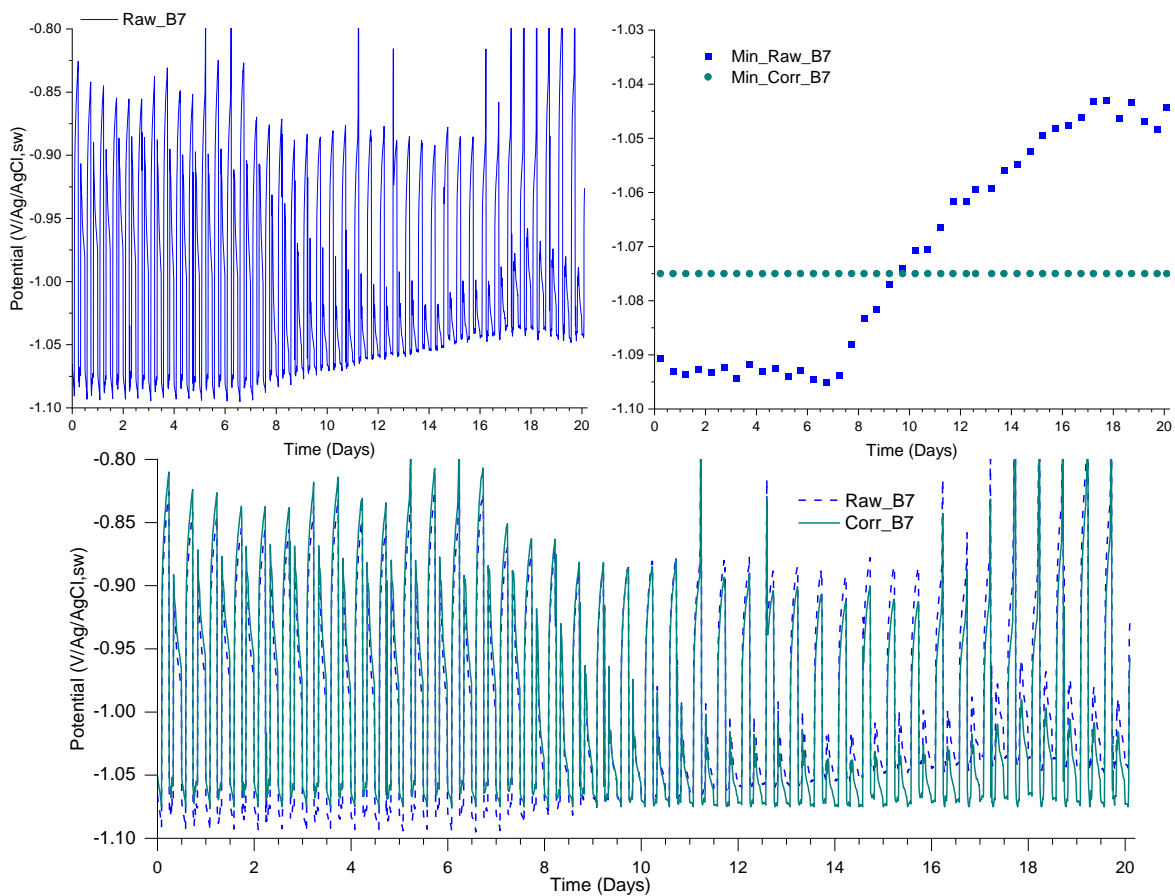


Figure V. 10: Potential data correction principle

## V.3 Results and Discussions

### V.3.1 Monitoring of CP parameters (I&E) over time

Every current curve presented in the followings figures has been plotted in current density. This assumes a constant surface of 80 cm<sup>2</sup> for each coupon. However, a consequence of the tidal zone is the variation of the active surface of the coupons during the immersion and emersion phases (when the steel surface is not totally immersed nor totally emerged). It is nevertheless interesting to relate this current (applied on the wet surface) to the total surface area of the coupon, which gives a current density "equivalent".

Moreover, in this part, as columns A & B give the same type of information, figures and presented results are extracted from the column B, chosen as an example. In addition, this column has been monitored for a longer time and gives data on a longer period. The behavior of column B will be discussed through the current and potential evolution of 4 representative coupons: B2, B3, B6 and B9.

#### V.3.1.1 Overview of column B after 20 days of tide exposure

Figure V.11 shows an overview of the first stages of CP efficiency along the tidal zone. This view permits a better comparison between the sample regarding their respective immersion rate (or altitude in the tidal zone). The evolution of CP parameters (current and potential) for the whole column are discussed below the figure V.11. However, the comparison between various coupons allow obtaining trends for the whole column based on the theoretical immersion rates, presented in table V.7 for the considered samples:

Table V. 5: Theoretical immersion rates of the considered samples

Coupon	B2	B3	B6	B9
Theoretical immersion rate	27% to 35%	35% to 42%	57% to 65%	84% to 100 %

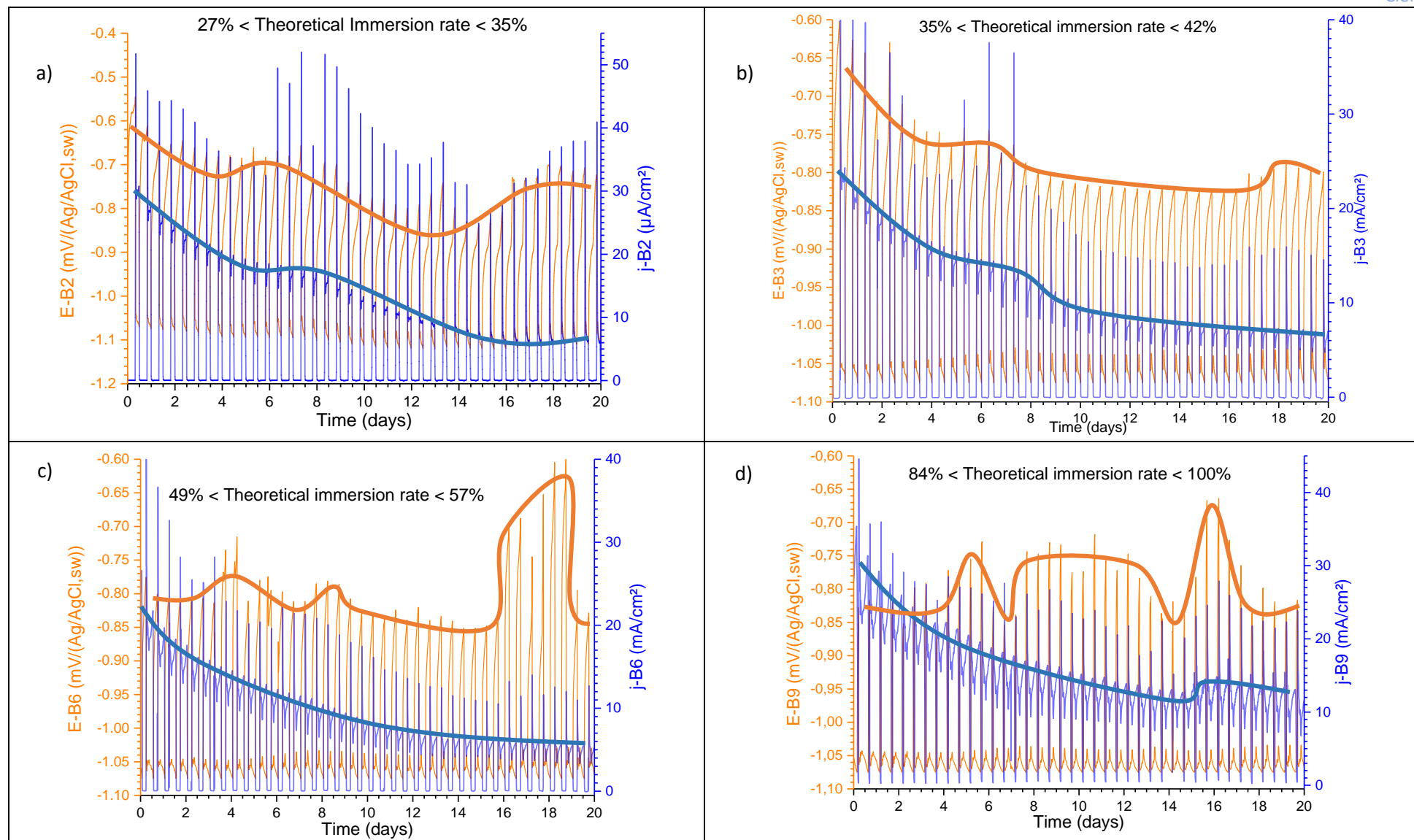


Figure V. 11: Current and potential evolution as a function of time of the coupons - a) B2 - b) B3 - c) B6 and d) B9

Figure V.11 - a) relate the CP parameters evolution for coupon B2. The potential (orange curve) is of course the highest when the coupon is emerged, and the lowest when the coupon is immersed. The CP current (blue curve) is null when the coupon is emerged and reaches a maximum when the whole coupon surface is immersed.

The potential of coupon B2 does not show any stabilization after 20 days. In other words, the average value of its potential is still fluctuating. The amplitude of the potential variation associated with the cyclic immersion does not decrease with time. These variations can be explained by the immersion rate. The top of the sample is emerged for 8h50 min and the bottom for 7h50 min each cycle. The time B2 remains immersed may not be sufficient for the formation of a protective layer of calcareous deposit. Indeed, under cathodic protection, a porous calcareous deposit forms on the steel surface [3]–[6], which could favor the persistence of humidity. The formation of a porous layer (of calcareous deposit and/or corrosion products) can favor the persistence of residual humidity at the steel surface when the coupons are no more immersed [7], [8]. A similar phenomenon corroborating this idea was visually observed for column C (6 months of free corrosion + CP) during a flood tide as presented in figure V.12. Here, the humidity is “attracted” by the porous layer because of capillarity strengths, wetting the steel before its immersion. This phenomenon, which would apply to coupons protected by CP when a porous calcareous deposit has formed, would permit the persistence of CP even during emerged periods, as observed previously [7].



Figure V. 12: Visualization of humidity trapped in porous layer on column C during flood tide.

In the case of B2, the formation of the calcareous deposit could not take place because of the low immersion time. Therefore, residual humidity could not be attracted or trapped on the sample surface. Thus, the drying was favored and the sample completely depolarized with each cycle. Consistently, the current fluctuation does not display any stabilization with time. For each cycle the initial current density demand is really high (the same order as in the DNV RPB 401 standard) as oxygen is highly available since it does not need to diffuse through a porous layer of calcareous deposit to reach the steel surface.

**For coupon B3** (which current and potential evolution overview is presented figure V.11 – c), the average potential value of the emerged coupon was rather stable after 20 days. It was measured around  $-0.610 \text{ V/Ag/AgCl}_{\text{sw}}$  the first day and around  $-0.810 \text{ V/Ag/AgCl}_{\text{sw}}$  the 20<sup>th</sup> day, after a slight increase the 16<sup>th</sup> day. This global decrease of the average emerged potential value can be interpreted as a consequence of the steel polarization and the calcareous deposit precipitation. The characteristic value of  $-0.8 \text{ V/Ag/AgCl}_{\text{sw}}$  was reached, in this case, the 8<sup>th</sup> day. Like the potential, the current density range decreases with time from  $40 \mu\text{A}/\text{cm}^2$  to  $14 \mu\text{A}/\text{cm}^2$ , as a consequence of the calcareous deposit formation.

The highest potential reached during emersion is quite variable along the column. It depends, but not clearly, on the altitude of the coupon. It varies, for a given coupon, with time but without clear tendency. **For coupon B6** (current and potential evolution over 20 days presented in figure V.11 - c), the highest potential is about  $-800/-850 \text{ mV/Ag/AgCl}_{\text{sw}}$  at days 1-3, increases up to  $-750 \text{ mV/Ag/AgCl}_{\text{sw}}$  at day 4, decreases down to  $-890 \text{ mV/Ag/AgCl}_{\text{sw}}$  at day 15 before to reach a maximum value of  $-620$

mV/Ag/AgCl<sub>sw</sub> at day 18. These values have to be carefully considered as they may not have a real signification. The maximum potential measured during emersion comes after a drying period which influences the potential of the  $\mu$ -reference electrode and could also mean a complete drying of the coupon surface around the  $\mu$ -reference electrode. In the latter case, the measured value does not have any meaning as the  $\mu$ -reference electrode is no more immersed in the residual electrolyte. These variations of potential are even more surprising regarding the current evolution. B6 current evolution displays the same trend as B3, with a progressive decrease in maximum current range over time. Every cycle B6 is polarized, calcareous deposit precipitates on its surface, decreasing the active surface and protecting the steel [6], [10]–[12]. In addition, the current demand of both coupons is of the same order: at day 1, the maximum current density measured for B6 is 40.0  $\mu\text{A}/\text{cm}^2$  (same as B3) versus 12.8  $\mu\text{A}/\text{cm}^2$  for day 20 (14  $\mu\text{A}/\text{cm}^2$  for B3). Yet, some variations in the current demand decrease are matching the variations of maximum potential value. The current is decreasing from 40 to 25.4  $\mu\text{A}/\text{cm}^2$  on days 1 to 3, then at day 3 it rises again at 28.0  $\mu\text{A}/\text{cm}^2$  and still decreases to 18.7  $\mu\text{A}/\text{cm}^2$  on day 6. Then from day 6 to day 16, the current decreases from 22.7 to 10.3  $\mu\text{A}/\text{cm}^2$  and for the last days, the average maximum current is about 11.5  $\mu\text{A}/\text{cm}^2$ . Finally, on the 20 days presented figure V.12 – a), the potential measured when coupon B6 is emerged remains sometimes below the protection potential threshold of -0.80 V/Ag/AgCl<sub>sw</sub> even if the current evolution would suggest a progressive decrease in maximal potential value.

**For B9**, as presented in figure V.11 – d), the measured maximum potential seems to vary rather randomly. No clear evolution is observed within the 20 first days. From day 1 to day 3, the potential remains below -0.8 V/Ag/AgCl<sub>sw</sub>, then from day 3 to day 5.7 there is a slight increase in maximum potential from -0.800 V/Ag/AgCl<sub>sw</sub> to -0.731 V/Ag/AgCl<sub>sw</sub>, and so on, with a maximum that continues to alternate between -0.866 V/Ag/AgCl<sub>sw</sub> and -0.662 V/Ag/AgCl<sub>sw</sub> (reached on day 16). Conversely, the current evolution with the tide cycles displays the expected decrease caused by the calcareous deposit precipitation. However, the very maximum of each cycle is rather dependent of the potential, as some local maximal current values are associated with local maximal potential values, for instance around day 16. The measured maximal current density was 44.8  $\mu\text{A}/\text{cm}^2$  at day 1, 15.2  $\mu\text{A}/\text{cm}^2$  at day 15 and 24  $\mu\text{A}/\text{cm}^2$  at day 20.

Finally, this experiment allows a continuous and individual monitoring of the potential for each sample as long as moisture persists on its surface. Thus, the potential does not give direct information on the electrolyte continuity but rather on the polarization (or depolarization) of the samples as the measure is performed within the residual humidity. On the other hand, the current is measured directly between the anode and the considered sample, so when the current is no longer measurable, it can be assumed that the electrolytic continuity has been broken. The CP persistence on longer time will be discussed in the following section.

### V.3.1.2 Comparison of the CP features at longer time for B2; B3; B6 and B9

This section focuses on the evolution of current and potential for 1 cycle for coupons B2; B3; B6 and B9, as presented in figures V.14 to V.17, on different times (8 days vs. 180 days vs. 320 days).

B9 could not be replaced by another sample because it is the only one which is exactly at the transition between the tidal zone and the low water zone (the permanently immersed zone, below the low tide level). Because B9 current measurement could not be achieved till 320 days, its current evolution is not detailed. Yet, its  $\mu$ -reference electrode still measured some coherent and interesting potential variation displayed in figure V.17. This suggests that the encountered technical problem might come

from connection box or connection to the DAS and not from the coupon itself. For B9, the comparison is then done between 8 days, 180 days and 320 days for the potential, and only between 8 days and 180 days for the current. Finally, as previously and for all the presented graphics of figures V.13 and V.14:

- The orange curves display the potential evolution over time
- The blue lines display the current demand evolution over time
- The blue crosses spot the average current demand
- The red line materializes the  $-0.800 \text{ V/Ag/AgCl}_{sw}$  potential threshold
- The dot grey lines show the sample position in tidal zone
- The dash lines are for the coupon evolution at 180 days and the dash dot lines for the evolution at 320 days.

Before going forward and because the figures presented in this part are quite complex to read and understand, it is necessary to divide the cycle in different steps to clarify further discussions:

- Figure 13 – a) highlights the emersion phase (ebb tide between the 2 dashed grey lines). The emersion of coupon lead to a sharp decrease of the protection current and a huge depolarization of the steel surface.
- Figure 13 – b) deals with the immersed time. The current is at its minimum ( $0 \mu\text{A}/\text{cm}^2$  here) while the potential gradually depolarizes.
- Figure 13 – c) displays the current and potential evolution for the immersion period. The current reaches its peak because of the consumption of all the oxygen trapped in the porous layer and the potential goes back to its coupling value.
- Figure 13 – d) relates the CP parameters evolution for the immersed period. The current and potential tend to stabilize at a coupling value.

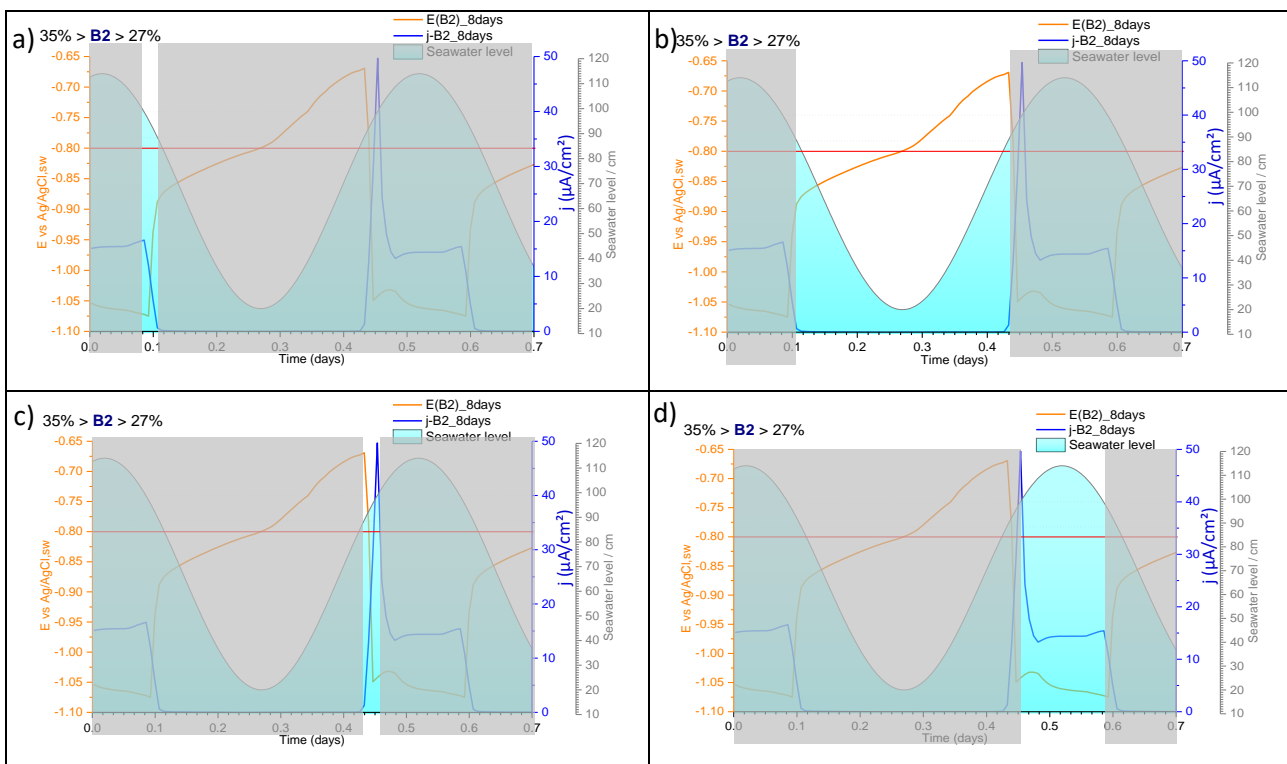


Figure V. 13: How to read the current and potential evolution for 1 cycle. Example chosen for coupon B2 at day 8. a) Emersion – b) Emerged phase – c) Immersion – d) Immersed period

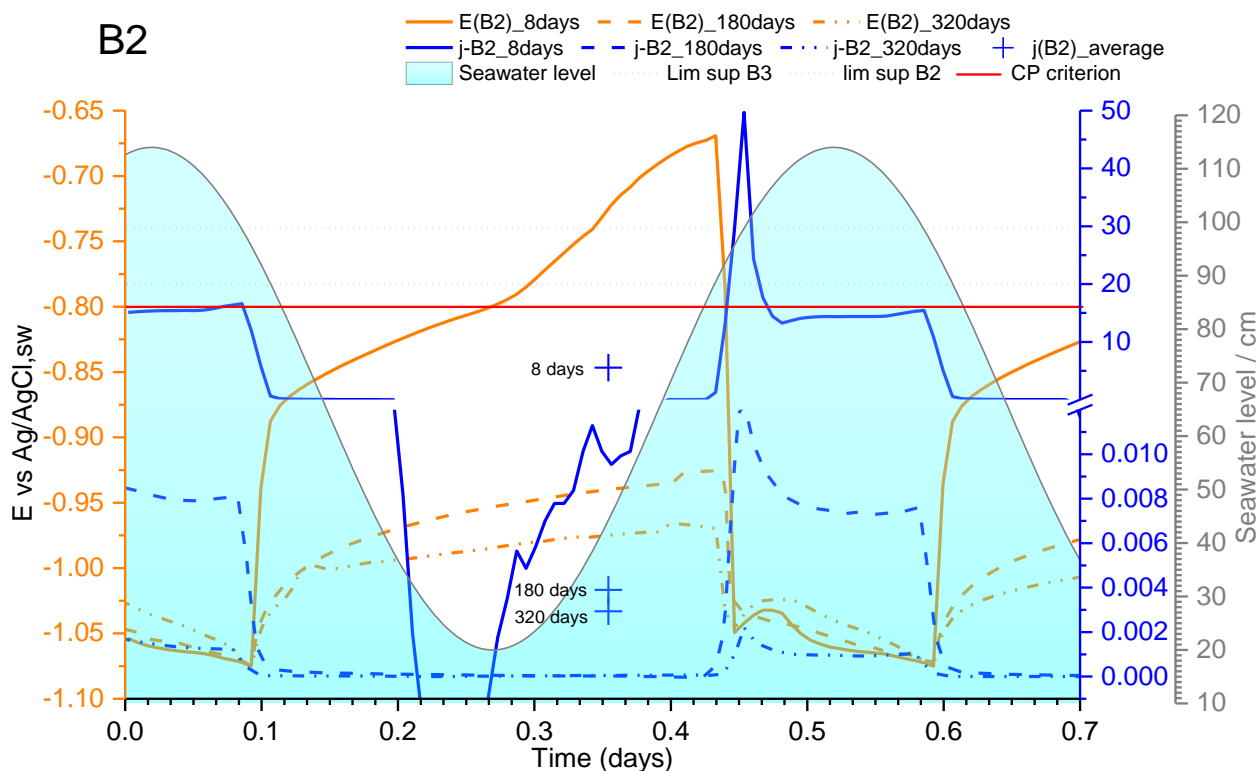


Figure V. 14: Comparison of the current and potential evolution for 1 cycle of coupon B2 at different times

On figure V.13, the CP efficiency is clearly observable for coupon B2. The depolarization is much less important for 180 days than 8 days and this phenomenon is even more noticeable for 320 days. The maximum potential values reached are respectively  $-0.668$  V/Ag/AgCl<sub>sw</sub> for 8 days,  $-0.925$  V/Ag/AgCl<sub>sw</sub> for 180 days and  $-0.967$  for 320 days. After 180 days (6 months) the depolarization range has been divided by 2. The abrupt depolarization caused by the emersion lasts about 12 min to reach  $-0.880$  V/Ag/AgCl<sub>sw</sub> after 8 days while it takes 26 min to reach  $-0.998$  V/Ag/AgCl<sub>sw</sub>. Then, for the 8 days curve, during the depolarization associated with emersion, a noticeable slope variation occurs at mid time of the emersion phase, which is correlated here with the decrease to potential values less negative than  $-0.800$  V/Ag/AgCl<sub>sw</sub>. This increase in potential from  $-0.792$  V/Ag/AgCl<sub>sw</sub> to  $-0.668$  V/Ag/AgCl<sub>sw</sub> must be linked to the access of O<sub>2</sub> to the steel surface allowing the corrosion process to start again till the next immersion. In other word, in the early stages, after 125 min of complete emersion (time determined after the seawater level has gone below the inferior limit of B2), the steel surface is no more protected and corrosion takes place.

However, this hypothesis has to be considered at the whole experiment scale. Indeed, 125 min after the complete emersion of B2 is the moment that also correspond to the lowest seawater level (21 cm). Then, this resumption in corrosion mechanisms must be linked to the rupture of electrolyte continuity because the distance between the coupon and the seawater level is at the longest at this moment. Consequently, no current at all (detectable or not) could run through the sample and the CP was not ensured any more. Conversely, for 180 days and 320 days the depolarization curve associated with emersion did not display any slope variation. However, a slight increase in potential is still noticed after 210 min of complete emersion for both longer times. This might be due to O<sub>2</sub> accessing to the steel surface. It probably took longer than for 8 days because the mineral layer covering the steel surface may hinder O<sub>2</sub> diffusion more than the one formed after 8 days of exposure.

After the complete immersion, at 8 days, the potential slightly increases because of the immersion of the coupon above and then goes back quickly to  $E_{\text{prot}}$ . In contrast, for 180 days and 320 days, the potential takes longer time to reach  $E_{\text{prot}}$  again. Yet, this slight increase in potential was higher for 320 days (maximum of  $-1.032 \text{ V/Ag/AgCl}_{\text{sw}}$  for 8 days vs  $-1.023 \text{ V/Ag/AgCl}_{\text{sw}}$  for 320 days). This phenomenon can be interpreted considering that the mineral layer covering the steel surface acts as a capacitor. The discharge of this capacitor takes longer time for 320 days, which shows that the time constant of this capacitor increases with time exposure. Consistently, it confirms the previous hypothesis of the mineral layer thickening with time.

The current changes are consistent with the potential variations. After 8 days, at the beginning of the emersion, it decreases sharply down to  $0 \text{ mA/cm}^2$  after the emersion phase and remains null for the whole emerged period. Then as soon as water starts to reach B2 surface, the current abruptly increases and reaches its maximum exactly when water reaches the upper limit of the coupon. Afterwards, during the immersed period, the curve displays a rapid decrease down to an almost steady state value ( $14.3 \text{ mA/cm}^2$ ) before the next emersion.

The values and the current range are of completely different order hence the Y axis had to be cut from  $0.01$  to  $0.012 \text{ mA/cm}^2$  to spread the scale of the 180-days and 320-days current vs time curves. This also spreads the slightest variations of the 8-day curve which in this case, has no physical meaning.

The maximum current density observed for 8 days is  $50 \text{ mA/cm}^2$ . It is  $0.012 (\pm 1\%) \text{ mA/cm}^2$  for 180 days and  $0.0023 (\pm 5\%) \text{ mA/cm}^2$ . Their plateaus are at  $0.007 (\pm 2\%) \text{ mA/cm}^2$  for 180 days vs  $9.6 \times 10^{-4} (\pm 13\%) \text{ mA/cm}^2$  for 320 days. Considering the % error of the latter value, it must be analyzed really carefully. With the exposure time and the increasing protective ability of the mineral layer covering the steel surface, the small current variation observable on the 8-day curve corresponding to B1 immersion is not spotted anymore for 180 and 320 days. Then, the current decrease due to emersion follows the same trend as the potential. The 320-day curve display a current decrease before the 180 days curve which in turn starts before the 8 days curve. In addition, as for the potentials, a huge step is spotted between 8 days and 180 days while the curves for 180 days and 320 are close.

Finally, the average current value evolution with time is consistent with the thickening and/or densification) of calcareous layer. The average current decreases with time, and is equal to  $5.71 \text{ mA/cm}^2$  for 8 days,  $0.0039 (\pm 3\%) \text{ mA/cm}^2$  for 180 days and  $0.0028 (\pm 4.5\%) \text{ mA/cm}^2$  for 320 days. In addition, for the 3 exposure times considered, the minimal current measured during the emerged period is  $j = 0$ . This indicates, that the thickening of the mineral layer does not permit to trap enough humidity on the concerned periods to permit a residual current to run through B2. However, its increasing protection level with time is consistent with the enlarged definition of the spread-out CP proposed in the section V.2.1.1 about B3.

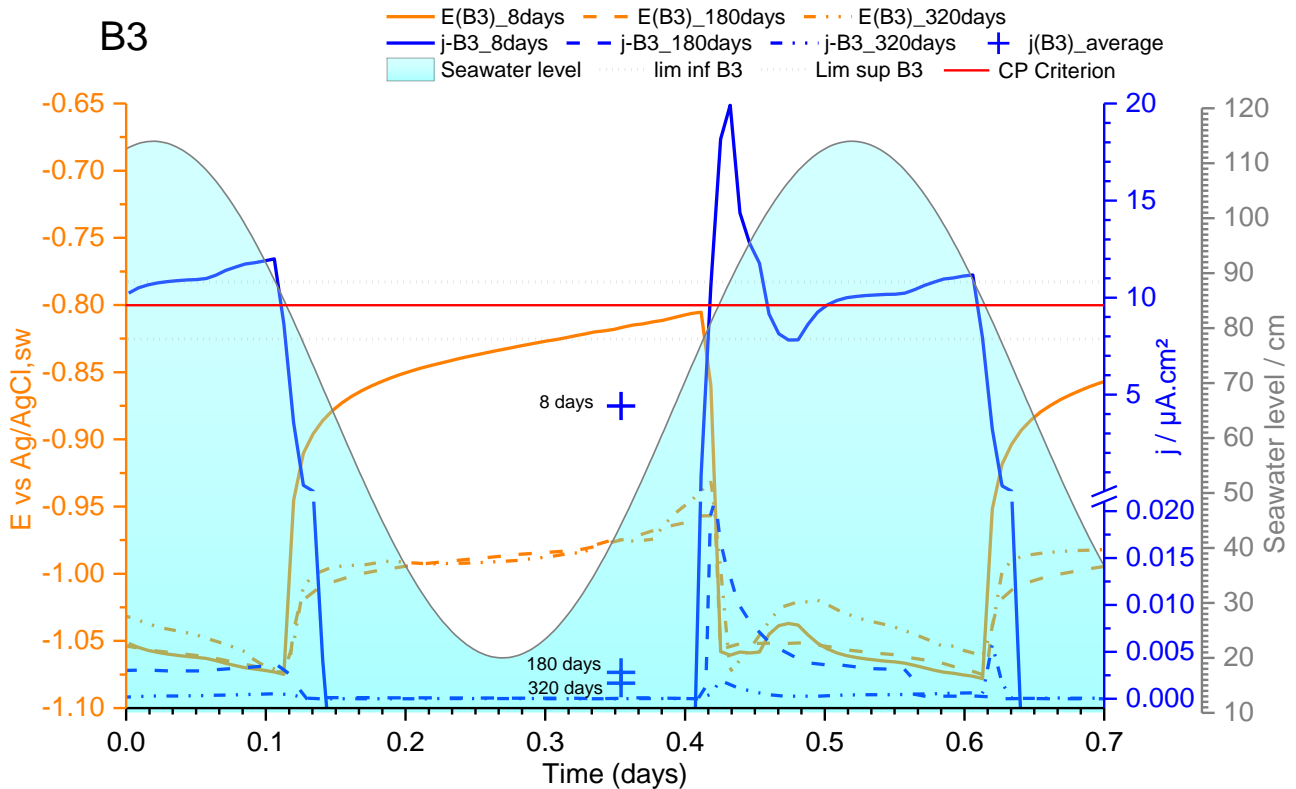


Figure V. 15: Comparison of the current and potential evolution for 1 cycle of coupon B3 at different times

Coupon B3 just below, with higher theoretical immersion rate (from 35% to 42%) presents similar evolution. The current and potential evolution of the 8-day curve will be thoroughly described before comparing it with the longer times.

Because of the emersion phase, the potential abruptly increases from  $-1.075$  V/Ag/AgCl<sub>sw</sub> up to  $-0.909$  V/Ag/AgCl<sub>sw</sub> within 15 min, i.e., the emersion duration. After the emersion phase, the potential curve is shaped as a characteristic depolarization curve, the steel continues to depolarize up to  $-0.803$  V/Ag/AgCl<sub>sw</sub> at the very end of the emerged period. The potential evolution is closely linked to the current evolution. As the water level is decreasing, the current is decreasing too (from 12 to  $0 \mu\text{A}/\text{cm}^2$ ) and consequently the potential increases. Then, the potential starts to decrease during a short period before the beginning of the immersion phase (about 3 min). In the meanwhile, the current density increases rapidly and reaches its highest value ( $20 \mu\text{A}/\text{cm}^2$ ) before the immersion of the whole coupon. This short period is most likely the consequence of the already formed calcareous deposit capillarity strengths attracting seawater and permitting CP to take place before the actual beginning of the immersion. Then, the potential may start to decrease and the current to increase as soon as the sample gets wet, i.e., before the immersion phase. Nonetheless it is possible to suspect the epoxy resin separation between the coupons to limit this phenomenon because of its inherent nature (as observed figure V.12 in the section V.3.1.1). This separation induces unavoidably a discontinuity in the mineral layer (during the first weeks of polarization), interrupting the capillarity strengths attracting the water. This effect might have an impact on steel polarization and CP efficiency. The experimental set up presented here does not permit to state whether this effect is important and could play a role for a long time.

During the immersed phase, the current decreases as the potential tends to stabilize at  $E_{\text{prot}}$ . Two slope variations can be seen in the current decrease before it reaches the immersed minimal value of  $7.75 \mu\text{A}/\text{cm}^2$ . The first one corresponds to the exact moment when B3 is fully immersed and thus the moment when the upper adjacent coupon B2 starts its immersion phase. The second slope variation correspond to 85% of immersion of B2 which might correlate with its maximal current peak. Then, the current curve of B3 reaches a minimum for 70% of immersion of B1 exactly corresponding of the maximum current demand of this coupon. As B1 needs a huge amount of current to be polarized, it decreases the current available for the coupons below (one by one) and even influences their protection potential. Finally, after reaching its minimal value linked to the polarization peak of each coupon above, the current of B3 increases again and so forth as the upper coupons start to emerge.

On the other hand, there was no current running through B3 during the whole emersion time. Another possibility is that the current is so low that the used measurement chain could not detect it. However, the coupon potential does not go back to OCP, and remains below the  $-0.8 \text{ V}/\text{Ag}/\text{AgCl}_{\text{sw}}$  threshold. From these observations, coupon B3 seems protected from day 8, although the protection current falls back to 0 between each cycle. Therefore, the steel surface might be protected and the corrosion rate significantly decrease even when the coupon is emerged. This suggests that the definition of the spread-out CP must be enlarged as the persistence seems not to be linked only to the current protection. Indeed, during the emersion phase and the first moments of the emerged period, the sample dries, the residual humidity trapped in the calcareous deposit layer decreases, the environment close to the coupon is more and more aerated thus the cathodic reaction rate is increased. During this more or less short period, the  $\text{HO}^-$  production increases without any electrolyte renewal, thus sharply increasing the pH and subsequently shifting the OCP of steel to more negative values. The OCP of the metal is actually linked to both  $\text{O}_2/\text{H}_2\text{O}$  and Fe-oxide(whatever is nature)/Fe redox potentials that both decrease, according to Nernst law, with increasing pH. The difference between the protection potential threshold, i.e.,  $-0.8 \text{ V}/\text{Ag}/\text{AgCl}_{\text{sw}}$ , and the OCP in highly alkaline environment may then be relatively low. This increase of pH may then slow down the variation of the OCP and may help keeping the steel exposed to a strongly alkaline, hence less corrosive, environment until the next immersed phase, i.e. until CP is re-activated.

The 180-days and 320-days curves display similar features for the whole emersion and emerged period. The depolarization associated with emersion has the same slope (same time response to depolarize) up to  $-1.00 \text{ V}/\text{Ag}/\text{AgCl}_{\text{sw}}$  for 320 days and  $-1.02 \text{ V}/\text{Ag}/\text{AgCl}_{\text{sw}}$  for 180 days. Then, both curves follow the same depolarization rate up to  $-0.933 \text{ V}/\text{Ag}/\text{AgCl}_{\text{sw}}$  for 320 days and  $-0.954 \text{ V}/\text{Ag}/\text{AgCl}_{\text{sw}}$  for 180 days. a distinct difference is observable between 180 days and 320 days during the immersed period. With the flood tide, the variations of potential induced by the immersion of upper coupons is higher for the 320-days curve than for the 8-days or 180-days curve. For 320-days curve, conversely to the other curves and because of the capacitor time constant of the mineral layer covering the coupon, the potential slowly decreases and does not go back to  $E_{\text{prot}}$  before the next immersion.

The variations of current are rather similar to those of B2. The 8-days curve shows really high values while smaller comparable values are observed for 180 and 320 days. The 320-days curve will be cautiously analyzed because its values present more than 10% of error.

After the brutal current increase due to the immersion phase, the 180-days curve reaches a maximum of  $0.020 (\pm 1\%) \mu\text{A}/\text{cm}^2$  and then decreases down to a plateau at  $0.003 (\pm 4\%) \mu\text{A}/\text{cm}^2$ . After 97 min of complete immersion, the 180-days current curve goes down to  $4.26 \times 10^{-4} (\pm 29\%) \mu\text{A}/\text{cm}^2$ , which corresponds to the current plateau of the 320-day curve. The too great measurement error due to the

chain measurement of the experimental device does not permit to extract reliable accurate conclusions about this phenomenon. In addition, the 320-days curve displays a current density peak ( $0.0058 \mu\text{A}/\text{cm}^2$ ) at the end of the emersion phase which is not observed for the previous cycle. This might be a measurement artefact. On the other hand, the average current densities for coupon B3 clearly shows the progressive impact of CP with time, associated in particular with the growth of the calcareous layer. There is once again a huge difference between the early-stage average current value and the 180-days and 320-days curves:  $4.39 \mu\text{A}/\text{cm}^2$  after 8 days,  $0.003 (\pm 4.5\%) \mu\text{A}/\text{cm}^2$  for 180-days curve and  $0.0016 (\pm 8\%) \mu\text{A}/\text{cm}^2$  for 320-days curve. Again, for B3, on the 3 exposure times considered, the minimal current measured during the emerged period is  $j = 0$ .

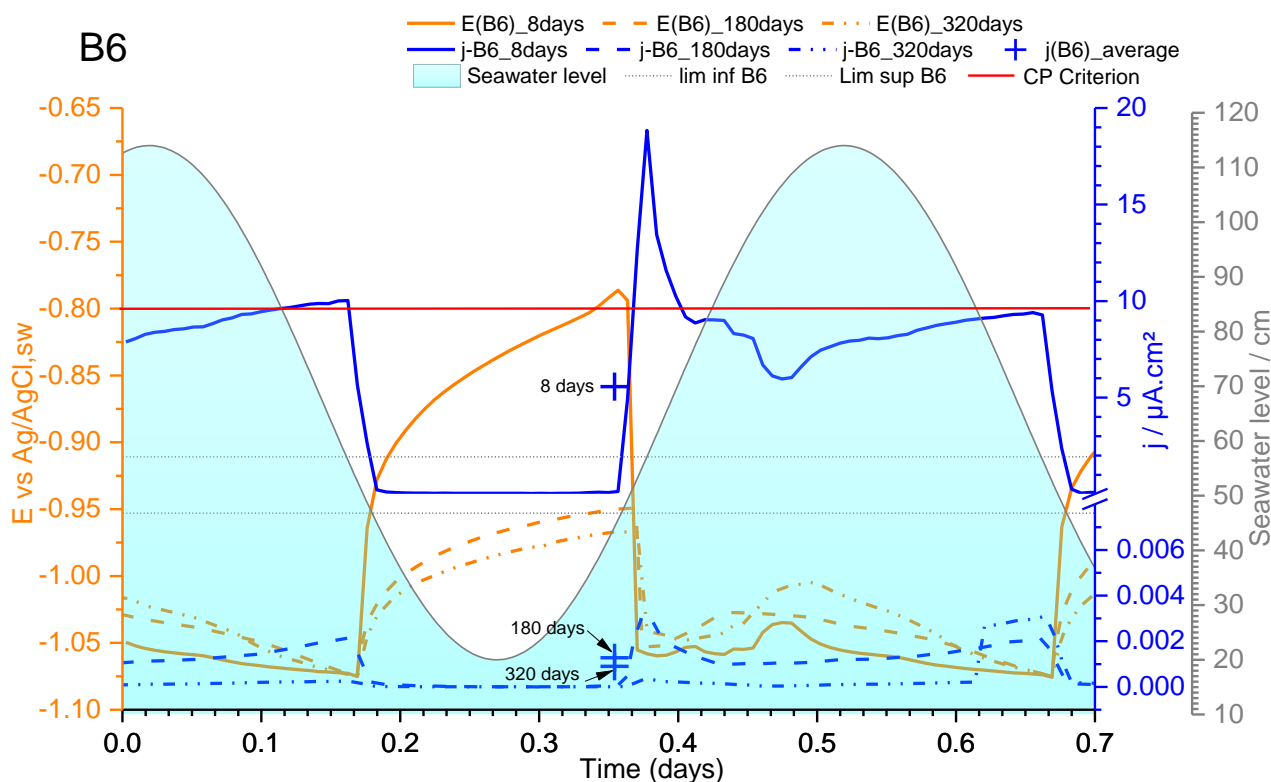


Figure V. 16: Comparison of the current and potential evolution for 1 cycle of coupon B6 at different times

Figure V.16 focuses on the coupon B6 in the low part of column B. As previously, its early stages behavior will be carefully described and discussed prior to compare it with the current and potential evolution of longer times.

The emersion phase leads to a rapid decrease of the current down to  $0.07 \mu\text{A}/\text{cm}^2$  and a rapid increase of the potential up to  $-0.950 \text{ V}/\text{Ag}/\text{AgCl}_{\text{sw}}$ . The potential increases slightly and regularly afterwards up to  $-0.820 \text{ V}/\text{Ag}/\text{AgCl}_{\text{sw}}$  before the coupon is immersed again, exactly as the potential of B3 does. The variation of the potential is really similar to the expected depolarization following an interruption of CP. It could easily illustrate the evolution of the coupon OCP after a CP interruption. Note that for coupon A6 of the column A (permanent CP for 9 months), the potential evolution (not shown here) once the coupon is no more immersed begins like observed for B6. After a sharp increase due to the emersion, increases slowly from  $-0.950$  to  $-0.860 \text{ V}/\text{Ag}/\text{AgCl}_{\text{sw}}$ . Then, a rapid increase up to  $-0.400 \text{ V}/\text{Ag}/\text{AgCl}_{\text{sw}}$ , may indicate the complete drying of the electrode. The final potential value would then have no meaning in this case.

Anyway, the current and potential evolutions for B6, presented in figure V.16, are very similar to those presented in figure V.15 for B3: similar depolarization shaped curve, similar current increase up to  $18.9 \mu\text{A}/\text{cm}^2$  ( $20.0$  for B3) starting a short time before immersion phase and reaching its maximum at 80% of complete immersion. Each subsequent current decrease fluctuation exactly corresponds to the associated potential fluctuation, both linked to the progressive immersion of the coupons above. In addition, the current flowing through B6 never reached 0, the (absolute) smallest value measured being  $0.07 \pm 2\% \mu\text{A}/\text{cm}^2$ . According to these observations, CP seems efficient here, despite of a slight apparent depolarization up to  $-0.78 \text{ V}/\text{Ag}/\text{AgCl}_{\text{sw}}$  which is still included in the error interval on the potential of the  $\mu$ -reference electrode due to a possible evaporation of water. During the emerged period, a small cathodic current is running through the coupon but it may be too small to polarize the coupon down to the measured potential. However, as noted for B3, the coupon may remain protected due to the synergetic effect of the high production of  $\text{HO}^-$  ions coupled with the small residual CP current. Moreover, as observed in Chapter 4, slightly insufficient CP (i.e., potential between  $-0.75$  and  $-0.8 \text{ V}/\text{Ag}/\text{AgCl}_{\text{sw}}$ ) can provide protection, in particular with the growth of a protective mineral (corrosion products + calcareous deposit) layer with time.

In addition, as for both previous coupons, 180-days and 320-days curves present values of the same order of magnitude. The sharp potential increase due to emersion displayed on the 8-days curve is slower for 180 days and even slower after 320 days of exposure. Yet, contrary to the previous curves, this depolarization has the same starting point whatever the exposure time considered. For 8 days, a slope variation could be observed at the end of the emerged phase. As for B2, this variation is more or less correlated with the decrease to potential values less negative than  $-0.800 \text{ V}/\text{Ag}/\text{AgCl}_{\text{sw}}$ . Since the 180-days and 320-days curves do not reach this threshold, no brutal slope variation is spotted. 180-days depolarization displays the same speed as the 320-days curve but with higher values. The potential increases up to  $-0.948 \text{ V}/\text{Ag}/\text{AgCl}_{\text{sw}}$  after 180 days vs  $-0.968$  after 320 days. Then, like for the upper coupons, after the immersion, the variations of potential have a wider range for the 320-days curve, indicating once again a higher capacitor time constant capacity of the mineral layer because of its thickening and/or densification. Consistently, the 3 curves presented here reach their maximum at different times. First, the 8-days curve reaches a local maximum while the 180-days curve potential increases and only after the 320-days curve reaches its maximum value. This tends to confirm the increasing time constant of the capacitor associated with the mineral layer covering the coupon.

The current curves display complementary features, with a huge step between the 8-days curve and the 180-days and 320-days curves. The maximum current measured at the immersion peak for the 180-days curve is  $0.0033 (\pm 4\%) \text{ mA}/\text{cm}^2$  and  $3.74 \times 10^{-4} (\pm 33\%) \text{ mA}/\text{cm}^2$  for the 320-day curve. Once again at the end of the emersion, the current increases for the 320-days curve. Since this phenomenon does not occur for the previous cycles, it seems to be an isolated phenomenon or measurement artefact. Yet the average currents testify for the progressive effects of CP. Coupon B6 needs less and less current to remain polarized as the exposure time increases:  $5.58 \text{ mA}/\text{cm}^2$  after 8 days,  $0.0013 (\pm 10\%) \text{ mA}/\text{cm}^2$  after 180 days and  $8 \times 10^{-4} \text{ mA}/\text{cm}^2 (\pm 16\%)$  for 320 days. The currents measured for B6 during the emerged phase are not reliable as their error intervals overpass 500%. However, it's still possible to say that even if the measure is not reliable, it does not mean that there is no current running through the coupon during the emerged phase but that the residual current is too low to be estimated with this measurement chain.

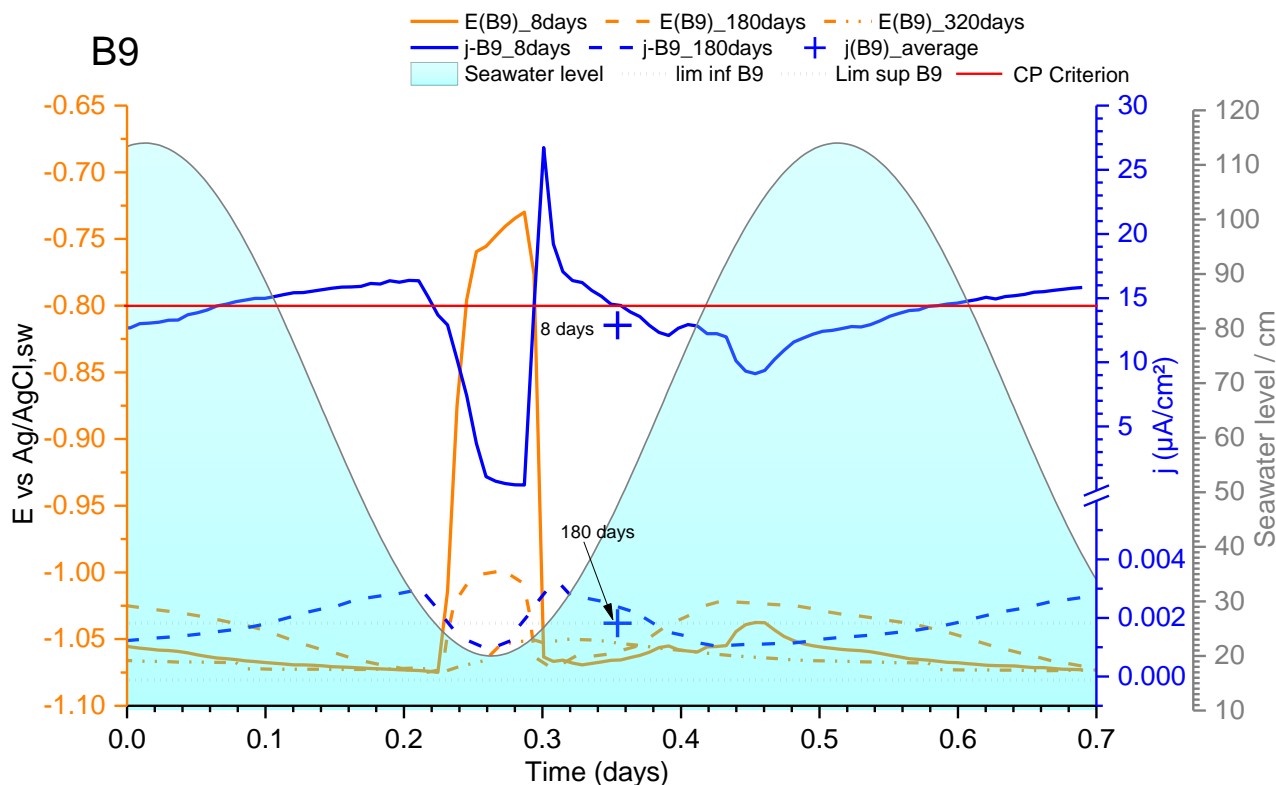


Figure V. 17: Comparison of the current and potential evolution for 1 cycle of coupon B6 at different times

Figure V.17 deals with B9 coupon. The minimum measured current value is about  $0.3 \mu\text{A}/\text{cm}^2$ . Coupon B9 is never totally emerged as it can be seen in Figure V.17. For the 8 day curve, when its short emersion period (about 58 min) begins, its potential increases rapidly to  $-0.800 \text{ V}/\text{Ag}/\text{AgCl}_{\text{sw}}$ , because of the emersion. Then the potential continues to increase, with smaller slope, up to  $-0.730 \text{ V}/\text{Ag}/\text{AgCl}_{\text{sw}}$  at the end of the emerged period. During the start of the emersion, the current decreases (simultaneously to the potential increase), down to a low value ( $7.43 \mu\text{A}/\text{cm}^2$ ) before decreasing even faster and lower ( $1.12 \mu\text{A}/\text{cm}^2$ ) till the end of the mid tide, i.e., at about 50% of its height. Then, during flood tide, the current still decreases but very slowly, down to an average of  $0.47 \mu\text{A}/\text{cm}^2$  at the end of the emerged phase. Afterward, the current quickly reaches its maximum right after the total immersion because of the  $\text{O}_2$  pulse associated with the  $\text{O}_2$  molecules entrapped in the pores of the calcareous layer. Then, as the oxygen is consumed and the coupon is polarized, the current decreases with complex variations characteristic of the successive immersion of the other coupons. The potential quickly goes back to  $-1.075 \text{ V}/\text{Ag}/\text{AgCl}_{\text{sw}}$ , and the slight variations also testify for the progressive immersion of the whole column.

With the increasing exposure time, the potential variations are becoming less and less observable as if the surface was always entirely immersed. The 8-days curve present a sharp slope variation during the emerged phase which could be linked to water surface motion strongly aerating the surface and exposing the  $\mu$ -reference electrode to air. After 180 days, the coupon depolarizes up to  $-0.999 \text{ V}/\text{Ag}/\text{AgCl}_{\text{sw}}$  at its maximum and  $-1.050 \text{ V}/\text{Ag}/\text{AgCl}_{\text{sw}}$  after 320 days. Then, during immersion, the potential varies with the successive immersion of the upper coupons. For the 180-days curve, the potential goes up to  $-1.020 \text{ V}/\text{Ag}/\text{AgCl}_{\text{sw}}$  and takes time to go back to  $E_{\text{prot}}$ . The 320-days curve does not even seem influenced by this phenomenon and still tends to slowly go back to  $E_{\text{prot}}$  after the slight depolarization of the immersion. Because the current demand of all coupons has considerably

decreased with time, it seems plausible that the influence of the upper coupons finally becomes negligible. The current evolution permits to clearly see the CP effect on longer times. Although the current evolution after 320 days could not be analyzed here, the comparison is still valid. The current evolution curve after 180 days of exposure displays smooth variations compare to the 8-days curve. The current density variation follows the tide level, reaching its maximum for the immersion  $0.0031 (\pm 4\%) \text{ mA/cm}^2$  and its minimum for the half emersion (low water level) and the polarization during its immersed period ( $0.00105 \pm 12\% \text{ mA/cm}^2$ ).

From the observation made above and the values extracted from the analysis of the graphs (also reported in table V.8), from the 3<sup>rd</sup> coupon (which immersion zone is located between 34.8% and 42.2%) CP seems to remain efficient even at low tide as soon as 8<sup>th</sup> day. At day 180, the whole column remains polarized below the protection potential threshold even during the emerged phase. This extremely slow depolarization, particularly for the upper samples B1 & B2, may be explained by a high  $\text{HO}^-$  production during the wet phase. As mentioned above, this is the period when the mineral layer covering the steel surface entraps residual humidity due to its inherent capillarity strengths, before the immersion phase and after the emersion phase. Actually, after the emersion phase, this phenomenon is most likely delaying the drying of the residual humidity. This allows a low current, responsible of the cathodic reaction reducing  $\text{O}_2$  into  $\text{HO}^-$ , running through the coupon. In addition, from day 8 (time) and coupon B6 (space), the CP current never goes back to 0. This enhances CP persistence as the cathodic reaction is always taking place, but this can also skew the results as this current persistence might be possible because of the proximity of the seawater level enhancing the persistence of electrolytic continuity. A doubt remains about the ability of the anode disposed on a wharf to polarize the steel surface located at mid tide zone in a tidal zone as wide as the La Rochelle tidal zone as seen in chapter 3. This residual current is not observed for the longer times because the system used for current did not permit the detection of so low currents. Yet, it is reasonable to assume its existence even though it was not observed.

Table V. 6: Synthesis of the current and potential evolutions for 8, 180 and 320 days

Theoretical immersion rate	B2			B3			B6			B9		
	26.6% to 34.8%			34.8% to 42.2%			49.4% to 56.6%			84% to 100%		
Immersed period (min)	95			124			204			662		
Exposure time (days)	8	180	320	8	180	320	8	180	320	8	180	320
$E_{\max}$ (V/Ag/AgCl <sub>sw</sub> )	-0.668	-0.925	-0.967	-0.804	-1.02	-1.0	-0.786	-0.950	-0.967	-0.730	-0.999	-1.050
$ j_{CP,\max} $ (mA/cm <sup>2</sup> )	50	0.012 ± 1%	0.0023 ± 5%	19.9	0.020 ± 1%	0.0021 ± 6%	18.9	0.0033 ± 4%	0.00041 ± 33%	26.8	0.0031 ± 4%	
$ j_{CP,\min,emerged} $ (mA/cm <sup>2</sup> )	0	0	0	0	0	0	0.04 ± 2%	N/A	N/A	0.47	0.001 ± 13%	
$ j_{CP,average} $ (mA/cm <sup>2</sup> )	5.71	0.0039 ± 3%	0.0028 ± 4.5%	4.4	0.0026 ± 4.5%	0.0016 ± 8%	5.5	0.0013 ± 10%	0.00080 ± 16%	12.9	0.0018 ± 7%	

On the other hand, it is clear that with time CP could protect, at least from the current and potential point of view, the less immersed coupons in this case. Nevertheless, like for B6, the downsizing of the tidal zone may enhance CP persistence by increasing the probability of electrolyte continuity.

Finally, to be complete, this approach must give information about the mineral layer composition to better understand the phenomena which occurred on the coupons.

### V.3.2 Mineral layer characterization

The observation of the mineral layer covering the coupons and its evolution along the column may give some information or clues about the processes that took place on the steel surfaces. After 9 months for column A and 16 months for column B, the coupons were firstly thoroughly analyzed via  $\mu$ -Raman spectroscopy to better observe the layers morphology and stratification and determine the location of the various detected compounds. Afterwards, the coupons were scrubbed to collect the whole mineral layer prior to crush it to powder and homogenize it to finally analyze the obtained powder via XRD.

#### V.3.2.1 Visual observation of the coupons previously analyzed from columns A & B after 9 and 16 months of exposure to tidal zone

The aim of this section is to deal with the information possible to harvest after 9 and 16 months of experiment only by observing the coupons of the columns A and B. Only coupons B2, B3, B6 and B9, detailed in section V.2.1, and the corresponding coupons of column A, will be detailed here.

From visual aspect (photographs presented in figure V.15), coupons A2 and B2 seem rather different. A2 is covered with an inhomogeneous layer. Mainly 3 strata could be distinguished: a black stratum close to steel surface, a blistering brown stratum and a white layer that has formed at the lower part of the coupon. This white layer seems to fill the lower blisters of the brown stratum and even overflow from the blisters. B2, on the other hand, displays an overlying white stratum at the upper part. Some blisters could be spotted too but the color could not be distinguished as the white layer covered it. Then, in the middle of the coupon, a black stratum in contact with the steel surface is seen. Finally, on the lower part of the coupon, a pulverulent white / beige stratum overlying the black one is present.

According to many studies of P. Refait et al. [7], [13]–[15], [16], who studied corrosion and cathodic protection of carbon steel in seawater and in tidal zones, the main corrosion products that form are:

- Magnetite  $\text{Fe}_3\text{O}_4$ , a black compound which is favored by cyclic immersion and cathodic protection. It is the main residual corrosion product forming under CP.
- Mackinawite, marker of SRB activity as the bacteria produce sulfide species, which precipitate with  $\text{Fe}^{\text{II}}$  ions to form  $\text{FeS}$  in deaerated environment.
- Sulphated green rust (and or carbonated green rust under CP) precipitates onto the steel surface in constant immersion as it was found in chapter 3 and in [7], [9], [13], [17]. It requires deaerated conditions to persist, as it is mainly composed of  $\text{Fe}^{\text{II}}$ . In aerated conditions, it is oxidized into magnetite and oxyhydroxides.
- Oxyhydroxides as goethite and lepidocrocite, brown / orange  $\text{Fe(III)}$  compounds, could be found in aerated environment.
- Aragonite ( $\text{CaCO}_3$ ) is a marker of cathodic zones as it forms in the outer part of the mineral layer in these zones. It is also the main component of the calcareous deposit resulting from CP by galvanic anode in seawater [3], [12], [18].
- As demonstrated in chapter 3 and in various articles about CP of carbon steel in tidal zone [7], [17], brucite could also precipitate under CP by galvanic anode in the tidal zone because of specific conditions, i.e., large pH increase, high dioxygen flow, etc.

So, considering this information, this strata organization suggests that the black layer is the first one to precipitate and / or the one with the lower oxidation number of Fe. In addition, A2 & B2 are rather high in the tidal zone, with an immersion rate between 26.6% and 34.8%. There are thus, on average, in a rather aerated environment that does not allow green rust persistence nor mackinawite formation. This black inner stratum could then be mainly composed of magnetite. Then, the blistering brown layer, clearly visible for A2 and barely discernible for B2, shows itself as the outer stratum of the corrosion product layer. It is probably mainly composed of goethite and lepidocrocite, both  $\text{FeOOH}$  phases resulting from the oxidation of green rust compounds. The corrosion mechanism proposed by Refait et al. [15] tends to indicate that this outer layer might be composed of a larger amount of goethite. Finally, the white layer seems to be calcareous deposit, which can form on the magnetite black inner layer, as magnetite is an electronic conductor, more precisely a semiconductor with low resistivity [19]. These photographs also suggest that the calcareous deposit, as a marker of CP, started to precipitate after a more or less long period of corrosion. This is consistent with the current and potential evolution described in section V.2.1.

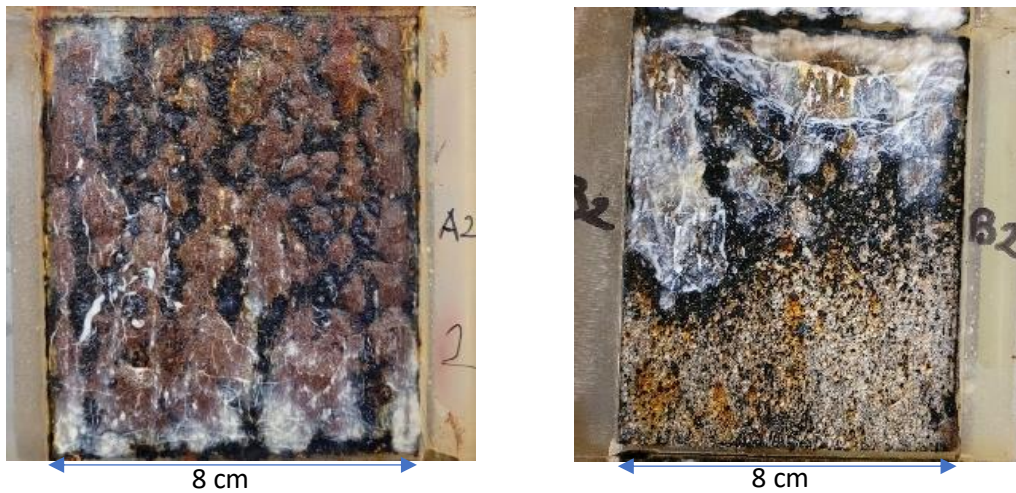


Figure V.18: Visual observation of upper coupons A2 (on the left) and B2 (on the right)

The images of coupons A3 & B3 are displayed in figure V.16. The theoretical immersion rates are now 34.8% to 42.2%. Once again, the visual aspects are really different. Indeed, the main difference lies in the amount of the outer white layer. While A3 is almost totally covered with this white layer, only a few areas are covered with this white compound on B3. Otherwise, the stratification seems similar on both samples with the same black and adherent layer overlaid by the white / beige rather pulverulent layer described above. In addition, the absence of the brown blistering layer, supposed to be composed of oxyhydroxides (and mainly goethite) must be noted. Yet, some brown traces can be spotted among this white / beige layer (mostly on B3). Finally, the thorough visual analysis of coupons A3 and B3 does not permit to visually detect corrosion product except for the brown spots and the black inner layer supposed to be magnetite, a residual product of CP whose formation is enhanced by cyclic immersion. This corrosion product combination may indicate a low corrosion rate compared to the previous coupons. The other outer white stratum seems to be the calcareous deposit with aragonite and probably brucite too. Consistently with the low amount of corrosion product, the large proportion of what seems to be 2 different compounds of calcareous deposit (most probably aragonite and brucite) tends to indicate that CP was efficient during most part of the experiment.

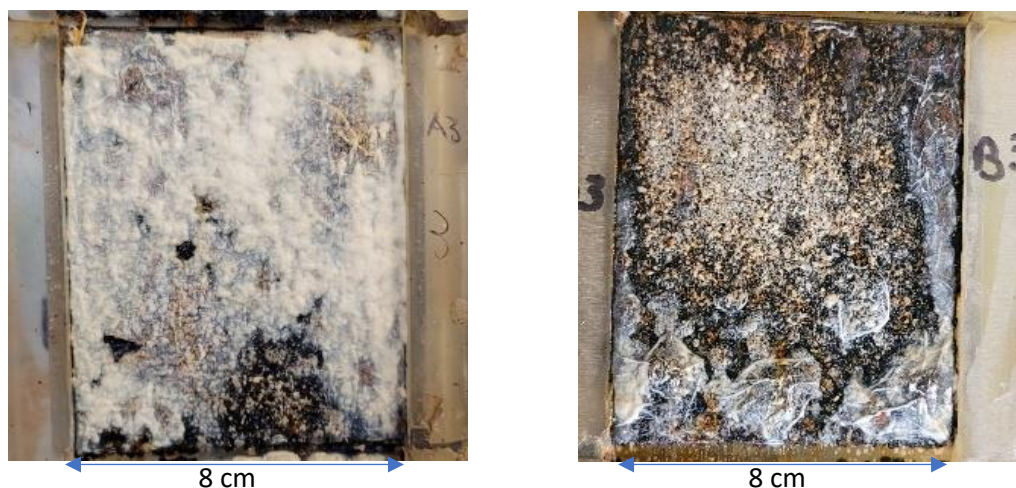


Figure V.19: Visual observation of coupons 3 from columns A (on the left) and B (on the right)

Coupons A6 & B6 are really similar, as shown in figure V.17. They are mainly covered with the magnetite black stratum adherent to the steel surface and on top of it, the pulverulent aragonite white beige stratum with really few brown traces of oxyhydroxides. As expected regarding the theoretical immersion rate from 56.6% to 64.6% of these coupons, from visual observation, CP seems efficient here as no evident markers of active corrosion are observed.

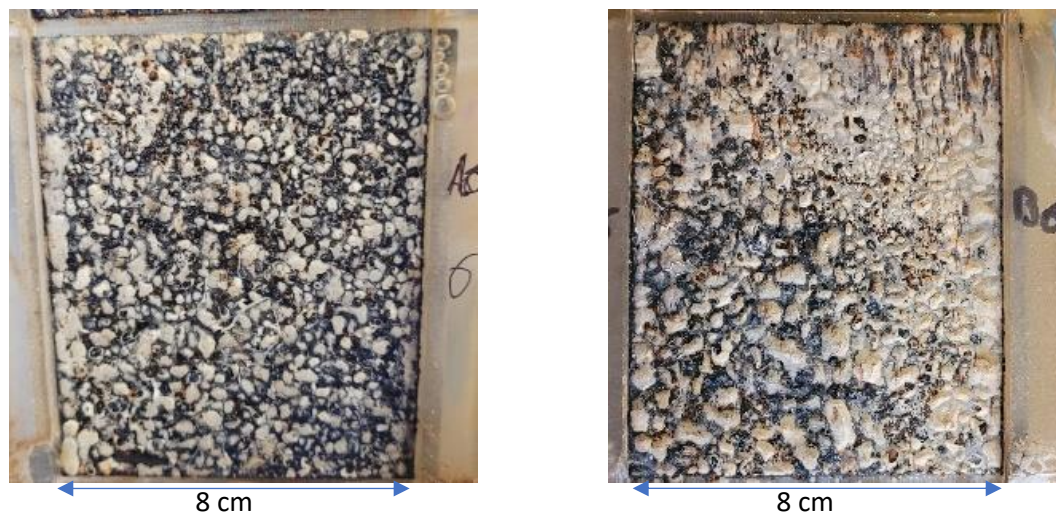


Figure V. 20 : Visual observation of coupon 6 from column A (on the left) and B (on the right)

Finally, the last level studied previously, with 84% to 100% of immersion rate, corresponds to coupons A9 & B9 (figure V.18). These coupons are similar and have a really different aspect from the others. However, no clear difference is noticed between the upper half part of the coupon subjected to cyclic immersion and the lower half part subjected to permanent immersion. Both are covered with a white almost transparent layer with large white/yellow blisters in some places. On those coupons, the magnetite black layer is not observed or in really few places where this white translucent layer was unexpectedly scrubbed during the experiment. Around the  $\mu$ -reference electrode, a black layer is spotted. In addition, on top of the calcareous deposit stratum, some dark green black traces are observed. This is most likely marine fouling or marine mud rather than green rust. Green rust forms in contact with steel and as mentioned above, this corrosion product is highly reactive to  $O_2$ . Finally, the features observed here suggest a high level of CP efficiency strongly decreasing the residual corrosion rate, which led to the formation of a thin film of magnetite, the main corrosion product usually observed under CP, below the calcareous deposit.

All the assumptions made from this visual analysis are based on experience and literature according to the corrosion mechanism in tidal zone and the CP influence on this corrosion process. This led to propose the presence of some of the corrosion products knowing their color and their formation mechanism to estimate the probability to find them according to the concerned theoretical immersion rates. Yet, these hypotheses are only speculations as long as the detection of these compounds is not confirmed by XRD or  $\mu$ -Raman spectroscopy. The characterization of the mineral layers is described in the following.

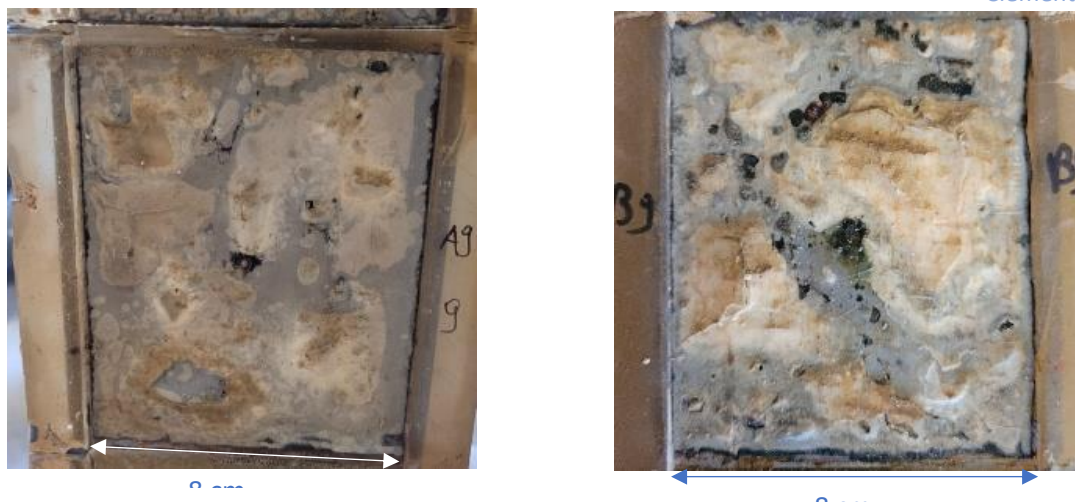


Figure V. 21: Visual observation of the lower coupon from column A (on the left) and B (on the right)

### V.3.2.2 Characterization of the mineral layer (XRD and Raman analysis)

The aim of this section is to confirm (or not) the hypotheses made above with the current and potential evolution and the visual analysis after the experiment. The mineral layer of both columns A (9 months experiment) and B (16 months experiment) were analyzed. XRD patterns are presented in figures 19 and 20, Raman spectra are presented in figures 21-23.

XRD results for all 10 coupons are displayed according to four zones: the higher part of the columns (Coupons 1 & 2), the mid-high part (coupons 3-5), the mid-low part (coupons 6-8) and the lower part (coupons 9 & 10). For each zone the diffractogram of the previously presented coupon is in full line and the diffractograms of the other coupons of the zone are displayed with dash lines to lighten the presentation and still allow comparison between coupons.

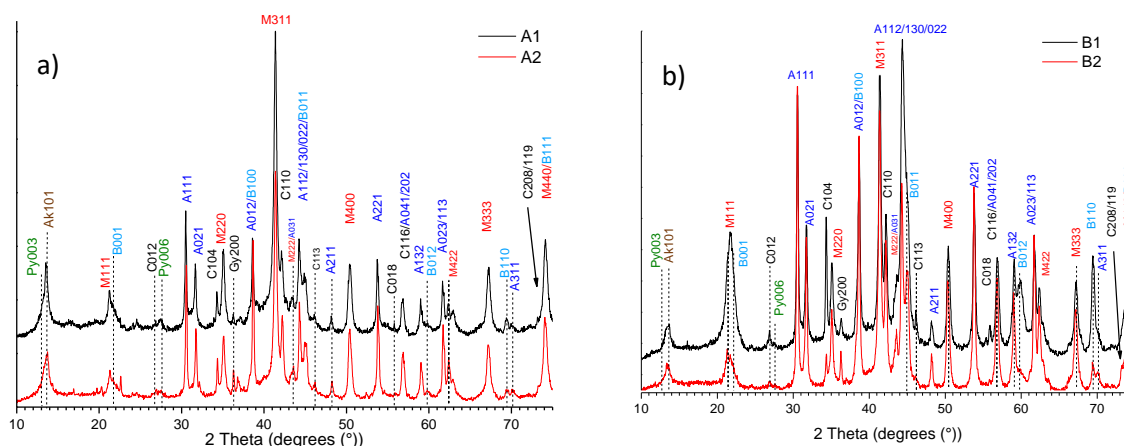


Figure V. 22: XRD analysis of the higher part of the column – a) coupons A1 & A2 – b) coupons B1 & B2

Coupons 1 and 2 of both columns A and B (see figure V.19) display similar characteristics, the main compounds identified via XRD analysis are magnetite  $\text{Fe}_3\text{O}_4$ , aragonite  $\text{CaCO}_3$ , brucite  $\text{Mg}(\text{OH})_2$ , and calcite  $\text{CaCO}_3$ . The most intense peak for A1 & A2 is M311, the main diffraction peak of magnetite. Magnetite is the main residual corrosion product and moreover, its precipitation is enhanced by the cyclic immersion occurring in the tidal zone. Indeed, during the emersion phase and the first stages of the emerged phase, previously formed green rusts could be oxidized to magnetite and oxyhydroxides (goethite  $\alpha\text{-FeOOH}$  and lepidocrocite  $\gamma\text{-FeOOH}$ ). Then, during the first stages of the immersed period,

lepidocrocite could be reduced to magnetite [7], [9], [15]. Therefore, magnetite can come from both residual corrosion process and tidal corrosion process briefly described above. The second most intense peak is A111, the aragonite main diffraction peak. Aragonite is a  $\text{CaCO}_3$  polymorph which precipitation is a direct consequence of CP. As the local interfacial pH increases because of  $\text{O}_2$  reduction, then the carbonic equilibrium is shifted in the sense of  $\text{CaCO}_3$  precipitation [20], [21]. In addition, some brucite peaks were found too, confirming the CP efficiency after a certain exposure time. As previously discussed, (cf. chapter 3) and as it was observed in 2013 and 2015 by P. Refait et al. [7], [17], brucite could precipitate under the action of CP by galvanic anode in the tidal zone. According to the potential of the coupons and the decreasing current needed to protect the coupon, the required minimal pH of 9.3 for brucite to precipitate may not be reached only due to the coupling with the galvanic anode [11]. Nevertheless, considering the hypothesis of residual humidity trapped in the mineral layer in electrolytical continuity with the bulk electrolyte, the chemical conditions are changed. In this case,  $\text{O}_2$  reduction is still active, continuously producing  $\text{HO}^-$  within the residual humidity without electrolyte renewal, thus the local pH may strongly increase. Firstly, a part of the  $\text{Ca}^{2+}$  ions present in the electrolyte film covering the steel surface is consumed, increasing the  $[\text{Mg}^{2+}]/[\text{Ca}^{2+}]$  ratio and then, as the pH still increases,  $\text{Mg}(\text{OH})_2$  precipitates. This mechanism is at the same time enhanced and limited by the evaporation of water. Indeed, as seawater evaporates,  $\text{Mg}^{2+}$  and  $\text{Ca}^{2+}$  (if not already consumed) concentrations increase. On the other hand, as water gradually evaporates, the electrolytical link is weakening, decreasing  $\text{HO}^-$  production down to 0, which obviously limits brucite precipitation.

Many peaks of calcite were also found which was rather unexpected as calcite precipitation is inhibited in natural seawater because of  $\text{Mg}^{2+}$  ions [22], [23]. In the previous chapters, calcite was either not found or came from marine fouling and shellfish. In the present case, no shellfish were observed except for A10 and B10 where calcified marine worms were observed. In addition, the seawater of the experimental set up presented in section V.1.1 was coming from a larger tank overflow upstream from the seawater inlet. This means that seawater was more or less decanted prior to reach our experimental tank. Consequently, the major part of marine fouling and shellfish fell in the bottom of the first tanks, which limited the source of calcite. Yet, as the seawater used for the experiment was natural seawater coming from the English Channel, smaller marine living organisms should have reached the tank with the coupons. As it has already been demonstrated, some marine bacteria strain could favor the formation of calcite in seawater [24], [25].

The identification of two compounds remain uncertain as really few peaks were clearly identified: Pyroaurite, a magnesian residual corrosion product induced by CP is barely detected with Py003 and Py006 main diffraction peaks. The first peak is convoluted with another one and the second has a really low intensity which barely allows its detection. Yet, its presence could be consistent with the experimental conditions the coupons were subjected to.

The presence of akaganeite, a corrosion product typical of chloride enriched environment, is also assumed, via the diffraction peak Ak101 identified at  $13.54^\circ$ . However, only one peak is not enough to affirm its presence in the mineral layer. So, only from the XRD analysis, the akaganeite detection could not be ascertained. Akaganeite could come from the previously described blisters. Assuming they might trap seawater due to their shape, the contained electrolyte enriches in  $\text{Cl}^-$  ions with the drying and the CP is disconnected, all the conditions for akaganeite formation are met.

On the other hand, B1 & B2 (figure V.19 – b) display almost the same features except for the intensity ratio between aragonite and magnetite. They are both the compounds with the most intense peaks

but for B1,  $A_{112} > M_{311}$  and for B2,  $A_{111} > M_{311}$ . Yet magnetite has been largely detected and there is no doubt of its abundance on the coupons. It is important to keep in mind that no precise quantification information can be extracted from this observation. Indeed, the analysis time for the presented diffractograms was rather quick in order not to oxidize the compound susceptible to react with  $O_2$  during the analysis, thus it does not allow performing Rietveld analysis to precisely determine the quantity of each phase. In addition, although the scrubbing of the surfaces has been done thoroughly it was not perfect and for coupons at levels 1 & 2 a part of the black inner layer (the magnetite stratum) remained on the steel and could not be analyzed. Observation of the intensity ratio between the compounds also depends on the amount of mineral layer left on the coupon, hence only trends can be extracted from these diffractograms.

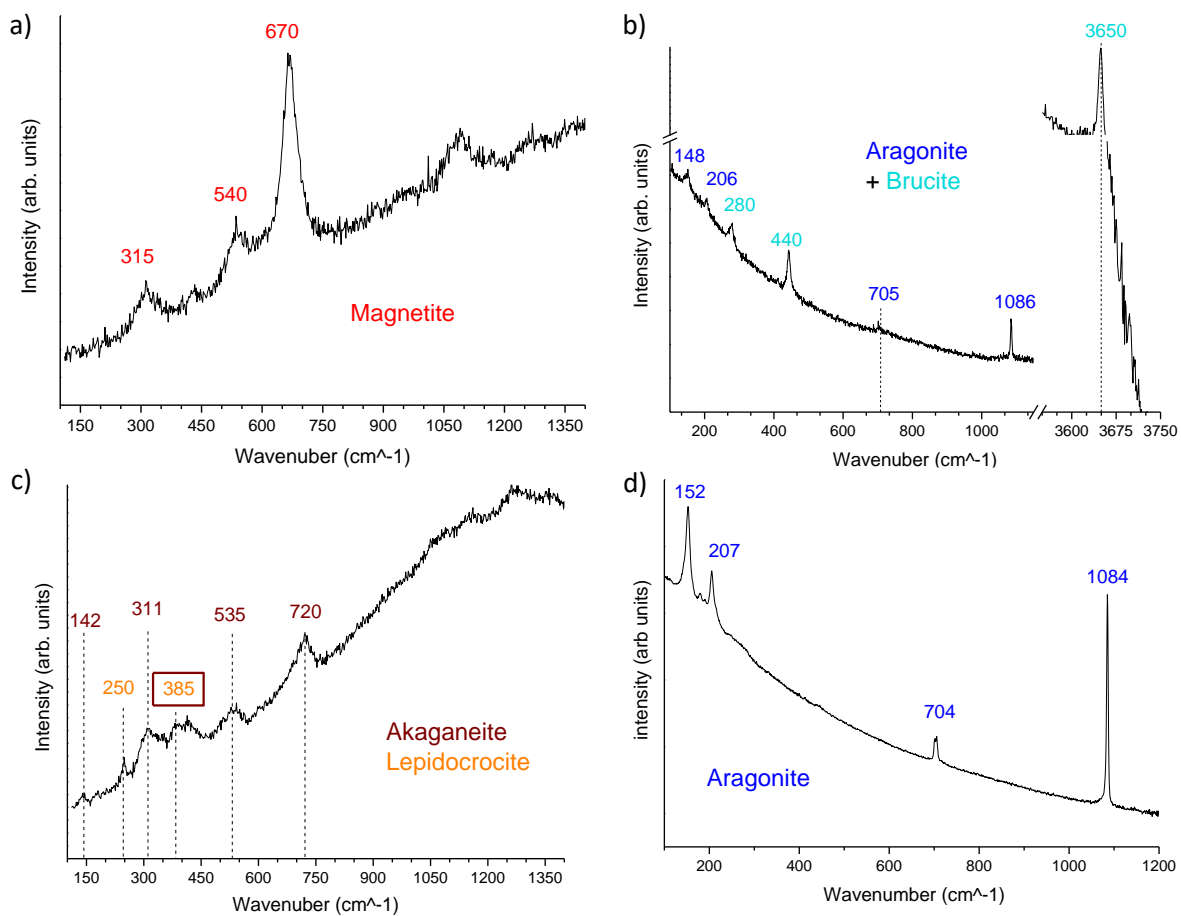


Figure V.23:  $\mu$ -Raman spectroscopy analysis of coupons A1 & 2 and B1 & 2 overview

Calcite and brucite were also detected on B1 and B2, but like for column A only few diffraction peaks were identified for those compounds showing the predominance of aragonite and magnetite compared to brucite and calcite. The B1 & B2 diffractograms (figure V.19 – b) also have the same issue with akaganeite and pyroaurite as diffractograms of A1 & A2. Py003 and Ak101 peaks seem convoluted, with a bigger impact of Ak101 as the peak is closer to the Ak101 position and Py003 looks more like a shoulder in this peak. Yet as previously, only one akaganeite diffraction peak is detected while a second pyroaurite peak (Py006) could be identified in spite of its extremely low intensity.

Raman analysis of coupons at levels 1 and 2 (figure V.20), i.e., at theoretical immersion rate from 14.8% to 34.8%, confirmed the previous hypothesis. Aragonite (figure V.20 – d) and magnetite (figure V.20 – a) were easily found due to their ubiquity on the coupons. Brucite could be found too in the white traces on the outer layer (figure V.20 – b). And finally, akaganeite was formally identified (figure V.20 – c). Lepidocrocite was frequently found with akaganeite. Its Raman scarce detection combined with its absence in the previous XRD patterns could mean that only a very small quantity of lepidocrocite may have formed. It must be reminded that if lepidocrocite can form because of the high O<sub>2</sub> access during the emerged period, it can be reduced to magnetite during the early stages of immersion as previously explained, according to the corrosion mechanism detailed in [7], [15]. However, these papers also explained that goethite should be found with magnetite in case of tidal corrosion. But they considered an already thick mineral layer with low access to oxygen close to the steel surface (favoring magnetite), a medium access to oxygen in the mineral layer (favoring goethite) and high O<sub>2</sub> flow on the outer part of the mineral layer (favoring lepidocrocite). Yet, in the case discussed for coupons between 14.8% and 34.8% of theoretical immersion rate, the tidal corrosion mechanism has been supposed active (in section V.2.1) for the early stages of the experiment. Initially, no layer at all was covering the coupons so at the very first stages the coupons were only in the case of high O<sub>2</sub> flow. With the progressive succession of CP periods (during the immersed phase) gradually reducing lepidocrocite to magnetite, and thus thickening the corrosion product layer, the outer stratum was exposed to high O<sub>2</sub> condition, consuming it to form lepidocrocite while the inner stratum was exposed to low O<sub>2</sub> conditions enhancing magnetite formation. According to this hypothesis, goethite may have formed in even fewer quantity than lepidocrocite. This may be one of the reasons it was not detected here. In addition, lepidocrocite detection combined with akaganeite is consistent with this mechanism. Seawater evaporation creates the required chloride enriched environment [26] for akaganeite to form and high O<sub>2</sub> flow conditions for lepidocrocite to form.

The next coupons at levels 3, 4, 5 (figure V.21 – a and V.21 – b) and 6, 7, 8, (figure V.21 – c and V.21 – d) for columns A and B, with a theoretical immersion rate from 34.8% to 56.6% and 56.6% to 84%, display a rather similar XRD analysis. For column A, M311 is still the most intense peak even if the average aragonite peaks are getting more and more intense compared to magnetite. Brucite peaks are also getting more and more intense, facilitating its identification. Conversely, calcite detection becomes less and less easy as aragonite proportion in the mineral layer increases with the increasing theoretical immersion rate. On the other hand, column B displayed really similar features as for lower immersion rates. Aragonite is the most predominant compound with A111 the most intense peak (for B3) and decreasing intensity ratio for magnetite with the increasing immersion rate. On column B, calcite is still easily detected maybe because of its longer experiment time which tends to increase the influence of calcite-producing bacteria. Brucite peaks are getting more defined too on column B (clearly observable for B011). These effects described for columns A and B could be interpreted as due to an increasing efficiency of CP compared to previous coupons. In addition, the same issue as for upper coupons is observed between pyroaurite and akaganeite as only one convoluted peak is detected. XRD analysis is not sufficient to certify the presence of one or both of them. Nevertheless, regarding the conclusions extracted from figure V.16, the XRD patterns for coupons A3, A4, and A5 are rather surprising. Indeed, coupon A3 was almost totally covered with a white layer visually similar to brucite (which was confirmed by Raman analysis) suggesting a limited residual corrosion kinetics. Nevertheless, this white layer could have been thin and its white color due to the homogeneous scattering of brucite particles in a layer mainly composed of aragonite. For B3, the XRD pattern and the analysis of the photographs are rather consistent with features indicating a low residual corrosion level since no oxyhydroxides were observed, and only a magnetite layer mainly overlaid by aragonite was present.

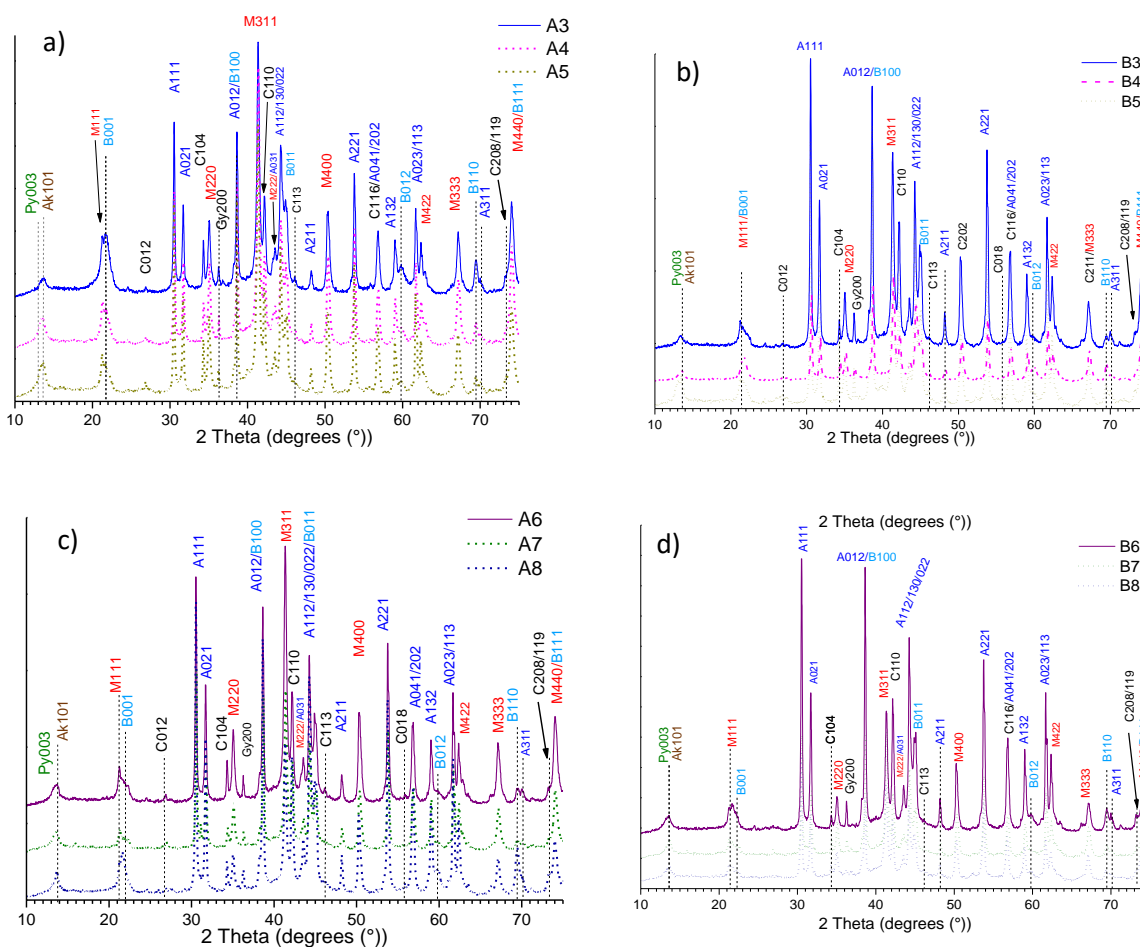


Figure V. 24: XRD analysis of – a) mid high part of column A (coupons A3, A4 and A5) – b) mid high part of column B (coupons B3, B4 and B5) – c) mid low part of column A (coupons A6, A7 and A8) – d) mid low part of column B (coupons B6, B7 and B8)

Raman analysis of these zones confirmed the XRD detection of magnetite, aragonite, brucite and akaganeite as presented in figure V.22. Lepidocrocite has been seldom detected due to the local character of the  $\mu$ -Raman spectroscopy analysis but as previously, its absence from XRD patterns demonstrate the small proportion of this corrosion product in the mineral layer. Brucite has been detected among a  $\text{CaCO}_3$  compound which is suspected to be calcite as no peak was detected at  $208\text{ cm}^{-1}$  (typical of aragonite). However, it was not possible to discriminate whether it was aragonite or calcite as the  $280\text{ cm}^{-1}$  peak is common for calcite and brucite and the characteristic  $712\text{ cm}^{-1}$  peak of calcite does not appear on the spectrum.

Raman analysis of the coupons 5 (see figure V.22) is really interesting as it clearly shows its transitional character with, at the same time, the detection of lepidocrocite (B5 mainly) and mackinawite (A5). Both of these spectra have been collected on coupons with the same immersion rate. This clearly highlights the ambivalent character of the mineral layer highly oxygenated on the outer part and enough deaerated in the extreme vicinity of the steel to allow Sulfated Reducing Bacteria (SRB) development, hence formation of FeS (figure V.22.g). This ambivalence tends to confirm the previous suggested mechanism of lepidocrocite formation. In addition, for coupon 6, akaganeite was detected on column A and suspected on column B (figure V.22.c). On the other hand, pyroaurite was detected

on column B (figure V.22.g). In other words, at least for coupon B5 (from 56.6% to 64.6% of immersion rate), both corrosion products with rather opposite formation mechanism (pyroaurite requires CP and is similar to green rust with magnesium instead of  $Fe^{II}$  while akaganeite is representative of corrosion with high  $O_2$  access) could coexist. In addition, this coupon is the closest to B6, the first coupon with detectable residual current. Its persistent protection may be due to the pH increase of the electrolyte trapped in its mineral layer. However, this tends to suggest that B5 may be in electrolyte continuity with the bulk electrolyte although no residual current is detected during the emerged phase. Then, a non-detectable residual current (because of the combination of a high ohmic drop and the accuracy limits of the DAS) could be running through the sample permitting a slow but continuous  $HO^-$  ions production maintaining a highly alkaline environment which could permit carbonate compounds formation and thus pyroaurite. It is then rather reasonable to suggest that even if pyroaurite was not detected for higher coupons, it does not mean pyroaurite did not form. Considering the global Raman analysis results, pyroaurite is most likely to form for coupon 5 rather than upper coupons. Indeed coupons 5 are the first coupons where FeS was detected, which suggests that the surface of these coupons remains wet enough to allow the formation of permanently deaerated zones inside the mineral layer. Thus, SRB could develop. This deaeration is favored by the thickening of the mineral layer. Indeed, as it remains wet, CP may stay active and calcareous deposit continues to precipitate. Consequently, pyroaurite formation becomes even more plausible for coupon 5.

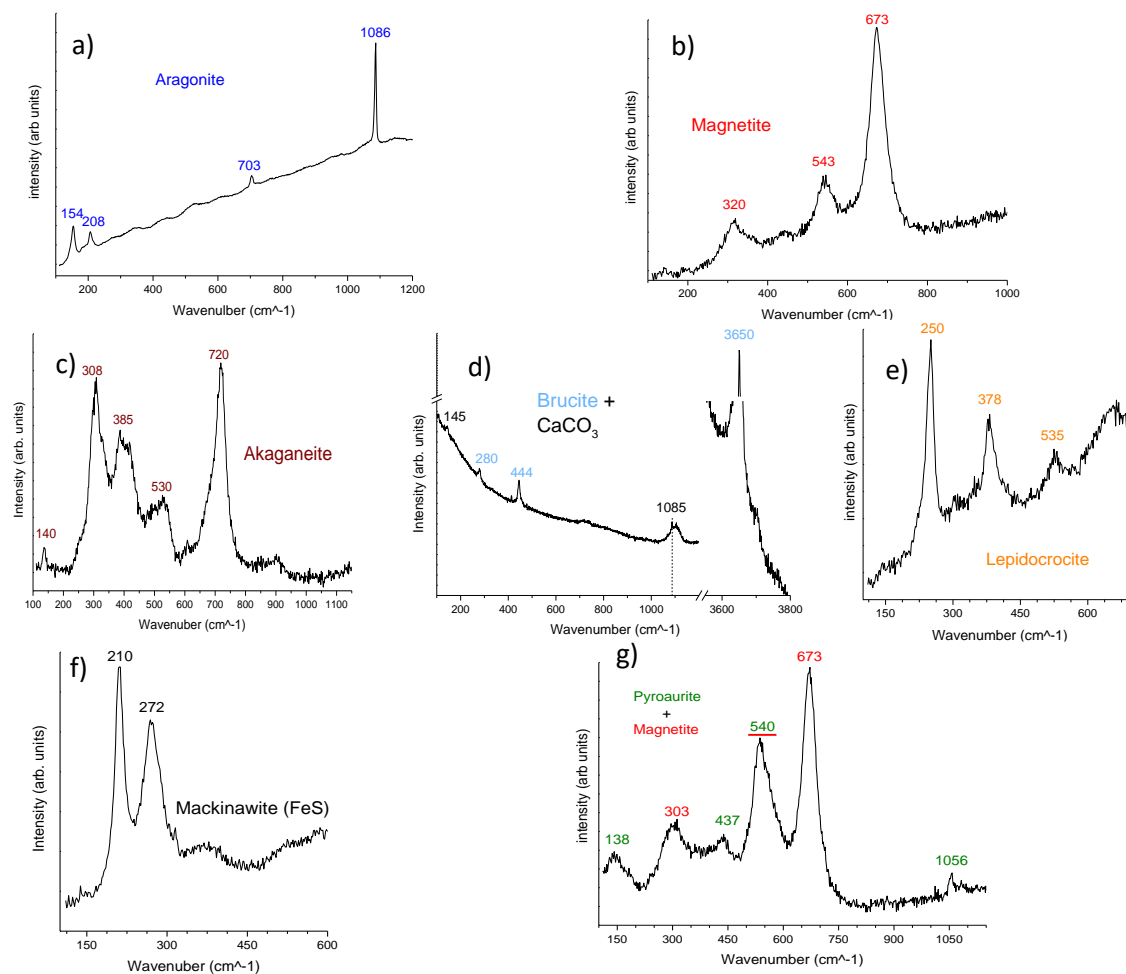


Figure V.25: Raman analysis overview for coupons immersed from 34.8% to 56.6% of columns A and B, i.e., coupons 3-5.

Finally, the last XRD patterns about coupons 9 and 10 of both columns (presented figure V.23 – a and V.23 – b) do not display any corrosion products diffraction peaks except for a small ambiguity between carbonated green rust and pyroaurite. As the coupons have an immersion rate from 84% to 100%, both compounds are likely to form, pyroaurite for the reasons mentioned above and carbonated green rust because it is the type of green rust which forms under CP in permanent immersion on pre-corroded surfaces. Indeed, the common green rust to precipitate in corrosion in constant immersion is the sulfated green rust. Under CP conditions the pH is increased, which shifts the carbonic equilibrium towards the  $\text{CO}_3$  compounds precipitation which leads to the formation of  $\text{GR}(\text{CO}_3)$  (or transformation of  $\text{GR}(\text{SO}_4)$  in  $\text{GR}(\text{CO}_3)$ ). Raman analysis of these coupons confirmed the XRD detection of calcite, aragonite and brucite. Magnetite (B9 only) was scarcely detected and FeS was found too. In addition, green rust have been frequently detected for coupons 10 and its formation is also strongly suspected on B9. Green rust spectrum found on A10 coupon is presented in figure V.24. Raman spectroscopy does not permit to differentiate the different types of green rusts. It is necessary to perform XRD analysis to discriminate whether it is sulfated green rust or carbonated green rust. Nonetheless, in the case presented in figure V.24 a large peak could be observed at  $1090\text{ cm}^{-1}$ . It is the typical band for  $\text{CO}_3$  based compounds such as calcite or aragonite [20]. The presence of this band and the uncertainty between pyroaurite and carbonated green rust indicate that the compound analyzed here must be  $\text{GR}(\text{CO}_3)$ . Ferrihydrite was detected together with the green rust. It may come from the oxidation of the green rust.

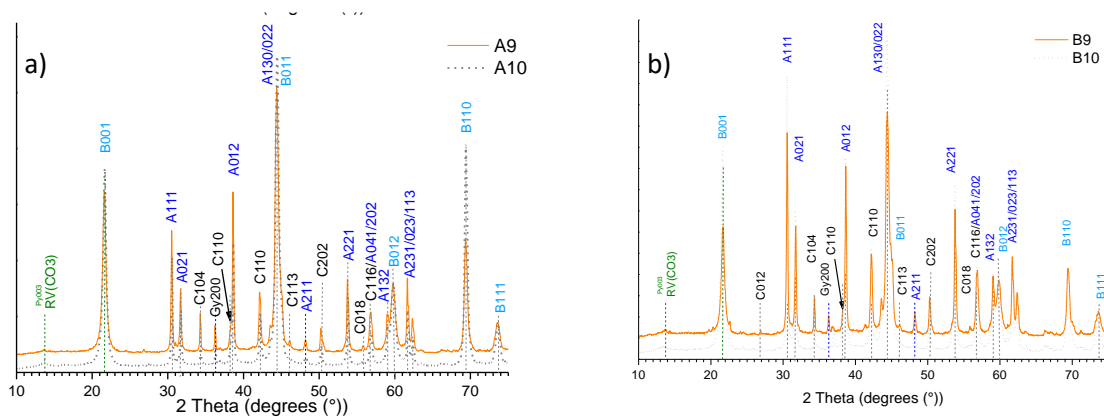


Figure V. 26: XRD analysis of the lower part of both columns – a) column A (coupons A9 and A10) – b) column B (coupons B9 and B10)

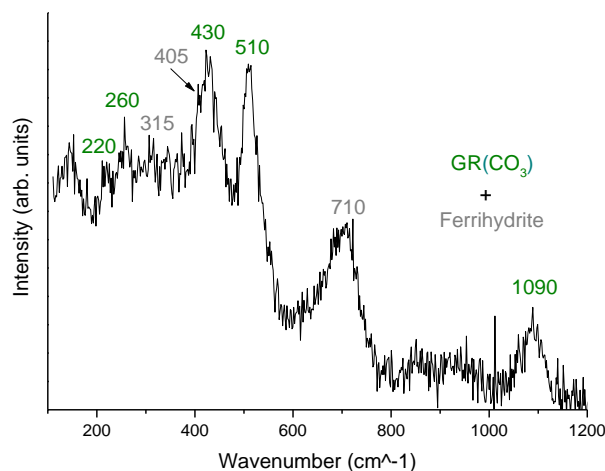


Figure V.27: Carbonated green rust (and ferrihydrite) spectrum collected on coupon A10

## Conclusions:

In conclusion, the experimental in situ monitoring of the cathodic protection parameters of samples under cathodic protection in simulated marine tidal zone allows getting close enough to real exposure conditions. The samples have been designed to be representative of the sheet piles installed in the ports while allowing analyses at different heights (by separating the coupons from the whole column).

After many difficulties related to the realization of the samples, the correct functioning of the tidal system, and the reliability of the  $\mu$ -reference electrodes used, this experiment allowed a continuous and individual monitoring of the potential for each sample as long as moisture persisted on its surface. It is important to note that the potential values were measured using a reference that is specific to the coupon. Thus, the potential does not give direct information on the electrolyte continuity but rather on the polarization (or depolarization) of the samples as the measurement is performed within the residual humidity on the coupon surface. On the other hand, the current is measured directly between the anode and the considered sample, so when the current is no longer measurable, it can be assumed that the electrolytic continuity has been broken.

From the observations made on the current and potential monitoring, it appears that CP efficiency is directly dependent of theoretical immersion rate and time. Indeed, from the 3<sup>rd</sup> coupon (theoretically immersed from 34.8% to 42.2% of the time) CP seems efficient as soon as the 8<sup>th</sup> day. At day 180, the whole column remains polarized below the protection potential threshold of  $-0.800 \text{ V/Ag/AgCl}_{sw}$  even during the emerged phase. The extremely slow depolarization observed, particularly for the upper coupons B1 & B2, may be explained by a high  $\text{HO}^-$  production during the wet phase. Actually, the coupons get wet before the immersion phase due to the capillarity strength of the porous mineral layer. After the emersion phase, the drying of the residual humidity is delayed by the same phenomenon.

In addition, from day 8 (time) and from coupon B6 (space), the current never went back to 0. This enhanced the CP efficiency because, if the coupling with the anode is maintained, then the anodic reaction on the steel surface, which remains the cathode, is decreased. However, this can also skew the results as this current persistence might only be possible because of the proximity of the seawater level, enhancing the persistence of electrolytic continuity. A large doubt remains about the ability of the anode disposed on a real wharf to polarize the steel surface located at mid tide zone in a large natural tidal zone. In addition, it is clear that with time, CP could protect, at least from the current and potential point of view, the highest coupons. Nevertheless, like for B6, the downsizing of the tidal zone may enhance CP persistence by increasing the probability of electrolyte continuity.

Finally, figure V.25 sums up all the detected compounds, the way they have been detected (XRD and / or Raman spectroscopy), and the confidence level of the detection discussed above. If a compound has been detected with both methods, no doubt remains about its presence in the mineral layer. A detection only by  $\mu$ -Raman spectroscopy could indicate a low fraction of the detected compound among the mineral layer as it is only detected locally. When a compound is suspected via XRD, it means that only one peak could have been identified, and its presence in the mineral layer cannot be ascertained.

All calcareous deposit components were found on each coupon, including calcite (according to the hypothesis of its precipitation due to bacteria activity). Magnetite, as a residual corrosion product and / or a corrosion product enhanced by cyclic immersion, was detected down to the level of coupons

9 (84% to 100% of theoretical immersion rate). Other corrosion products such as lepidocrocite, pyroaurite, green rusts and mackinawite have been scarcely detected as their precipitation is disfavored by CP, and could only be detected locally.

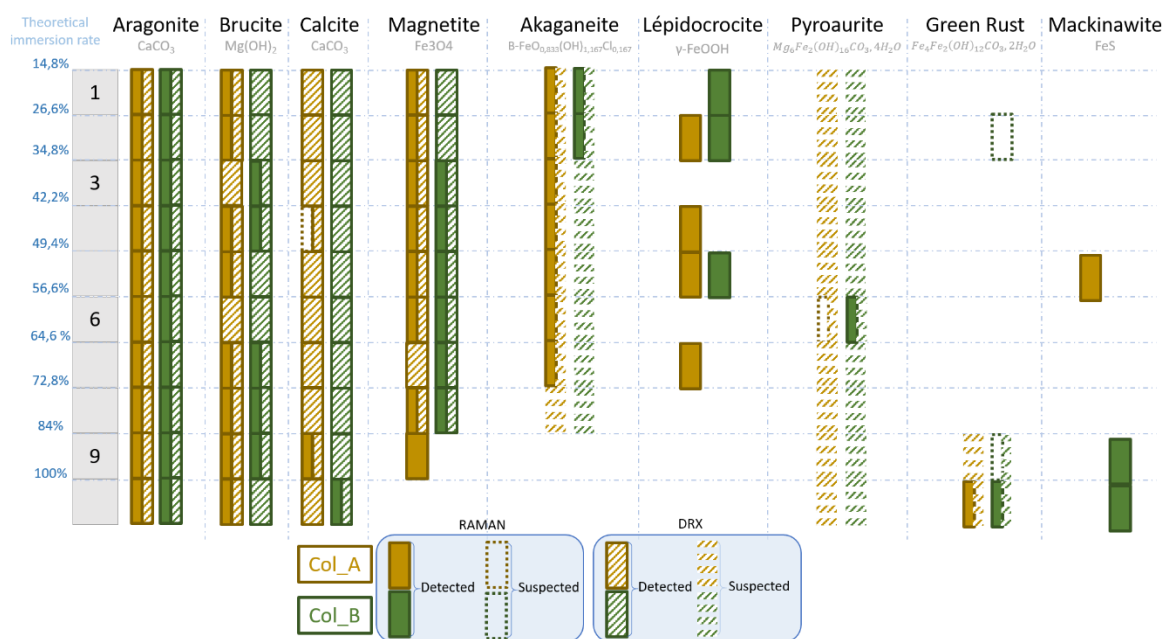


Figure V. 28 : Comparison of the detected corrosion products and existence domain of corrosion product regarding their theoretical immersion rate

Yet the low detection of lepidocrocite, a Fe(III) oxyhydroxide that forms in highly oxygenated conditions, occurred at the level of coupons 7 (between 64.6% to 72.2% of immersion), and that of akaganeite as well (maybe down to the level of coupons 8 for akaganeite). It is then reasonable to assume that the synergetic effect between high CP efficiency and less aerated conditions prevented the formation of Fe<sup>III</sup> compounds below the level of coupons 7. Only Fe<sup>II</sup>-based compounds, e.g. FeS and green rusts, were detected at the level of coupons 10, together with magnetite at the level of coupons 9. At the level of coupons 8, magnetite is the only identified corrosion product.

Pyroaurite, suspected in most cases but not formally identified except maybe in one case (B6), can be considered as a typical product of the residual corrosion process occurring under CP, as it contains Fe<sup>III</sup>, produced by corrosion, Mg<sup>II</sup>, and carbonate due to CP. It may form instead of the Fe<sup>II</sup>-Fe<sup>III</sup> isomorphous carbonated green rust when the dissolved Fe concentration is too low for the green rust to form.

Finally, the detection of FeS for coupon A5 (immersion rate from 49.4% to 56.6%) indicates that the mineral layer remained permanently wet for a sufficiently long time to allow SRB growing in deaerated areas, thus producing the sulfide species required for FeS formation.

Nonetheless, it is essential to keep in mind that the tidal system did not work all the time and long periods of immersion or emersion occurred during the whole experiment time. Then, the presented results may be considered cautiously, especially concerning the corrosion product detection and abundance, since corrosion may have been active during the long emerged periods. On the other hand, it also demonstrates the sturdiness of the CP persistence as every sample displayed features of protected steel despite of all the tidal system disruptions. In that sense, to confirm the CP persistence and strengthen this argument, corrosion rate and / or mass loss estimation should have been

performed. Unfortunately, the experiment design and the encountered difficulties did not allow evaluating the corrosion rate of the coupons as a function of time and immersion rate.

Finally, from all the observations made above, CP efficiency persistence in the tidal zone is dependent on 2 parameters, immersion rate and exposure time. The longer the steel is exposed, the better the steel is protected, as the growing mineral layer favors the persistence of humidity inside its pores and thus electrolytical continuity and CP persistence.

## References

- [1] B. Trémillon and G. Durand, « Electrochimie - Préliminaires à l'étude de l'électrolyse », *Opérations unitaires. Génie de la réaction chimique*, vol. 1, n° J 1 602, sept. 1999, doi: 10.51257/a-v1-j1602.
- [2] K. Zakowski, J. Orlikowski, K. Darowicki, M. Czekajlo, P. Iglinski, and K. Domanska, « The Effect of Increasing the Amount of Indium Alloying Material on the Efficiency of Sacrificial Aluminium Anodes », *Materials*, vol. 14, n° 7, p. 1755, avr. 2021, doi: 10.3390/ma14071755.
- [3] K. Akamine and Isamu Kashiki, « Corrosion protection of steel by calcareous electrodeposition in seawater (Part 1) », *Zairyo-to-Kankyo*, vol. 51, p. 496-501, 2002.
- [4] K. Akamine and I. Kashiki, « Corrosion protection of steel by calcareous electrodeposition in seawater (Part 2) », *Zairyo-to-Kankyo*, vol. 52, p. 401-407, 2003.
- [5] Y. Yang, J. Scantlebury, and E. Koroleva, « A Study of Calcareous Deposits on Cathodically Protected Mild Steel in Artificial Seawater », *Metals*, vol. 5, n° 1, p. 439-456, mars 2015, doi: 10.3390/met5010439.
- [6] C. Carré, P. Gunkel-Grillon, A. Serres, M. Jeannin, R. Sabot, and T. Quiniou, « Calcareous electrochemical precipitation, a new method to trap nickel in seawater », *Environ Chem Lett*, vol. 15, n° 1, p. 151-156, mars 2017, doi: 10.1007/s10311-016-0602-2.
- [7] Ph. Refait, M. Jeannin, R. Sabot, H. Antony, and S. Pineau, « Corrosion and cathodic protection of carbon steel in the tidal zone: Products, mechanisms and kinetics », *Corrosion Science*, vol. 90, p. 375-382, janv. 2015, doi: 10.1016/j.corsci.2014.10.035.
- [8] R. E. Melchers and R. Jeffrey, « Corrosion of long vertical steel strips in the marine tidal zone and implications for ALWC », *Corrosion Science*, vol. 65, p. 26-36, déc. 2012, doi: 10.1016/j.corsci.2012.07.025.
- [9] J. Duboscq, « Corrosion des aciers en milieu marin: processus se déroulant dans les zones cathodiques », Thèse de Doctorat, La Rochelle Université, 2019.
- [10] A. Zanibellato, « Synthèse et études physico-chimiques d'un agglomérat calco-magnésien formé sur un acier en milieu marin : un éco-matériau pour la protection du littoral », Thèse de Doctorat, Université de La Rochelle, La Rochelle, 2016.
- [11] C. Deslouis, D. Festy, O. Gil, V. Maillot, S. Touzain, and B. Tribollet, « Characterization of calcareous deposits in artificial sea water by impedances techniques: 2-deposit of  $Mg(OH)_2$  without  $CaCO_3$  », *Electrochimica Acta*, vol. 45, n° 11, p. 1837-1845, févr. 2000, doi: 10.1016/S0013-4686(99)00403-X.
- [12] S. Elbeik, A. C. C. Tseung, and A. L. Mackay, « The formation of calcareous deposits during the corrosion of mild steel in sea water », *Corrosion Science*, vol. 26, n° 9, p. 669-680, janv. 1986, doi: 10.1016/0010-938X(86)90032-6.
- [13] Ph. Refait, M. Jeannin, R. Sabot, H. Antony, and S. Pineau, « Electrochemical formation and transformation of corrosion products on carbon steel under cathodic protection in seawater », *Corrosion Science*, vol. 71, p. 32-36, juin 2013, doi: 10.1016/j.corsci.2013.01.042.
- [14] Ph. Refait, D. D. Nguyen, M. Jeannin, S. Sable, M. Langumier, and R. Sabot, « Electrochemical formation of green rusts in deaerated seawater-like solutions », *Electrochimica Acta*, vol. 56, n° 18, p. 6481-6488, juill. 2011, doi: 10.1016/j.electacta.2011.04.123.
- [15] P. Refait, S. Pineau, R. Sabot, H. Antony, et M. Jeannin, « Mécanismes de la corrosion des aciers au carbone en zone de marnage », *Matériaux & Techniques*, vol. 101, n° 5-6, p. 501, 2013, doi: 10.1051/mattech/2013084.
- [16] J. Duboscq, R. Sabot, M. Jeannin, et P. Refait, « Localized corrosion of carbon steel in seawater: Processes occurring in cathodic zones », *Materials and Corrosion*, vol. 70, n° 6, p. 973-984, juin 2019, doi: 10.1002/maco.201810675.
- [17] M. Jeannin, R. Sabot, H. Antony, S. Pineau, and P. Refait, « Effets des ruptures et reprises de protection cathodique sur la couche de produits de corrosion des aciers en zone de marnage », *Matériaux & Techniques*, vol. 101, n° 5-6, p. 503, 2013, doi: 10.1051/mattech/2013086.

- [18] K. Mantel, W. H. Hartt, and T. Chen, « Substrate, Surface Finish, and Flow Rate Influences on Calcareous Deposit Structure », *Corrosion*, vol 48, n°6, p. 489-500, 1992, doi: 10.5006/1.3315965.
- [19] K. L. Lopez Maldonado, P. de la Presa, M. A. de la Rubia, P. Crespo, J. de Furtos, A. Hernando, J. A. Matutes Aquino, and J. T. Elizade Galindo, « Effects of grain boundary width and crystallite size on conductivity and magnetic properties of magnetite nanoparticles », *J. Nanopart. Res.*, vol. 16, n° 7, p. 12, 2014, doi: 10.1007/s11051-014-2482-.
- [20] C. Carré, A. Zanibellato, M. Jeannin, R. Sabot, P. Gunkel-Grillon, et A. Serres, « Electrochemical calcareous deposition in seawater. A review », *Environ Chem Lett*, vol. 18, n° 4, p. 1193-1208, juill. 2020, doi: 10.1007/s10311-020-01002-z.
- [21] C. Carré, A. Zanibellato, N. Achgare, P.-Y. Mahieux, Ph. Turcry, M. Jeannin and R. Sabot., « Electrochemical limestone synthesis in seawater binds metal grids and sediments for coastal protection », *Environ Chem Lett*, vol. 18, n° 5, p. 1685-1692, sept. 2020, doi: 10.1007/s10311-020-01019-4.
- [22] Ch. Barchiche, C. Deslouis, D. Festy, O. Gil, Ph. Refait, S. Touzain and B. Tribollet., « Characterization of calcareous deposits in artificial seawater by impedance techniques 3 - Deposit of CaCO<sub>3</sub> in presence of Mg(II) », *Electrochimica Acta*, vol. 48, n° 12, p. 1645-1654, mai 2003, doi: 10.1016/S0013-4686(03)00075-6.
- [23] C. Deslouis, D. Festy, O. Gil, P. Refait, S. Touzain, et B. Tribollet, « Characterization of calcareous deposits in artificial seawater by impedance techniques I - Deposit of CaCO<sub>3</sub> without Mg(OH)<sub>2</sub> », p. 11, 1998.
- [24] J. Vincent, B. Colin, I. Lanneluc, R. Sabot, V. Sopéna, Ph. Turcry, P.-Y. Mahieux, Ph. Refait, M. Jeannin and S. Sablé « New Biocalcifying Marine Bacterial Strains Isolated from Calcareous Deposits and Immediate Surroundings », *Microorganisms*, vol. 10, n° 1, p. 76, déc. 2021, doi: 10.3390/microorganisms10010076.
- [25] B. Colin, J. Vincent, L. Kozirowski, A. Frein, I. Lanneluc, R. Sabot, Ph. Refait, S. Sablé and M. Jeannin, « Calcareous deposit formation under cathodic polarization and marine biocalcifying bacterial activity », *Bioelectrochemistry*, vol. 148, p. 108271, déc. 2022, doi: 10.1016/j.bioelechem.2022.108271.
- [26] R. Anouar, « Dessalement de l'eau de mer par congélation sur parois froides : aspect thermodynamique et influence des condition opératoires », Thèse de Doctorat, Université Claude Bernard Lyon 1, Lyon, 2011.





## *General Conclusion and Prospects*



Finally, the problem addressed in this PhD research concerns the understanding of the parameters and mechanisms involved in the persistence of CP on carbon steel in the tidal zone. The challenges included defining spatiotemporal limits (such as maximum height and duration) of the persistence of CP at low tide. The stakes of this work go beyond the understanding of electrochemical mechanisms, but could ultimately help to reduce the carbon footprint of structures in tidal zones, while lowering their installation and maintenance costs. To tackle such a problematic, 3 main areas of investigation were pursued.

- ① For the first one (Chapter III), coupons of carbon steel under CP in natural exposure conditions (La Rochelle commercial seaport) were considered. This study, based on a posteriori XRD and  $\mu$ -Raman spectroscopy analysis, revealed a varying composition of the mineral layer along the tidal zone. In any case, corrosion products and calcareous deposit compounds were identified. The analyzed coupons displayed features comparable to constant immersion for the lowest ones and to splash zone for the highest coupons. An uncommon amount of brucite, indicative of spread-out CP mechanisms, was found around and above the mid tide zone. Yet brucite cannot be the only marker of CP efficiency. In addition, FeS (a “residual corrosion” product) have been detected up to 47.4% immersion rate, demonstrating the persistent humidity within the dense mineral layer of the coupon. To more accurately define the spatial limit of CP persistence, corrosion rates were qualitatively estimated. According to the nature of the detected compounds and the estimated corrosion rate, CP could still be efficient up to **45-52% immersion rate**, which corresponds to 69-74% of the total height of the tidal zone. The study has been led only on 10 cm square coupons whereas the column was made up of an alternation of coupons and long plates (10 cm x 50 cm). It appears that the transition zone between efficient CP and corroded coupons is precisely situated on one of the long plates (which has not been analyzed yet). The thorough analysis of this long sample should permit to determine the exact position of the transition zone.
- ② The second one (Chapter IV) dealt with the mechanisms occurring on polarized carbon steel protected (-950 mV/Ag/AgCl<sub>3M</sub>) and insufficiently protected (-750 mV/Ag/AgCl<sub>3M</sub>) under thin seawater layers. The aim was to artificially reproduce the conditions of ebb and low tides.
  - Firstly, the considered potential plays a role in the mineral layer formation on the steel surface. Even though CP considerably decreases the corrosion rate, a “residual” corrosion process remains active. Therefore, the film of “residual” corrosion products must be considered as it may be responsible for differences in the slope of the anodic part of polarization curves and the formation of corrosion products during the emerged period (for steel in tidal situation). The protective character of the samples was evaluated through  $R_p$  and  $R_{ct}$  values.  $R_{ct}$  is the strongest for -950 mV/Ag-AgCl<sub>3M</sub> indicating that the deposit is denser and less porous. For the higher applied potential of -750 mV/Ag-AgCl<sub>3M</sub>, CP is less efficient and the residual corrosion rate is higher. However, the experiments were run for a longer period so that the residual corrosion film was necessarily thicker and/or covered a more important part of the surface. Because the aragonite particles are larger (finer XRD peaks, for insufficiently protected steel), the inherent pores within the aragonite layer are wider. Consequently, dissolved O<sub>2</sub> may easily reach the outer surface of the thin corrosion product film. The finite-length diffusion process revealed by EIS then corresponds to O<sub>2</sub> diffusion through the pores of the corrosion product film. The thickness of this film corresponds to the thickness of the diffusion layer. The semi-infinite diffusion process revealed by EIS for well protected samples conversely corresponds to O<sub>2</sub> diffusion inside the much thicker and denser aragonite layer.

- The second objective of this study was to discuss the impact of thin layers of electrolyte on the calcareous deposit properties. The electrolyte resistance  $R_e$  proved to be significantly higher for the smaller seawater layer thickness (of 1 mm). The average  $R_e$  is three times higher for 1 mm compared to 5mm ( $280 \Omega \text{ cm}^2$  vs  $90 \Omega \text{ cm}^2$ ). The increased resistance to migration would then explain the slower formation of the aragonite layer and the slower depolarization of the sample after CP interruption.

The other observed effect of seawater layer thickness is the increased protective ability of the calcareous deposit, which is more pronounced at  $E_{CP} = -950 \text{ mV}/_{\text{Ag-AgCl-3M}}$ . The XRD patterns and the much higher  $R_{ct}$  value would indicate that the layer obtained for the well protected sample under 1 mm of seawater was much less porous. On the other hand, the delayed formation of aragonite for 1mm of seawater may be due to the growth of an underlying  $\text{Mg}(\text{OH})_2$  thin film, promoted by the great accessibility of oxygen.

Finally, an insufficient CP can enhance the formation of thick aragonite layer covering a thin film of residual corrosion products. This aragonite layer displays a similar protective ability to that of the calcareous deposit obtained under correct CP. On the other hand, a thin electrolyte layer increases the protective character of the calcareous deposit formed on a well-protected steel surface. This is more likely because of the formation of  $\text{Mg}(\text{OH})_2$ , which may induce, in particular, a reinforcement of the deposit during depolarization.

- 3 And for the last one (Chapter V), simulating a tidal zone with natural seawater at a laboratory scale permitted a continuous monitoring of the CP parameters (current and potential) prior to the characterization of the mineral layer. To our knowledge, such an experiment has not been realized yet. The first challenge was the experimental set up. The samples have been designed to be representative of carbon steel structure exposed to tides while allowing analysis at different heights (as it was done in *Chapter III*) with individual reference electrode set in the same plan as the steel surface of each coupon. The tide simulation device, the seawater alimentation and the long-term continuous monitoring of CP parameters were critical elements of the experimental setup.

Finally, from current (representative of the electrolyte continuity) and potential (dependent on the coupon moisture, not on the electrolyte continuity) analysis, CP appears to be efficient from **34.8% to 42.2% theoretical immersion rate** as early as day 8. For longer times, the entire column seemed to be protected even during the emerged phases. In addition, from day 8 and from coupon B6 (56.6% to 64.6% theoretical immersion rate), the current never returned to 0 during the emersion of the coupon. It is clear that with time, CP could protect, at least from the current and potential point of view, the highest coupons. Nevertheless, like for B6, the downsizing of the tidal zone may enhance CP persistence by increasing the probability of electrolyte continuity.

All the analyzed coupons displayed corrosion products and calcareous deposit compounds. FeS was detected up to 49.4% to 56.6% of theoretical immersion rate. The nature and amount of corrosion products detected must be considered cautiously because of the multiple tide simulation system disruptions leading to more or less long immersed and / or emerged periods. On the other hand, this demonstrates the spread-out CP efficiency as every sample displayed features of protected steel despite of all the tidal system disruptions.

Finally, CP efficiency persistence in the tidal zone is dependent on 2 parameters: immersion rate and exposure time. The longer the steel is exposed, the better the steel is protected, as the growing of the mineral layer favors the persistence of the electrolyte film continuity.

To globally conclude about the problematic, *Chapter III* and *V* display similar findings. In the in-situ study (*Chapter III*), CP persistence was observed up to immersion rates ranging from 45% to 52%, while during the initial stages of the study in the simulated tidal zone (*Chapter V*), CP remained active up to 34.8% to 42.2% of theoretical immersion rate. Furthermore, both studies led to the identification of mackinawite up to 47.4% of immersion rate in the La Rochelle commercial seaport and 49.4% of theoretical immersion rate for the laboratory study. This confirms the hypothesis of residual humidity persistence which likely facilitates the CP persistence. In the laboratory study, the entire column was protected (from current and potential point of view) after 180 days of exposure. As mentioned, the laboratory scale conditions may have enhanced CP persistence because of the limited tide amplitude favoring electrolyte continuity between the coupons and the bulk electrolyte. *Chapter IV*, which delves into CP under thin electrolyte layers helped understanding the phenomenon involved during ebb tide and aligns with the assumed mechanism of brucite formation in the tidal zone. Finally, to summarize the spread-out CP mechanisms: the steel surface undergoes immersion and gets polarized by CP, creating a localized highly alkaline environment that promotes the formation of calcareous deposit and residual corrosion products such as magnetite, mackinawite and / or pyroaurite. Then during the first stages of seawater withdrawal, the steel surface remains wet, allowing a residual current to go on flowing hence providing protection. However, this residual current is gradually decreasing as the seawater level recedes, mainly because of the increasing electrolyte resistance of the residual humidity due to drying and gravity flow. As seen in *Chapter IV*, CP under thin electrolyte layers promotes the formation of dense and protective aragonite layer. This current persistence out of water increases the pH within the mineral layer covering the steel (calcareous deposit and residual corrosion products) by continuously producing  $\text{HO}^-$  ions without electrolyte renewal. The chemical environment created by residual current promotes dense aragonite and brucite formation while hindering the depolarization effect. It may also shift the corrosion potential of the steel towards more negative values, further limiting the residual corrosion processes. Depending on the altitude (in the tidal zone) of the surface, the slow depolarization, i.e., CP persistence, could be attributed to the chemical environment created within the mineral layer during the immersed and emersion period (polarized phase). Alternatively, it could result from the combination of the residual current running through the surface and the chemical condition in the vicinity of the steel. For higher surfaces, spread-out CP is more likely associated to chemical environment whereas for lower surfaces, the slow depolarization is the consequence of the synergetic effect of residual current and chemical environment.

Finally, CP efficiency on uncoated carbon steel in the tidal zone is a complex mechanism that primarily depends on the amplitude of the tides (i.e., the altitude of the steel surface considered). Although a 6 m and a 1 m high tidal zones share similarities, they do not exactly permit the same level of CP efficiency. This discrepancy arises due to the proximity between splash zone and low water zone which promotes electrolyte continuity and thus residual current. Additionally, the time of exposure plays a key role as the mineral requires time to create to afterwards permit the mechanism discussed above. Another parameter to consider is the immersion rate which qualifies the frequency of wet periods. In any case CP seems efficient up to **45% of immersion rate** (for wide tidal zone).

Although these research findings provide intriguing clues and elements to address the problem, there is still much work to be done. As mentioned in *Chapter III* long plates (10 cm x 50 cm) separating the analyzed zones have yet to be analyzed. Their thorough study could lead to a more accurate definition of the transition zone between protected coupons and those subjected to corrosion. Moreover, these plates, being five times taller than the coupons, may exhibit slightly different behavior due to an increased probability of a macro-galvanic cell forming between the top and bottom of each plate. This could provide additional insight about the behavior of protected continuous structure exposed to tidal zone.

Similarly, in *Chapter V*, 1 long plate of (10 cm x 110 cm) have been exposed to the simulated tidal zone for each column of coupons. The aim was to ensure that the columns were representative of continuous structure and, as for the *Chapter III*, to consider the macro-galvanic cells likely to form between the top (most aerated part: high tide zone) and the bottom (least aerated part: low tide zone) of the plates. In addition, for the Naval Group Laboratory experiment, a whole column of sample has not been treated yet. These coupons were left exposed to free tidal corrosion mechanisms for 6 months prior to be protected by CP for the 10 following months. Studying them will help refine the understanding of the spread-out CP mechanisms and bringing it closer to real structures exposed to tidal zone. This improved comprehension is particularly valuable for older structures exposed to the marine environment, where steel sacrificial thickness serves as the only corrosion protection system. Towards the end of their lifespan, it is often more cost-effective to protect these structures with a CP device to extend their operational life, rather than replacing them. Finally, EIS measurements were punctually performed on each sample to qualify the characteristics of the outer layer and track their evolution over the whole experiment time. As it is crucial to precisely identify the nature of the compounds covering the sample and to understand the electrochemical mechanisms which occurred on the surface to understand the meaning of the obtained curves, I have not been through the data yet.

*Chapter IV* initiated fundamental research about cathodic protection under thin layers of electrolyte. Since this was the first of its kind, the study was performed horizontally to understand, at first approach, the mechanisms involved in these conditions. However as mentioned in introduction of *Chapter IV*, creating a uniform electrolyte film thinner than 1 mm onto a steel surface is quite challenging. In addition, to be more representative of the tidal zone conditions, the considered surface must be studied in a vertical position. Thus, a complementary work to understand the CP mechanisms within the mineral layer from a fundamental perspective is required. Since the aim is to understand the spread-out CP mechanisms themselves rather than their initialisation, it is necessary to first form a calcareous deposit layer on the steel surface to perform further experimentation. Subsequently, the steel, coated with the calcareous deposit must be wet (or not) with seawater and then partially immersed vertically in so that only the bottom of the electrode is immersed in the bulk electrolyte. This set up ensures that the deposit remains moist due to capillary forces that enable it to trap seawater. In this configuration, electrolytic continuity is ensured enabling various electrochemical tests (such as polarisation, current measurement, EIS, polarisation resistance, etc.) to be carried out on the emerged surface of the steel.

Besides, all the studies presented here focused on the qualitative analysis of the data and the understanding of the mechanisms since the chosen experiments were either run for the first time or set up during former PhD works. It would be really interesting and complementary to precise the CP efficiency levels to focus on quantitative studies led on similar experimental set ups such as:

- Quantitative phase analysis of the mineral layer covering the steel coupons,
- Quantitative estimation of the porosity and thickness of the calcareous deposit obtained under thin electrolyte thickness,
- Quantitative estimation of the residual corrosion rate not only as a function of the height (or immersion rate) but also as a function of the time of exposure.

Since this PhD work was the first one to focus on the CP mechanisms and efficiency persistence in the tidal zone, it was chosen to study this issue on uncoated carbon steel. However, most of the current structure exposed to marine environments are coated with anticorrosion paints. It is important to note that CP mechanisms occurring on bare steel and on painted steel are significantly different. CP of coated carbon steel in the tidal zone must be investigated too. Furthermore, all the mechanisms discussed in this manuscript are based on the seawater flow and / or its entrapment in the mineral layer. Obviously, the active surface and the flow conditions between a coated and uncoated surface are antipodal. The presented work does not permit to conclude about the potential protection of steel surface under a scratch located in the tidal zone, as there is no certainty about electrolyte continuity in such a scenario.

Finally, the last topic to be addressed concerns the ecological impacts of the release of Al-Zn-In anode material in the open marine environment as many topics are still to be understood. Indium contributes only 0.01–0.04% of the anode's material but its low natural occurrence in the environment (0.05 ppm in the Earth's crust) suggests that these anodes could become a notable new source of indium in the marine environment. Indium has not been extensively studied in previous environmental research due to its low concentration and inherent analytical issue. Data on indium in the marine environment are scarce and are primarily discussed in the context of geochemical processes. Currently, there is no available data for indium concentrations in the European marine environment, with concentrations in the Mediterranean Sea and the Atlantic Ocean ranging below 0.6–1.6 pmol kg<sup>-1</sup>, and even lower concentrations reported in the Sea of Japan. [1]

There are no established guidelines for aluminum (Al) concentrations in seawater on a national or international level. An Australian marine water guideline suggested a no-effect concentration (NOEC) of total Al, based on toxicity tests with 11 marine species. These tests showed that both dissolved and particulate Al could be toxic to marine organisms, with certain species. The NOEC for oysters was 100 µg/L, indicating low sensitivity [1]. This proposed NOEC value is considerably higher than the actual measured concentrations of dissolved Al in the marine environment. Some studies have examined the impact of Al emissions from galvanic anodes, primarily in harbor settings or laboratory experiments [1]. Consistently, experiments conducted in tanks filled with seawater (without sediment) revealed high concentrations of aluminum in settled particles and suspended particulate matter. Then, it has been suggested that, under environmental conditions, the dissolved fraction of Al in seawater is not significant due to the dilution effects [1]. For instance, a study led in the La Rochelle commercial Seaport, observed a significant increase in Al concentrations in sediment near anodes in a harbor basin, while water concentrations of Al did not rise significantly due to dilution effects. Trace elements found in bivalves are detected in significantly higher quantities in harbor areas compared to a reference site (former oyster beds unaffected by harbor influences) [2]. This indicates that, in addition to naturally

occurring trace elements, human activities have a notable impact on the accumulation of these metals in scallops [2]. In this study an overestimated value of the anode material mass consumed per year in the La Rochelle commercial seaport has been calculated at **1.38 mg/L**. In real conditions (considering the harbor as an open area with seawater renewal between each tide) the concentration decreases significantly and can be deemed safe for marine ecosystems [2].

Besides, in aluminum-based anodes, zinc is the second most abundant metal, contributing 2.5–5.75% to the total anode mass. In this case, the primary dissolved species among the degradation products is  $\text{Al}(\text{OH})_4^-$ . However, despite Zn being a minor component of the anodes, the exposure to  $\text{Zn}^{2+}$  ions might be higher than that to  $\text{Al}(\text{OH})_4^-$  ions, because of the solubility properties of both compounds [3]. Tank experiments with Zn anodes demonstrated an increase of  $\text{Zn}^{2+}$  ions in the water and precipitation as hydroxide, but also in form of complexes or attached to suspended matter. Emissions from Al anodes were analyzed in a seawater tank and found that the dissolved Zn fraction initially increased but later decreased due to sorption to suspended particulate matter and dilution effects during water renewal. The toxicity of Zn emissions from galvanic anodes on sea urchin embryos, demonstrated low or no damage compared to Zn and Al salts. On the other hand, *Crassostrea gigas* proved to be more sensitive to Zn emission from galvanic anodes but only moderate effects at mild Zn concentrations were observed [1]. Consequently, the observed effects attributed to the Al-Zn-In alloy anodes could primarily result from  $\text{Zn}^{2+}$  ions, hence the importance of minimizing the zinc content in such alloys. Nevertheless, the impact on oyster metabolism appears to be less significant compared to the pure Zn anode [3].

Actually, as a part of my PhD work, I was initially asked to investigate the ecotoxicological impact of corrosion products of aluminium-based anodes, widely used in seawater [1]. During the exploratory phase of my project, a substantial part of my efforts was dedicated to this study. Indeed, my experiments at the commercial port of La Rochelle were located exactly on one of the study sites of Marine Barbarin's PhD work (defended in 2022), which focused on monitoring the quality of seaport environment [4]. Given the complementary nature of our theses, I was able to help with the design and dimensioning of cathodic protection for an experiment dealing with the impact of Al-Zn-In anode corrosion products impact on the health of the bivalve *Mimachlamys varia*.

However, given the scope of my work and the experimental design, conception and planning required for the experiments carried out at Naval Group's corrosion laboratory (*Chapter V*), it was decided to narrow my focus on the core of my subject, i.e., the cathodic protection of carbon steels in the tidal zone. Furthermore, the research field concerning the impact of corrosion products from aluminium-based anodes is notably intricate and extensive, with many aspects yet to be defined and explored. It is worth noting that this avenue of research alone could potentially serve as the subject for an entire PhD thesis.

## References:

- [1] T. Kirchgeorg, I. Weinberg, M. Hörnig, R. Baier, M. J. Schmid, and B. Brockmeyer, « Emissions from corrosion protection systems of offshore wind farms: Evaluation of the potential impact on the marine environment », *Marine Pollution Bulletin*, vol. 136, p. 257-268, nov. 2018, doi: 10.1016/j.marpolbul.2018.08.058.
- [2] M. Barbarin, C. Turquois, E. Dubillot, V. Huet, C. Churlaud, F. Muttin and H. Thomas, « First quantitative biomonitoring study of two ports (marina, commerce) in French littoral area: Evaluation of metals released into the marine environment and resulting from galvanic anodes », *Science of The Total Environment*, vol. 857, p. 159244, janv. 2023, doi: 10.1016/j.scitotenv.2022.159244.
- [3] N. Imbert-Auvray, D. Fichet, P.-E. Bodet, P. Ory, R. Sabot, Ph. Refait and M. Graber, « Metabolomics-Based Investigation on the Metabolic Changes in *Crassostrea gigas* Experimentally Exposed to Galvanic Anodes », *Metabolites*, vol. 13, n° 7, p. 869, juill. 2023, doi: 10.3390/metabo13070869.
- [4] M. Barbarin, « Environnement & espaces portuaires : suivi de la qualité du milieu pour une meilleure compréhension de l'effet de variables environnementales à une échelle spatio-temporelle », Thèse de Doctorat, La Rochelle Université, La Rochelle, 2022.





## **Résumé**

Ces travaux s'intéressent aux mécanismes mis en jeu dans la protection cathodique (PC) en zone de marnage (ZdM, zone verticale balayée par les marées). En effet, une étude de 2015 menée par Ph. Refait et coll. a mis en exergue une persistance de la PC même pendant les périodes émergées, a priori impossible à cause du retrait de l'eau de mer. Comprendre les mécanismes intervenant dans cette protection étendue pourrait, à terme, permettre de réduire l'impact environnemental de la conception et la maintenance de structures telles que les éoliennes offshore. Une première étude, sur toute la hauteur de la ZdM du port de commerce de La Rochelle, a permis de mettre en évidence que la PC pourrait être considérée efficace jusqu'à 45% de taux d'immersion (soit 74% de la hauteur de la ZdM). En parallèle, une étude menée au LaSIE visait à s'interroger de façon plus fondamentale sur le comportement de l'acier à marée descendante. Pour cela, des échantillons disposés à l'horizontal, sous de fines couches d'électrolyte (1 mm ou 5 mm) ont été placés en condition de protection satisfaisante (-950 mV/Ag/AgCl<sub>3M</sub>) et en condition de sous-protection (-750 mV/Ag/AgCl<sub>3M</sub>). Il apparaît alors qu'une protection insuffisante conduit à la formation d'une épaisse couche d'aragonite recouvrant une fine couche de produits de corrosion résiduels. De plus, une fine couche d'eau de mer augmente le caractère protecteur du dépôt formé sous PC suffisante (-950 mV/Ag/AgCl<sub>3M</sub>). Enfin, à mi-chemin entre les deux études précédentes, le dernier axe de recherche évoqué ici a permis de suivre l'évolution des paramètres de PC au cours des marées pendant 16 mois. Aux temps courts (8 j), la PC était efficace jusqu'à 40% d'immersion alors que toute la colonne était protégée pour des temps plus longs (180 j). Finalement, la persistance de la PC en ZdM est multifactorielle. Elle dépend de l'amplitude des marées, du temps d'exposition ainsi que du taux d'immersion. Son efficacité a été démontrée valable jusqu'à 45% d'immersion, pour des ZdM étendues.

## **Summary**

This PhD work focuses on understanding the mechanisms involved in cathodic protection (CP) in tidal zones (vertical zone between high tide and low tide levels). In 2015 a study by led by Ph. Refait *et al.* highlighted the unexpected persistence of CP even during emerged periods, which theoretically should not occur because of seawater withdrawal. Understanding the mechanisms involved in this spread-out CP could ultimately contribute to diminish the environmental impact of production and maintenance of structures such as offshore wind turbines. An initial study, covering the entire height of the La Rochelle commercial port tidal zone, showed that CP could be considered effective up to 45% of immersion rate (i.e. 74% of the tidal zone height). On the other hand, a study carried out at LaSIE laboratory aimed to investigate the behavior of steel during ebb tides in a more fundamental way. To this purpose, samples were set horizontally under thin layers of seawater (1 mm or 5 mm) and polarised under conditions of sufficient protection (-950 mV/Ag/AgCl<sub>3M</sub>) and insufficient protection (-750 mV/Ag/AgCl<sub>3M</sub>). Insufficient protection led to the formation of a thick layer of aragonite overlying a thin residual corrosion products layer. In addition, a thin layer of seawater enhances the protective character of the deposit formed under sufficient CP (-950 mV/Ag/AgCl<sub>3M</sub>). Furthermore, in the last research axis mentioned here, the evolution of CP parameters was monitored for 16 months of tidal cycles. For short periods (8 days), CP remained effective up to 40% of immersion rate, while the entire column was protected for longer times (180 days). Finally, the persistence of CP in tidal zone is multifactorial. It depends on tidal amplitude, exposure time and immersion rate. Its effectiveness has been demonstrated to be valid up to 45% immersion, for extended tidal zones.